



Czech Technical University in Prague
Faculty of Nuclear Sciences and Physical Engineering



DISSERTATION THESIS

Prague, 2010

Radek Fučík



Czech Technical University in Prague
Faculty of Nuclear Sciences and Physical Engineering



DISSERTATION THESIS

Advanced Numerical Methods for Modelling Two-Phase Flow in Heterogeneous Porous Media

Radek Fučík

A thesis submitted to the Faculty of Nuclear Sciences and Physical Engineering, Czech Technical University in Prague, in partial fulfilment of the requirements for the degree Doctor of Philosophy (Ph. D.) in Mathematical Engineering.

Český překlad anglického názvu: **Pokročilé numerické metody pro modelování dvoufázového proudění v heterogenním porézním prostředí**

Autor: Ing. Radek Fučík

Obor: Matematické inženýrství

Druh práce: Disertační práce

Vedoucí práce: Ing. Jiří MIKYŠKA, Ph.D.

Katedra matematiky, Fakulta jaderná a fyzikálně inženýrská, České vysoké učení technické v Praze

Školitel-Specialista: Tissa H. Illangasekare PhD, PE, P.Hyd, DEE, DWRE, AMAX Distinguished Chair of Environmental Science and Engineering and Professor of Civil Engineering Director, Center for Experimental Study of Subsurface Environmental Processes (CESEP) Colorado School of Mines, Golden, CO 80401, USA

Abstrakt: Práce představuje matematický model dvoufázového nemísivého a nestlačitelného proudění v rigidním heterogenním porézním prostředí. V rámci práce jsou shrnuta testovací řešení. Dále je odvozeno numerické schéma založené na metodě konečných objemů (VCFVM), které umožňuje zkoumat dynamický efekt v kapilárním tlaku. Numerické schéma je testováno pomocí analytických a semianalytických řešení a následně využito pro simulaci laboratorních experimentů s kapilárním tlakem za dynamických podmínek. Význam dynamického efektu v matematických modelech je diskutován za použití laboratorních dat s důrazem na materiálová rozhraní. V druhé části práce je prezentováno pokročilé numerické schéma založené na smíšené-hybridní metodě konečných prvků (MHFE) společně s nespojitým Galerkinovým (DG) přístupem. Toto numerické schéma je schopeno řešit vícefázové proudění v porézním prostředí s ostrými materiálovými rozhraními. Kromě toho může simulovat akumulaci nesmáčivé fáze na materiálovém rozhraní. MHFE-DG metoda je testována pomocí analytických a semianalytických řešení. Dále je tato metoda použita na simulaci několika dvourozměrných úloh popsanych v literatuře. Všechny modely mohou být použity pro realistické tekutiny a materiálové vlastnosti určené pomocí laboratorních experimentů.

Klíčová slova: Proudění v porézním prostředí, dvoufázové proudění, kapilarita, dynamický efekt v kapilárním tlaku, analytická řešení, Buckleyho-Leverettovo řešení, McWhorterovo-Sunadovo řešení, metoda konečných objemů, hybridní-smíšená metoda konečných prvků, nespojitá Galerkinova metoda, rozšířená kapilární podmínka na rozhraní, bariérový efekt.

***Title:* Advanced Numerical Methods for Modelling Two-Phase Flow in Heterogeneous Porous Media**

Author: Radek Fučík

Abstract: The thesis presents a mathematical model of two-phase immiscible and incompressible flow in a non-deformable heterogeneous porous material including the definition of the capillary pressure under dynamic conditions and summarizes available benchmark solutions. A numerical scheme based on the vertex-centered finite volume method (VCFVM) is developed and used to investigate the dynamic effect in capillarity. The VCFVM numerical scheme is tested using the benchmark solutions and then used to simulate laboratory experiment with capillary pressure under dynamic conditions. The importance of the dynamic effect in the mathematical models is discussed using the laboratory-determined data emphasizing the significance of the capillarity under dynamic conditions at material interfaces. In the second part of the thesis, an advanced mixed-hybrid finite element (MHFE) method with the discontinuous Galerkin (DG) approach is adopted. The numerical scheme is capable of solving multiphase flow problems in porous media with sharp material interfaces. Additionally, it can simulate the non-wetting phase pooling at material interfaces. In order to show its applicability, the MHFE-DG method is tested against benchmark solutions using laboratory data from literature. All models can be used for realistic fluid and material properties determined by means of the laboratory experiments.

Key words: Flow in porous medium, two-phase flow, capillarity, dynamic effect in capillary pressure, closed-form solutions, Buckley-Leverett solution, McWhorter-Sunada semi-analytical solution, vertex-centered finite volume method, mixed-hybrid finite element method, discontinuous Galerkin method, extended capillary pressure condition, barrier effect

I confirm having prepared the thesis by my own and having listed all used sources of information in the bibliography.

Radek Fučík

Prague, June 11, 2010

State of Art

In the past decades, the interest in understanding and prediction of multiphase flow in the subsurface has increased extensively due to the widespread increase of awareness of the most alarming contemporary problems such as the water contamination by organic solvents. Additionally, the importance of the traditional petroleum engineering problems increases as the worldwide reserves of the *easily-obtainable-petroleum* are running low. Compared to the previous decades, the unflagging boom in the increasing computer power allows to develop more complex, reliable, and accurate mathematical models capable of simulating such multiphase flow problems in the subsurface.

A reliable model of capillarity is one of the key aspects in the modelling of multiphase flow of immiscible and incompressible fluids in porous media. In most past modelling efforts, various capillary pressure–saturation models by Brooks and Corey [10] or van Genuchten [48] were developed based on laboratory experiments where the capillary pressure and saturation were measured under equilibrium conditions. However, the question has been raised on whether these static models capture the dynamic behavior accurately when the fluid phases are in motion. Recently, alternative models based on both empirical and theoretical approaches have been proposed to deal with these dynamic effects associated with fluid flow.

Another interest is focused upon the Non-Aqueous Phase Liquid (NAPL) behavior at sharp texture transitions in the petroleum reservoirs or contaminated aquifers. Laboratory experiments show that such material inhomogeneities can increase the retention of the contaminants immensely. Therefore, it is desirable to develop mathematical and numerical models such that the behavior of the NAPLs is simulated correctly. These models then serve as a key tool when dealing with various multiphase flow problems in the industry, ecology, and cutting-edge technology.

Research Goals

The primary goal of the dissertation thesis is to investigate flow of two immiscible and incompressible fluids (phases) in heterogeneous porous materials using mathematical models.

In details, the main goals of this thesis are

- to present a mathematical model of two-phase immiscible and incompressible flow in a non-deformable heterogeneous porous material including the dynamic effect in the capillary pressure,
- to present an overview of available benchmark solutions,
- to develop a numerical scheme that can be used to investigate the dynamic effect in capillarity,
- to discuss the importance of such integration of the dynamic effect in the mathematical model using the laboratory-determined data, and
- to develop a higher-order numerical method capable of solving the multiphase flow problems in a porous medium with sharp material interfaces.

The models should be applicable for realistic fluid and material properties determined by means of laboratory experiments.

Methods Used

There are two distinct numerical schemes developed in this thesis. First, a numerical model capable of simulating the dynamic effect in capillarity is based on the Vertex-Centered Finite Volume Method (VCFVM) in one dimension. The time discretization is carried out using the backward Euler scheme. The resulting non-linear system of equations is solved using the Newton-Raphson iteration method, where the Jacobi matrix is block tri-diagonal. A special method is developed to treat conditions at material interfaces and verified using benchmark solutions.

Another numerical scheme is designed to simulate the multiphase flow in heterogeneous porous media that is based on the Implicit-Pressure-Explicit-Saturation (IMPES) approach, where the Mixed-Hybrid Finite Element (MHFE) method is used together with the Discontinuous Galerkin (DG) approximation. The resulting systems of linear equations are solved either by direct solvers (for smaller systems) or iteratively using the Conjugate Gradient (CG) method.

Stability of the numerical schemes is achieved using the upwind technique and the slope limiter procedure when using the higher-order MHFE-DG approach.

Research Results

In this thesis, we present the complete derivation of both numerical schemes. The numerical schemes are verified using benchmark solutions developed by Buckley and Leverett [11], McWhorter and Sunada [80], van Duijn and de Neef [28], and by the author [45], [46].

The importance of the dynamic effect in capillarity is investigated using the VCFVM. The validity of the numerical scheme is discussed by means of the semi-analytical solutions. The numerical scheme is used to simulate a drainage experiment where the sand and fluid properties were known. Then, the numerical scheme is used to simulate a laboratory experiment in a homogeneous column including three major models of the dynamic effect coefficient τ and the respective results are presented and discussed. The presented numerical scheme can handle porous medium heterogeneity and it is used to simulate a fictitious experimental setup with two different sands. As a result, the penetration time of air phase through layered porous medium for models including dynamic effects varied between 50% to 150% compared to static models of capillary pressure-saturation relationship. Additionally, the accumulation time of air at a material interface (i.e., delay of the air at the interface due to capillary barrier effect) is investigated as a function of the ratio between air-entry pressure values of the adjacent sands emphasizing the differences between the dynamic and static capillary pressure models.

The MHFE-DG method is tested using the benchmark solutions available for two-phase flow in homogeneous and heterogeneous porous media. Additionally, a comparison with the VCFVM is quantified using L_1 and L_2 error norms. It is found that the MHFE-DG approach involves less numerical diffusion than the VCFVM when simulating an advection dominated flow. In case of capillarity driven flow, both VCFVM and MHFE-DG methods give similar results for the one-dimensional benchmark solutions. A series of simulations is computed for two-phase flow problems in heterogeneous porous media showing that the MHFE-DG numerical scheme simulates the behavior of fluids at material interfaces in agreement with laboratory determined data. Additionally, the difference between the first-order finite volume (MHFE-FV) and the second-order discontinuous Galerkin (MHFE-DG) approach is found to be less important in all two-dimensional simulations with both gravity and capillarity included.

List of Notation	vii
Introduction	1
1. Modelling Immiscible Fluid Flow in Porous Medium	5
1.1. Porous Medium	5
1.2. Phase	5
1.3. Continuum Approach to Porous Medium	6
1.4. Porosity	7
1.5. Single Phase Flow	7
1.5.1. Mass Balance	7
1.5.2. Darcy Law	8
1.6. Multiphase Flow	9
1.6.1. Saturation	9
1.6.2. Residual Saturation	10
1.6.3. Effective Saturation	10
1.6.4. Governing Equations	10
1.7. Capillarity	10
1.7.1. Microscale Capillarity	11
1.7.2. Macroscale Capillarity: Static Case	12
1.7.3. Macroscale Capillarity: Dynamic Case	13
1.7.4. Capillary Hysteresis	14
1.8. Relative Permeability	15
1.9. Fluid Behavior at Material Interfaces	16
1.10. Problem Formulations	18
1.10.1. Pressure–Saturation Formulation	18
1.10.2. Flow Potential–Saturation Formulation	19
2. Benchmark Solutions	21
2.1. One-Dimensional Saturation Equation	21
2.2. Pure Advection Case	23
2.2.1. Method of Characteristics	24
2.2.2. Entropy Condition : Convex Hull Construction	25
2.2.3. Analytical Solution	26
2.3. Advection and Diffusion Case in Homogeneous Medium	27

2.3.1.	Derivation of Semi-Analytical Solution	28
2.3.2.	Solution of Integral Equation	30
2.4.	Advection and Diffusion Case in Heterogeneous Medium	30
3.	Significance of Dynamic Effect in Capillary Pressure	35
3.1.	Fully Implicit Vertex-Centered Finite Volume Method in 1D	36
3.1.1.	Numerical Scheme	36
3.1.2.	Material Interfaces	38
3.1.3.	Initial and Boundary Conditions	39
3.1.4.	Numerical Solution	39
3.2.	Verification of Numerical Scheme	42
3.2.1.	Benchmark I	42
3.2.2.	Benchmark II	43
3.2.3.	Benchmark III	43
3.2.4.	Benchmark IV	44
3.2.5.	Benchmark V	44
3.2.6.	Experimental Order of Convergence	45
3.2.7.	Benchmark VI: Barrier Effect Verification	46
3.3.	Simulation of Laboratory Experiment	46
3.3.1.	Description of Experimental Setup	47
3.3.2.	Numerical Simulation	48
3.3.3.	Dynamic Coefficient Sensitivity Analysis	53
3.4.	Numerical Simulations in Layered Medium	55
3.4.1.	Simulation 1: Laboratory Measured Sands	55
3.4.2.	Simulation 2: Entry Pressure Sensitivity Analysis	57
3.5.	Concluding Remarks	60
4.	A Higher-Order Scheme for Two-Phase Flow in Layered Media	61
4.1.	Mixed-Hybrid Finite Element & Discontinuous Galerkin Method	62
4.1.1.	Velocity Approximation	63
4.1.2.	System of Equations for Capillary Potentials	66
4.1.3.	Discretization of Volumetric Balance Equation	69
4.1.4.	System of Equations for Wetting-Phase Potentials	71
4.1.5.	Saturation Approximation	72
4.1.6.	Time Discretization of Saturation Equation	76
4.1.7.	Slope Limiter	77
4.1.8.	Computational Algorithm	78
4.2.	Verification of Numerical Scheme in Homogeneous Medium	80
4.2.1.	Benchmark I	80
4.2.2.	Benchmark II	83
4.2.3.	Benchmark III	85
4.3.	Simulation of Flow in Layered Media	86
4.3.1.	Benchmark IV	86
4.3.2.	Benchmark V	88
4.3.3.	Barrier Effect Test Problem in Layered Porous Medium	90
4.4.	Application of MHFE-DG Method in 2D Heterogeneous Problems	94
4.4.1.	Low Permeable Lens in a Sandbox	94
4.4.2.	Highly Heterogeneous Medium	102
4.4.3.	Inclined Interface	110
4.5.	Concluding Remarks	115

Conclusion	117
A. Piecewise Linear Basis Functions	119
A.1. Piecewise Linear Basis Functions in 1D	119
A.2. Piecewise Linear Basis Functions in 2D	119
B. Fluid and Material Properties	121
B.1. Fluids	121
B.2. Sand A	122
B.3. Sand B	123
B.4. Sand C	124
B.5. Sands D and E	125
B.6. Sands F and G	125
B.7. Sands H, I, J, and K	126
B.8. Sand L and M	127
Bibliography	129

Abbreviations

Abbreviation	Meaning	Page
CESEP	Center of Experimental Study of Subsurface Environmental Processes	3
DNAPL	Dense Non-Aqueous Phase Liquid	6
DG	Discontinuous Galerkin method	62
<i>EOC</i>	Experimental Order of Convergence	45
FD	Finite Difference method	62
FVM	Finite Volume Method	62
IMPES	Implicit-Pressure-Explicit-Saturation method	62
LNAPL	Light Non-Aqueous Phase Liquid	6
MHFE	Mixed-Hybrid Finite Element method	62
NAPL	Non-Aqueous Phase Liquid	6
ODE	Ordinary Differential Equation	75
REV	Representative Elementary Volume	7
RK	Runge-Kutta method	76
VCFVM	Vertex-Centered Finite Volume Method	36

Indices

Subscripts

Notation	Meaning	Page
α	General phase index	
w	Wetting phase related quantity	11
n	Non-wetting phase related quantity	11
c	Capillary pressure related quantity	
$micro$	Microscopic scale related quantity	7
$macro$	Macroscopic scale related quantity	7

Superscripts

Notation	Meaning	Page
-1	Inverse function	17
d	Dimension of the related space (e.g., \mathbb{R}^d)	18
\mathcal{D}	Dirichlet boundary condition	18
$i, i + 1$	Time levels	37
ini	Initial value of a quantity	39
I, II	Indicators for two different porous media	17
\mathcal{N}	Neumann boundary condition	18
num	Numerical solution	45
an	Analytical solution	45
T	Matrix transpose	40

Latin symbols

Notation	SI Units	Description	Page(s)
A	$[m\ s^{-\frac{1}{2}}]$	McWhorter and Sunada flow rate coefficient	27
$B(x_0, r)$	$[m]^3$	Ball in \mathbb{R}^3 centered around x_0 with radius r	7
\mathbf{C}	$[-]$	Runge-Kutta coefficient	77
D	$[m^2\ s^{-1}]$	Capillary diffusion function.	22
F	$[s^{-1}]$	Specific source/sink term.	8
f_α	$[-]$	Fractional flow function of the phase α	22
\mathbf{F}	$[s^{-1}]$	Right-hand-side of a system of ordinary differential equations	76
g, \mathbf{g}	$[m\ s^{-2}]^d$	Gravitational acceleration ($g = 9.81\ ms^{-2}$)	14, 8
G	$[-]$	Function used in modified iteration schemes	30
h	$[m]$	Mesh size	45
\mathbf{K}	$[m^2]^{d \times d}$	Absolute permeability tensor in \mathbb{R}^d	8
K	$[m^2]$	Intrinsic soil permeability	8
k_r	$[-]$	Relative permeability function	10
n	$[-]$	Van Genuchten parameter	13
\mathbf{n}	$[m]$	Outward unit normal	18
$\mathcal{N}_{K,E}$	$[-]$	Set of all neighboring elements of side E	78
m	$[-]$	Van Genuchten parameter	13
p	$[kg\ m^{-1}\ s^{-2}]$	Fluid pressure (macroscopic)	8
p_c	$[kg\ m^{-1}\ s^{-2}]$	Capillary pressure	12
p_c^{eq}	$[kg\ m^{-1}\ s^{-2}]$	Static capillary pressure	13
p_d	$[kg\ m^{-1}\ s^{-2}]$	Entry pressure	12
q	$[-]$	Number of material interfaces	39
r	$[m]$	Radius	7
Re	$[-]$	Reynolds number	9
s	$[m\ s^{-1}]$	Fractional shock speed	25
S_α	$[-]$	Saturation of the phase α	9
$S_{r,\alpha}$	$[-]$	Residual saturation of the phase α	10
$S_{e,\alpha}$	$[-]$	Effective saturation of the phase α	10
S^*	$[-]$	Buckley and Leverett postshock value	25
S_0	$[-]$	Boundary value of S_w	24
S_i	$[-]$	Initial and/or boundary value of S_w	24
T	$[s]$	Final time of numerical simulation	36
\mathbf{u}	$[m\ s^{-1}]$	Macroscopic apparent velocity	8
\mathbf{u}_T	$[m\ s^{-1}]$	Total velocity	22, 62
u_{shock}	$[m\ s^{-1}]$	Shock velocity	25
V, W	$[m]$	Vertex in \mathbb{R}	37
\mathbf{V}, \mathbf{W}	$[m]^d$	Vertex in \mathbb{R}^d	64
V	$[m^3]$	Volume	7
\mathbf{x}	$[m]^d$	Position vector	19
x_{RH}	$[m]$	Rankine–Hugoniot shock front position	26

Greek symbols

Notation	SI Units	Description	Page(s)
α	$[kg^{-1} m s^2]$	Van Genuchten parameter	13
α_S	$[-]$	Stauffer scaling parameter	14
ϵ	$[-]$	Order of convergence of a numerical scheme	45
ϵ_{tol}	$[-]$	Tolerance used in the stability check procedure	80
η	$[-]$	Parameter used in the method of characteristics	24
γ	$[-]$	Void space indicator function	7
Γ	$[-]$	Subset of boundary	18
δ	$[m]$	Mean diameter of grain size	9
λ_α	$[kg^{-1} m s]$	Mobility of the phase α	10
λ	$[-]$	Brooks and Corey pore size distribution index	13
λ_t	$[kg^{-1} m s]$	Total mobility	22
μ	$[kg m^{-1} s^{-1}]$	Dynamic viscosity	6
ν	$[m^2 s^{-1}]$	Kinematic viscosity	9
π	$[kg m^{-1} s^{-2}]$	Microscopic pressure	12
π_c	$[kg m^{-1} s^{-2}]$	Microscopic capillary pressure	12
ρ	$[kg m^{-3}]$	Volumetric density	6
σ	$[kg s^{-2}]$	Surface tension	11
τ	$[kg m^{-1} s^{-1}]$	Dynamic effect coefficient	13
Φ	$[-]$	Porosity	7
ψ	$[kg m^{-1} s^{-2}]$	Flow potential	19
ψ_c	$[kg m^{-1} s^{-2}]$	Capillary potential	19
ψ_c^{eq}	$[kg m^{-1} s^{-2}]$	Static capillary potential	19
ω	$[-]$	Contact angle	11
Ω	$[-]$	Domain in \mathbb{R}^d	18
$\zeta_{\Delta t}$	$[-]$	Time step modification factor	42, 80
ζ_{it}	$[-]$	Number of successive convergent solutions	42
ζ_{in}	$[-]$	Number of successive time steps	80
ζ_ℓ	$[-]$	Maximal number of iterations	42
ζ_G	$[-]$	Tolerance in the Newton–Raphson method	42

Mathematical Toolbox

Tool	Description	Page
$ A _d$	$ A _d = \int_A 1$ Lebesgue's measure in \mathbb{R}^d , $d = 1, 2, 3$.	6
δ_{AB}	$\delta_{AB} = \begin{cases} 1 & \text{if } A = B \\ 0 & \text{otherwise.} \end{cases}$ Kronecker symbol.	64
$H(\text{div}, \Omega)$	Space of functions with square-integrable weak divergences.	63
$L_k(\Omega)$	Space of functions whose absolute value raised to the k -th power has a finite Lebesgue integral over Ω .	45
$\#M$	Number of elements in a set M	68
$[\mathbf{x}]_j$	j -th component of vector \mathbf{x}	63

Motivations

Today, most of the industrially developed countries invest substantial amount of resources to understand and protect drinking water in the subsurface. Due to industrial activities, the water saturated zones of aquifers are endangered by substances with a very low solubility in water such as oil or chlorinated hydrocarbons. When these substances, generally referred to as Non-Aqueous Phase Liquids (NAPLs), enter the aquifer, they can serve as a long-time source of groundwater contamination. A prediction of their behavior in the subsurface is an important step towards their partial or complete removal from the contaminated area. Therefore, two-phase processes have been studied intensively in engineering, soil physics, and hydrogeology over several decades [5], [57].

Currently, there exists two principal approaches in the prediction of flow and transport in the subsurface: laboratory experiments and mathematical modelling. Multiple mathematical models have been developed based on the Darcy law [23] that describes a linear relationship between the velocity of water and the pressure gradient in a column filled with a porous material. By means of the laboratory experiments, the material and fluid properties are determined and further investigated in order to verify the mathematical models. As a result, mathematical models calibrated on these laboratory determined data serve as a reliable instrument in simulation of flow in porous media in the real-life applications.

The propagation of NAPLs through water saturated zones is usually driven by two primary mechanisms. The NAPL is displaced due to external forces (externally imposed flow, gravity) and capillarity. Capillary forces, well observed in thin tubes called *capillaries*, originate from the contact of a solid matrix and two immiscible phases within the porous material. Not only in porous media, this phenomenon of capillarity plays an important role also in many other fields, for instance, the capillary action is essential for the drainage of constantly produced tear fluid from the eye. Especially in heterogeneous porous materials, the capillary forces have an important impact on the flow across interfaces between materials with different capillarity properties. These capillary forces are responsible for the complex entrapment morphologies of NAPL shown in the figure on page 2.

In this thesis, we address several topics concerning flow of two immiscible and incompressible fluids (phases) in homogeneous and heterogeneous porous materials.

A reliable model of capillarity is the key aspect in the modelling of two-phase flow of immiscible and incompressible fluids in porous media. Various capillary pressure-saturation models by Brooks and Corey [10] or van Genuchten [48] were developed based on laboratory experiments where the capillary pressure and saturation were measured under equilibrium conditions. However, both empirical and theoretical studies indicate that these *static* capillary pressure models



The behavior of NAPL in heterogeneous porous materials. Pictures show a light non-aqueous phase liquid (red spill) in a water saturated layered medium with an inclined interface (left) and highly heterogeneous medium with random distribution of heterogeneities (right), respectively (provided by CESEP, Colorado School of Mines).

may not be suitable to model behavior of fluids when the system is in motion. Thus, a modified capillary pressure–saturation relationship has been proposed that includes an additional term which is referred to as the *dynamic effect* term. In order to understand implications of the dynamic effect in capillarity, several laboratory experiments and mathematical simulations have been carried out by various researchers. However, many questions still remain unanswered such as the influence of the dynamic effect coefficient on a flow in heterogeneous porous materials. Additionally, a suitable functional model for the dynamic effect term with respect to the saturation is still unknown.

A lot of mathematical models have been developed that describe the displacement and transport processes in the subsurface. Currently, there exists a series of commercial software packages like Fluent or MODFLOW that are used to model NAPL contamination problems and are quite often employed in environmental projects of cleanup of *old ecological contaminations*. Most of them are based on the basic finite difference (FD) or finite volume (FV) methods that have only a first–order of accuracy. This implies that their results are usually distorted by numerical diffusion. These deficiencies can be resolved using a higher–order numerical scheme based on the mixed-hybrid finite element (MHFE) method that allows for accurate representation of the velocities across sides of a finite element. Additionally, such approach can be further improved by using the discontinuous Galerkin (DG) method that approximates saturation as piecewise discontinuous per elements since the saturation is usually discontinuous across material interfaces. In a series of papers [63], [64], [65], such a combined MHFE-DG approach was investigated and a numerical scheme suitable for simulating flow in heterogeneous porous media has been proposed. However, some aspects of this MHFE-DG method have not been fully resolved such as thorough investigation of the convergence of the numerical scheme or a simulation of NAPL pooling at material interfaces referred to as the *capillary barrier effect*.

The text is organized in four chapters in the following way.

In Chapter 1, we present fundamental description of the mathematical model of multiphase flow in porous media. We emphasize the differences between the definitions of the capillary pressure p_c at the micro–scale and macro–scale. In particular, we focus on the *dynamic effect* in the capillary pressure–saturation relationship developed in [49], [50], [54], and [56]. We conclude Chapter 1 by a summary of the mathematical model represented by a system of partial differential equations supplied with the initial and boundary conditions.

In Chapter 2, we present a brief overview of the analytical and semi-analytical solutions together referred to as the *benchmark solutions*. First, we describe the Buckley and Leverett analytical solution applicable to pure hyperbolic problems. Then, a family of semi-analytical solutions are described that can be obtained for pure diffusion and advection–diffusion problems

in both homogeneous and layered porous materials. We extended applicability of these semi-analytical solutions to a larger set of input conditions and even to a larger family of admissible problems than in the original paper [80].

In Chapter 3, the significance of the dynamic effect in the capillary pressure–saturation relationship is investigated. We propose a fully implicit numerical scheme based on the Vertex-Centered Finite Volume Method (VCFVM) capable of solving systems of multiphase flow equations with the dynamic effect in capillarity. We use the benchmark solutions summarized in Chapter 2 to verify that the numerical scheme converges for the static (classical) model of the capillary pressure p_c . These numerical solutions obtained using the static p_c are used as a reference solution when investigating the significance of the dynamic effect in the capillary pressure.

In Chapter 4, we consider a higher-order numerical scheme that is suitable for simulation of the two-phase flow including the capillary barrier effect with static capillary pressure only. A numerical method is derived that combines the Mixed-Hybrid Finite Element (MHFE) and the Discontinuous Galerkin (DG) methods. The numerical scheme is based on [4], [33], [65], [63], and during its derivation, several important modifications are proposed to assure the existence and uniqueness of the numerical solution. Our main goal is to extend the MHFE-DG method for heterogeneous porous media to simulate pooling effects at material interfaces (the barrier effect). The benchmark solutions from Chapter 2 are used to investigate convergence of the MHFE-DG method. To demonstrate its applicability, several laboratory experiments in heterogeneous porous media are simulated.

In Appendix A, we describe basis functions of the piecewise linear discontinuous Galerkin space in \mathbb{R}^1 and \mathbb{R}^2 . In Appendix B, the description of all sand and fluid parameters, to which we refer in the text, is presented for convenience.

Acknowledgment

This dissertation thesis could not be written without the long-term cooperation between the Department of Mathematics, Faculty of Nuclear Sciences and Physical Engineering, Czech Technical University in Prague and the Center for Experimental Study of Subsurface Environmental Processes (CESEP), Colorado School of Mines, Golden, Colorado.

First of all, I would like to thank my supervisor Ing. Jiří Mikyška, Ph. D., Czech Technical University in Prague, Faculty of Nuclear Sciences and Physical Engineering for his guidance, help and support during the preparation of this thesis. I am also grateful to Prof. Tissa H. Illangasekare, CESEP, Colorado School of Mines, Golden, Colorado, for providing experimental datasets and for his ideas and insights into the field concerning flow and transport in porous media. I would also like to thank Prof. Toshihiro Sakaki for many helpful discussions on the dynamic effect in capillarity, for providing the experimental datasets, and also for kind preparation of sand samples shown in Appendix B.

Special thanks belong to doc. Ing. Dr. Michal Beneš, Czech Technical University in Prague, Faculty of Nuclear Sciences and Physical Engineering whose enthusiasm and foresight allowed the cooperation with Colorado School of Mines. I am also indebted to him for introducing me into the mathematical modelling and for providing guidance and support throughout my scientific life.

The work was written within the framework of the following projects:

- Internal grant No. CTU0803514/2008 of the Czech Technical University in Prague,
- Project "Applied Mathematics in Technical and Physical Sciences" MSM 6840770010, Ministry of Education of the Czech Republic.

- Project "Environmental modelling" KONTAKT ME878, Ministry of Education of the Czech Republic.
- Project "Jindřich-Nečas Center for Mathematical Modelling" LC06052, Ministry of Education of the Czech Republic.
- National Science Foundation through the award 0222286 (CMG RESEARCH: "Numerical and Experimental Validation of Stochastic Upscaling for Subsurface Contamination Problems Involving Multiphase Volatile Chlorinated Solvents").
- Project "Mathematical Modelling of Multiphase Porous Media Flow" 201/08/P567 of the Czech Science Foundation (GA ČR).

Innumerable computer software tools were used during preparation of the numerical results and the text of the thesis. I would like to especially acknowledge the use of OFELI, a C++ language library of finite elements together with UMFPACK, a set of routines for solving unsymmetric sparse linear systems, [24], [25], [26], [27]. A commercial software Comsol Multiphysics was used for generating two-dimensional meshes.

The text was typeset in $\text{\LaTeX} 2_{\epsilon}$ with the help of KOMA-Script. All figures and graphs were created with *Asymptote*.

In this chapter, we present an introduction to the mathematical modelling of the multiphase flow of immiscible and incompressible fluids in a porous medium. First, we describe the fundamental terminology and give definitions of the respective physical quantities. Then, we provide governing equations for single and two-phase flow.

1.1. Porous Medium

A *porous medium* is a body composed of a persistent *solid matrix* (also called *solid phase*) and a *void space* (or a *pore space*), [5]. Figure 1.1 shows an example of a two-dimensional cross-section of a porous medium filled with two liquid phases: water and oil.

In its most general sense, almost every material around us can be considered as porous if it contains void space within. However, this definition is not useful for the development of a relevant mathematical model. When in contact with water, for instance, a slice of the famous *Emmental cheese* has a significantly different behavior than a *bath sponge*, although they fit the commonly used definition. Once wetted, the sponge will absorb substantial amount of water by its microscopic interconnected pore network due to capillarity. In contrast, the capillary forces will be negligible in the case of large, single cheese holes.

The size and morphology is the key in understanding processes in a porous medium. Hence, the following assumptions are placed upon the geometry and dimensions of the porous medium, [2]:

- A. The pore space is interconnected since no flow can take place in a disconnected void space.
- B. The dimensions of the void space must be sufficiently large compared to the dimensions of the fluid molecules.
- C. The dimensions of the pore space must be small enough so that the fluid flow is governed by adhesive forces at fluid-solid interfaces and cohesive forces at fluid–fluid interfaces in multiphase systems. This excludes cases like a network of pipes from the definition of porous medium.

1.2. Phase

A phase is considered as a chemically homogeneous portion of a system that is separated from other such portions by a definite physical boundary.

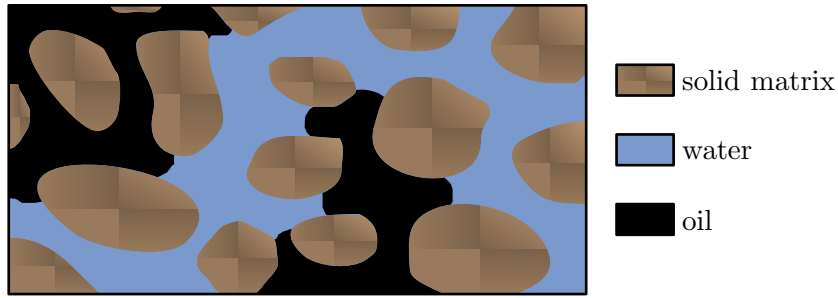


Figure 1.1.: Illustration of a porous medium filled with water and oil (two-phase system).

The necessity of a definite physical boundary between two or more phases implies that no more than one gaseous phase can be present in a multiphase system since gases are always completely miscible. A phase can be formed from one or more fluids and it is characterized by its *dynamic viscosity* μ [$Pa\ s$] and *volumetric mass density* ρ [$kg\ m^{-3}$].

Flow of water and other phases such as oil, chlorinated hydrocarbons, CO_2 , or air in porous media is studied in the majority of cases. Generally, we use the abbreviation NAPL which stands for the Non-Aqueous Phase Liquid, i.e., liquids immiscible with water. These liquids can be further divided into dense NAPLs (DNAPLs) and light NAPLs (LNAPLs) with higher and lower density than water, respectively.

1.3. Continuum Approach to Porous Medium

Consideration of different dimension scales is important in the modelling of flow in porous media. Figure 1.2 depicts different magnifications of a porous medium from the *macroscale* (a) through the *microscale* (b) to the molecular *nanoscale* (c).

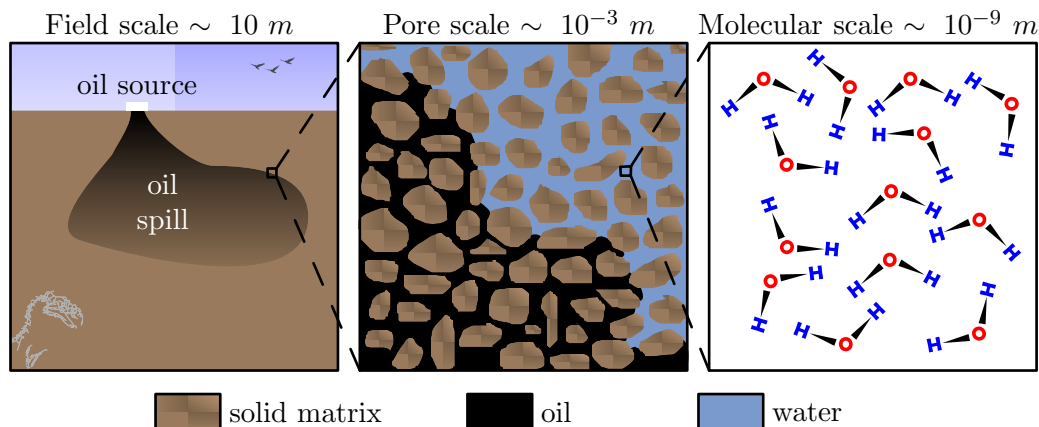


Figure 1.2.: Different scales in a porous medium illustrates a typical contamination problem.

Equations of fluid dynamics in porous media need to be provided with a set of boundary and initial conditions. However, as shown in Figure 1.2, the boundary conditions for a macroscopic problem can neither be prescribed at microscale nor at molecular scale due to practically random geometry of the porous medium. In order to develop a mathematical model, a concept of porous medium as a continuum at macroscopic scale is needed.

At each point of the macroscale continuum, an average of the microscopic quantities over a *representative elementary volume (REV)* is assigned. Bear and Verruijt [5] define the REV

as a volume that is sufficiently large to statistically estimate all relevant parameters of the void space configuration and small enough to be considered as a negligible portion of the total volume from the macroscopic scale. If such a REV cannot be found then the presented macroscopic theory of flow in porous media cannot be applied.

This process leads to *macroscopic equations* that are independent of the exact description of the microscopic configuration, because only statistical properties of the porous medium and the fluid phases are taken into account. Furthermore, at the macroscale microscopic (or even nanoscopic) physical quantities are represented only as averages over a chosen volume which may lead to the lack of information such as interfacial contact surface between the fluid–fluid and fluid–solid systems.

1.4. Porosity

Porosity ϕ is a macroscopic quantity that describes the ratio of void space within a volume of a porous material to that volume. Mathematically, the porosity is defined as

$$\phi(\mathbf{x}_0) = \frac{1}{|V|_3} \int_V \gamma(\mathbf{x}) d\mathbf{x}, \quad (1.1)$$

where the volume $V = B(x_0, r)$ is a ball of a radius r centered around x_0 and γ is the indicator function of the void space of the porous medium in a volume V given by

$$\gamma(\mathbf{x}) = \begin{cases} 1 & \text{for } \mathbf{x} \text{ in the void space,} \\ 0 & \text{for } \mathbf{x} \text{ in the solid matrix,} \end{cases} \quad \forall \mathbf{x} \in V. \quad (1.2)$$

In (1.2) the macroscale porosity is obtained by averaging the microscopic void space indicator function over V , where V has to be chosen such that the value of the averaged quantity does not depend on the exact size of the averaging volume. A rough plot of porosity values in function of the averaging volume size r is sketched in Figure 1.3. In an infinitesimally small volume, the porosity is strictly 0 or 1 based on a given position inside a solid grain or void space, respectively. As the averaging volume increases in size, the porosity becomes more or less constant up to a limit, where macroscopic inhomogeneities occur (fractures, different grain sizes, etc.). The averaging volume V is considered as the representative elementary volume REV, if there exist radii r_{micro} and r_{macro} such that the value of the averaged quantity does not depend on the radius r within the range

$$r_{micro} \ll r \ll r_{macro}. \quad (1.3)$$

Another way to obtain macroscopic quantities out of the microscale variables is the homogenization technique which is based on the mathematical theory on asymptotic functional expansion, [61]. Some of its principles have been discussed in [40].

1.5. Single Phase Flow

We first summarize equations describing flow of a single phase only. In the following, we apply the mass-conservation law to the fluid in porous medium and present the famous *Darcy law*.

1.5.1. Mass Balance

Let us consider a porous domain Ω filled with a single fluid phase. Macroscopic fluid mass conservation law, or the *continuity theorem*, is expressed by the following partial differential

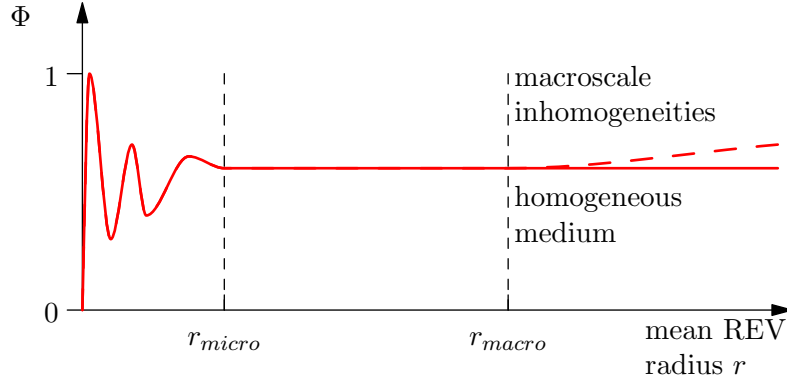


Figure 1.3.: Porosity as a function of the REV mean radius r .

equation

$$\frac{\partial(\phi \varrho)}{\partial t} + \nabla \cdot (\varrho \mathbf{u}) = \varrho F, \quad \text{in } \Omega, \quad (1.4)$$

where the quantities have the following meaning:

$\phi(\mathbf{x})$	$[-]$	Porosity of the porous medium defined in (1.1).
$\mathbf{u}(t, \mathbf{x})$	$[m \text{ s}^{-1}]$	<i>Macroscopic apparent velocity.</i> This velocity is observed at the macroscale. On the microscopic level, the flow takes only place through the pore channels of the porous medium where the average velocity \mathbf{u}/ϕ is observed, see [2].
$\varrho(t, \mathbf{x})$	$[kg \text{ m}^{-3}]$	<i>Volumetric mass density</i> of the fluid that can depend on position or pressure for a compressible fluid.
$F(t, \mathbf{x})$	$[s^{-1}]$	Specific source/sink term.

1.5.2. Darcy Law

By using the local averaging techniques [114], [94] or the homogenization procedure [61], the momentum conservation of the Navier-Stokes equation at the microscale can be reduced to a macroscopic principle

$$\mathbf{u} = -\frac{1}{\mu} \mathbf{K}(\nabla p - \varrho \mathbf{g}), \quad (1.5)$$

where the quantities have the following meaning:

$\mathbf{u}(t, \mathbf{x})$	$[m \text{ s}^{-1}]$	Macroscopic apparent velocity already introduced in (1.4).
$\mathbf{K}(\mathbf{x})$	$[m^{-2}]$	Symmetric tensor of <i>absolute permeability</i> , that can depend on position in the case of heterogeneous medium. In homogeneous and isotropic porous medium, $\mathbf{K} = K \mathbf{I}$, where \mathbf{I} is the identity tensor and K is the scalar absolute permeability, also called <i>intrinsic soil permeability</i> .
$\mu(t, \mathbf{x})$	$[Pa \text{ s}]$	Dynamic viscosity of the fluid.
$p(t, \mathbf{x})$	$[Pa]$	<i>Fluid pressure.</i>
\mathbf{g}	$[m \text{ s}^{-2}]$	Gravitational acceleration vector.

This principle was first described by Henry Darcy, a French engineer who investigated the flow of water in vertical homogeneous sand filters in connection with the fountains of the city of Dijon. In 1856, he published his observations and the law (1.5) in [23]. It is valid only for slow flows of Newtonian fluids through porous media with rigid solid matrices.

The validity range of Darcy law can be expressed by the *Reynolds number* Re given by

$$Re = \frac{\delta}{\nu} \|\mathbf{u}\|. \quad (1.6)$$

It is a dimensionless quantity that characterizes the ratio of the fluid velocity $\|\mathbf{u}\|$ with respect to the fluid *kinematic viscosity* ν [$m^2 s^{-1}$] and the representative microscopic length δ [m] describing the mean diameter of grain size in the solid matrix. The Darcy law (1.5) is valid for values of Re from 1 (fine sand) to 10 (coarse sand), which represents most of the practical porous media problems. More complex nonlinear Darcy law has to be employed for greater values of Re , e.g., for modelling of flow in a very close vicinity of large pumping or recharging wells, or in very porous matters like cavernous limestone or larger stones [5]. In this thesis, we assume that (1.5) holds in all considered cases.

1.6. Multiphase Flow

In this section, we study basics of the two-phase flow in a porous medium, but the respective quantities can be generalized for a multi-phase flow formulation as well. We resume the definitions and explanations presented in [2], [5], and [57].

1.6.1. Saturation

Let us consider a REV of a porous medium occupied by several phases. At a microscale, every point of the REV is occupied either by the solid phase or by exactly one of the fluid phases. Let γ_α denotes the indicator function of the fluid phase α defined by a formula similar to (1.2) as

$$\gamma_\alpha(t, \mathbf{x}) = \begin{cases} 1 & \text{if } \mathbf{x} \text{ belongs to phase } \alpha \text{ at time } t \\ 0 & \text{otherwise} \end{cases} \quad \forall \mathbf{x} \in \Omega. \quad (1.7)$$

This α -phase indicator function allows us to define a dimensionless macroscopic quantity called *saturation* S_α [-] of the phase α by the relation

$$S_\alpha(t, \mathbf{x}_0) = \frac{\int_{REV} \gamma_\alpha(t, \mathbf{x}) d\mathbf{x}}{\int_{REV} \gamma(t, \mathbf{x}) d\mathbf{x}}, \quad (1.8)$$

where $\mathbf{x}_0 \in REV$.

The α -phase saturation S_α expresses the volumetric ratio of the phase α to the total void space at a given position \mathbf{x} and time t . Therefore, the saturation is always bounded between 0 and 1,

$$0 \leq S_\alpha \leq 1, \quad (1.9)$$

and the sum of the α -phase saturations over all phases in the system is 1

$$\sum_{\alpha} S_\alpha = 1. \quad (1.10)$$

By Greek subscripts α or β , we denote quantities that correspond to the phase α or β , respectively.

1.6.2. Residual Saturation

It is well known that water cannot be displaced entirely from a porous medium. Thus, a *residual saturation* $S_{r,w}$ is introduced which expresses the minimal water saturation that will retain in the porous medium due to adhesion effects with respect to the solid matrix. Additionally, a residual saturation $S_{r,n}$ can be also defined for the non-aqueous phase which expresses the irreducible portion of such phase that cannot be mechanically displaced. The remnant non-aqueous phase can be further reduced by diminishing the surface tension of the phase by the chemical substances called *surfactants* or by increasing the temperature, [2].

1.6.3. Effective Saturation

The *effective saturation* $S_{e,\alpha}$ [-] defined as

$$S_{e,\alpha} = \frac{S_\alpha - S_{r,\alpha}}{1 - \sum_{\beta} S_{r,\beta}} \quad (1.11)$$

describes only the volumetric portions of the fluid phase that can be displaced mechanically.

1.6.4. Governing Equations

The main idea behind equations describing the multi-phase flow is based on the assumption that every fluid phase α in the porous medium is governed by its continuity theorem (1.4) and Darcy law (1.5), whereas the momentum transfer between the phases is negligible. The α -phase mass balance takes the following form

$$\frac{\partial(\phi \varrho_\alpha S_\alpha)}{\partial t} + \nabla \cdot (\varrho_\alpha \mathbf{u}_\alpha) = \varrho_\alpha F_\alpha, \quad (1.12)$$

and the Darcy law for the phase α reads as

$$\mathbf{u}_\alpha = -\frac{1}{\mu_\alpha} \mathbf{K}_\alpha (\nabla p_\alpha - \varrho_\alpha \mathbf{g}). \quad (1.13)$$

The continuity theorem (1.12) includes the saturation as a consequence of the reduction of the void space volume ϕV in (1.4) into a volume $\phi S_\alpha V$ occupied by the phase α . In (1.13) the α -phase permeability tensor \mathbf{K}_α is a function of S_α and can be decomposed into

$$\mathbf{K}_\alpha = k_{r,\alpha}(S_\alpha) \mathbf{K}, \quad (1.14)$$

where the function $k_{r,\alpha}$ is the *relative permeability* of the phase α which describes the decrease of the permeability due to the presence of other phases. Its definition and models are further discussed later in Section 1.8. The term $k_{r,\alpha}/\mu_\alpha$ is frequently denoted as the α -phase *mobility* λ_α ,

$$\lambda_\alpha = \frac{k_{r,\alpha}}{\mu_\alpha}, \quad (1.15)$$

which allows to rewrite the Darcy law as

$$\mathbf{u}_\alpha = -\lambda_\alpha \mathbf{K} (\nabla p_\alpha - \varrho_\alpha \mathbf{g}). \quad (1.16)$$

1.7. Capillarity

From now on, we will consider only a flow of two phases in porous media. In order to close the system of equations for the two-phase flow given in the previous sections, i.e., (1.12), (1.16), and (1.10), we add one more equation to the system that models the macroscopic effects of the capillary forces and describes the difference between the phase pressures.

1.7.1. Microscale Capillarity

On a pore scale, a single phase flow is governed by pressure forces arising from the pressure gradient within the void space and the exterior gravitational force. The sharp interfaces between fluid phases in multiphase flows on the microscale give rise to the *capillary force*. This force is evoked by *surface tension* σ [$J\ m^{-2}$] of both phases at their interface and called *interfacial tension*. The interfacial tension is caused by both molecular coherence within each of the phases and the adhesion effects between the phases and the solid matrix.

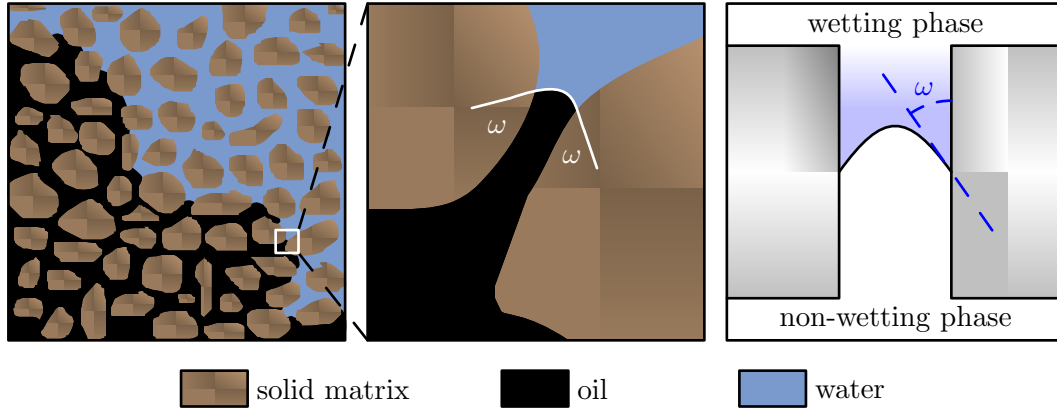


Figure 1.4.: Interface between two phases in detail. The contact angle ω characterizes the meniscus at the fluid-fluid-solid interface (right figure) and defines the wetting phase (water) and non-wetting phase (air, oil, ...).

Figure 1.4 shows the interface in a pore channel between two solid grains. At the fluid-fluid interface, the equilibrium of forces leads to a curved form of the interface due to capillarity. Let us consider two immiscible phases (e.g. water and air). The interaction of the three different phases, where the third phase is the solid matrix, results in a *contact angle* ω depicted in Figure 1.4. The influence of these forces decreases with the distance from the interface.

When the phases are in mechanical equilibrium, the *Young's equation* gives the following expression for the surface tensions at the phase interface :

$$\sigma_{S-1} = \sigma_{S-2} + \sigma_{1-2} \cos \omega, \quad (1.17)$$

where σ_{S-1} , σ_{S-2} and σ_{1-2} are the respective surface tension forces at solid phase–fluid 1 interface, solid phase–fluid 2 interface and fluid 1–fluid 2 interface as shown in Figure 1.5. From (1.17), the contact angle ω can be explicitly given as

$$\omega = \arccos \left(\frac{\sigma_{S-2} - \sigma_{S-1}}{\sigma_{1-2}} \right). \quad (1.18)$$

The contact angle α allows us to distinguish between the *wetting* and the *non-wetting* phases. The fluid phase with an *acute* contact angle is referred to as the wetting phase with respect to the solid matrix and the other fluid (fluid 1 in Figure 1.5), while the fluid phase with an *obtuse* contact angle is the non-wetting phase (fluid 2 in Figure 1.5). This notation allows us to develop more general two-phase flow models with a wetting and a non-wetting phase regardless of the factual nature of the fluid phases, [2]. In the latter, the subscripts w and n are used for quantities related to the wetting and non-wetting phase, respectively.

The *microscopic capillary pressure* π_c [Pa] is defined as the difference between the non-wetting phase pressure and the wetting phase pressure at the phase interface,

$$\pi_c = \pi_n - \pi_w. \quad (1.19)$$

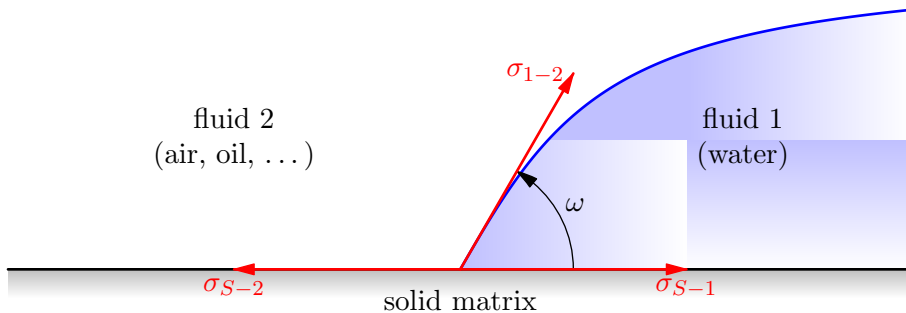


Figure 1.5.: Interface tension and wetting angle at equilibrium.

The curved interface between both phases is preserved by a discontinuity in microscopic pressure of each phase. The capillary pressure is thus the height of the jump and it is always a non-negative quantity,

$$\pi_c \geq 0, \quad (1.20)$$

because the pressure p_n in the non-wetting phase is larger than the pressure p_w in the wetting phase at the interface as a consequence of the definition of wettability.

1.7.2. Macroscale Capillarity: Static Case

In order to be able to describe the differences between the macroscale phase pressures p_w and p_n given in (1.16), we need to upscale capillary pressure (1.19). The natural way is to introduce the *macroscopic capillary pressure* p_c by the same definition as (1.19)

$$p_c = p_n - p_w, \quad (1.21)$$

where p_w and p_n are the macroscopic phase pressures that can be either averaged from the microscale pressures π_α , see [2] or [57], or defined by thermodynamic constitutive relationships as in [56]. The macroscopic capillary pressure is a function of state variables such as the phase saturations, temperature, and interfacial areas between fluids or a fluid and the solid matrix, [56].

By p_c^{eq} , we denote the capillary pressure–saturation relationship determined under the static conditions, i.e., in the state of thermodynamic equilibrium. Such *static capillary pressure–saturation* relationship is obtained by measuring the phase pressures difference during slow drainage or imbibition laboratory experiments. Traditionally, they are used in the modelling of a multi-phase flow independently of the flow conditions as long as the hysteretic effects can be neglected.

In this thesis, we assume that the static capillary pressure function p_c^{eq} has the following mathematical properties, [60]:

1. $p_c^{eq} = p_c^{eq}(S_w)$,
2. p_c^{eq} is continuously differentiable in $(0, 1)$,
3. p_c^{eq} is strictly decreasing with respect to S_w ,
4. $p_c^{eq} \rightarrow p_d \geq 0$ as $S_w \rightarrow 1 - S_{r,n}$,

where p_d [Pa] is the *entry pressure*. The entry pressure p_d is the capillary pressure at full saturation and is considered as the minimal capillary pressure required to displace the wetting

phase at its maximal saturation from the largest occurring pore. Among others, the following two static capillary pressure–saturation models satisfying these conditions are commonly used.

Brooks and Corey [10] developed a mathematical model for $p_c^{eq} \leftrightarrow S_w$ in the form

$$S_{e,w}(p_c^{eq}) = \left(\frac{p_c^{eq}}{p_d} \right)^\lambda \quad \text{for } p_c^{eq} \geq p_d, \quad (1.22)$$

where the parameter λ [–] describes pore distribution of the grains in a porous material. Small values of λ belong to single grain size material, while large values indicate a highly non-uniform material, [57]. This parametrization of the $p_c^{eq} \leftrightarrow S_w$ relation simulates the *DNAPL pooling* (or *physical barrier effect*) described later in Section 1.9. From (1.22), the static capillary pressure p_c^{eq} can be expressed as

$$p_c^{eq}(S_w) = p_d S_{e,w}^{-\frac{1}{\lambda}} \quad \text{for } S_{e,w} \in (0, 1]. \quad (1.23)$$

Another model, developed by van Genuchten [48], treats the capillary pressure–saturation relationship as

$$S_{e,w}(p_c^{eq}) = [1 + (\alpha p_c^{eq})^n]^m \quad \text{for } p_c^{eq} \geq 0. \quad (1.24)$$

Usually, the parameters m and n are coupled as

$$m = 1 - \frac{1}{n}, \quad (1.25)$$

and they characterize the pore structure of the porous medium. The last parameter α is given in [Pa^{-1}]. It follows from (1.24) that the expression for $p_c^{eq}(S_w)$ reads as

$$p_c^{eq}(S_w) = \frac{1}{\alpha} \left(S_{e,w}^{-\frac{1}{m}} - 1 \right)^{\frac{1}{n}} \quad \text{for } S_{e,w} \in (0, 1]. \quad (1.26)$$

Unlike the Brooks-Corey capillary pressure (1.23), the van Genuchten model (1.26) is unable to model the barrier effect, because $p_c = 0$ at full water saturation.

1.7.3. Macroscale Capillarity: Dynamic Case

In 1978, Stauffer [110] published an experimentally supported theory that the relationship

$$p_c^{eq} = p_n - p_w \quad (1.27)$$

holds only if the system is in equilibrium. Therefore, it is of great concern whether the classical models such as Brooks and Corey (1.23) or van Genuchten (1.26) can be used in (1.21) when the system is not in equilibrium. The following modification to the phase pressure difference equation is proposed by Stauffer

$$p_n - p_w = p_c^{eq} - \tau \frac{\partial S_w}{\partial t}, \quad (1.28)$$

where τ [$kg \, m^{-1} \, s^{-1}$] is the *dynamic capillary pressure coefficient*. Equation (1.28) is referred to as the *dynamic effect* in the capillary pressure–saturation relationship, or, for the sake of brevity, the *dynamic capillary pressure*, [78].

Decades later, a thermodynamic basis of the capillary pressure was derived by Hassanizadeh and Gray in a series of papers [49], [50], [51], [53], [55], and [56]. They show that the macroscopic capillary pressure p_c is solely an intrinsic property of the system and that (1.28) is a result of the Coleman and Noll method of exploitation of the *Second Law of Thermodynamics*, [56], [79].

Consequently, we use the ansatz (1.28) as the constitutive relationship for the macroscopic capillary pressure defined by (1.21)

$$p_c = p_c^{eq} - \tau \frac{\partial S_w}{\partial t}. \quad (1.29)$$

Stauffer [110] proposed the following model for the dynamic effect coefficient (denoted here by τ_S)

$$\tau_S = \frac{\alpha_S \mu_w \phi}{K \lambda} \left(\frac{p_d}{\rho_w g} \right)^2, \quad (1.30)$$

where $\alpha_S = 0.1 [-]$ denotes a scaling parameter and $g [m s^{-2}]$ is the gravitational acceleration. Both λ and p_d are the Brooks and Corey parameters from (1.23).

The Stauffer model for the dynamic effect coefficient τ_S was obtained by correlating experimental data. The values of τ_S vary between $\tau_S = 2.7 \cdot 10^4 Pa \cdot s$ and $\tau_S = 7.7 \cdot 10^4 Pa \cdot s$ [77, page 27]. In case of the sands used in this work (cf. Table B.2), (1.30) gives higher values of τ_S than for the sands used by Stauffer. Other researchers suggest that the magnitude of τ should be smaller, i.e., in the order of $10^2 - 10^3 Pa \cdot s$ according to [22], or, on the other hand, it should be higher, i.e., in the order of $10^4 - 10^8 Pa \cdot s$ as estimated by [54]. Furthermore, the dynamic coefficient may depend on averaging scales as well as saturation, see [94], [95]. As the influence of the averaging scales was not found to be important in [106], we do not consider this dependence here.

1.7.4. Capillary Hysteresis

The relationship between capillary pressure and saturation depends on a type of the displacement process (i.e., imbibition or drainage) as it is subject to *capillary hysteresis*. In general, the capillary pressure depends on the complete history of drainage and imbibition cycles whereas it is always bounded by the *primary drainage* and *primary wetting* curves, [20], [57], [85], [86]. These curves are shown in Figure 1.6. The red curves are valid for the primary drainage of a fully water saturated medium and the blue curves correspond to the case, where the porous medium is subsequently imbibed (wetted) to the maximal water saturation.

The capillary hysteresis can be significantly observed in the *ink bottle* effect when a capillary tube of axial symmetry having periodical variations in radius has its lower end immersed in water (air-water system), the water will rise through the tube until the hydrostatic pressure in the tube equilibrates to the capillary pressure. Then, if the tube is raised in the water, some water will drain out and a new equilibrium level will establish. When the interface meniscus is advancing and approaches the narrow part of the tube, it *jumps* through the neck (imbibition). When receding, it halts without passing through the neck. This phenomenon explains why a given capillary pressure corresponds to a higher saturation on the drainage curve than on the imbibition curve in Figure 1.6.

In most fluid-flow problems of practical interest, the capillary hysteresis can be neglected because the flow regime usually dictates that one or the other capillary pressure–saturation curve will apply. A general theoretical description of the capillary hysteresis model was proposed in a series of papers [72], [73], [96]. In [99] Philip derived similarity solutions for a horizontal redistribution problem which was later addressed in [100] that included fluid–fluid and fluid–solid interfacial areas in the model of capillary hysteresis. According to [6], [7], and [52], it is possible to develop a mathematical model that can treat both the capillary hysteresis and the dynamic effect in the capillarity more accurately than (1.29). However, such mathematical model requires additional experimental data and is subject to further investigation. Therefore, we do not consider capillary hysteresis in this thesis.

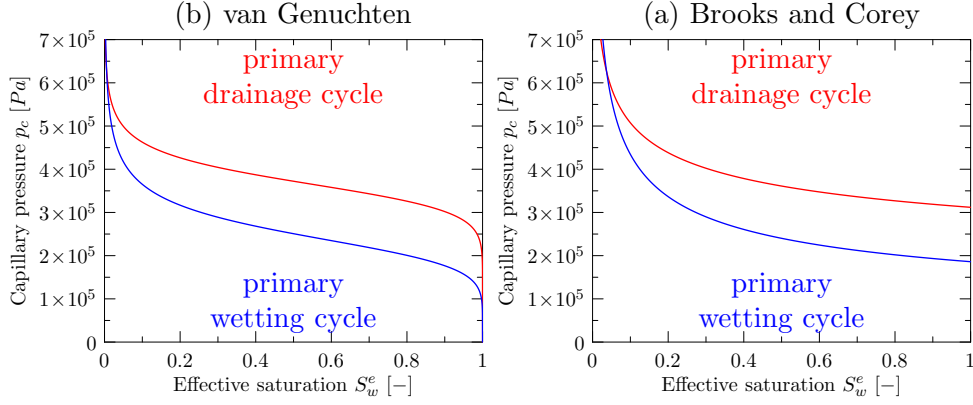


Figure 1.6.: Typical capillary pressure curves $p_c(S_w)$ after (a) Brooks-Corey and after (b) van Genuchten for both drainage and imbibition (wetting) cycles.

1.8. Relative Permeability

The relative permeability $k_{r,\alpha}$ defined by (1.14) models the fact that the flow paths of a fluid are hindered by the presence of other phases. It can be considered as a scaling factor that obeys the constraint

$$0 \leq k_{r,\alpha} \leq 1. \quad (1.31)$$

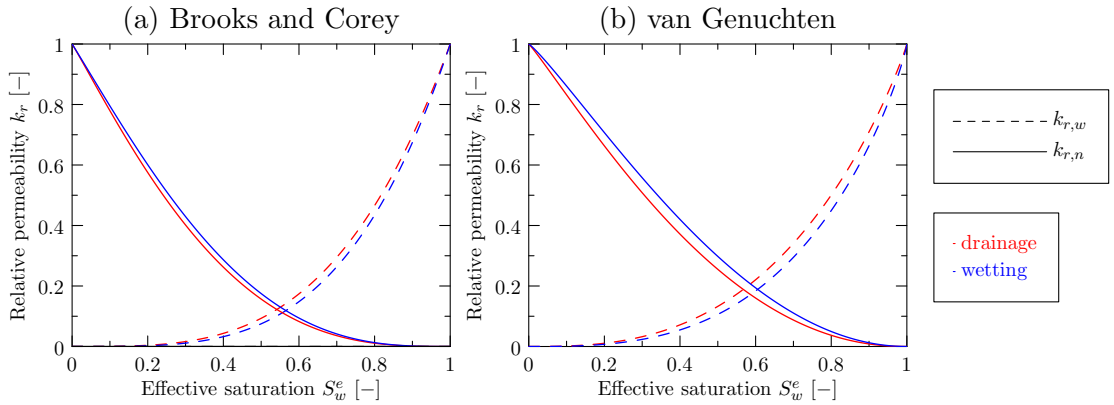


Figure 1.7.: Relative permeability functions based on imbibition and drainage capillary curves.

For the two-phase flow in porous media, the mathematical models for the relative permeability functions $k_{r,w}$ and $k_{r,n}$ can be deduced from the models of the capillarity by the relations (see [57]):

$$k_{r,w}(S_w) = S_{e,w}^A \left(\frac{\int_0^{S_{e,w}} [p_c^{eq}(v)]^{-B} dv}{\int_0^1 [p_c^{eq}(v)]^{-B} dv} \right)^C, \quad (1.32a)$$

$$k_{r,n}(S_w) = (1 - S_{e,w})^A \left(\frac{\int_0^{S_{e,w}} [p_c^{eq}(v)]^{-B} dv}{\int_0^1 [p_c^{eq}(v)]^{-B} dv} \right)^C, \quad (1.32b)$$

where only the static capillary pressure function p_c^{eq} is used. Simulations by pore-network models [68], [92], have shown that the dynamics of the system affects negligibly the relative permeability functions. Therefore, we assume that the relative permeabilities depend on saturations only. The following two classical models are presented in [57].

The *Burdine* mathematical model for the relative permeability functions [12], [13] can be obtained by substituting the Brooks and Corey static capillary pressure function p_c^{eq} defined by (1.23) into (1.32) with $A = B = 2$ and $C = 1$,

$$k_{r,w}(S_w) = S_{e,w}^{3+\frac{2}{\lambda}}, \quad (1.33a)$$

$$k_{r,n}(S_w) = (1 - S_{e,w})^2 (1 - S_{e,w}^{1+\frac{2}{\lambda}}). \quad (1.33b)$$

It is common to refer to (1.33) in conjunction with (1.23) as the *Brooks and Corey model*.

The *Mualem* mathematical model for relative permeability functions [87] can be obtained by substituting the van Genuchten capillary pressure model (1.26) into (1.32) with $A = \frac{1}{2}$, $B = 1$, and $C = 2$,

$$k_{r,w}(S_w) = S_{e,w}^{\frac{1}{2}} \left(1 - (1 - S_{e,w}^{\frac{1}{m}})^m \right)^2, \quad (1.34a)$$

$$k_{r,n}(S_w) = (1 - S_{e,w})^{\frac{1}{3}} (1 - S_{e,w}^{\frac{1}{m}})^{2m}. \quad (1.34b)$$

Equations (1.34) and (1.26) are usually referred to as the *van Genuchten model*.

1.9. Fluid Behavior at Material Interfaces

In this section, we describe the behavior of two fluids at a sharp material interface between materials with different capillary pressure–saturation curves. We extend the approach of [90] to the case of the dynamic capillary pressure–saturation relationship. A similar approach can be found in [60] where the authors present a variational formulation of the interfacial conditions.

Let us consider an initially fully water saturated column with two sands separated by a sharp interface. The situation at the interface is illustrated in Figure 1.8. Since no mass is lost or produced at the material interface, the mass conservation law states that the normal component of the *mass flux*

$$\varrho_\alpha \mathbf{u}_\alpha \cdot \mathbf{n} \text{ is continuous across the interface,} \quad (1.35)$$

where \mathbf{n} denotes a unit normal to the interface as illustrated in Figure 1.8.

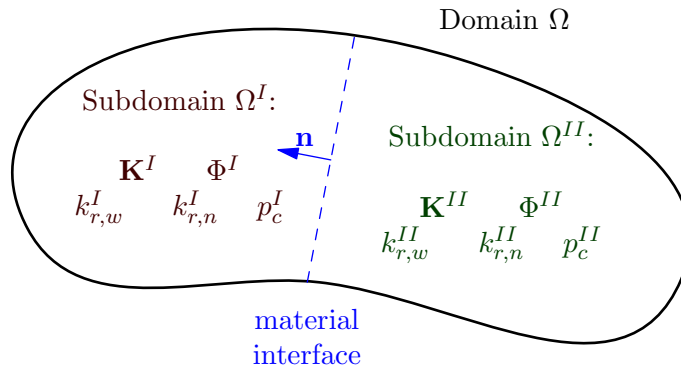


Figure 1.8.: The sharp interface between two different porous media.

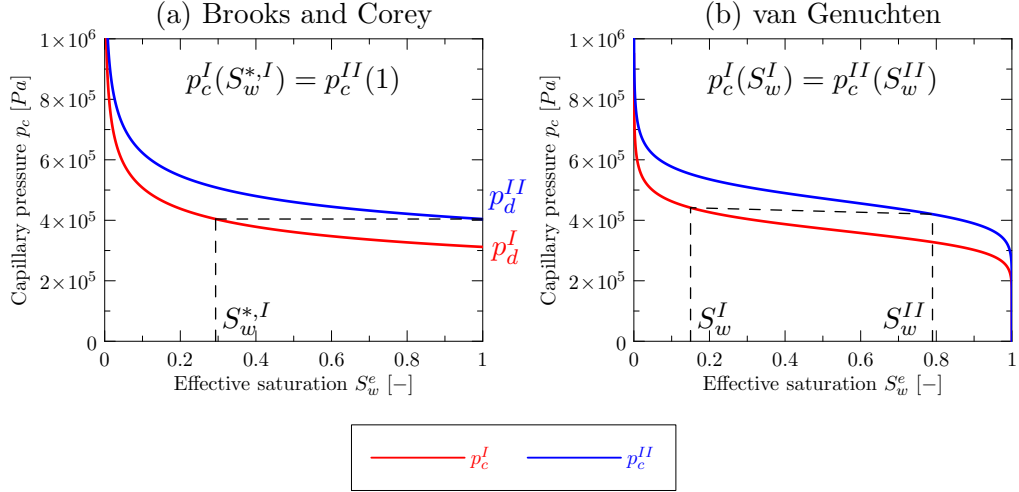


Figure 1.9.: The typical Brooks and Corey (a) and van Genuchten (b) capillary pressure curves for two different sands and the saturations at a material interface.

As in [90], we assume that a mobile wetting phase is present on both sides of the interface which implies the following continuity condition for p_w :

$$p_w \text{ is continuous across the interface,} \quad (1.36)$$

If a non-wetting phase is present on both sides of the interface, p_n is also assumed to be continuous which implies the continuity of the capillary pressure p_c in that case. On the other hand, if the non-wetting phase is not present but approaches the material interface, the following situation can occur. As the non-wetting phase reaches the material interface from the coarse sand (denoted by the superscript I), the interfacial capillary pressure p_c^I increases. When p_c^I is lower than the entry pressure p_d^{II} of the finer medium, the non-wetting phase cannot penetrate the interface and accumulates (pools) at the interface. This is referred to as the *barrier effect*. Once the capillary pressure p_c^I exceeds the entry pressure threshold p_d^{II} , the non-wetting phase enters the finer sand. In Figure 1.9, typical van Genuchten (a) and Brooks and Corey (b) capillary pressure curves (1.26) and (1.23) for two different porous media are shown. Note that the barrier effect is simulated by the Brooks and Corey model only since the van Genuchten capillary pressure–saturation relationship gives $p_c = 0$ at full water saturation.

Altogether, the condition at the material interface is established in the following form:

$$\begin{aligned} S_n^{II} = 0 \quad \text{and} \quad p_c^I = p_d^{II}, \quad \text{if } p_c^I < p_d^{II}, \\ p_c^I = p_c^{II}, \quad \text{otherwise.} \end{aligned} \quad (1.37)$$

Eq. (1.37) is referred to as the *extended capillary pressure condition* [30], [90]. In the case of static capillary pressure, a unique value of the wetting phase saturation $S_w^{I,*}$ can be associated with the threshold value of the capillary pressure for the static model such that

$$S_w^{I,*} = (p_c^I)^{-1}(p_d^{II}), \quad (1.38)$$

see Figure 1.9.

We assume that the condition (1.37) holds also for the dynamic capillary pressure in the form

$$\begin{aligned} S_n^{II} = 0 \quad \text{and} \quad p_c^{II} = p_d^{II}, \quad \text{if } p_c^I < p_d^{II}, \\ p_c^{eq,I} - \tau^I \frac{\partial S_w^I}{\partial t} = p_c^{eq,II} - \tau^{II} \frac{\partial S_w^{II}}{\partial t}, \quad \text{otherwise.} \end{aligned} \quad (1.39)$$

In contrast to the static capillary pressure model, the threshold saturation cannot be uniquely associated with the entry pressure of the finer sand as in (1.38) because the value of the dynamic capillary pressure depends on the dynamics of the system through the time derivative of the saturation. Consequently, the required entry pressure threshold p_d can be reached for higher values of S_w^I than in the static case.

1.10. Problem Formulations

We consider flow of two immiscible and incompressible fluids in a polygonal domain Ω in \mathbb{R}^d (with $d = 1$ or 2). We assume that the phase densities ϱ_α are constant and the porosity is constant in time, i.e., the solid matrix of the porous medium is rigid.

1.10.1. Pressure–Saturation Formulation

In this subsection, we devise a formulation of two-phase immiscible and incompressible flow on the macroscale. We rewrite all the relevant equations presented in the previous sections (1.10), (1.12), (1.13), and (1.28) as:

$$\phi \frac{\partial S_w}{\partial t} + \nabla \cdot \mathbf{u}_w = F_w, \quad (1.40a)$$

$$\phi \frac{\partial S_n}{\partial t} + \nabla \cdot \mathbf{u}_n = F_n, \quad (1.40b)$$

$$\mathbf{u}_w = -\lambda_w \mathbf{K} (\nabla p_w - \rho_w \mathbf{g}), \quad (1.40c)$$

$$\mathbf{u}_n = -\lambda_n \mathbf{K} (\nabla p_n - \rho_n \mathbf{g}), \quad (1.40d)$$

$$p_c = p_c^{eq} - \tau \frac{\partial S_w}{\partial t} = p_n - p_w, \quad (1.40e)$$

$$S_w + S_n = 1, \quad (1.40f)$$

where the unknown functions are the saturations $S_\alpha = S_\alpha(t, \mathbf{x})$ and the phase pressures $p_\alpha = p_\alpha(t, \mathbf{x})$ for all $t > 0$ and \mathbf{x} inside Ω , $\alpha \in \{w, n\}$.

The governing equations (1.40) are subject to an initial condition

$$S_\alpha = S_\alpha^{ini}, \quad \text{in } \Omega, \quad \alpha \in \{w, n\}, \quad (1.41)$$

and boundary conditions

$$\mathbf{u}_\alpha \cdot \mathbf{n} = u_\alpha^{\mathcal{N}} \quad \text{on } \Gamma_{\mathbf{u}_\alpha} \subset \partial\Omega, \quad (1.42a)$$

$$S_w = S_w^{\mathcal{D}} \quad \text{on } \Gamma_{S_w} \subset \partial\Omega, \quad (1.42b)$$

$$p_\alpha = p_\alpha^{\mathcal{D}} \quad \text{on } \Gamma_{p_\alpha} \subset \partial\Omega, \quad (1.42c)$$

where \mathbf{n} denotes the outward unit normal to the boundary $\partial\Omega$ with respect to Ω and $\alpha \in \{n, w\}$. The superscripts \mathcal{N} and \mathcal{D} stand for the Neumann and Dirichlet type boundary condition, respectively. Initial condition (1.41) and boundary conditions (1.42) should be consistent with (1.40e) and (1.40f).

In the case of flow of a gas phase in an unsaturated porous medium, the mathematical formulation (1.40) can be reduced into a single equation under the assumption that the changes in pressure of the gaseous phase are negligible throughout the domain Ω . Assuming p_n to be at a constant (atmospheric) pressure, the gradient of the wetting-phase pressure p_w can be directly expressed as

$$\nabla p_w = \underbrace{\nabla p_n}_0 - \nabla p_c = -\nabla p_c. \quad (1.43)$$

Combining the Darcy law (1.40c) and the continuity theorem (1.40a) for the wetting-phase, we obtain

$$\phi \frac{\partial S_w}{\partial t} - \nabla \cdot (\lambda_w \mathbf{K} (-\nabla p_c - \rho_w \mathbf{g})) = F_w, \quad (1.44)$$

where p_c is given by (1.40e). Equation (1.44) is a single equation for the wetting-phase saturation S_w and is referred to as the Richards equation [102].

1.10.2. Flow Potential–Saturation Formulation

Since we assume that both fluids are incompressible, we can simplify the notation of the governing equations (1.40) by introducing the *flow potential* ψ_α as

$$\psi_\alpha = p_\alpha - \varrho_\alpha \mathbf{g} \cdot \mathbf{x}, \quad (1.45)$$

where \mathbf{x} is the position vector and $\alpha \in \{w, n\}$. Similarly to the definition of the capillary pressure (1.21), we define the *capillary potential* as

$$\psi_c = \psi_n - \psi_w. \quad (1.46)$$

Using (1.45) and the expressions for the macroscale capillary pressure p_c (1.21) and (1.29), we obtain

$$\psi_c = p_n - p_w - (\rho_n - \rho_w) \mathbf{g} \cdot \mathbf{x} \quad (1.47a)$$

$$= p_c - (\rho_n - \rho_w) \mathbf{g} \cdot \mathbf{x} \quad (1.47b)$$

$$= p_c^{eq} - \tau \frac{\partial S_w}{\partial t} - (\rho_n - \rho_w) \mathbf{g} \cdot \mathbf{x} \quad (1.47c)$$

$$= \psi_c^{eq} - \tau \frac{\partial S_w}{\partial t}, \quad (1.47d)$$

where ψ_c^{eq} stands for the *static capillary potential*,

$$\psi_c^{eq} = p_c^{eq} - (\varrho_n - \varrho_w) \mathbf{g} \cdot \mathbf{x}. \quad (1.48)$$

Consequently, the system of equations (1.40) can be rewritten in the following form

$$\phi \frac{\partial S_w}{\partial t} + \nabla \cdot \mathbf{u}_w = F_w, \quad (1.49a)$$

$$\phi \frac{\partial S_n}{\partial t} + \nabla \cdot \mathbf{u}_n = F_n, \quad (1.49b)$$

$$\mathbf{u}_w = -\lambda_w \mathbf{K} \nabla \psi_w, \quad (1.49c)$$

$$\mathbf{u}_n = -\lambda_n \mathbf{K} \nabla \psi_n, \quad (1.49d)$$

$$\psi_c = \psi_c^{eq} - \tau \frac{\partial S_w}{\partial t} = \psi_n - \psi_w, \quad (1.49e)$$

$$S_w + S_n = 1, \quad (1.49f)$$

where the unknown functions are the saturations $S_\alpha = S_\alpha(t, \mathbf{x})$ and the phase potentials $\psi_\alpha = \psi_\alpha(t, \mathbf{x})$ for all $t > 0$ and \mathbf{x} inside Ω , $\alpha \in \{w, n\}$.

The governing equations (1.49) are subject to an initial condition

$$S_\alpha = S_\alpha^{ini}, \quad \text{in } \Omega, \quad (1.50)$$

and boundary conditions

$$\mathbf{u}_\alpha \cdot \mathbf{n} = u_\alpha^{\mathcal{N}} \quad \text{on } \Gamma_{\mathbf{u}_\alpha} \subset \partial\Omega, \quad (1.51a)$$

$$S_w = S_w^{\mathcal{D}} \quad \text{on } \Gamma_{S_w} \subset \partial\Omega, \quad (1.51b)$$

$$\psi_\alpha = \psi_\alpha^{\mathcal{D}} \quad \text{on } \Gamma_{\psi_\alpha} \subset \partial\Omega, \quad (1.51c)$$

for $\alpha \in \{w, n\}$. Initial condition (1.50) and boundary conditions (1.51) should be consistent with (1.49e) and (1.49f).

In this chapter, we review the currently available analytical and semi-analytical solutions (i.e., *the benchmark solutions*) that can be obtained if several assumptions are placed upon the problem formulation (1.40). These benchmark solutions can be derived for a one-dimensional two-phase flow problem without sources or sinks ($F_w = F_n = 0$) and with zero gravity ($\mathbf{g} = 0$). As we show in Section 2.1, the set of equations (1.40) can be reduced into a single evolution equation for the wetting phase saturation $S_w = S_w(t, x)$ in the form

$$\phi \frac{\partial S_w}{\partial t} = \underbrace{-u_T \frac{\partial f_w}{\partial x}}_{\text{advection term}} + \underbrace{\frac{\partial}{\partial x} \left[D \frac{\partial S_w}{\partial x} \right]}_{\text{static capillary pressure term}} + \underbrace{\frac{\partial}{\partial x} \left[\frac{\lambda_w \lambda_n}{\lambda_w + \lambda_n} K \frac{\partial}{\partial x} \left(\tau \frac{\partial S_w}{\partial t} \right) \right]}_{\text{dynamic effect term}}. \quad (2.1)$$

In the latter, we divide the benchmark solutions based upon a combination of the three terms (advection, static capillary pressure, and dynamic effect) that are present in (2.1). In Section 2.2, we present the *Buckley and Leverett* analytical solution for the pure advection version of (2.1) with $D = 0$ and $\tau = 0$. Then, in Sections 2.3 and 2.4, we discuss semi-analytical solutions for an advection–diffusion equation in homogeneous and layered porous media, respectively, with $D \neq 0$ and $\tau = 0$ in (2.1).

According to [1], [34], [88], or [109], equation (2.1) belongs to the family of *Sobolev equations* when $\tau \neq 0$. In these papers, the existence and uniqueness of a solution is shown under several restrictions placed upon the coefficients of (2.1). To the best of our knowledge, there is no benchmark solution available for the case of partial differential equation (2.1) with the advection, diffusion, and dynamic effect terms when coefficients are highly nonlinear as is the case for the Brooks and Corey or van Genuchten models.

Based on [21] and [31], a semi-analytical solution can be obtained for a simplified (linearized) equation (2.1) as an extension of the Buckley and Leverett solution. However, we are currently unaware of how these semi-analytical solutions can be extended for the case of highly non-linear coefficients that are considered in this thesis in (2.1).

2.1. One-Dimensional Saturation Equation

In this section, we derive the one-dimensional benchmark equation (2.1) from the phase pressures–saturations formulation (1.40) given in Section 1.10.1 with $F_w = F_n = 0$ and $\mathbf{g} = \mathbf{0}$.

We sum equations (1.40a) and (1.40b) and by using (1.40f), we obtain

$$\frac{\partial}{\partial x} (u_w + u_n) = 0. \quad (2.2)$$

Defining the *total velocity* u_T as

$$u_T = u_w + u_n, \quad (2.3)$$

equation (2.2) implies that u_T is constant in space. Thus, we establish an equation for the wetting phase pressure $p_w = p_w(t, x)$ by substituting (1.40c) and (1.40d) into (2.3) as

$$-\underbrace{(\lambda_w + \lambda_n)}_{\lambda_t} K \frac{\partial p_w}{\partial x} - \lambda_n K \frac{\partial p_c}{\partial x} = u_T, \quad (2.4)$$

where $\lambda_t = \lambda_w + \lambda_n$ denotes the *total mobility* function. By the definition of the relative permeabilities $k_{r,w}$ and $k_{r,n}$ (see Figure 1.7), $\lambda_t(S_w)$ is positive for all wetting-phase saturations S_w (see Figure 1.7). We express the gradient of p_w as

$$\frac{\partial p_w}{\partial x} = -\frac{\lambda_n}{\lambda_t} \frac{\partial p_c}{\partial x} - \lambda_t^{-1} K^{-1} u_T. \quad (2.5)$$

We use (2.5) to eliminate p_w from the Darcy velocity (1.40c) to obtain

$$u_w = \lambda_w K \frac{\partial p_w}{\partial x} = \frac{\lambda_w}{\lambda_t} u_T - \frac{\lambda_w \lambda_n}{\lambda_t} K \frac{\partial p_c}{\partial x}. \quad (2.6)$$

Next, we combine (2.6) and the continuity equation (1.40a),

$$\phi \frac{\partial S_w}{\partial t} = -u_T \frac{\partial}{\partial x} \left(\frac{\lambda_w}{\lambda_t} \right) - \frac{\partial}{\partial x} \left(\frac{\lambda_w \lambda_n}{\lambda_t} K \frac{\partial p_c}{\partial x} \right). \quad (2.7)$$

In (2.7) we expand the gradient of p_c using the dynamic effect in capillary pressure–saturation relationship (1.40e) as follows

$$\frac{\partial p_c}{\partial x} = \frac{\partial}{\partial x} \left(p_c^{eq}(S_w) - \tau(S_w) \frac{\partial S_w}{\partial t} \right), \quad (2.8a)$$

$$= \frac{dp_c^{eq}(S_w)}{dS_w} \frac{\partial S_w}{\partial x} - \frac{\partial}{\partial x} \left(\tau(S_w) \frac{\partial S_w}{\partial t} \right). \quad (2.8b)$$

For convenience, we introduce the fractional flow function f_α of the α -phase as

$$f_\alpha = \frac{\lambda_\alpha}{\lambda_t}, \quad \alpha \in \{w, n\}, \quad (2.9)$$

and the function D as

$$D = -\frac{\lambda_w \lambda_n}{\lambda_w + \lambda_n} K \frac{dp_c^{eq}}{dS_w}. \quad (2.10)$$

Note that the fractional flow functions have the following properties

$$0 \leq f_\alpha \leq 1, \quad (2.11a)$$

$$f_\alpha = 1, \text{ if } S_\alpha = 1, \quad (2.11b)$$

$$f_\alpha = 0, \text{ if } S_\alpha = 0, \quad (2.11c)$$

$$f_w + f_n = 1, \quad (2.11d)$$

where $\alpha \in \{w, n\}$. Using this notation, equation (2.7) reads as

$$\phi \frac{\partial S_w}{\partial t} = -u_T \frac{\partial f_w}{\partial x} + \frac{\partial}{\partial x} \left[D \frac{\partial S_w}{\partial x} \right] + \frac{\partial}{\partial x} \left[\frac{\lambda_w \lambda_n}{\lambda_w + \lambda_n} K \frac{\partial}{\partial x} \left(\tau \frac{\partial S_w}{\partial t} \right) \right]. \quad (2.12)$$

Since all of the coefficients are either constant or depend on S_w only, equation (2.12) is a nonlinear partial differential equation for S_w . Typical shapes of functions f_w and D are shown in Figure 2.1. Once S_w is known, the wetting-phase pressure can be easily obtained from (2.5) in the form

$$\frac{\partial p_w}{\partial x} = -f_n \frac{dp_c^{eq}}{dS_w} \frac{\partial S_w}{\partial x} + f_n \frac{\partial}{\partial x} \left(\tau \frac{\partial S_w}{\partial t} \right) - \lambda_t^{-1} K^{-1} u_T. \quad (2.13)$$

We shall discuss only the equation (2.1) for the wetting-phase saturation S_w since we consider p_w as a saturation-dependent variable due to (2.13).

In the following sections, we consider benchmark solutions for (2.12) in a space–time domain $\Omega \times (0, T)$ for initial and boundary conditions illustrated in Figure 2.2.

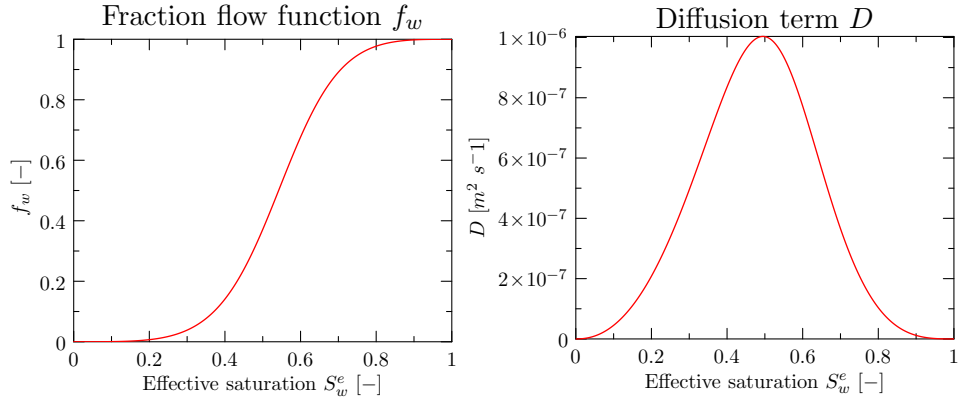


Figure 2.1.: Typical shapes of functions f_w and D .

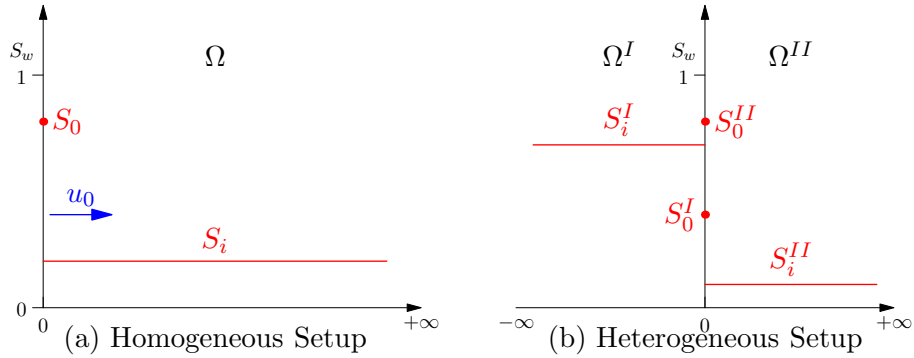


Figure 2.2.: Benchmark problems setup.

2.2. Pure Advection Case

Neglecting the capillarity and the dynamic effect term in (2.1), we get a pure advection equation in a homogeneous porous medium domain $\Omega = (0, +\infty)$

$$\phi \frac{\partial S_w}{\partial t} = -u_T \frac{\partial f_w}{\partial x} \quad (2.14)$$

for which we set-up the following Riemann problem. The equation (2.14) is strictly hyperbolic and thus we prescribe a boundary condition for S_w at the inflow boundary. Let us assume that the inflow boundary is placed at $x = 0$, i.e., $S_w(t, 0) = S_0$. The total velocity u_T is either prescribed or implied by the boundary condition (1.42a) and we assume that $u_T = u_T(t)$ is an integrable non-negative function. Initially, the domain Ω is filled with constant wetting phase saturation $S_w(0, x) = S_i$ with $S_i < S_0$ as shown in Figure 2.2a. In the following subsections, we shall describe the derivation of the analytical solution for the case $S_0 > S_i$ only. In order to obtain the analytical solution for the other case $S_0 < S_i$, we use (1.40f) and (2.11d) and rewrite (2.14) in terms of the non-wetting phase saturation as

$$\phi \frac{\partial S_n}{\partial t} = -u_T \frac{\partial f_n}{\partial x}. \quad (2.15)$$

The initial and boundary conditions of the Riemann problem read in terms of the non-wetting phase saturation as $S_w(0, x) = 1 - S_i$ and $S_n(t, 0) = 1 - S_0$, whilst the total velocity remains unchanged. Therefore, denoting by $\tilde{S}_i = 1 - S_i$ and $\tilde{S}_0 = 1 - S_0$, we get $\tilde{S}_i < \tilde{S}_0$ which is formally the same Riemann problem as in the previous case.

2.2.1. Method of Characteristics

The analytical solution of (2.14) can be derived using the modified method of characteristics for non-convex flux functions and is referred to as the Buckley and Leverett solution. A modification of the method of characteristics is necessary due to the existence of an inflexion point of the function f_w as depicted in Figure 2.3. The Buckley and Leverett analytical solution is very well understood in the literature, c.f. [2], [11], [19], [42], [66], [74]. Therefore, we only recapitulate the most important aspects of its construction.

We use the chain rule to expand the right-hand-side of (2.14) as

$$\phi \frac{\partial S_w}{\partial t} = -u_T \frac{df_w(S_w)}{dS_w} \frac{\partial S_w}{\partial x}. \quad (2.16)$$

A characteristic is a curve in the (t, x) -plane, along which the solution $S_w(t, x)$ of the Riemann problem (2.14) is constant. We consider a parametrization $\eta \mapsto (t, x)$ of such curve and we assume differentiability of $x = x(\eta)$ and $t = t(\eta)$ for all η . Since S_w is constant along the characteristics,

$$S_w(\eta) = S_w(t(\eta), x(\eta)) = \text{const.} \quad (2.17)$$

We differentiate (2.17) with respect to η as follows

$$\frac{dS_w}{d\eta} = \frac{\partial S_w}{\partial t} \frac{dt}{d\eta} + \frac{\partial S_w}{\partial x} \frac{dx}{d\eta} = 0. \quad (2.18)$$

Comparing (2.18) and (2.16), we obtain

$$\frac{dt}{d\eta} = \phi, \quad (2.19a)$$

$$\frac{dx}{d\eta} = \frac{df_w(S_w)}{dS_w} u_T. \quad (2.19b)$$

Combining (2.19a) and (2.19b), we get

$$\frac{dx}{dt} = \frac{1}{\phi} \frac{df_w(S_w)}{dS_w} u_T. \quad (2.20)$$

By integrating (2.20) from 0 to t , a *smooth rarefaction wave* is obtained for convex functions f_w in the implicit form

$$x(t, S_w) = \frac{1}{\phi} \frac{df_w}{dS_w}(S_w) \int_0^t u_T(z) dz. \quad (2.21)$$

The convexity or concavity of f_w implies that its first derivative is a monotonous function and thus (2.21) can be inverted to obtain the solution $S_w(t, x)$. Due to the existence of the inflexion point of f_w shown in Figure 2.3, this is not the case in the Buckley and Leverett problem and only a *weak solution* exists which involves both shock (due to convexity of f_w) and rarefaction (due to concavity of f_w) waves. In order to determine the weak solution to the non-convex scalar conservation law, we consider the Oleinik *entropy condition* in Theorem 2.1, [74].

Theorem 2.1 (Entropy condition (Oleinik)). *A weak solution $S_w(t, x)$ is the vanishing-viscosity solution to a general scalar conservation law (2.14), if all discontinuities have the property that*

$$\frac{f_w(S_w) - f_w(S_0)}{S_w - S_0} \geq s \geq \frac{f_w(S_w) - f_w(S_i)}{S_w - S_i}, \quad (2.22)$$

for all $S_i \leq S_w \leq S_0$, where

$$s = \frac{f_w(S^*) - f(S_0)}{S^* - S_0} \quad (2.23)$$

is the (*fractional*) shock speed and S^* is the postshock value that is constant in time defined by the relationship

$$f_w(S^*) - f(S_i) = \frac{df_w}{dS_w}(S^*)(S^* - S_i). \quad (2.24)$$

The term *fractional* shock speed is used because the shock speed u_{shock} is for all $t > 0$ defined as

$$u_{shock}(t) = s u_T(t). \quad (2.25)$$

If the function f_w has no inflexion, then $S^* = S_i$ and the shock speed $u_{shock}(t)$ is given by the *Rankine-Hugoniot condition* [74]

$$u_{RH} = \frac{f_w(S_0) - f_w(S_i)}{S_0 - S_i} u_T(t). \quad (2.26)$$

2.2.2. Entropy Condition : Convex Hull Construction

The entropy-satisfying solution to the Riemann problem (2.14) can be determined by constructing the convex hull of the set

$$\mathfrak{S} = \{(S_w, y) : S_i \leq S_w \leq S_0, \quad y \leq f_w(S_w)\}. \quad (2.27)$$

As shown in Figure 2.3, the convex hull of a set is the smallest convex set that contains the original set. The upper boundary of the convex hull is composed of a tangential from a point $[S_i, f(S_i)]$ to the graph at a point $[S^*, f(S^*)]$. The value S^* is exactly the postshock value defined by (2.24). The straight part of the upper boundary represents a shock jumping from $S_w = S_i$ to $S_w = S^*$, while the rest of the upper boundary that follows the graph $f_w(S_w)$ corresponds to the rarefaction wave. Moreover, the slope of the straight segment equals to the fractional shock speed s defined in Theorem 2.1.

If f_w is convex, then the convex hull construction gives a single line segment (single shock) and if f_w is concave, the convex hull coincides with \mathfrak{S} (single rarefaction).

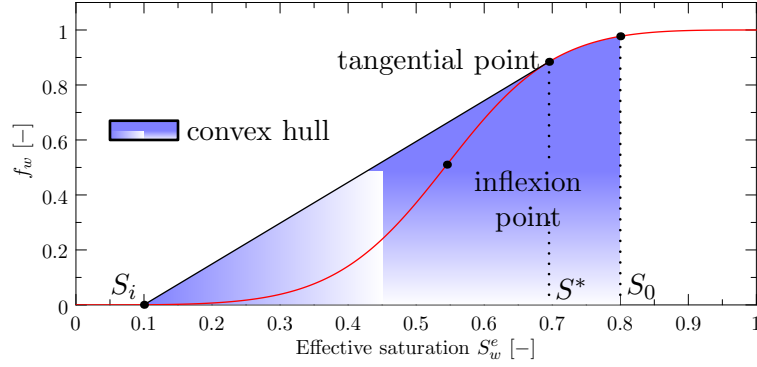


Figure 2.3.: Convex hull construction of the set \mathfrak{S} , model Brooks and Corey, $S_0 = 0.8$, $S_i = 0.1$.

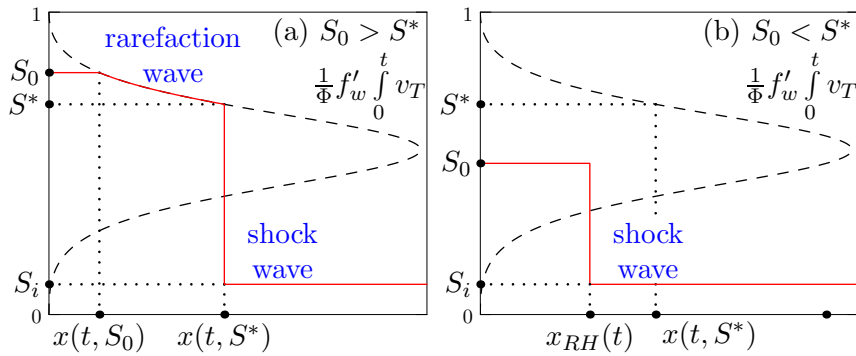


Figure 2.4.: Illustration of the Buckley and Leverett analytical solution, model Brooks and Corey, $S_i = 0.1$, (a) $S_0 = 0.8$, and (b) $S_0 = 0.5$. If (a) $S_0 > S^*$, the solution of the Riemann problem contains a rarefaction wave and a shockwave, while the solution consists of a single shockwave if (b) $S_0 < S^*$.

2.2.3. Analytical Solution

In this subsection, we finalize the derivation of the analytical solution. Let the value of S^* be computed from the equation (2.24). If $S^* < S_0$, the solution of the Riemann problem (2.14) contains a shockwave as well as a rarefaction wave, see Figure 2.4a. If $S^* > S_0$, there is only a shockwave with the Rankine-Hugoniot shock speed $u_{RH}(t)$ and the shock front position $x_{RH}(t)$ can be expressed as

$$x_{RH}(t) = \frac{1}{\Phi} \frac{f(S_0) - f(S_i)}{S_0 - S_i} \int_0^t u_T(z) dz. \quad (2.28)$$

Hence, the Buckley and Leverett analytical solution is given by the following implicit formula:

$$\left[\begin{array}{l} \text{If } S_0 \geq S^* : \\ \text{If } S_0 < S^* : \end{array} \right. \left\{ \begin{array}{ll} S_w(t, x) \text{ is solution of } x = x(t, S_w), & \text{if } S^* \leq S_w \leq S_0, \\ S_w(t, x) = S_0 & \text{for } x \leq x(t, S_0), \\ S_w(t, x) = S_i & \text{for } x \leq x(t, S^*), \\ S_w(t, x) = S_0 & \text{for } x \leq x_{RH}(t), \\ S_w(t, x) = S_i & \text{for } x \leq x_{RH}(t). \end{array} \right. \quad (2.29)$$

The Buckley and Leverett analytical solution is illustrated in Figure 2.5.

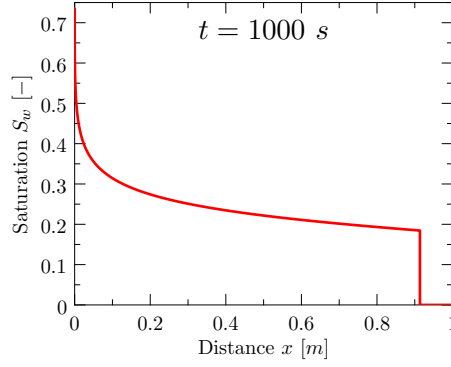


Figure 2.5.: Example of the Buckley and Leverett analytical solution for $S_0 = 0.735$, $u_T(t) = 10^{-4} \text{ m s}^{-1}$, and $S_i = 0$. We used Sand A whose parameters are given in Table B.2 (page 122).

2.3. Advection and Diffusion Case in Homogeneous Medium

In this subsection, we consider static capillary pressure $p_c = p_c^{eq}$ and homogeneous porous medium in $\Omega = (0, +\infty)$. We can include both pure diffusion ($u_T = 0$, $D \neq 0$, and $\tau = 0$) and advection–diffusion ($u_T \neq 0$, $D \neq 0$, and $\tau = 0$) cases into a family of *semi-analytical (self-similar) closed-form* solutions that can be derived for (2.1). Here, a special inflow boundary velocity u_w is assumed as

$$u_w(t, 0) = u_0(t) = At^{-\frac{1}{2}}. \quad (2.30)$$

As a consequence of (2.2), we assume the total velocity in the form

$$u_T(t) = Ru_0(t) = RAt^{-\frac{1}{2}}, \quad (2.31)$$

where $R \in (-\infty, 1]$ indicates the semi-permeability of the boundary at $x = +\infty$, see [45]. Therefore, we consider the equation (2.1) in the following form

$$\phi \frac{\partial S_w}{\partial t} = -RAt^{-\frac{1}{2}} \frac{\partial f_w}{\partial x} + \frac{\partial}{\partial x} \left[D \frac{\partial S_w}{\partial x} \right] \quad (2.32)$$

with a constant initial saturation $S_w(0, x) = S_i$ in Ω and boundary conditions

$$S_w(t, 0) = S_0, \quad (2.33a)$$

$$S_w(t, +\infty) = S_i, \quad (2.33b)$$

for $t \in (0, T)$.

If $R = 1$, the boundary at $x = +\infty$ is fully permeable such that $u_w(t, +\infty) = u_0(t)$ for all $t \in (0, T)$. The case $R = 0$ indicates impermeable boundary at $x = +\infty$ causing $u_n(t, +\infty) = u_w(t, +\infty) = 0$, $u_w(t, 0) = -u_0(t)$, and, therefore, $u_T(t) = 0$ for all $t \in (0, T)$ (pure diffusion, or *counter-current flow* case). Originally, only these two values of R were considered by McWhorter and Sunada for this type of problem, when they derived a semi-analytical solution in [80] (see also [18] and [81]). We studied multiple functional choices of the total velocity $u_0 = u_0(t)$ and the parameter R in [8], [9], [43], [47]. In [41] and [44] we showed that the range for R can be extended between 0 and 1. Finally, for the sake of derivation of the semi-analytical solution in heterogeneous porous medium, we extended $R \in (-\infty, 1]$ in [45], [46], and [42]. The negative values of R correspond to a situation, where the wetting phase is injected at $x = +\infty$ with velocities $u_w(t, +\infty) = Ru_0(t)$ and $u_n(t, +\infty) = 0$.

As in the case of the pure advection Riemann problem (2.14), we distinguish between cases $S_0 > S_i$ and $S_0 < S_i$. If $S_0 > S_i$, the wetting-phase boundary velocity (2.30) is positive, i.e. $A > 0$ and the wetting-phase saturation, initially at S_i , will increase in time. In the opposite case, i.e., if $S_0 < S_i$, the wetting-phase velocity at the inlet u_0 is negative, i.e. $A < 0$, which implies that the total velocity u_T is also negative. Using (1.40f) and (2.11d), we rewrite (2.32) in terms of the non-wetting phase saturation S_n as

$$\phi \frac{\partial S_n}{\partial t} = -RA t^{-\frac{1}{2}} \frac{\partial f_n}{\partial x} + \frac{\partial}{\partial x} \left[D \frac{\partial S_n}{\partial x} \right], \quad (2.34)$$

and the initial and boundary conditions are given as

$$S_n(t, 0) = 1 - S_0 =: \tilde{S}_0, \quad \text{for } t > 0, \quad (2.35a)$$

$$S_n(0, x) = 1 - S_i =: \tilde{S}_i, \quad \text{for } x > 0, \quad (2.35b)$$

where $\tilde{S}_0 > \tilde{S}_i$. Equation (2.34) with the conditions (2.35) is formally the same as in the previous case. Therefore, without loss of generality, we derive the semi-analytical solution for the equation (2.32) and the case $S_0 > S_i$ only.

2.3.1. Derivation of Semi-Analytical Solution

In order to derive the McWhorter and Sunada closed-form solution, we introduce a function $F = F(S_w)$ as

$$F = f_w^{norm} - \frac{D}{At^{-\frac{1}{2}}(1 - Rf_w(S_i))} \frac{\partial S_w}{\partial x}, \quad (2.36)$$

where by f_w^{norm} , we denoted the *normalized* fractional flow function

$$f_w^{norm} = R \frac{f_w - f_w(S_i)}{1 - Rf_w(S_i)}. \quad (2.37)$$

A substitution

$$\lambda(S_w(t, x)) = xt^{-\frac{1}{2}}, \quad (2.38)$$

where the relationship $\lambda = \lambda(S_w)$ is assumed to be monotonous, allows to express the partial derivatives of $S_w(t, x)$ in the following form

$$\frac{\partial S_w}{\partial x} = \left(\frac{d\lambda(S_w)}{dS_w} \right)^{-1} t^{-\frac{1}{2}} \quad \text{and} \quad \frac{\partial S_w}{\partial t} = -\frac{1}{2} \left(\frac{d\lambda(S_w)}{dS_w} \right)^{-1} \lambda(S_w) t^{-1}. \quad (2.39)$$

Substituting the partial derivative $\partial S/\partial x$ given by (2.39) into (2.36), we obtain

$$F(S_w) = f_w^{norm}(S_w) - \frac{D(S_w)}{A(1 - Rf_w(S_i))} \left(\frac{d\lambda(S_w)}{dS_w} \right)^{-1}, \quad (2.40)$$

which reveals that $F = F(S_w)$ since variables x and t were eliminated. Equation (2.36) allows us to rewrite (2.32) in terms of F as

$$\phi \frac{\partial S_w}{\partial t} = -At^{-\frac{1}{2}}(1 - Rf_w(S_i)) \frac{\partial F}{\partial x}. \quad (2.41)$$

Using the fact that

$$\frac{\partial F}{\partial x} = \frac{dF}{dS_w} \frac{\partial S_w}{\partial x}, \quad (2.42)$$

the substitution of (2.39) into (2.41) leads to

$$-\phi \frac{1}{2} \left(\frac{d\lambda(S_w)}{dS_w} \right)^{-1} \lambda(S_w) t^{-1} = -A t^{-\frac{1}{2}} (1 - Rf_w(S_i)) \frac{dF(S_w)}{dS_w} \left(\frac{d\lambda(S_w)}{dS_w} \right)^{-1} t^{-\frac{1}{2}}, \quad (2.43)$$

from which the solution of (2.32) is obtained in the inverted form

$$\frac{2A(1 - Rf_w(S_i))}{\Phi} \frac{dF}{dS_w}(S_w(t, x)) = x t^{-\frac{1}{2}} = \lambda, \quad (2.44)$$

for all values of $S_w \in [S_i, S_0]$.

To obtain equation for the unknown function F , we differentiate (2.44) with respect to S_w

$$\frac{d^2 F}{dS_w^2} = \frac{\phi}{2A(1 - Rf_w(S_i))} \frac{d\lambda}{dS_w}, \quad (2.45)$$

where we substitute for $d\lambda/dS_w$ from (2.40) to get the following differential equation for $F = F(S_w)$

$$\frac{d^2 F}{dS_w^2} = -\frac{\phi}{2A^2(1 - Rf_w(S_i))^2} \frac{D}{F - f_w^{norm}}. \quad (2.46)$$

This equation can be integrated twice (see [45]) and using the conditions $F(S_0) = 1$ and $F'(S_0) = 0$, which follow from the boundary conditions (2.33a) and (2.33b), respectively, we obtain

$$F(S_w) = 1 - \frac{\phi}{2A^2(1 - Rf_w(S_i))^2} \int_{S_w}^{S_0} \frac{z - S_w}{F(z) - f_w^{norm}(z)} D(z) dz. \quad (2.47)$$

Taking into account that $F(S_i) = 0$, equation (2.47) yields

$$A^2 = \frac{\phi}{2(1 - Rf_w(S_i))} \int_{S_i}^{S_0} \frac{z - S_i}{F(z) - f_w^{norm}(z)} D(z) dz, \quad (2.48)$$

which is the integral expression that relates A and the boundary saturation S_0 .

Finally, we substitute (2.48) into (2.47) and obtain the integral equation for the unknown function $F = F(S_w)$

$$F(S_w) = 1 - \frac{\int_{S_w}^{S_0} \frac{z - S_w}{F(z) - f_w^{norm}(z)} D(z) dz}{\int_{S_i}^{S_0} \frac{z - S_i}{F(z) - f_w^{norm}(z)} D(z) dz}. \quad (2.49)$$

Differentiation of (2.49) with respect to S_w reveals that dF/dS_w (used in (2.44)) is obtained from

$$\frac{dF}{dS_w}(S_w) = \frac{\int_{S_w}^{S_0} \frac{D(z)}{F(z) - f_w^{norm}(z)} dz}{\int_{S_i}^{S_0} \frac{z - S_i}{F(z) - f_w^{norm}(z)} D(z) dz}. \quad (2.50)$$

2.3.2. Solution of Integral Equation

The integral equation (2.49) can be solved numerically [45]. We propose two iteration schemes suitable for obtaining the solution $F = F(S_w)$ for nearly all ranges of the input parameters S_0 , S_i , and R . Using the functional transformation

$$G = \frac{D}{F - f_w^{norm}}, \quad (2.51)$$

these iteration schemes read as

$$G_{k+1}(S_w) = D(S_w) + G_k(S_w) \left(\frac{f_w^{norm}(S_w) + \frac{S_w}{S_0} \int_{S_i}^{S_0} (v - S_w) G_k(v) dv}{\int_{S_i}^{S_0} (v - S_i) G_k(v) dv} \right), \quad (2.52)$$

which is referred to as *Variant A* and

$$G_{k+1}(S_w) = [D(S_w) + G_k(S_w) f_w^{norm}(S_w)] \left(1 - \frac{\frac{S_w}{S_0} \int_{S_i}^{S_0} (v - S_w) G_k(v) dv}{\int_{S_i}^{S_0} (v - S_i) G_k(v) dv} \right)^{-1}. \quad (2.53)$$

which is referred to as *Variant B*.

When the function $G = G(S_w)$ is obtained using the iteration schemes (2.52) or (2.53), the solution $F = F(S_w)$ is computed from

$$F = f_w^{norm} + \frac{D}{G}, \quad (2.54)$$

and its derivative dF/dS_w from

$$\frac{dF}{dS_w}(S_w) = \frac{\int_{S_w}^{S_0} G(z) dz}{S_0 \int_{S_i}^{S_0} (z - S_i) G(z) dz}. \quad (2.55)$$

Finally, the solution $S_w = S_w(t, x)$ of the equation (2.32) is given implicitly by (2.44).

In Figure 2.7 and 2.6, we show typical shapes of the semi-analytical solutions for multiple choices of the parameters R and S_0 , respectively. A more detailed description of the McWhorter and Sunada solution in the homogeneous medium is given in [45] and [42]. We also provide an implementation of the semi-analytical solution in [39].

2.4. Advection and Diffusion Case in Heterogeneous Medium

When dealing with a layered porous medium, we need to simulate the conditions at material interfaces using equation (1.37). In order to verify that the behavior of fluids is simulated correctly by a numerical method, we need to use a suitable benchmark solution.

In [28] and [29] van Duijn *et al.* derived a semi-analytical solution for the pure diffusion form of (2.1) in $\Omega = \mathbb{R}$ for a porous medium with a single material discontinuity placed at $x = 0$. Inspired by their problem formulation, we found that two McWhorter and Sunada problem formulations for homogeneous media (2.32) in $\Omega^I = (-\infty, 0]$ and $\Omega^{II} = [0, +\infty)$, respectively,

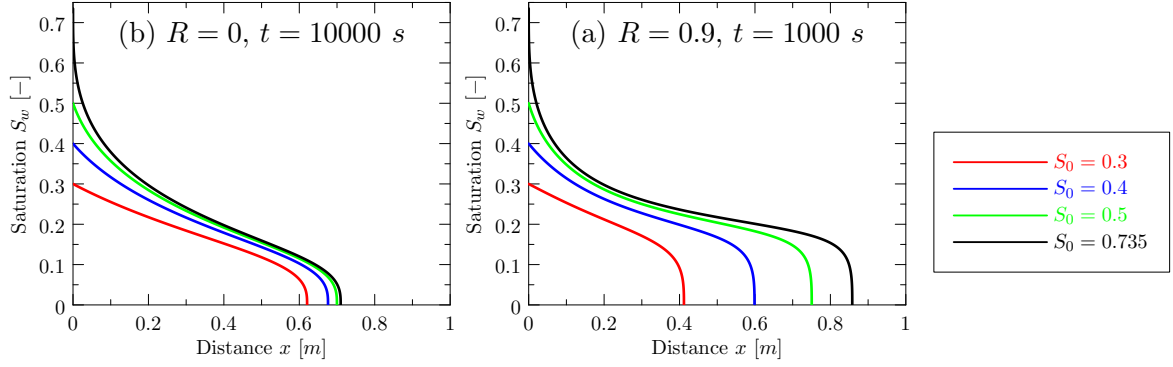


Figure 2.6.: Example of the McWhorter and Sunada semi-analytical solution for multiple choices of S_0 , $u_t(0) = A(S_0) t^{-\frac{1}{2}} \text{ m s}^{-1}$, $S_i = 0$, and (a) $R = 0$ or (b) $R = 0.9$. We used Sand A with parameters given in Table B.2 (page 122).

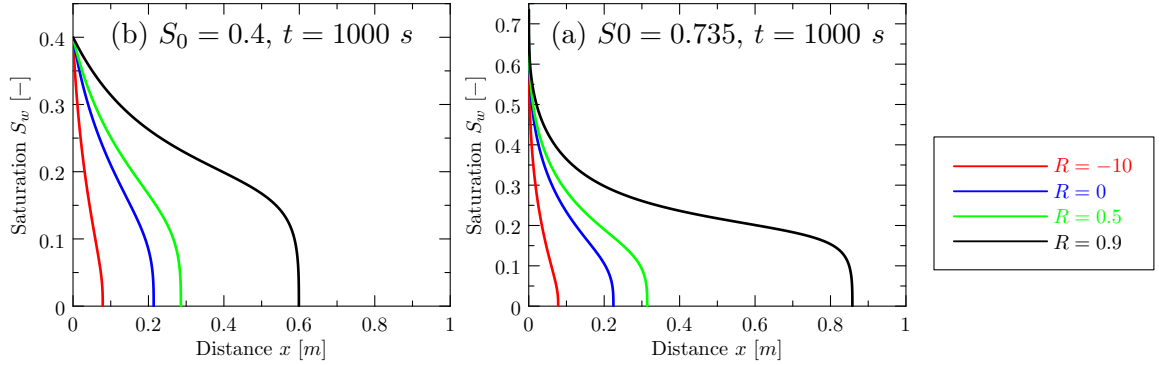


Figure 2.7.: Example of the McWhorter and Sunada semi-analytical solution for multiple choices of R , $u_t(0) = A(S_0) t^{-\frac{1}{2}} \text{ m s}^{-1}$, $S_i = 0$, and (a) $S_0 = 0.5$ or (b) $S_0 = 0.735$. We used Sand A with parameters given in Table B.2 (page 122).

can be combined to find a solution satisfying the continuity of the phase velocities (1.35) and the extended capillary condition (1.37) for the respective boundary values S_0^I and S_0^{II} , [46], [42]. In the following, by superscripts I and II , we shall denote the quantities corresponding to the McWhorter and Sunada problem formulation in Ω^I and Ω^{II} , respectively.

Under this notation, the system of the two-phase flow equations can be given as

$$\phi^I \frac{\partial S_w}{\partial t} = -RA^I t^{-\frac{1}{2}} \frac{\partial f_w^I}{\partial x} + \frac{\partial}{\partial x} \left[D^I \frac{\partial S_w}{\partial x} \right] \quad \text{in } \Omega^I, \quad (2.56a)$$

$$\phi^{II} \frac{\partial S_w}{\partial t} = -RA^{II} t^{-\frac{1}{2}} \frac{\partial f_w^{II}}{\partial x} + \frac{\partial}{\partial x} \left[D^{II} \frac{\partial S_w}{\partial x} \right] \quad \text{in } \Omega^{II}, \quad (2.56b)$$

and the initial and boundary conditions described below are given such that the semi-analytical solution can be obtained in both subdomains, see Figure 2.2b.

For Ω^I , we set

$$S_w(t, 0) = S_0^I, \quad \text{for all } t > 0, \quad (2.57a)$$

$$S_w(t, -\infty) = S_i^I, \quad \text{for all } t > 0, \quad (2.57b)$$

$$S_w(0, x) = S_i^I, \quad \text{for all } x < 0, \quad (2.57c)$$

and for Ω^{II} , we set

$$S_w(t, 0) = S_0^{II}, \quad \text{for all } t > 0, \quad (2.58a)$$

$$S_w(t, +\infty) = S_i^{II}, \quad \text{for all } t > 0, \quad (2.58b)$$

$$S_w(0, x) = S_i^{II}, \quad \text{for all } x > 0. \quad (2.58c)$$

In Ω^{II} , the wetting flux is given as

$$u_w^{II}(t, 0) = A^{II}t^{-\frac{1}{2}}, \quad (2.59)$$

and using the definition of the ratio R in (2.31), the total flux becomes $u_T = A^{II}Rt^{-\frac{1}{2}}$. The unknown interfacial saturations S_0^I and S_0^{II} are determined using the continuity of the fluxes (1.35) and the continuity of the capillary pressures (1.37) which reads as

$$p_c^I(S_0^I) = p_c^{II}(S_0^{II}). \quad (2.60)$$

We transform the problem in Ω^I to take advantage of the McWhorter and Sunada semi-analytical solution described in the previous section. This is done by a substitution of $\tilde{x} = -x$ in Ω^I . The transformed wetting-phase velocity \tilde{u}_w^I at $\tilde{x} = 0$ becomes

$$u_w^I(t, 0) = A^I t^{-\frac{1}{2}}. \quad (2.61)$$

At the interface, the wetting-phase flux is continuous (1.35), which allows to couple of both left and right subdomain problems together by requiring

$$A^I = -A^{II}. \quad (2.62)$$

Note that in (2.62) fluxes have opposite signs after the transformation $\tilde{x} = -x$. The total flux is constant in space throughout both subdomains and continuous across the interface. The value of the transformed total flux is

$$\tilde{u}_T = -u_T = -A^{II}Rt^{-\frac{1}{2}} = A^I R t^{-\frac{1}{2}}. \quad (2.63)$$

Consequently, the same value of the parameter R must be used in both subdomains.

The negative value of the flux in the McWhorter and Sunada formulation corresponds to the fact that $S_0 < S_i$. Thus, to obtain a positive value of A in one subdomain and a negative value of A in the other (c.f. (2.62)), either

$$S_0^I > S_i^I, \quad \text{and} \quad S_0^{II} < S_i^{II}, \quad (2.64a)$$

or

$$S_0^I < S_i^I, \quad \text{and} \quad S_0^{II} > S_i^{II}, \quad (2.64b)$$

must hold.

The existence of the semi-analytical solution for the porous medium with a material discontinuity is equivalent to the existence of saturations S_0^I and S_0^{II} such that the continuity condition (2.62) holds. Both A^I and A^{II} are functions of S_0^I , R , S_i^I , and S_0^{II} , R , S_i^{II} , respectively, but the explicit relationship fulfilling (2.62) is unknown and has to be determined numerically together with (2.60). If a solution of (2.62) exists, then it is unique due to monotonic relationship between A and S_0 and can be computed using the bisection method (see [45]).

Figure 2.8 shows typical shapes of such semi-analytical solutions for the pure diffusion ($R = 0$) and the advection–diffusion cases ($R \neq 0$). A more detailed description of the semi-analytical solution including a computational algorithm is presented in [46] and [42]. As in the homogeneous case, an implementation is available in [38].

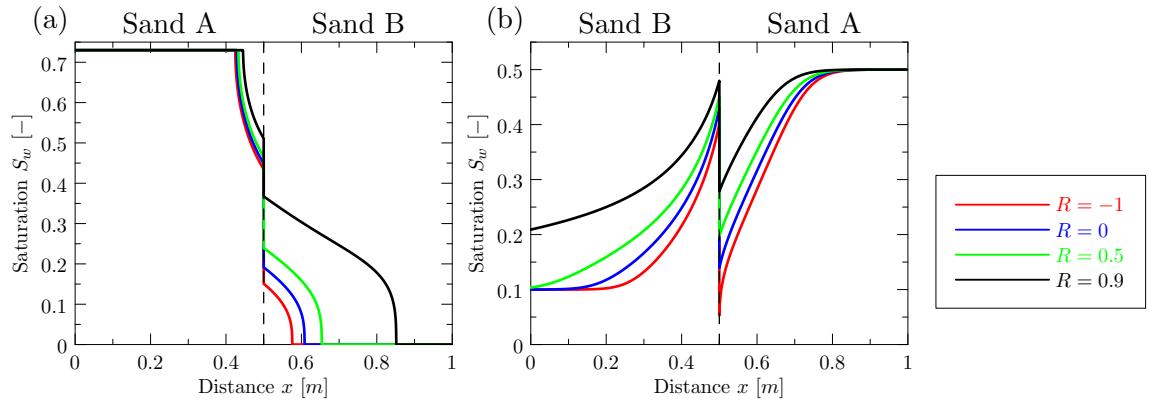


Figure 2.8.: Example of the semi-analytical solution in a heterogeneous porous medium for multiple choices of R and (a) $S_i^I = 0.265$, $S_i^{II} = 1$ or (b) $S_i^I = 0.9$, $S_i^{II} = 0.4$. As a porous material, we used Sand A and Sand B with parameters given in Table B.2 and B.3, respectively.

Mathematical prediction of flow of immiscible and incompressible fluids in porous media requires reliable models of capillary pressure–saturation relationships. In most past modelling efforts, various capillary pressure–saturation models (such as Brooks and Corey (1.23) or van Genuchten (1.26)) were developed based on laboratory experiments where capillary pressure and saturation were measured under equilibrium conditions. As described in Section 1.7.3, alternative models based on both empirical and theoretical approaches have been proposed to deal with these dynamic effects associated with the fluid flow [49], [50], [54], [56].

In unsaturated flow modelling, the two-phase flow system is simplified using the Richards equation (1.44), where the pressure of the non-wetting phase (air) is assumed to be constant throughout the domain. Using this simplification, in [67] the dynamic effect was not found to be of importance for a given heterogeneous system that was studied. Other numerical studies on the dynamic effect in capillary pressure models have been reported in [78], [77], or [97]. However, the implications of using the dynamic capillary pressure models in general two-phase models (without the assumption of constant non-wetting phase pressure) have not been fully investigated. In [59] the authors present a semi-implicit numerical scheme based on the upwind finite volume method, where the material interfaces in heterogeneous system are handled using the Lagrange multiplier method. In a subsequent paper [60], the idea has been further developed and the extended capillary pressure condition (1.37) takes the form of a variational inequality. In all these and other studies such as [14] or [91], only constant dynamic effect coefficient was assumed. However, experimental data in [104], [105], and [106] suggest that this coefficient depends on water saturation. We believe that this is critical especially in heterogeneous porous media.

We focus on the study of the implications of the use of dynamic effect in the capillary pressure–saturation relationship in modelling of flow of water and air in homogeneous and heterogeneous porous media described by (1.49) with the respective initial (1.50) and boundary (1.51) conditions. We propose a numerical scheme to model these cases of dynamic flow. Subsequently, this numerical scheme is verified by comparing with the semi-analytical solutions for the static capillary pressure developed earlier and presented in [80], [45] for homogeneous cases and [46] for a layered system. By means of the experimental order of convergence (defined later by (3.36)), we show that the developed numerical scheme is convergent and can be reliably used for simulating flow in both homogeneous and heterogeneous porous media systems. Various models of dynamic effects in capillary pressure defined through the empirical dynamic effect coefficient τ are investigated and compared to the static model of capillary pressure.

Our primary goal is to simulate the drainage flow regimes in a vertically placed one-dimensional column filled with either homogeneous or layered porous medium and determine the importance of the dynamic effect in capillary pressure–saturation relationship. We compare the numerical solutions obtained for various models of the dynamic effect coefficient τ to those computed using the static (*classical*) capillary pressure $p_c = p_c^{eq}$ and/or to the laboratory measured data.

The chapter is organized in the following way. In Section 3.1, we derive the fully implicit vertex-centered finite volume method for the system of two-phase flow equations (1.49). In Section 3.2, we verify its reliability using the benchmark solutions presented in Chapter 2. In Section 3.3, we describe a laboratory experiment of drainage in a homogeneous porous medium carried out at CESEP and discuss results of our numerical simulations that were performed in order to reproduce the experimentally measured data. We present a detailed numerical study on the dynamics of drainage flow regimes in heterogeneous porous media in Section 3.4. Concluding remarks are summarized in Section 3.5.

3.1. Fully Implicit Vertex-Centered Finite Volume Method in 1D

We use the vertex-centered finite volume method (VCFVM) to obtain a time fully implicit numerical scheme capable of solving the two-phase flow system of equations (1.49) in a one-dimensional porous medium. In the following sections, we describe the numerical scheme in details, focus on the conditions at material interfaces, and summarize how the initial and boundary conditions are implemented in the numerical scheme.

3.1.1. Numerical Scheme

We shall use the following form of the ψ_w – S_w formulation (1.49):

$$\phi \frac{\partial S_w}{\partial t} + \frac{\partial}{\partial x} u_w - F_w = 0, \quad (3.1a)$$

$$-\phi \frac{\partial S_w}{\partial t} + \frac{\partial}{\partial x} u_n - F_n = 0, \quad (3.1b)$$

$$u_w = -\lambda_w K \frac{\partial}{\partial x} \psi_w, \quad (3.1c)$$

$$u_n = -\lambda_n K \frac{\partial}{\partial x} (\psi_w + \psi_c), \quad (3.1d)$$

for all $x \in \Omega = (0, L)$ and all $t \in (0, T)$, where L [m] denotes the length (or height) of the domain (or column) and T [s] is the final time of the simulation. Initial and boundary conditions will be considered later.

Let us consider an ordered set of *vertices* $\mathcal{V} = \{V_k : k = 1, 2, \dots, N\}$ such that

$$(\forall V_{k_1}, V_{k_2} \in \mathcal{V})(k_1 < k_2 \Rightarrow 0 < V_{k_1} < V_{k_2} < L).$$

We construct a set of dual vertices $\mathcal{W} = \{W_k : k = 0, 1, \dots, N\}$ such that $W_0 = 0$, $W_N = L$, and for all $k = 0, 1, \dots, N$, vertex V_k is placed in the center of the *finite volume* $K_k = [W_k, W_{k+1}]$, see Figure 3.1.

We define the distance between successive points from \mathcal{V} and \mathcal{W} as $\Delta V_k = |V_{k+1} - V_k|_1$ and $\Delta W_k = |W_k - W_{k-1}|_1$, respectively. For any natural number k , we denote by ξ_k the mean value of a quantity or function ξ over a finite volume K_k . Next, as we need to address the values of a quantity ξ in the middle of two adjacent vertices V_k and V_{k+1} , we introduce the notation $\xi_{k+\frac{1}{2}} = \xi(\cdot, W_k)$.

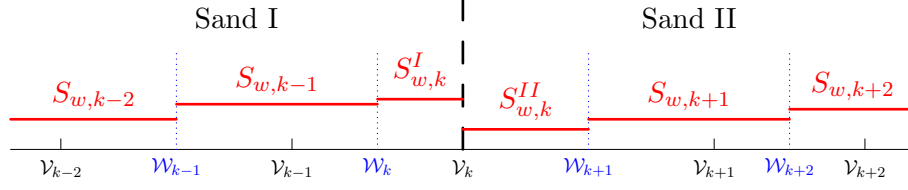


Figure 3.1.: Vertex-centered finite volume method applied to a one-dimensional domain.

Finally, we discretize the time interval $[0, T]$ by a set \mathcal{T} ,

$$\mathcal{T} = \{0 = t_0 < t_1 < \dots < t_M = T\}, \quad (3.2)$$

and we denote the time increments by $\Delta t_i = t_{i+1} - t_i$. By a superscript i , we denote the value of ξ on a time level $t = t_i$, i.e., $\xi^i = \xi(t_i, \cdot)$.

Integrating (3.1a) and (3.1b) over a finite volume K_k and a time interval $[t_i, t_{i+1}]$, we get

$$\int_{t_i}^{t_{i+1}} \int_{K_k} \phi \frac{\partial S_w}{\partial t} + \int_{t_i}^{t_{i+1}} \int_{K_k} \frac{\partial u_w}{\partial x} - \int_{t_i}^{t_{i+1}} \int_{K_k} F_w = 0, \quad (3.3a)$$

$$\int_{t_i}^{t_{i+1}} \int_{K_k} -\phi \frac{\partial S_w}{\partial t} + \int_{t_i}^{t_{i+1}} \int_{K_k} \frac{\partial u_n}{\partial x} - \int_{t_i}^{t_{i+1}} \int_{K_k} F_n = 0. \quad (3.3b)$$

In (3.3) we assume ϕ to be constant over K_k so that the finite volume K_k does not contain any material interfaces. Therefore, the integrals in (3.3) are evaluated as

$$\frac{\phi_k}{\Delta t_i} (S_{w,k}^{i+1} - S_{w,k}^i) + \frac{1}{\Delta W_k} (u_{w,k+1/2}^{i+1} - u_{w,k-1/2}^{i+1}) - F_{w,k}^{i+1} = 0, \quad (3.4a)$$

$$-\frac{\phi_k}{\Delta t_i} (S_{w,k}^{i+1} - S_{w,k}^i) + \frac{1}{\Delta W_k} (u_{n,k+1/2}^{i+1} - u_{n,k-1/2}^{i+1}) - F_{n,k}^{i+1} = 0, \quad (3.4b)$$

where the integrated source/sink term in (3.1a) and (3.1b) is denoted by

$$F_{\alpha,k}^{i+1} = \frac{1}{\Delta W_k \Delta t_i} \int_{t_i}^{t_{i+1}} \int_{K_k} F_n, \quad \alpha \in \{w, n\}. \quad (3.5)$$

We use the upwind technique [57], [74] to compute the discrete Darcy velocities $u_{w,k+1/2}^{i+1}$ and $u_{n,k+1/2}^{i+1}$ in (3.4) as

$$u_{w,k+1/2}^{i+1} = -\lambda_{w,k+1/2}^{upw,i+1} K \frac{\psi_{w,k+1}^{i+1} - \psi_{w,k}^{i+1}}{\Delta V_k}, \quad (3.6a)$$

$$u_{n,k+1/2}^{i+1} = -\lambda_{n,k+1/2}^{upw,i+1} K \frac{\psi_{w,k+1}^{i+1} - \psi_{w,k}^{i+1} + \psi_{c,k+1}^{i+1} - \psi_{c,k}^{i+1}}{\Delta V_k}, \quad (3.6b)$$

where $\lambda_{\alpha,k+1/2}^{upw,i+1}$ denotes the α -phase mobility taken in the upstream direction with respect to the gradient of the phase potential ψ_α , i.e.,

$$\lambda_{w,k+1/2}^{upw,i+1} = \begin{cases} \lambda_w(S_{w,k+1}^{i+1}), & \text{if } (\psi_{w,k+1}^{i+1} - \psi_{w,k}^{i+1}) \geq 0, \\ \lambda_w(S_{w,k}^{i+1}), & \text{otherwise,} \end{cases} \quad (3.7a)$$

$$\lambda_{n,k+1/2}^{upw,i+1} = \begin{cases} \lambda_n(S_{n,k+1}^{i+1}), & \text{if } (\psi_{n,k+1}^{i+1} - \psi_{n,k}^{i+1} + \psi_{c,k+1}^{i+1} - \psi_{c,k}^{i+1}) \geq 0, \\ \lambda_n(S_{w,k}^{i+1}), & \text{otherwise.} \end{cases} \quad (3.7b)$$

The discrete capillary potential $\psi_{c,k}^{i+1}$ reads as

$$\psi_{c,k}^{i+1} = \psi_c^{eq}(S_{w,k}^{i+1}) - \tau(S_{w,k}^{i+1}) \frac{S_{w,k}^{i+1} - S_{w,k}^i}{\Delta t_i}. \quad (3.8)$$

3.1.2. Material Interfaces

At a material interface, the properties of the porous media are discontinuous. By superscripts L and R , we denote the quantities that correspond to the left (between W_{k-1} and V_k) and right (between V_k and W_k) hand side of the interface, respectively (c.f., Figure 1.5). Since the normal components of the phase velocities u_α are continuous across the interface (1.35), the integration of the derivative of the velocity in (3.3) gives the same result as in (3.4). However, the discontinuity in porosity ϕ and saturation S_w requires to split the integral in the left hand sides of (3.3a) and (3.3b) into two parts

$$\int_{t_i}^{t_{i+1}} \int_{K_k} \phi \frac{\partial S_w}{\partial t} = \int_{t_i}^{t_{i+1}} \int_{W_{k-1}}^{V_k} \phi^L \frac{\partial S_w^L}{\partial t} + \int_{t_i}^{t_{i+1}} \int_{V_k}^{W_k} \phi^R \frac{\partial S_w^R}{\partial t}. \quad (3.9a)$$

Then, using the same technique as in (3.4), the resulting numerical scheme reads as

$$\begin{aligned} \frac{\phi_k^L}{2\Delta t_i} (S_{w,k}^{L,i+1} - S_{w,k}^{L,i}) + \frac{\phi_k^R}{2\Delta t_i} (S_{w,k}^{R,i+1} - S_{w,k}^{R,i}) + \\ \frac{1}{\Delta W_k} (u_{w,k+1/2}^{i+1} - u_{w,k-1/2}^{i+1}) - F_{w,k}^{i+1} = 0, \end{aligned} \quad (3.10a)$$

$$\begin{aligned} -\frac{\phi_k^L}{2\Delta t_i} (S_{w,k}^{L,i+1} - S_{w,k}^{L,i}) - \frac{\phi_k^R}{2\Delta t_i} (S_{w,k}^{R,i+1} - S_{w,k}^{R,i}) + \\ \frac{1}{\Delta W_k} (u_{n,k+1/2}^{i+1} - u_{n,k-1/2}^{i+1}) - F_{n,k}^{i+1} = 0. \end{aligned} \quad (3.10b)$$

An additional equation that relates $S_{w,k}^{L,i+1}$ and $S_{w,k}^{R,i+1}$ in (3.10) is given by the extended capillary condition (1.39). Assuming without loss of generality that $p_d^L < p_d^R$, equation (1.39) can be discretized as

$$S_{w,k}^{R,i+1} = 1 \quad \text{and} \quad p_{c,k}^{R,i+1} = p_d^R, \quad (3.11a)$$

if $p_c^L(S_{w,k}^{L,i+1}) < p_d^R$, and

$$\begin{aligned} p_c^{eq,L}(S_{w,k}^{L,i+1}) - \tau^L(S_{w,k}^{L,i+1}) \frac{1}{\Delta t_i} (S_{w,k}^{L,i+1} - S_{w,k}^{L,i}) - \\ p_c^{eq,R}(S_{w,k}^{R,i+1}) + \tau^R(S_{w,k}^{R,i+1}) \frac{1}{\Delta t_i} (S_{w,k}^{R,i+1} - S_{w,k}^{R,i}) = 0, \end{aligned} \quad (3.11b)$$

otherwise.

Equation (3.11) requires both values of the interfacial saturations $S_{w,k}^{L,i}$ and $S_{w,k}^{R,i}$ from the previous time level in contrast to the static case ($\tau^L = \tau^R = 0$), where it suffices to remember the saturation on the *coarser* side of the material interface only (i.e., $S_{w,k}^{L,i}$), since the capillary pressure function p_c^{eq} can be easily inverted in (3.11). In the dynamic case, however, the interfacial saturations $S_{w,k}^{L,i}$ and $S_{w,k}^{R,i}$ depend on the saturations on all previous time levels $S_{w,k}^{L,j}$ and $S_{w,k}^{R,j}$, $j = i-1, i-2, \dots, 0$, which would significantly increase the computational time with increasing i . To avoid such a recursion, we remember the values $S_{w,k}^{L,i}$ and $S_{w,k}^{R,i}$ from the previous time step at both sides of all material interfaces in Ω .

3.1.3. Initial and Boundary Conditions

The numerical scheme (3.4) is supplied by the initial and boundary conditions (1.50) and (1.51), respectively. The initial condition for the wetting phase saturation is given as

$$S_{w,k}^0 = S_w^{ini}(V_k), \quad \forall k. \quad (3.12)$$

The conditions at boundary points $\partial\Omega = \{W_0, W_N\}$ are discretized as

$$u_{\alpha,0-1/2} = -u_{\alpha}^N(W_0), \quad \text{if } W_0 \subset \Gamma_{\mathbf{u}_{\alpha}}, \quad (3.13a)$$

$$u_{\alpha,N+1/2} = u_{\alpha}^N(W_N), \quad \text{if } W_N \subset \Gamma_{\mathbf{u}_{\alpha}}, \quad (3.13b)$$

$$S_{w,1} = S_w^D(W_0), \quad \text{if } W_0 \subset \Gamma_{S_w}, \quad (3.13c)$$

$$S_{w,N} = S_w^D(W_N), \quad \text{if } W_N \subset \Gamma_{S_w}, \quad (3.13d)$$

$$\psi_{w,1} = \psi_w^D(W_0), \quad \text{if } W_0 \subset \Gamma_{\psi_w}, \quad (3.13e)$$

$$\psi_{w,N} = \psi_w^D(W_N), \quad \text{if } W_N \subset \Gamma_{\psi_w}, \quad (3.13f)$$

where $\alpha \in \{w, n\}$. If the Neumann boundary velocities are prescribed, we use (3.13a) or (3.13b) instead of the discrete Darcy velocities (3.6) in (3.4).

3.1.4. Numerical Solution

System of Nonlinear Equations

The system of nonlinear equations (3.4), (3.10), (3.11), and (3.13) can be represented in a vector form as

$$\mathbf{G}(\mathbf{y}^{i+1}) = \mathbf{0}, \quad (3.14)$$

where $\mathbf{G} : \mathbb{R}^{2N+q} \rightarrow \mathbb{R}^{2N+q}$ is a vector function and \mathbf{y}^{i+1} is a vector of $(2N+q)$ -unknowns, where q is the number of material interfaces in Ω . By k_1, k_2, \dots, k_q , we denote indices of the vertices placed at the material interfaces. The components of the vector \mathbf{y}^{i+1} are for all $k = 1, 2, \dots, N$ given by

$$[\mathbf{y}^{i+1}]_{2k-1} = \begin{cases} S_{w,k}^{L,i+1} & \text{if } k \in \{k_1, k_2, \dots, k_q\}, \\ S_{w,k}^{i+1} & \text{otherwise,} \end{cases} \quad (3.15a)$$

$$[\mathbf{y}^{i+1}]_{2k} = \psi_{w,k}^{i+1}, \quad (3.15b)$$

and for all $j = 1, 2, \dots, q$, by

$$[\mathbf{y}^{i+1}]_{2N+j} = S_{w,k_j}^{R,i+1}. \quad (3.16)$$

The components of the vector function \mathbf{G} in (3.14) read for all $k = 1, 2, \dots, N$ as

$$[\mathbf{G}(\mathbf{y}^{i+1})]_{2k-1} = \begin{cases} \text{left hand side of (3.10a)}, & \text{if } k \in \{k_1, k_2, \dots, k_q\}, \\ S_{w,1} - S_w^D(W_0), & \text{if } k = 1 \text{ and } W_0 \subset \Gamma_{S_w}, \\ S_{w,N} - S_w^D(W_N), & \text{if } k = N \text{ and } W_N \subset \Gamma_{S_w}, \\ \text{left hand side of (3.4a)}, & \text{otherwise,} \end{cases} \quad (3.17a)$$

$$[\mathbf{G}(\mathbf{y}^{i+1})]_{2k} = \begin{cases} \text{left hand side of (3.10b)}, & \text{if } k \in \{k_1, k_2, \dots, k_q\}, \\ \psi_{w,1} - \psi_w^D(W_0), & \text{if } k = 1 \text{ and } W_0 \subset \Gamma_{\psi_w}, \\ \psi_{w,N} - \psi_w^D(W_N), & \text{if } k = N \text{ and } W_N \subset \Gamma_{\psi_w}, \\ \text{left hand side of (3.4b)}, & \text{otherwise,} \end{cases} \quad (3.17b)$$

and for all $j = 1, 2, \dots, q$, as

$$[\mathbf{G}(\mathbf{y}^{i+1})]_{2N+j} = \text{left hand side of (3.11b)}. \quad (3.18)$$

Under this notation, the system of nonlinear equations (3.14) has the following structure. There is always a pair of equations

$$[\mathbf{G}(\mathbf{y}^{i+1})]_{2k-1} = 0, \quad (3.19)$$

$$[\mathbf{G}(\mathbf{y}^{i+1})]_{2k} = 0, \quad (3.20)$$

for all $k = 1, 2, \dots, N$ that couples at most 6 unknowns

$$[\mathbf{y}^{i+1}]_{\max\{2k-3,1\}}, \quad [\mathbf{y}^{i+1}]_{\max\{2k-2,1\}}, \quad (3.21a)$$

$$[\mathbf{y}^{i+1}]_{2k-1}, \quad [\mathbf{y}^{i+1}]_{2k}, \quad (3.21b)$$

$$[\mathbf{y}^{i+1}]_{\min\{2k+1,2N\}}, \quad [\mathbf{y}^{i+1}]_{\min\{2k+2,2N\}}. \quad (3.21c)$$

In case of a layered porous medium with q material interfaces, the system of nonlinear equation (3.14) includes q equations at material interfaces (3.11) that depend only on two unknowns $[\mathbf{y}^{i+1}]_{2k_j-1} = S_{w,k_j}^{L,i+1}$ and $[\mathbf{y}^{i+1}]_{2N+j} = S_{w,k_j}^{R,i+1}$ for $j = 1, 2, \dots, q$.

Newton–Raphson Method

We use the Newton–Raphson iteration method to solve the nonlinear vector equation (3.14) in the form

$$\mathbf{y}_{\ell+1}^{i+1} = \mathbf{y}_{\ell}^{i+1} - [\mathbf{G}'(\mathbf{y}_{\ell}^{i+1})]^{-1} \mathbf{G}(\mathbf{y}_{\ell}^{i+1}), \quad (3.22)$$

where \mathbf{G}' denotes the Jacobi matrix of the vector function \mathbf{G} . As a starting vector ($\ell = 0$) in (3.22), we choose

$$\mathbf{y}_0^{i+1} = \mathbf{y}^i, \quad (3.23)$$

where \mathbf{y}^i is the vector that corresponds to the previous time step t_i . Note that when $i = 0$, we use the initial condition (3.12) for $S_{w,k}^0$ and we always choose hydrostatic $\psi_{w,k}^0$ as an initial guess for \mathbf{y}_0^1 .

We rewrite (3.22) in the form

$$\Delta \mathbf{y}_{\ell+1}^{i+1} = -[\mathbf{G}'(\mathbf{y}_{\ell}^{i+1})]^{-1} \mathbf{G}(\mathbf{y}_{\ell}^{i+1}), \quad (3.24)$$

where

$$\Delta \mathbf{y}_{\ell+1}^{i+1} = \mathbf{y}_{\ell+1}^{i+1} - \mathbf{y}_{\ell}^{i+1}. \quad (3.25)$$

It follows from (3.24) that the increment $\Delta \mathbf{y}_{\ell+1}^{i+1}$ of the vector \mathbf{y}_{ℓ}^{i+1} is the solution of a linear system of equations

$$[\mathbf{G}'(\mathbf{y}_{\ell}^{i+1})] \Delta \mathbf{y}_{\ell+1}^{i+1} = -\mathbf{G}(\mathbf{y}_{\ell}^{i+1}). \quad (3.26)$$

In each iteration of (3.24), the solution of (3.26) is the most expensive step from the computational point of view. In order to diminish the required amount of work, we take advantage of the structure of the system of equations (3.14) introduced by (3.17) and (3.21) and solve the linear system (3.26) in the following way. We represent (3.26) as

$$\begin{pmatrix} \mathbf{G}'_{11} & \mathbf{G}'_{12} \\ \mathbf{G}'_{21} & \mathbf{G}'_{22} \end{pmatrix} \begin{pmatrix} \mathbf{z}_1 \\ \mathbf{z}_2 \end{pmatrix} = \begin{pmatrix} \mathbf{w}_1 \\ \mathbf{w}_2 \end{pmatrix}, \quad (3.27)$$

where

$$\mathbf{G}'_{11} \in \mathbb{R}^{2N \times 2N} : \quad [\mathbf{G}'_{11}]_{j,k} = [\mathbf{G}'(\mathbf{y}_\ell^{i+1})]_{j,k}, \quad (3.28a)$$

$$\mathbf{G}'_{21} \in \mathbb{R}^{q \times 2N} : \quad [\mathbf{G}'_{21}]_{m,k} = [\mathbf{G}'(\mathbf{y}_\ell^{i+1})]_{2N+m,k}, \quad (3.28b)$$

$$\mathbf{G}'_{22} \in \mathbb{R}^{q \times q} : \quad [\mathbf{G}'_{22}]_{m,n} = [\mathbf{G}'(\mathbf{y}_\ell^{i+1})]_{2N+m,2N+n}, \quad (3.28c)$$

$$\mathbf{G}'_{12} \in \mathbb{R}^{2N \times q} : \quad [\mathbf{G}'_{12}]_{j,n} = [\mathbf{G}'(\mathbf{y}_\ell^{i+1})]_{j,n}, \quad (3.28d)$$

$$\mathbf{w}_1 \in \mathbb{R}^{2N} : \quad [\mathbf{w}_1]_j = -[\mathbf{G}(\mathbf{y}_\ell^{i+1})]_j, \quad (3.28e)$$

$$\mathbf{w}_2 \in \mathbb{R}^q : \quad [\mathbf{w}_2]_m = -[\mathbf{G}(\mathbf{y}_\ell^{i+1})]_{2N+m}, \quad (3.28f)$$

$$\mathbf{z}_1 \in \mathbb{R}^{2N} : \quad [\mathbf{z}_1]_j = [\Delta \mathbf{y}_{\ell+1}^{i+1}]_j, \quad (3.28g)$$

$$\mathbf{z}_2 \in \mathbb{R}^q : \quad [\mathbf{z}_2]_m = [\Delta \mathbf{y}_{\ell+1}^{i+1}]_{2N+m}, \quad (3.28h)$$

for all $j, k = 1, 2, \dots, 2N$, and $m, n = 1, 2, \dots, q$.

The linear system (3.27) can be regarded as a block system of two linear equations with two unknowns \mathbf{z}_1 and \mathbf{z}_2 . Assuming that \mathbf{G}'_{11} is non-singular, we express \mathbf{z}_1 from the first equation in (3.27) in terms of \mathbf{z}_2 as

$$\mathbf{z}_1 = \mathbf{G}'_{11}{}^{-1} (\mathbf{w}_1 - \mathbf{G}'_{12} \mathbf{z}_2). \quad (3.29)$$

We use (3.29) in the second equation in (3.27) to get a single linear equation for the unknown vector \mathbf{z}_2

$$\left(-\mathbf{G}'_{21} \mathbf{G}'_{11}{}^{-1} \mathbf{G}'_{12} + \mathbf{G}'_{22} \right) \mathbf{z}_2 = \mathbf{w}_2 - \mathbf{G}'_{21} \mathbf{G}'_{11}{}^{-1} \mathbf{w}_1. \quad (3.30)$$

The vector \mathbf{z}_2 determined as the solution of (3.30) is then substituted in (3.29). Altogether, the solution of (3.27) is obtained in the form

$$\mathbf{z}_1 = \mathbf{G}'_{11}{}^{-1} \left[\mathbf{w}_1 - \mathbf{G}'_{12} \left(\mathbf{G}'_{22} - \mathbf{G}'_{21} \mathbf{G}'_{11}{}^{-1} \mathbf{G}'_{12} \right)^{-1} \left(\mathbf{w}_2 - \mathbf{G}'_{21} \mathbf{G}'_{11}{}^{-1} \mathbf{w}_1 \right) \right], \quad (3.31a)$$

$$\mathbf{z}_2 = \left(\mathbf{G}'_{22} - \mathbf{G}'_{21} \mathbf{G}'_{11}{}^{-1} \mathbf{G}'_{12} \right)^{-1} \left(\mathbf{w}_2 - \mathbf{G}'_{21} \mathbf{G}'_{11}{}^{-1} \mathbf{w}_1 \right). \quad (3.31b)$$

The following algorithm is used to compute (3.31):

1. Solve $\mathbf{G}'_{11} \mathbf{q} = \mathbf{w}_1$ and $\mathbf{G}'_{11} \mathbf{Q} = \mathbf{G}'_{12}$, where $\mathbf{q} \in \mathbb{R}^{2N}$ and $\mathbf{Q} \in \mathbb{R}^{2N \times q}$. It follows from (3.17) and (3.28a) that the matrix \mathbf{G}'_{11} is block tridiagonal with 2×2 -blocks and thus we use the Thomas algorithm to compute $\mathbf{q} = \mathbf{G}'_{11}{}^{-1} \mathbf{w}_1$ and $\mathbf{Q} = \mathbf{G}'_{11}{}^{-1} \mathbf{G}'_{12}$. Note that the Thomas algorithm is not expensive from computational point of view since the number of arithmetic operations depends linearly on the size of the matrix.
2. Solve $(\mathbf{G}'_{22} - \mathbf{G}'_{21} \mathbf{Q}) \mathbf{z}_2 = \mathbf{w}_2 - \mathbf{G}'_{21} \mathbf{q}$. Recall that the matrix $(\mathbf{G}'_{22} - \mathbf{G}'_{21} \mathbf{Q})$ is a $q \times q$ -matrix, where q denotes the number of material interfaces in the domain, which is usually a very small number. Consequently, we use the direct Gaussian elimination method to compute $\mathbf{z}_2 = (\mathbf{G}'_{22} - \mathbf{G}'_{21} \mathbf{Q})^{-1} (\mathbf{w}_2 - \mathbf{G}'_{21} \mathbf{q})$.
3. Solve $\mathbf{G}'_{11} \mathbf{z}_1 = (\mathbf{w}_1 - \mathbf{G}'_{12} \mathbf{z}_2)$ again using the Thomas algorithm and obtain $\mathbf{z}_1 = \mathbf{G}'_{11}{}^{-1} (\mathbf{w}_1 - \mathbf{G}'_{12} \mathbf{z}_2)$.
4. Set $\Delta \mathbf{y}_{\ell+1}^{i+1} = \begin{pmatrix} \mathbf{z}_1 \\ \mathbf{z}_2 \end{pmatrix}$.

Note that if no material interfaces are present in the medium ($q = 0$), we solve $\mathbf{G}'_{11} \mathbf{z}_1 = \mathbf{w}_1$ using the Thomas algorithm only and set $\Delta \mathbf{y}_{\ell+1}^{i+1} = \mathbf{z}_1$.

Line Search Strategy

The Newton–Raphson method (3.22) seeks the next iteration $\mathbf{y}_{\ell+1}^{i+1}$ in the direction $\Delta\mathbf{y}_{\ell+1}^{i+1}$ in the domain of definition of \mathbf{G} towards the solution of (3.14), where $\Delta\mathbf{y}_{\ell+1}^{i+1}$ is the solution of (3.26). If \mathbf{y}_{ℓ}^{i+1} is in a sufficiently close neighborhood of the solution, the iteration method has a quadratic convergence, [2]. Otherwise,

$$\mathbf{y}_{\ell+1}^{i+1} = \mathbf{y}_{\ell}^{i+1} + \Delta\mathbf{y}_{\ell+1}^{i+1} \quad (3.32)$$

may move too far away from the neighborhood causing the iteration method to stagnate or diverge. In order to avoid the stagnation, we use the line search strategy with a modifier $\eta \in (0, 1]$, i.e., we search for $\mathbf{y}_{\ell+1}^{i+1}$ in the form

$$\mathbf{y}_{\ell+1}^{i+1} = \mathbf{y}_{\ell}^{i+1} + \eta\Delta\mathbf{y}_{\ell+1}^{i+1}, \quad (3.33)$$

where η is the largest value in the set $\{1, 1/2, 1/4, \dots\}$ such that

$$\|\mathbf{G}(\mathbf{y}_{\ell}^{i+1} + \eta\Delta\mathbf{y}_{\ell+1}^{i+1})\|_2 \leq \left(1 - \frac{\eta}{4}\right) \|\mathbf{G}(\mathbf{y}_{\ell}^{i+1})\|_2, \quad (3.34)$$

see [2]. In some cases, the iteration process is unable to decrease $\|\mathbf{G}(\mathbf{y}_{\ell}^{i+1})\|_2$ under the required threshold after the maximal number of iterations ζ_{ℓ} or the minimal admissible line search modifier ζ_{η} and thus we decrease the time step Δt_i by a factor denoted by $\zeta_{\Delta t}$ and restart the iteration procedure. On the other hand, if the process is convergent for at least ζ_{it} successive time steps, we increase the time step Δt_i by the factor of $\zeta_{\Delta t}$. We stop the iteration process, when $\|\mathbf{G}(\mathbf{y}_{\ell}^{i+1})\|_2$ is lower than a stopping threshold criterion ζ_G . The typical values of parameters are $\zeta_{\ell} = 100$, $\zeta_{\eta} = 10^{-4}$, $\zeta_{\Delta t} = 1.5$, $\zeta_{it} = 1000$, and $\zeta_G = 10^{-6}$.

3.2. Verification of Numerical Scheme

We test the numerical scheme (3.4) on the analytical and semi-analytical solutions introduced in Chapter 2. These are available for the static capillary pressure model ($\tau = 0$) and no gravity ($g = 0$) only. The convergence of the numerical scheme is investigated for a homogeneous and heterogeneous porous medium, respectively, by means of the experimental order of convergence.

We consider a one dimensional domain $\Omega = (0, 1)$ filled with a porous medium initially fully saturated by water. In the following simulations, we use laboratory-measured sand properties provided by CESEP to verify the numerical model under realistic conditions. Parameters of these sands are described in Tables B.2–B.4 in Appendix B. Since our aim is to simulate the laboratory experiment held in CESEP, we use the sand A (the *Ohji sand*) in the presented numerical experiments.

In each benchmark problem I.–V., water is displaced by air due to an imposed flux at the boundary. We select the final time T such that the front of the benchmark solution stays inside the domain $\Omega = (0, 1)$.

3.2.1. Benchmark I : Pure Advection

We use the pure advection benchmark (2.14) (see Section 2.2) with $S_0 = 0.265$ (residual water saturation), $S_i = 1$ (maximal water saturation), and $u_T(t) = 10^{-4} \text{ m s}^{-1}$.

In the numerical formulation (3.4), we set $S_w^{ini} = S_i = 1$ and at the inlet ($x = 0$), we prescribe the Neumann boundary condition as $u_n^N(t, 0) = u_T(t) = 10^{-4} \text{ m s}^{-1}$ and $\psi_w^D(t, 0) = 0 \text{ Pa}$. We choose the final time $T = 1000 \text{ s}$ such that the front of the analytical solution stays inside Ω . In Figure 3.2, we compare the numerical solutions computed on regular meshes with mesh sizes h to the Buckley and Leverett analytical solution.

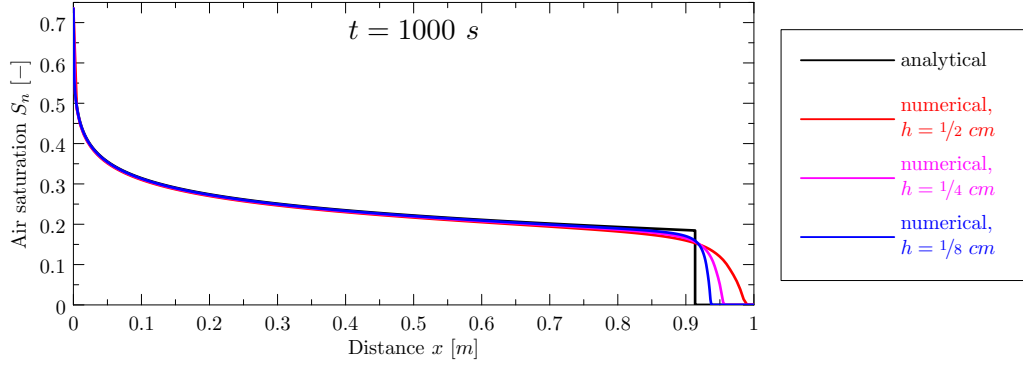


Figure 3.2.: Numerical solutions computed for multiple choices of the finite volume size h compared to the Buckley and Leverett analytical solution; $t = 1000$ s and $\Delta t/h = 2$ s/cm is kept constant.

3.2.2. Benchmark II : Pure Diffusion in Homogeneous Medium

We use the pure diffusion benchmark problem formulation (2.32) (see Section 2.3) with $R = 0$ (and thus $u_T = 0$), $S_0 = 0.5$, and $S_i = 1$.

In the numerical formulation (3.4), we set $S_w^{ini} = S_i = 1$ and prescribe the following boundary conditions. At the inlet ($x = 0$), we set the Dirichlet boundary condition for $S_w^D(t, 0) = S_0 = 0.5$ and $\psi_w^D(t, 0) = 0$ Pa and at $x = 1$ m, we impose zero Neumann boundary velocities $u_n^N(t, 1) = u_w^N(t, 1) = 0$ ms⁻¹. By choosing the final time of the simulation as $T = 15000$ s, we assure that the air-front stays inside Ω during the simulation. We compute the numerical solutions on a series of regular meshes with decreasing mesh sizes h and compare them to the McWhorter and Sunada semi-analytical solution in Figure 3.3.

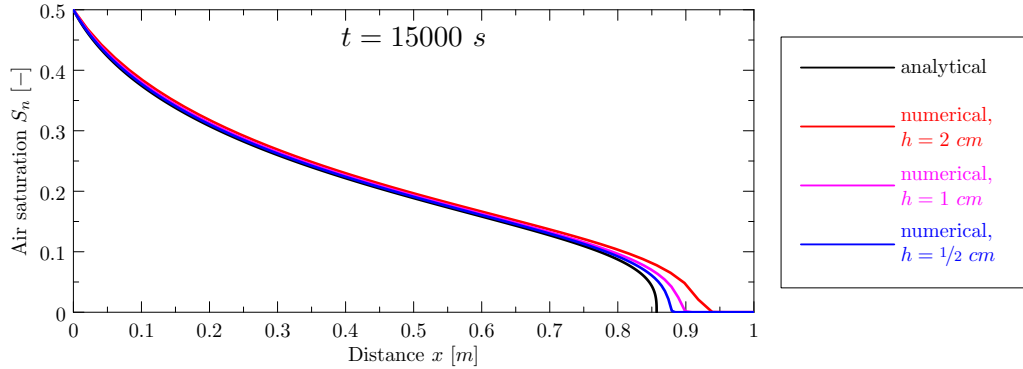


Figure 3.3.: Numerical solution of the pure diffusion McWhorter and Sunada problem in a homogeneous porous medium; $t = 15000$ s and $\Delta t/h^2 = 4$ s/cm² is kept constant.

3.2.3. Benchmark III : Advection and Diffusion in Homogeneous Medium

We test both advection and diffusion by means of the McWhorter and Sunada problem formulation (2.32) with $R = 0.92$, $S_0 = 0.5$ and $S_i = 1$. We use (2.48) to compute the McWhorter and Sunada input flux rate parameter A which, for the selected parameters S_0 and R , is $A = 1.53 \cdot 10^{-3}$ ms^{-1/2}.

In the numerical formulation (3.4), we set $S_w^{ini} = S_i = 1$ and prescribe the following boundary conditions. At the inlet ($x = 0$), we set the air and water Neumann boundary velocities to $u_n^N(t, 0) = At^{-1/2}$ and $u_w^N(t, 0) = (R - 1)At^{-1/2}$, respectively. At the outlet ($x = 1$ m), we set

$u_w^{\mathcal{N}}(t, 1) = RAt^{-\frac{1}{2}} \text{ ms}^{-1}$ and $S_w^{\mathcal{D}}(t, 1) = S_i = 1$. We choose the final time $T = 1000 \text{ s}$ such that the air-front stays inside Ω . We compute the numerical solutions on a series of regular meshes with decreasing mesh sizes and compare them to the semi-analytical solution in Figure 3.4.

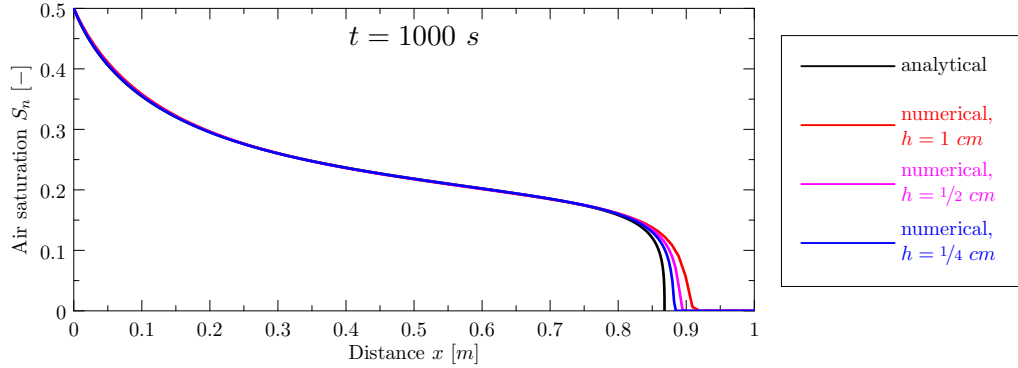


Figure 3.4.: Numerical solution of the advection–diffusion McWhorter and Sunada problem in a homogeneous porous medium; $t = 1000 \text{ s}$ and $\Delta t/h^2 = 4 \text{ s/cm}^2$ is kept constant.

3.2.4. Benchmark IV : Pure Diffusion in Layered Medium

We consider the pure diffusion benchmark problem with a single material discontinuity (2.56) (see Section 2.4) with $R = 0$, $S_i^I = 0.3$, and $S_i^{II} = 1$ with the problem setup sketched in Figure 2.2b. We assume that Ω is composed of homogeneous subdomains filled with Sands A and B in $\Omega^I = [0, 1/2]$ and $\Omega^{II} = [1/2, 1]$, respectively, where sand B is finer than sand A. The sand properties are shown in Table B.2 and B.3 in Appendix B.

In the numerical model (3.4), we set the following initial and boundary conditions. Initially, $S_w(0, x) = 0.3$ in Ω^I and $S_w(0, x) = 1$ in Ω^{II} . At $x = 0$, we prescribe $S_w^{\mathcal{D}}(t, 0) = 0.3$ and a constant water pressure $\psi_w^{\mathcal{D}}(t, 0) = 0 \text{ Pa}$, while on the other boundary at $x = 1$, we set $u_w^{\mathcal{N}}(t, 1) = u_w^{\mathcal{N}}(t, 1) = 0 \text{ ms}^{-1}$. We compute the numerical solutions on a series of meshes and compare them to the van Duijn and de Neef semi-analytical solution [28] in Figure 3.5.

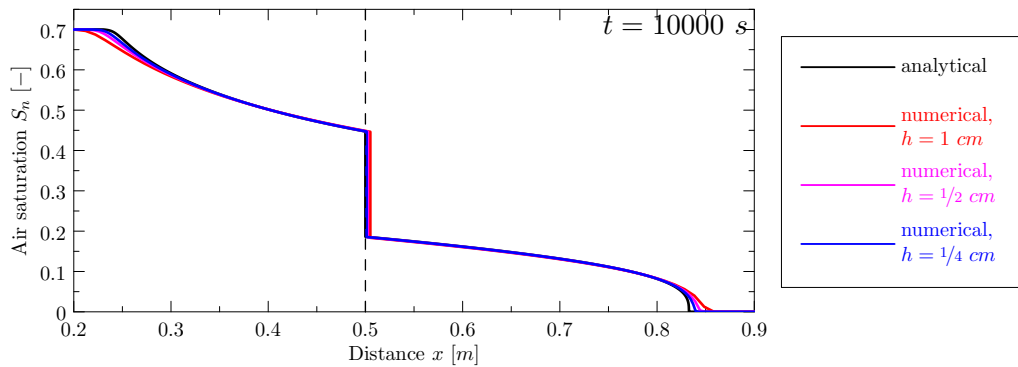


Figure 3.5.: Numerical solution of the pure diffusion problem in a layered porous medium; $t = 10000 \text{ s}$ and $\Delta t/h^2 = 4 \text{ s/cm}^2$ is kept constant.

3.2.5. Benchmark V : Advection and Diffusion in Layered Medium

We consider the semi-analytical solution for the diffusion and advection driven flow in a porous medium with a single material discontinuity (2.56) with $R = 0.9$, $S_i^I = 0.3$, and $S_i^{II} = 1$. We

use the same setup of the domain Ω as in the previous case.

In the numerical model (3.4), we consider the following initial and boundary conditions. Initially, $S_w(0, x) = 0.3$ in Ω^I and $S_w(0, x) = 1$ in Ω^{II} . At $x = 0$, we set $S_w^D(t, 0) = 0.3$ and $\psi^D(t, 0) = 0$ Pa. The boundary conditions at $x = 1$ read as $u_n^N(t, 1) = 0$ ms⁻¹ and $u_w^N(t, 1) = RA t^{-\frac{1}{2}}$, where $A = 5.61 \cdot 10^{-4}$ ms^{- $\frac{1}{2}$} . The numerical solutions compared to the semi-analytical are shown in Figure 3.6.

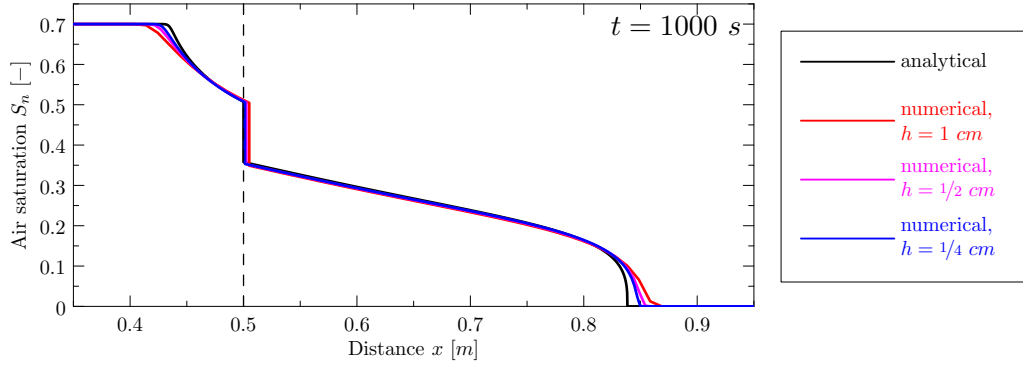


Figure 3.6.: Numerical solution of the advection–diffusion problem in a layered porous medium; $t = 1000$ s and $\Delta t/h^2 = 4$ s/cm² is kept constant.

3.2.6. Experimental Order of Convergence

For each benchmark solution, we evaluate the experimental order of convergence eoc which estimates the theoretical order of convergence ϵ of the numerical scheme. The experimental order of convergence is computed using the L_1 or L_2 norm of the difference between the numerical S_w^{num} and the semi-analytical solution S_w^{an} at the final time of the simulation. For numerical solutions on two regular meshes with mesh sizes h_1 and h_2 denoted as S_{w,h_1}^{num} and S_{w,h_2}^{num} , respectively, we expect their error norms to be in the form

$$\|S_{w,h_1}^{num} - S_w^{an}\|_k = C (h_1)^\epsilon, \quad (3.35a)$$

$$\|S_{w,h_2}^{num} - S_w^{an}\|_k = C (h_2)^\epsilon, \quad (3.35b)$$

where C is some positive constant and $k = 1, 2$. In (3.35) we assume that $\Delta t \propto h$ and $\Delta t \propto h^2$ for pure advection and advection-diffusion problems, respectively. Using (3.35), the order of convergence ϵ is approximated by the experimental order of convergence eoc_k as

$$\epsilon \approx eoc_k(h_1, h_2) = \frac{\ln \|S_{w,h_1}^{num} - S_w^{an}\|_k - \ln \|S_{w,h_2}^{num} - S_w^{an}\|_k}{\ln h_1 - \ln h_2}, \quad (3.36)$$

$k = 1, 2$.

In Table 3.1, the values of eoc show the convergence rate of the numerical solution towards the exact solution. These values are typical for a first-order numerical scheme with upwind technique, [74]. The experimental orders of convergence indicate that the numerical solution converges to the analytical solution in both homogeneous and heterogeneous benchmarks.

The numerical approximation of the discontinuous fronts is not sharp if the advection term dominates the flow in Figures 3.2, 3.4, and 3.6. This is due to the upwind technique which involves excessive numerical diffusion in the numerical scheme.

Figures 3.5 and 3.6 show that the jump in saturations across the interface in the case of the heterogeneous porous medium is determined correctly.

$h_1 \rightarrow h_2$ [cm]	eoc_1					eoc_2				
	I	II	III	IV	V	I	II	III	IV	V
2 \rightarrow 1	0.18	0.93	0.68	0.82	0.47	0.20	0.74	0.34	0.48	0.29
1 \rightarrow 1/2	0.62	0.93	0.74	0.89	0.99	0.38	0.76	0.47	0.55	0.58
1/2 \rightarrow 1/4	0.77	0.89	0.76	0.91	1.12	0.39	0.66	0.55	0.55	0.67
1/4 \rightarrow 1/8	0.75	0.88	0.85	0.91	1.12	0.36	0.75	0.61	0.56	0.73
1/8 \rightarrow 1/16	0.80	0.80	0.87	0.92	1.04	0.40	0.74	0.70	0.55	0.65
1/16 \rightarrow 1/32	0.83	0.67	0.75	0.96	1.01	0.41	0.64	0.66	0.55	0.64
1/32 \rightarrow 1/64	0.85	0.52	0.63	0.96	1.00	0.43	0.58	0.72	0.54	0.65

Table 3.1.: Experimental orders of convergence eoc_1 and eoc_2 computed for Benchmark Problems I–V in L_1 and L_2 norms, respectively.

3.2.7. Benchmark VI: Barrier Effect Verification

In principle, the benchmark solutions derived by van Duijn and de Neef [28] and Fučík *et al.* [46] cannot simulate the barrier effect described in Section 1.9 because they always require a non-zero flux of the non-wetting phase across the material interface. In order to verify simulation of the barrier effect using our numerical scheme, we use the problem formulation described in [58], [57, page 275]. Here, a non-wetting phase, denoted as DNAPL A (see Table B.1, page 121), displaces water from an initially fully water-saturated, vertically placed column shown in Figure 3.7. At the inlet ($x = 0$), the DNAPL velocity is given as $u_n(t, 0) = 3.57 \cdot 10^{-5} \text{ m s}^{-1}$ whereas the water velocity is zero. At the bottom of the column, the maximal wetting-phase saturation $S_w = 1$ is prescribed and the water pressure is kept constant at $2 \cdot 10^5 \text{ Pa}$. The column consists of three sand layers and two different sands denoted as Sand D and E; their properties are given in Tables B.5, respectively. The sharp material interfaces are placed at $x = 0.145 \text{ m}$ and $x = 0.345 \text{ m}$, see Figure 3.7. The final time of the simulation $T = 1650 \text{ s}$ is chosen such that the DNAPL front stays inside the domain $\Omega = [0, 0.5]$.

In Figure 3.8, we show numerical results computed on a series of regular meshes with mesh size h . The presented results agree with the results obtained by the Fully-Upwind Galerkin method shown in [57, Fig. 5.39, on page 286] and, therefore, the numerical scheme (3.4) treats the extended capillary pressure condition (1.37) correctly.

3.3. Simulation of Laboratory Experiment

In this section, we use the numerical scheme (3.4) to simulate a drainage laboratory experiment [106] in order to investigate how the numerical solutions are affected by the use of the dynamic effect in capillarity in comparison with the experimentally measured data and with numerical solutions obtained using the standard, static capillary pressure–saturation relationship.

First, we describe the experimental setup and procedure. We also describe the technique that were used to determine three functional models of the dynamic effect coefficient $\tau = \tau(S_w)$ and summarize other relevant data that will be later used in the numerical simulations as input parameters. Then, we simulate the drainage flow regime under dynamic conditions using the measured data and the models for the capillary pressure–saturation relationship under static and dynamic conditions. As a result, we present and discuss measured and numerically simulated time evolution of the saturation and capillary pressure.

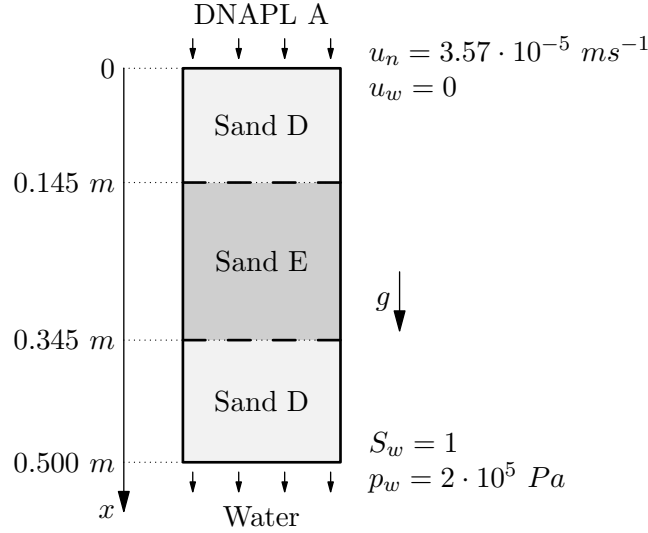


Figure 3.7.: Geometric configurations with boundary conditions of a three-layered porous medium for Benchmark Problem VI (redrawn from [57, Fig. 5.30, on page 275]).

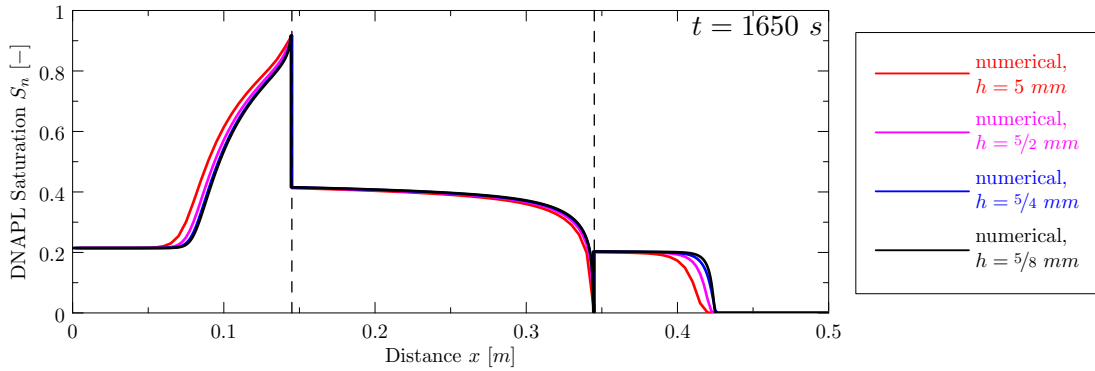


Figure 3.8.: Numerical solutions of Benchmark Problem VI. The time step Δt is chosen adaptively.

3.3.1. Description of Experimental Setup

The experiment consisted of a single, vertically placed 10 cm long Tempe cell uniformly filled with a homogeneous field sand from a site Ohji sampled in Tokyo, Japan, [104], [105], [106]. A schematic view of the experimental apparatus is shown in Figure 3.9. The following detailed description of the apparatus and measurement procedure was provided by Prof. Sakaki (edited):

Two tensiometers were installed in the middle of the sample height (at $x = 5 \text{ cm}$) for water pressure measurement. The porous cup was glued to a brass tubing connector that was connected to a pressure transducer. Roughly 2.5 cm of the porous cup penetrated into the sand sample. Pressure readings from the two tensiometers were averaged and used as the capillary pressure p_c based on the assumption that air equilibrates to atmospheric faster than the interval over which water pressures are measured using the pressure transducers. This assumption has been confirmed in separate experiments using the same experimental procedure and apparatus (e.g., porous media, Tempe cell) where both the air and water pressures were quantified at the column midpoint for a selected subset of experiments conducted in this study (results not shown). These separate experiments found that the air phase rapidly

equilibrates to atmospheric pressure at the column midpoint, the measurement location. Using a two-phase flow numerical model [14], it was further confirmed that the air phase pressure at the column midpoint, when a suction of -80 cm water is applied at the column midpoint, is less than -0.2 cm water after 2.5 minutes. This suggests that it is appropriate to assume that the water pressure measured by the two tensiometers in this study can be considered as the capillary pressure.

A soil moisture sensor was installed in the middle of the sample height to quantify water saturation. The moisture sensor uses capacitance to measure the apparent dielectric constant of the surrounding medium. The moisture sensor was installed with the prongs in a vertical orientation (one on top of the other) to minimize interferences with the flow path (see Figure 3.9). Under the given sensor configuration, the sampling volume of the moisture sensor is enclosed within a vertical thickness of $1.0 - 1.5$ cm [76]. This can be considered to be sufficiently small for the measured water saturation to be considered a point-value [108], [104]. The measured water pressure is representative of the mid slice with a thickness of 0.64 cm. Thus, it is appropriate to assume that the retention curves constructed using the measured capillary pressure and water saturation values are those at the midpoint in the soil column.

In these experiments, it was also crucial that measurements of the water pressure and saturation were made at the same time. The response time of the water pressure (pressure transducer and porous cups) and saturation measuring systems were tested and found to respond quickly (on the order of 1 to 2 seconds for the pressure measurement, whereas the soil moisture sensor response was almost instantaneous). It was thus assumed that the response times were within the necessary tolerance as pressure and saturation were quantified every 15 seconds in both the static and dynamic experiments.

Finally, the ceramic porous plate at the bottom of the column was replaced by a hydrophilic Nylon membrane. The membrane was glued onto a perforated acrylic plate that has the same dimensions as the porous plate. It was further assumed that potential dynamic effects within the membrane were negligible since the membrane was initially water-saturated and no change in saturation occurred during the experiment [14]. The bottom of the column was connected to a constant-head reservoir whose elevation can be varied. A more detailed description of the modification of the Tempe cell is provided in [104].

The Ohji sand is denoted as sand A and its physical properties are given in Table B.2 in Appendix B. Initially, the column was flushed with water such that no air phase was present inside. A series of slow drainage steps was carried out in order to determine the capillary pressure-saturation relationship in equilibrium $p_c^{eq} = p_c^{eq}(S_w)$. The fitted Brooks and Corey model parameters are shown in Table B.2 (page 122). Then, a series of fast drainage and imbibition experiments was performed and values of the capillary pressure and the air saturation were measured by probes sensors in the middle of the column. In the primary drainage cycle, the measured τ exhibited a dependency on saturation shown in Figure 3.10. Therefore, three models were fitted and evaluated and their explicit formulae are given in Table B.2, [106].

3.3.2. Numerical Simulation

We use the numerical scheme (3.4) to simulate the experimental setup using a one-dimensional domain sketched in Figure 3.11, Case 1. We compare the time evolution of the simulated and

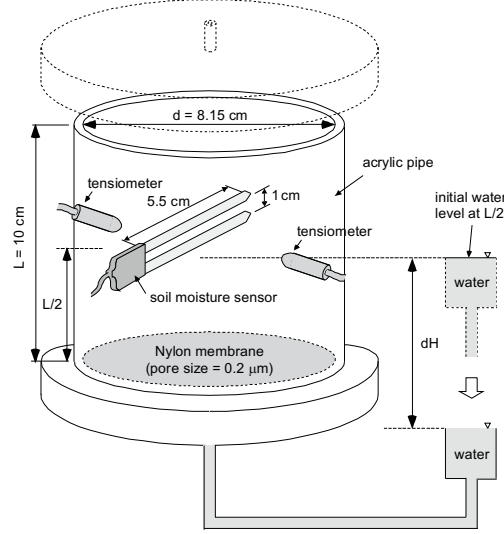


Figure 3.9.: A schematic view of the experimental apparatus. The top boundary was exposed to the atmosphere through a small hole on the top cap. The bottom boundary was connected to the constant-head water reservoir. Water pressure was measured with two tensiometers and averaged. (Provided by Prof. Sakaki, [104], [106].)

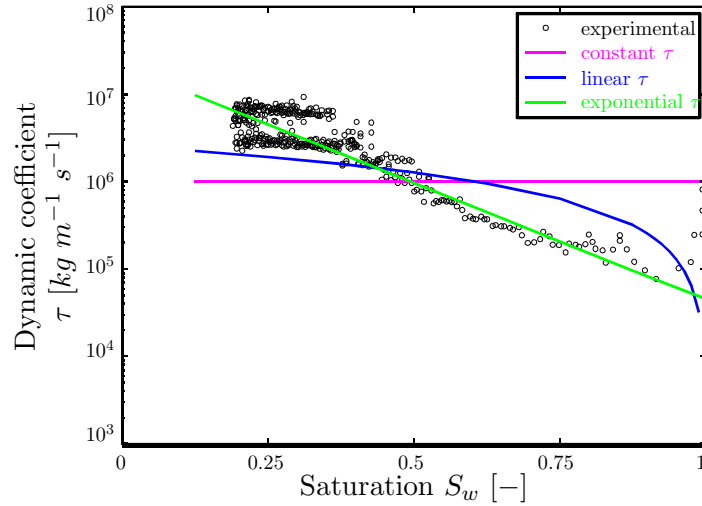


Figure 3.10.: Fitted models of dynamic coefficient τ (log-scale) to the observed laboratory data (after Sakaki *et al.*, 2010, [106]).

measured air saturation $S_n(t, 5 \text{ cm})$ and capillary pressure $p_c(t, 5 \text{ cm})$ in the middle of the column using the static and dynamic models for the capillary pressure.

Initially, the column is fully water-saturated such that $S_w(0, x) = 1$ for all $x \in (0, 1)$. At the upper boundary, $u_w^N(t, 0) = 0 \text{ m s}^{-1}$ and the air pressure is assumed to be constant and equal to the atmospheric pressure $p_n(t, 0) = 10^5 \text{ Pa}$. At the lower boundary, we prescribe the water outflow u_{water} (solid line in Figure 3.12) that was measured during the laboratory experiment, i.e., $u_w^N(t, 10 \text{ cm}) = u_{water}(t)$. Due to the presence of the hydrophilic membrane that does not allow air to penetrate, we set $u_n^N(t, 10 \text{ cm}) = 0 \text{ m s}^{-1}$.

The resulting time evolution of the air saturation S_n and the capillary pressure p_c in the middle of the column are shown in Figure 3.13. In Figure 3.13, the solutions have non-smooth

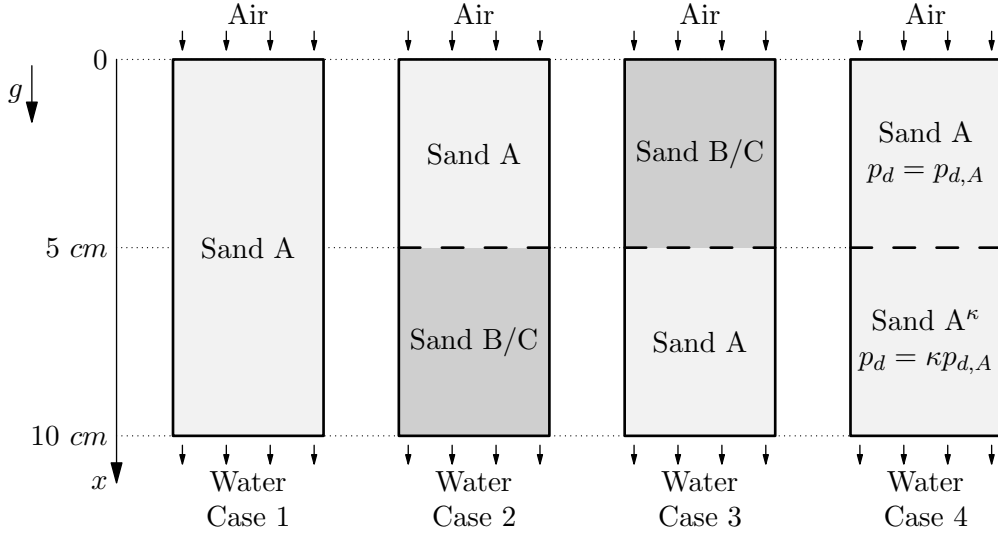


Figure 3.11.: A sketch of homogeneous (Case 1) and layered (Cases 2–4) configurations of the porous medium. In each case, the porous medium is placed vertically and fully water-saturated $S_w = 1$ at $t = 0$ s. The gravitational acceleration vector \mathbf{g} points in the positive x -direction.

shapes but those are caused solely by the non-smoothness of the prescribed flux of water at $x = 10$ cm. Since the temporal derivative of the air saturation is directly influenced by the given flux, the non-smoothness is magnified in the values of the dynamic capillary pressure given by (1.29). This is why the bumps do not appear in the case of the static capillary pressure. In Figure 3.15, we show profiles of the saturation and capillary pressure at $t = 300$ s obtained using the experimentally measured outflow. To assure that the differences among the numerical solutions with respect to different models of $\tau(S_w)$ are not caused by the non-smoothness of the prescribed flux, we use a smooth functional approximation of the boundary flux that preserves the total mass of the effluent water in the form

$$u_{water}^*(t) = 3.7 \cdot 10^{-5} \exp(-1.7 \cdot 10^{-3}t) + 7.4 \cdot 10^{-7} \text{ [ms}^{-1}\text{]}. \quad (3.37)$$

In Figure 3.12, the measured flux of water is compared to its smooth functional approximation u_{water}^* . As shown in Figure 3.14, the numerical solutions computed with u_{water}^* are smooth alternatives to the bumpy shaped solutions in Figure 3.13. Apparently, the bumpiness of the capillary pressure is not caused by the numerical scheme and the non-smoothness of the prescribed flux does not affect significantly the overall time evolution of the solutions.

The influence of different models of the dynamic effect coefficient τ on the numerical solution of the air saturation S_n is negligible (see Figures 3.13 and 3.14). On the other hand, their influence on the capillary pressure p_c is important in cases, where there is a temporal change in S_n because the time derivative of S_n is multiplied by the dynamic effect coefficient τ in equation (1.29). Lower parts of Figures 3.13 and 3.14 show time evolution of p_c for various models of $\tau = \tau(S_w)$ compared to the static p_c (red line) and also to the laboratory measured values (black dashed line). The values of p_c for the static, linear, and loglinear model of τ are strictly increasing in time which agrees to the laboratory measured evolution of p_c . However, the values of p_c with the constant model for τ exhibit different behavior. First at $t = 3$ min, the value of p_c rapidly jumps to 4800 Pa. Then, it strictly decreases towards the values of the static p_c . In the first 10 minutes of the simulation, the saturation S_n in the middle of the column steeply increases from 0 to 0.25. In Figure 3.10, the linear and exponential models for τ have more than one order of magnitude lower values than the constant model for the values of $S_w \in (0.75, 1)$ that correspond to $S_n \in (0, 0.25)$. Consequently, the dynamic effect term in (1.29) gives substantially

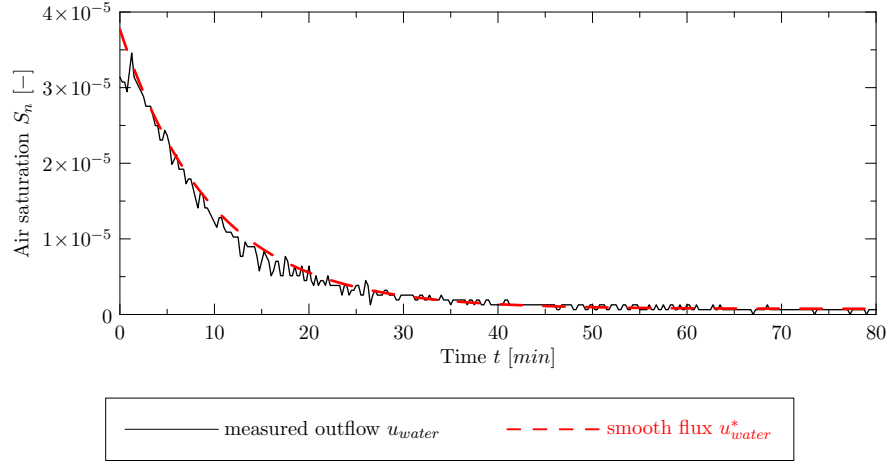


Figure 3.12.: Measured and smoothly approximated water outflow from the column at $x = 10 \text{ cm}$.

higher values of τ for the constant model than for the other models which explains the different time evolution of p_c in Figures 3.13 and 3.14.

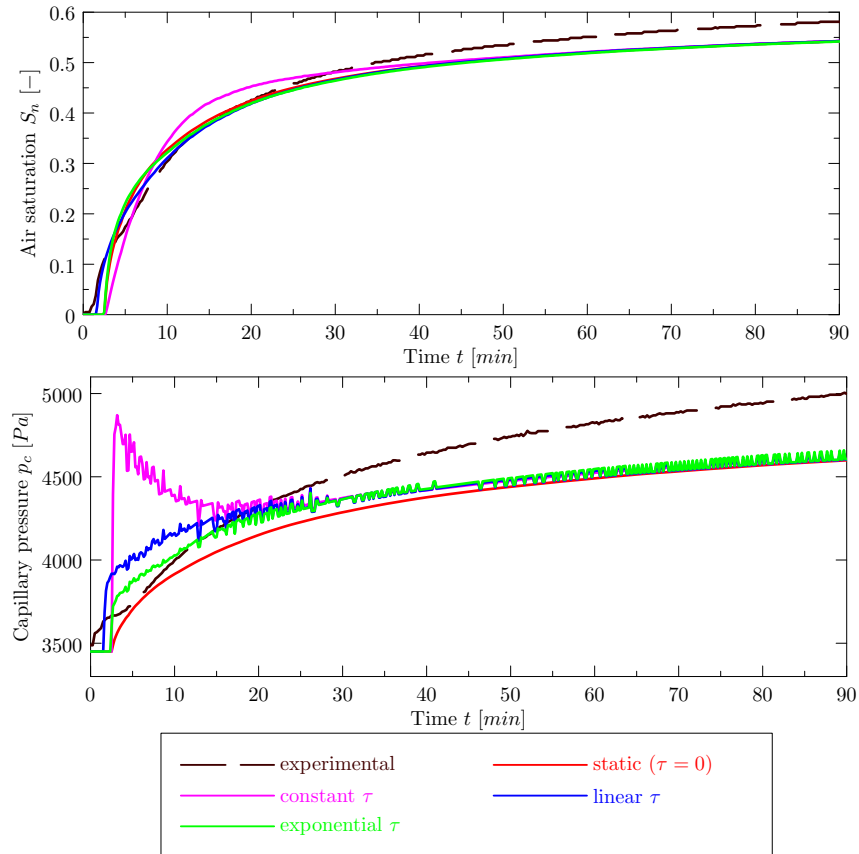


Figure 3.13.: Numerical solutions and measured laboratory values of S_n and p_c in the middle of the column for various models of $\tau = \tau(S_w)$. Numerical solutions were obtained with $N = 400$ nodes, adaptive time stepping strategy, and by using laboratory measured flux (see the solid line in Figure 3.12) through the lower boundary.

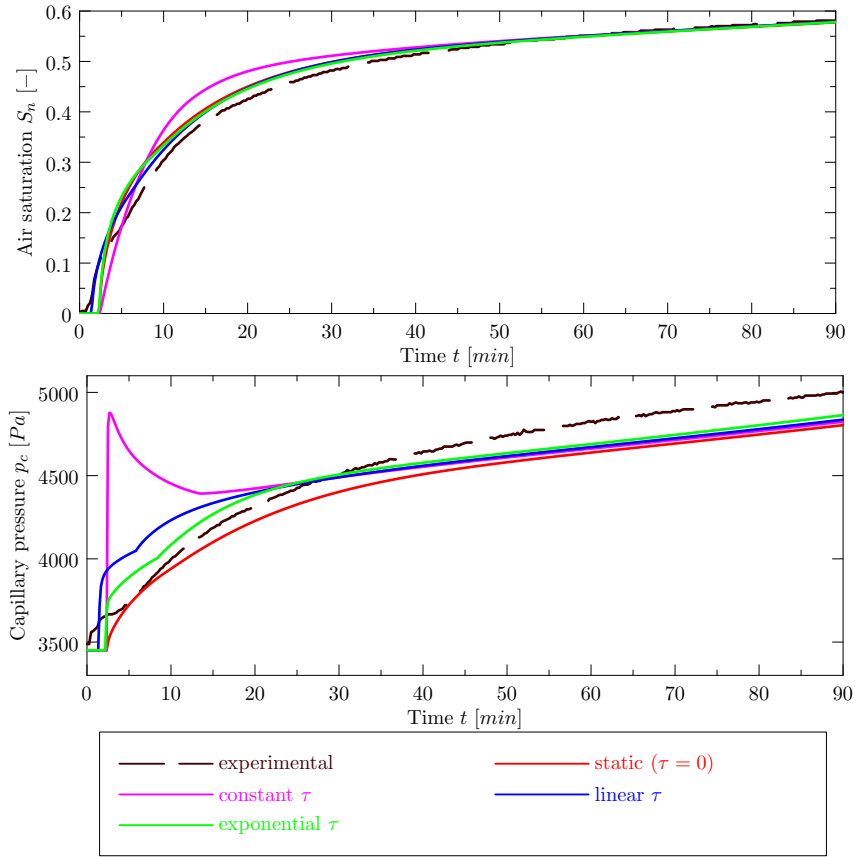


Figure 3.14.: Numerical solutions and measured laboratory values of S_n and p_c in the middle of the column for various models of $\tau = \tau(S_w)$. Numerical solutions were obtained with $N = 400$ nodes, adaptive time stepping strategy, and by using smooth flux (see the dashed line in Figure 3.12) through the lower boundary.

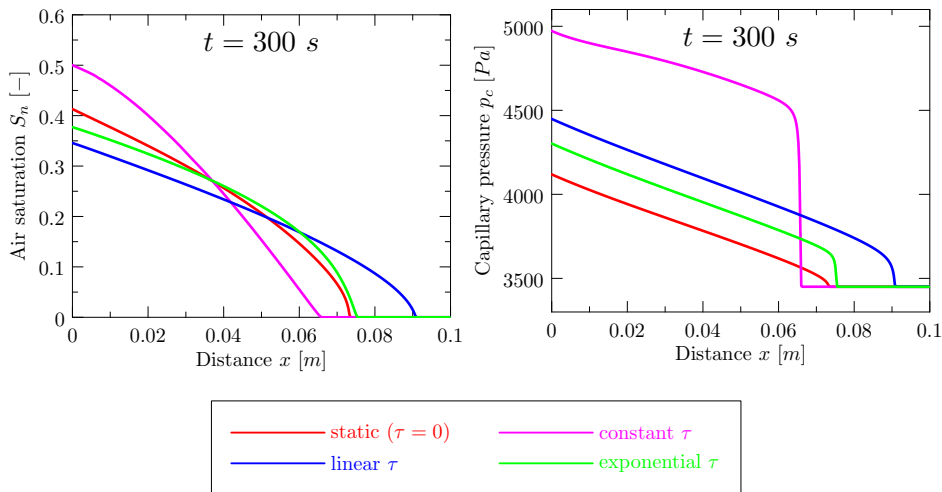


Figure 3.15.: Example of the numerical solutions obtained with $N = 800$ nodes and adaptive time stepping strategy. Distribution of the air saturation S_n and capillary pressure p_c at $t = 300$ s shows the differences among the solutions using multiple models of the dynamic coefficient $\tau = \tau(S_w)$.

3.3.3. Dynamic Coefficient Sensitivity Analysis

In order to assure that the different time evolution of p_c for the constant model of τ is caused by the magnitude of the dynamic effect term in (1.29) only and not by the choice of the functional dependency of $\tau = \tau(S_w)$, we present a sensitivity analysis of the numerical solution on the absolute value of the dynamic effect coefficient. As in the previous section, we use the numerical scheme (3.4) to simulate the laboratory experiment using the smoothed water flux u_{water}^* . We multiply the three measured dynamic coefficient models by 2, 4, 6, and 8, respectively, and observe the time evolution of S_n and p_c in the middle of the column in Figures 3.16–3.18.

The evolution of the air saturation obtained using the amplified dynamic coefficients τ are nearly identical to the results in Figure 3.14 which mimic the experimental conditions and laboratory determined values. On the other hand, the evolution of the capillary pressure using the amplified dynamic coefficients exhibits a rapid increase in the beginning of the simulation (from 0 to 1 minute in Figure 3.16, from 0 to 10 minutes in Figure 3.17, or from 0 to 15 minutes in Figure 3.18). Then, the capillary pressure decreases smoothly towards the solution obtained using the static model (the dashed line in Figures 3.16–3.18). The change in monotonicity in time of p_c is observed for all of the considered functional models $\tau = \tau(S_w)$ and is directly proportional to the magnitude of the dynamic effect coefficient. Consequently, the different time evolution of p_c with constant τ with respect to the linear and exponential models for τ in Figures 3.13 and 3.14 is due to large values of τ_{const} with respect to τ_{lin} and τ_{exp} for high wetting-phase saturation in Figure 3.10.

While the change in saturation is negligible in Figures 3.13–3.18, the magnitude of the capillary pressure with the dynamic effect may differ substantially from the static model.

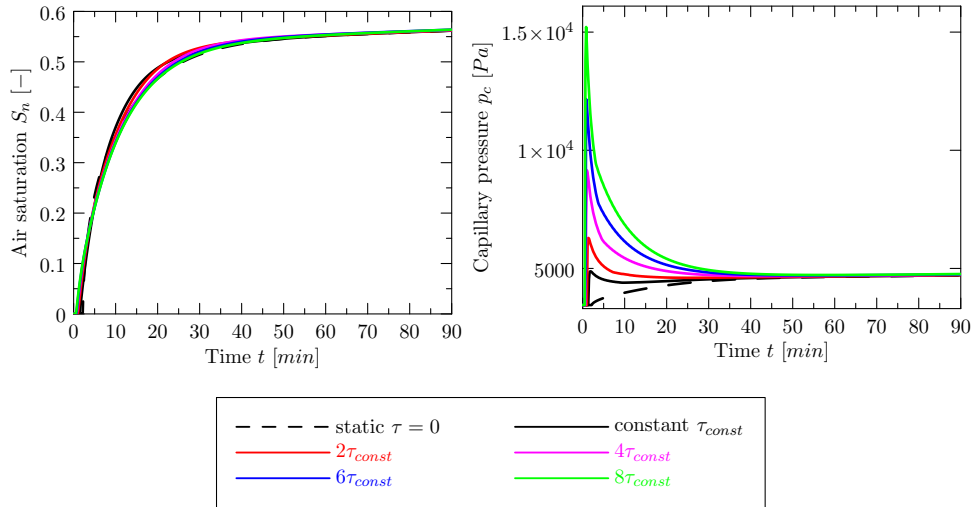


Figure 3.16.: Numerically simulated evolution of S_n and p_c in the middle of the column obtained using the smooth flux u_{water}^* through the lower boundary, $N = 400$ nodes and adaptive time stepping strategy. The static capillarity model is compared to the dynamic models of p_c with the constant model of $\tau(S_w) = \tau_{const}$ and its multiples (sensitivity analysis).

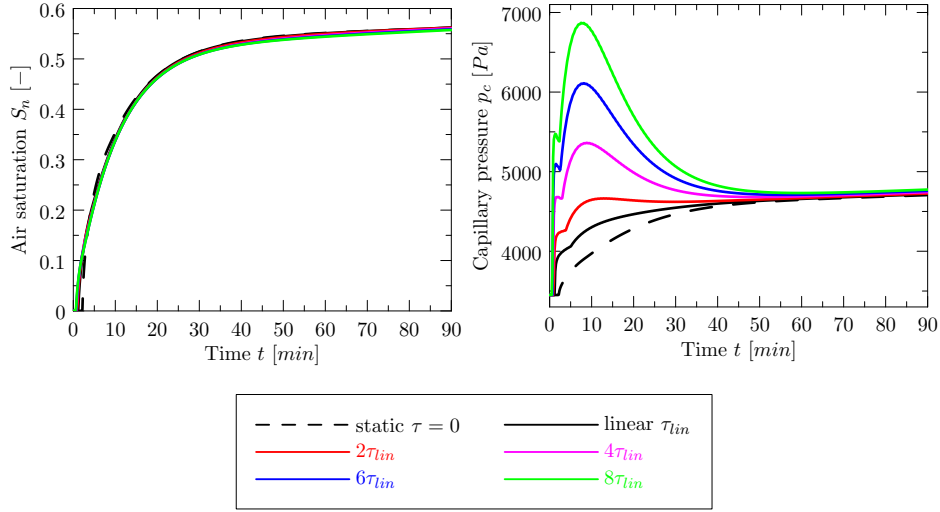


Figure 3.17.: Numerically simulated evolution of S_n and p_c in the middle of the column obtained using the smooth flux u_{water}^* through the lower boundary, $N = 400$ nodes and adaptive time stepping strategy. The static capillarity model is compared to the dynamic models of p_c with the linear model of $\tau(S_w) = \tau_{lin}(S_w)$ and its multiples (sensitivity analysis).

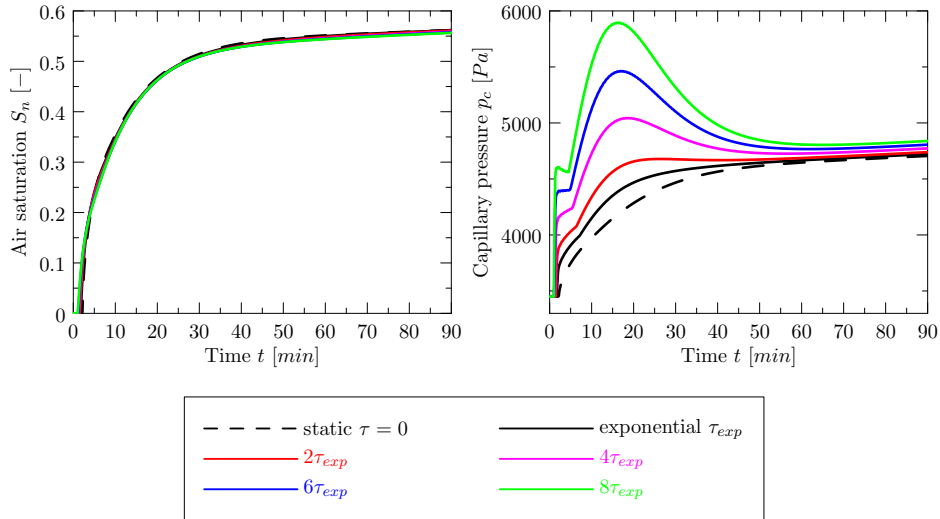


Figure 3.18.: Numerically simulated evolution of S_n and p_c in the middle of the column obtained using the smooth flux u_{water}^* through the lower boundary, $N = 400$ nodes and adaptive time stepping strategy. The static capillarity model is compared to the dynamic models of p_c with the exponential model of $\tau(S_w) = \tau_{exp}(S_w)$ and its multiples (sensitivity analysis).

3.4. Numerical Simulations in Layered Medium

As described in Section 1.9, the magnitude of the capillary pressure plays a crucial role in the propagation of fluids across material interfaces, when the non-wetting fluid flows from a coarser to a finer porous material. In this section, we investigate effects of different dynamic capillary pressure models on the behavior of the air phase at heterogeneity interfaces. Since no laboratory experiment involving dynamic capillary pressure is available for such a case, only a numerical simulation is provided in this section. Similar to the setup of the laboratory experiment in Section 3.3, we consider a vertically-placed column filled with two different sands (denoted as I and II). Both sands are separated by a sharp interface in the middle of the column, see Figure 3.11, Cases 2 and 3. Initially, the column is fully water-saturated. At $t = 0$, the water starts to flow out of the column at $x = 10 \text{ cm}$ and its flow rate is given by the smooth flux u_{water}^* defined by (3.37) because our goal is to mimic the conditions from the laboratory experiment described in the previous section. In the numerical simulation, we use the same initial and boundary conditions as in Section 3.3.2, i.e., $S_w(0, x) = 1$ for all $x \in (0, 1)$, at the upper boundary, $u_w^N(t, 0) = 0 \text{ ms}^{-1}$ and the air pressure is assumed to be at constant atmospheric pressure $p_n(t, 0) = 10^5 \text{ Pa}$, and at the lower boundary, we set $u_n^N(t, 10 \text{ cm}) = 0 \text{ ms}^{-1}$ and prescribe $u_w^N(t, 10 \text{ cm}) = u_{water}(t)$ for Simulation 1 (Section 3.4.1) and $u_w^N(t, 10 \text{ cm}) = 10^{-4} \text{ ms}^{-1}$ for Simulation 2 (Section 3.4.2), respectively.

3.4.1. Simulation 1: Laboratory Measured Sands

There is no known laboratory measured model for the dynamic coefficient τ for the sand B or C and the air-water system. However, the Stauffer model $\tau_{S,B}$ and $\tau_{S,C}$ given by (1.30) can be computed for these sands, respectively.

In order to estimate functional models $\tau = \tau(S_w)$, we scale the three functional models obtained in the laboratory experiment by the ratio between the Stauffer models τ_S^I and τ_S^{II} such that

$$\frac{\tau_S^I}{\tau_S^{II}} = \frac{\tau^I(S_w)}{\tau^{II}(S_w)}, \quad \forall S_w. \quad (3.38)$$

Using this technique, we produced the dynamic effect coefficients $\tau = \tau(S_w)$ for the sands B and C, see Tables B.3 and B.4, respectively.

In Figure 3.19, we show the front position of the air saturation in time for different models of the dynamic coefficient $\tau = \tau(S_w)$. First, the air flows from the fine to the coarse sand (Figures 3.19a and 3.19c) and then, we consider the opposite configuration (Figures 3.19b and 3.19d), where the barrier effect is simulated. The barrier effect, modelled by the Brooks and Corey model (1.23) and the extended capillary pressure condition (1.39) for the capillary pressure p_c , implies that the non-wetting fluid (air) cannot enter the finer sand unless its capillary pressure at the interface is higher than the entry pressure p_d of the finer sand. In all cases, the use of the linear model of $\tau = \tau(S_w)$ causes faster propagation of the air front in the porous media whereas the exponential model does not influence the speed substantially with respect to the use of the static capillary pressure. The constant model of $\tau = \tau(S_w)$ exhibited a different behavior in different situations. In Figure 3.19a and 3.19b, for instance, the solution obtained with constant τ has a substantially slower front propagation than other solutions. We believe that this is because the constant model overestimates the dynamic coefficient for high wetting-phase saturation S_w (see Figure 3.10).

The delay of the non-wetting phase at the interface due to barrier effect differs when various configurations of sands are used. In the case of sand B with lower entry pressure than sand C (Figure 3.19b), the time required to penetrate the finer medium is generally smaller when using the dynamic models of capillarity than in the case of the static capillary pressure. However, in

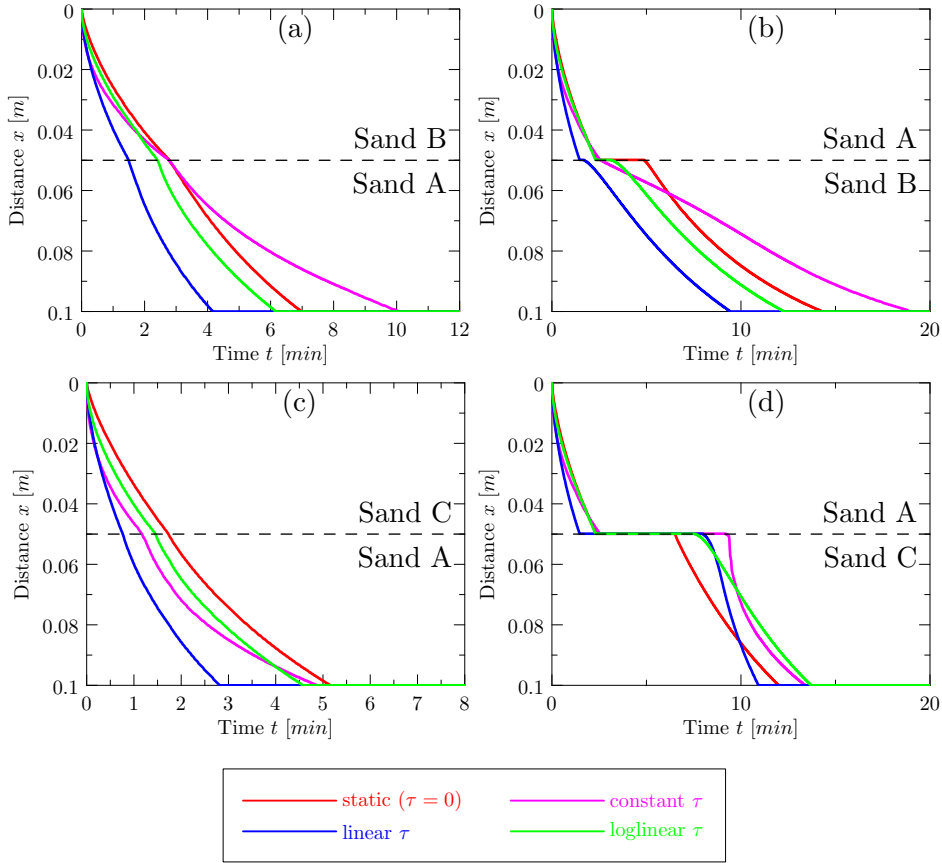


Figure 3.19.: Time evolution of the front position of the air saturation. Note that both sands B and C are finer than sand A. Therefore, figures (b) and (d) shows situations where the barrier effect is simulated: Simulation 1.

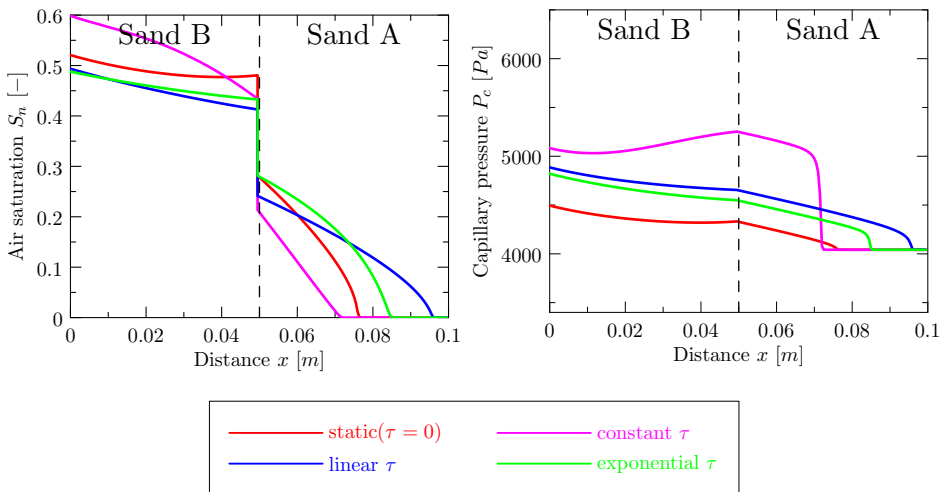


Figure 3.20.: Distribution of the air saturation S_n and capillary pressure p_c in Ω at $t = 500$ s for the sand A–sand B configuration for various models of $\tau = \tau(S_w)$. Numerical solutions are obtained with $N = 400$ nodes and adaptive time stepping strategy. Simulation 1.

case of finer sand C, these penetration times are comparable, or even larger than in the static case (Figure 3.19d).

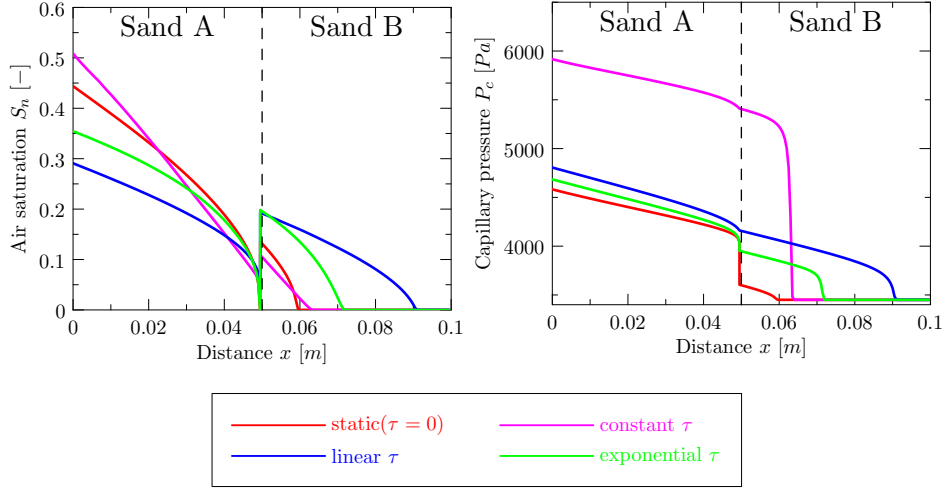


Figure 3.21.: Distribution of the air saturation S_n and capillary pressure p_c in Ω at $t = 200$ s for the sand B–sand A configuration. Numerical solutions are obtained with $N = 400$ nodes and adaptive time stepping strategy. Simulation 1.

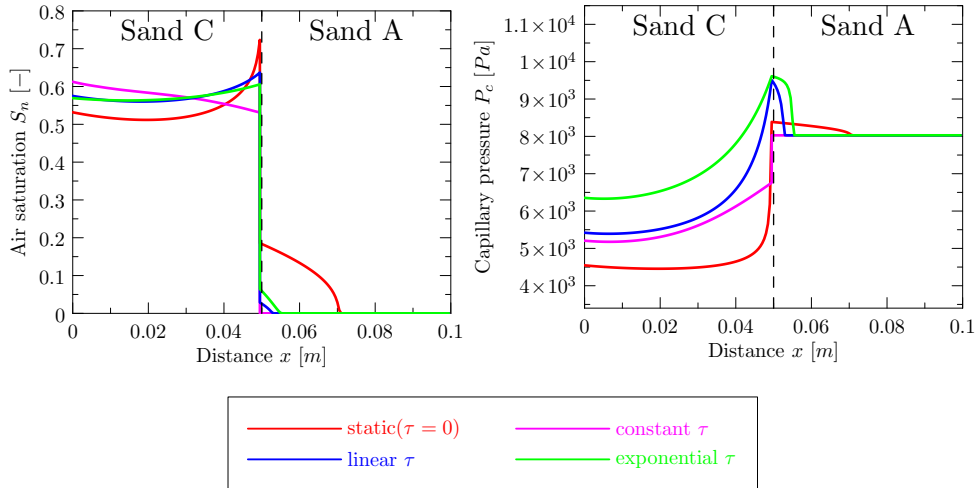


Figure 3.22.: Distribution of the air saturation S_n and capillary pressure p_c in Ω at $t = 500$ s for the sand A–sand C configuration. Numerical solutions are obtained with $N = 400$ nodes and adaptive time stepping strategy. Simulation 1.

3.4.2. Simulation 2: Entry Pressure Sensitivity Analysis

We use a layered medium configuration sketched in Figure 3.11 (Case 4) in order to investigate sensitivity of the propagation speed on the ratio between the entry pressures of layers consisting of sand A overlying sand A^κ . The value of the entry pressure in sand A^κ is defined as

$$p_{d,A^\kappa} = \kappa p_{d,A}, \quad (3.39a)$$

where $p_{d,A}$ denotes the entry pressure of the sand A and

$$K_{A^\kappa} = \frac{1}{\kappa^2} K_A, \quad (3.39b)$$

where K_A denotes the intrinsic permeability of the sand A. The intrinsic permeability K_{A^κ} in (3.39) is evaluated using the Leverett scaling $p_c \propto \sqrt{\Phi/K}$ (c.f. [75]) which is in agreement with

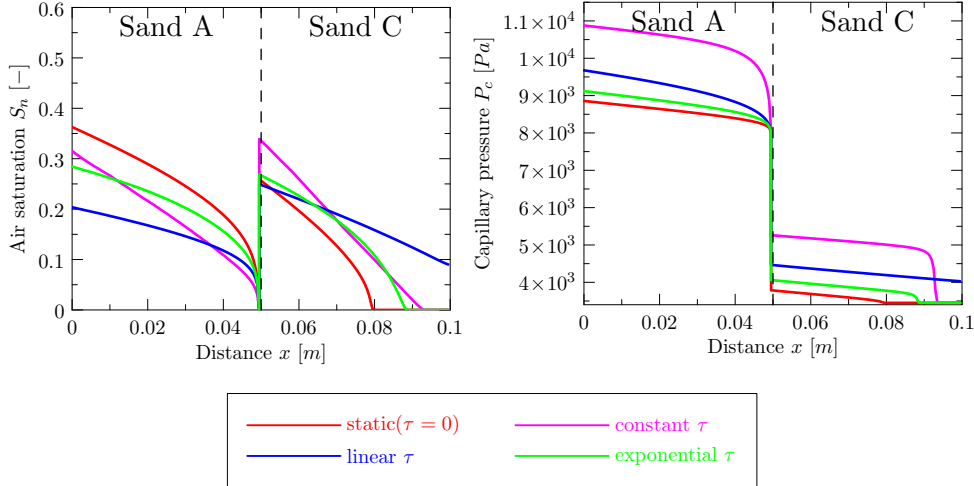


Figure 3.23.: Distribution of the air saturation S_n and capillary pressure p_c in Ω at $t = 200$ s for the sand C–sand A configuration. Numerical solutions are obtained with $N = 400$ nodes and adaptive time stepping strategy. Simulation 1.

the Hagen–Poiseuille law, see [107], [111]. We assume that porosities in both sands are the same. Unlike in the previous case, we prescribe constant flow rate $u_w(t, 10 \text{ cm}) = 10^{-4} \text{ m s}^{-1}$ at the lower boundary of the column. Figure 3.24 shows times when the air phase reaches the bottom boundary (at $x = 10 \text{ cm}$) using the dynamic or static models of capillary pressure. As shown by the long-dashed line in Figure 3.24, the propagation speed of the linear model of τ is almost two times faster than in the case of the static capillary pressure (dash-dotted line, $\tau = 0$) when the medium is homogeneous ($\kappa = 1$). Then, by increasing κ (i.e., coarse top, fine bottom), the travel time of the air-front for the linear model of $\tau = \tau(S_w)$ increases and approximately at $\kappa \approx 1.7$, it crosses the curve corresponding to the static capillary pressure. In the case of the loglinear model, the travel times are similar to the static case when κ is near 1 and they become larger for $\kappa > 1.3$. The constant model has a substantially slower propagation speed with respect to the static case for all considered values of κ . These results agree with the findings shown in Figure 3.19, where the ratio between the entry pressures is $\kappa_{A/B} = 1.17$ and $\kappa_{A/C} = 2.33$ for the sand A–sand B and sand A–sand C configurations, respectively.

In order to explain different delays at the interface observed in Figure 3.19a and 3.19b, we focus on the situations where the barrier effect is simulated, i.e., $\kappa > 1$. In Figure 3.25, we plot accumulation times as a function of κ . Here, the accumulation time is defined as the delay between the times when the non-wetting phase reaches and penetrates the material interface, respectively. In Figure 3.25, the results approximately correspond to the already observed behavior of different simulated delays due to barrier effect in Figure 3.19a and 3.19b (see the points $p_{d,B}/p_{d,A}$ and $p_{d,C}/p_{d,A}$ in Figure 3.25). In general, the accumulation times for $\kappa < 2$ are notably lower and for $\kappa > 3$ substantially higher when using the dynamic effect in capillarity compared to the reference curve with static capillary pressure (drawn as dash-dotted). Additionally, for higher differences in entry pressures, the curves tend to a steady state and when using the dynamic model of capillarity, the accumulation times are more than three times higher than in the case of the static capillary pressure. Hence, in case of a heterogeneous medium, the inclusion of the dynamic effect in the capillary pressure may substantially change the simulated evolution of the flow since the entry pressure of the finer porous media can be achieved sooner or later than in the static case (see Figures 3.19 and 3.24).

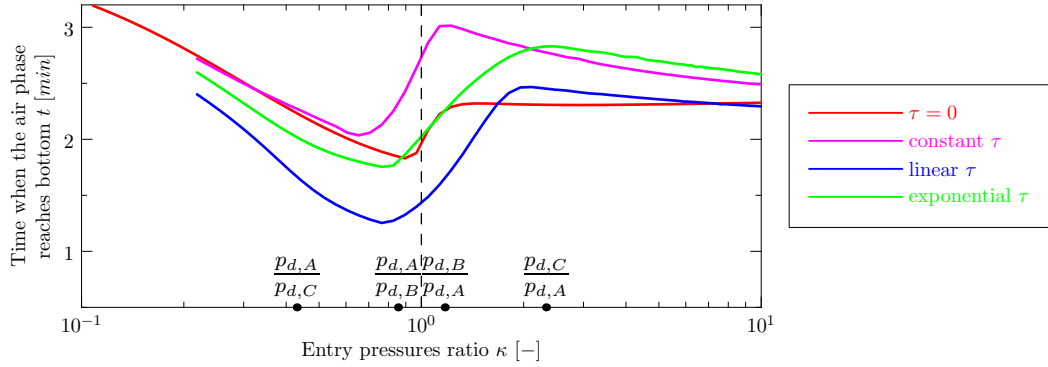


Figure 3.24.: Times when the air phase reaches the lower boundary for the case of layered configuration of porous media shown in Figure 3.11 (case 4) for multiple choices of the ratio κ between the entry pressure of sand A overlying sand A^κ , i.e., $\kappa = p_{d,A^\kappa}/p_{d,A}$: Simulation 2.

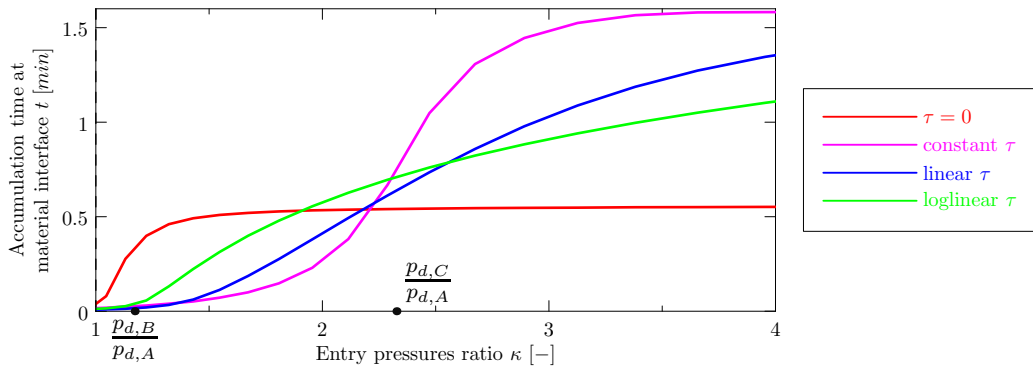


Figure 3.25.: Accumulation time of the air phase at the material interface ($x = 5 \text{ cm}$ for the case of layered configuration of porous media shown in Figure 3.11 (case 4) for multiple choices of the ratio κ between the entry pressure of sand A overlying sand A^κ , i.e., $\kappa = p_{d,A^\kappa}/p_{d,A}$: Simulation 2.

3.5. Concluding Remarks

A one-dimensional numerical scheme of two-phase incompressible and immiscible flow is presented that enables simulation of two-phase flow in both homogeneous and heterogeneous media under dynamic capillary pressure conditions, where the treatment of the conditions at the material interfaces is not numerically trivial. The numerical scheme is verified and its order of convergence is estimated using the semi-analytical solutions for homogeneous and heterogeneous porous medium, respectively.

Laboratory measured parameters were used in the numerical simulation of the dynamic capillary pressure including three models of the dynamic effect coefficient $\tau = \tau(S_w)$. The numerical solutions for the dynamic effect in the capillary pressure show that the dynamic effect has a significant impact on the magnitude of the capillary pressure while the change in the saturation profiles may be considered negligible in some cases. The constant model of τ showed rather unrealistic profile of the numerical approximation of the capillary pressure when compared to the laboratory measured data.

The results of simulations indicate that the dynamic effect may not be so important in drainage problems in a homogeneous porous medium, but, it may be important in heterogeneous media where the capillarity governs flow across material interfaces. The linear model of τ accelerates the flow of air across the interface for both configurations of the coarse and fine porous media, when the ratio between entry pressures of the media is close to 1. In all other cases, the use of the dynamic effect seems to increase the time needed for the non-wetting fluid to accumulate at a finer sand interface (delay due to barrier effect). This suggests that without dynamic effects, the travel time of the non-wetting phase can be possibly estimated to be smaller or larger than the actual time. The conclusion can be settled by a laboratory experiment only.

In this chapter, our aim is to develop a higher-order numerical scheme suitable for simulating flow of two immiscible and incompressible phases in heterogeneous porous media. Unlike in the previous chapters, we consider only static capillary pressure $p_c = p_c^{eq}$. In order to model two-phase flow in heterogeneous porous materials, a large number of numerical methods has been developed based on the finite difference (FD), finite volume (FV), or finite element (FE) methods. These methods have typically low accuracy and their experimental order of convergence usually gives values lower than 1, see [82, page 63]. The conventional FD method is strongly influenced by the mesh quality and orientation, which makes the method unsuitable for a large number of real world problems modelled using unstructured grids [101]. There have been attempts to improve the accuracy of the FD or FV approach on unstructured meshes by using multi-point flux approximation techniques [93]. However, such techniques have not been demonstrated to be of value for heterogeneous media, [65]. Another effort to develop a higher-order numerical scheme was based on the mixed-hybrid finite element (MHFE) method such as [89] or [32]. However, none of these proposed MHFE formulations were able to simulate two-phase flow in heterogeneous porous media with discontinuities in saturations at material interfaces that are caused by different capillary pressure functions (cf. Section 1.9). Recently, Hoteit and Firoozabadi [63], [64], [65] developed a higher-order numerical method that combines the MHFE approach and the discontinuous Galerkin (DG) method, together denoted as MHFE-DG. Their approach can be used to model two-phase flow in heterogeneous porous media with sharp jumps in saturation across material interfaces. However, their scheme fails in simulating the capillary barrier effect. We extend the main ideas presented in [4], [33], [63], [64], [65], and [84], in order to develop a model suitable for modelling two-phase flow of immiscible and incompressible fluids in porous medium with material inhomogeneities. The MHFE-DG approach is a modern, interesting method that allows for accurate representation of the phase velocities across sides of a finite element and approximates saturation as piecewise discontinuous per elements. This facilitates discretization of the two-phase flow problems especially in case of heterogeneous porous materials and fractured media, where the saturation is often discontinuous across sharp heterogeneity interfaces.

Our primary goal is to investigate applicability of the MHFE-DG method to problems in heterogeneous porous materials, where the flow is mostly driven by the capillarity. We focus on the behavior of the non-wetting phase at material discontinuities. Although the authors in [65] claim that their numerical scheme is capable of simulating the barrier effect, we found the opposite. In [65] they support their statement by using the van Duijn and de Neef semi-

analytical solution (see Section 2.4). However, they misinterpreted the findings of van Duijn and de Neef [28], [29] because such a solution cannot simulate the NAPL pooling. Thus, we improve the MHFE-DG approach by incorporating the extended capillary pressure condition (1.37) and we propose several modifications that enable simulating the barrier effect described in Section 1.9. Moreover, we use a more straightforward mathematical derivation when assembling the system of linear equations for the unknown variables than in [65].

This chapter is organized in the following way. In Section 4.1, we present a complete derivation of the MHFE-DG numerical scheme based on [65]. In contrast to [65], our numerical scheme is capable of simulating the barrier effect. In the final subsection of Section 4.1, we summarize the MHFE-DG method and describe the computational algorithm. In Section 4.2, we test the MHFE-DG method in 1D using the analytical and semi-analytical solutions introduced in Chapter 2. Additionally, we compare these results to the numerical results obtained using the VCFVM discussed in Chapter 3. In Section 4.3, we test the MHFE-DG approach using benchmark solutions for layered porous media in 1D and 2D. In Section 4.4, we use the MHFE-DG method to simulate problems of two-phase flow in two-dimensional heterogeneous porous materials, where the barrier effect is simulated. In the final Section 4.5, we summarize our findings and discuss benefits of the MHFE-DG method.

4.1. Mixed-Hybrid Finite Element & Discontinuous Galerkin Method

In this section, we present a detailed derivation of the MHFE-DG method. First, we present the formulation of the mathematical model and the variational formulation of the MHFE method. Then, we discuss the spatial approximation of the velocities in the lowest order Raviart-Thomas space and construct systems of linear equations. Next, we use the discontinuous Galerkin method to discretize the evolution equation for the wetting-phase saturation and obtain a system of Ordinary Differential Equations (ODE) which is solved numerically by using the forward Euler method. Finally, we summarize the computational algorithm of the MHFE-DG method.

We recall the complete set of equations (1.49, page 19) in $\Omega \subset \mathbb{R}^d$, where $d = 1$ or 2 . Summing (1.49a) and (1.49b), we obtain the following equation for the divergence of the *total velocity* (see (2.3))

$$\nabla \cdot \mathbf{u}_t = \nabla \cdot (\mathbf{u}_w + \mathbf{u}_n) = F_w + F_n, \quad \text{in } \Omega. \quad (4.1)$$

As in [65], we rewrite the definition of the total velocity \mathbf{u}_t in the following way

$$\mathbf{u}_t = \mathbf{u}_w + \mathbf{u}_n, \quad (4.2a)$$

$$= -\lambda_t \mathbf{K} \nabla \psi_w - \lambda_n \nabla \psi_c, \quad (4.2b)$$

$$= \mathbf{u}_a + f_n \mathbf{u}_c, \quad (4.2c)$$

where the velocity \mathbf{u}_a has the same driving force as the velocity \mathbf{u}_w but with a smoother mobility λ_t and the velocity \mathbf{u}_c includes the capillary driving forces,

$$\mathbf{u}_a = -\lambda_t \mathbf{K} \nabla \psi_w, \quad (4.3a)$$

$$\mathbf{u}_c = -\lambda_t \mathbf{K} \nabla \psi_c. \quad (4.3b)$$

In contrast to [65] where the capillary velocity \mathbf{u}_c is defined as

$$\mathbf{u}_c^{Hoteit} = -\lambda_n \mathbf{K} \nabla \psi_c, \quad (4.4)$$

we use the definition (4.3b). Later in Section 4.1.1, in order to obtain an explicit expression for $\nabla \psi_c$, we will need to invert $\lambda_t \mathbf{K}$ in the relationship (4.3b). This is always possible since $\lambda_t = \lambda_t(S_w)$ is strictly positive for all S_w . However, similar inversion cannot be done using the definition (4.4) since the non-wetting phase mobility λ_n vanishes as $S_w \rightarrow 1$.

The phase velocities \mathbf{u}_w and \mathbf{u}_n , can be expressed in terms of \mathbf{u}_a and \mathbf{u}_c as

$$\mathbf{u}_w = f_w \mathbf{u}_a, \quad (4.5a)$$

$$\mathbf{u}_n = f_n \mathbf{u}_a + f_n \mathbf{u}_c. \quad (4.5b)$$

In order to express the velocities \mathbf{u}_a and \mathbf{u}_c in terms of the phase velocities \mathbf{u}_w and \mathbf{u}_n , we consider the inverse relationship:

$$\mathbf{u}_a = \begin{cases} 0 & \text{if } f_w = 0, \\ f_w^{-1} \mathbf{u}_w & \text{otherwise,} \end{cases} \quad (4.6a)$$

$$\mathbf{u}_c = \begin{cases} -\mathbf{u}_w & \text{if } f_n = 0, \\ \mathbf{u}_n & \text{if } f_w = 0, \\ f_n^{-1} \mathbf{u}_n - f_w^{-1} \mathbf{u}_w & \text{otherwise,} \end{cases} \quad (4.6b)$$

where we assume that the value of the fractional flow functions are nonzero ($f_\alpha \neq 0$), if $\mathbf{u}_\alpha \neq 0$, $\alpha \in \{w, n\}$. This assumption is consistent with the definition of the phase mobility, i.e., the α -phase mobility cannot be zero if the phase velocity is nonzero. The evolution equation for the wetting phase saturation (1.49a) in terms of \mathbf{u}_a reads as

$$\phi \frac{\partial S_w}{\partial t} + \nabla \cdot (f_w \mathbf{u}_a) = F_w. \quad (4.7)$$

We consider a spatial discretization \mathcal{K}_h of the polygonal domain Ω consisting of elements K , where K are segments in \mathbb{R} or triangles in \mathbb{R}^2 and $h > 0$ is the *mesh size* defined as the maximum element diameter. We assume that the mesh is regular and conforming, i.e., the intersection of two elements is either empty, a vertex, or an edge. We denote by \mathcal{V}_h the set of all vertices V of \mathcal{K}_h , by \mathcal{E}_h the set of all sides of \mathcal{K}_h , and by \mathcal{E}_h^{int} and \mathcal{E}_h^{ext} the set of interior and exterior sides of \mathcal{K}_h , respectively. By \mathcal{E}_K , we denote the set of all sides of an element $K \in \mathcal{K}_h$.

4.1.1. Velocity Approximation

We assume, that the velocities \mathbf{u}_α , where $\alpha \in \{w, n, a, c\}$, belong to the functional space $\mathbf{H}(\text{div}, \Omega)$ which is the space of functions with square-integrable weak divergences,

$$\mathbf{H}(\text{div}, \Omega) = \{\mathbf{v} \in [L^2(\Omega)]^d; \nabla \cdot \mathbf{v} \in L^2(\Omega)\}. \quad (4.8)$$

\mathbf{RT}_0 Space

On each element $K \in \mathcal{K}_h$, we shall approximate the phase velocities \mathbf{u}_α in the lowest order Raviart–Thomas space $\mathbf{RT}_0(K)$, [16], [17]. The space $\mathbf{RT}_0(\mathcal{K}_h) \subset \mathbf{H}(\text{div}, \Omega)$ is a space of vector functions having on each element $K \in \mathcal{K}_h$ the form

$$[\mathbf{v}]_j = a_K^j + b_K^j [\mathbf{x}]_j, \quad (4.9)$$

where $[\mathbf{x}]_j$ denotes the j -th component of the vector \mathbf{x} , $j = 1, 2, \dots, d$. Note that the requirement that $\mathbf{RT}_0(\mathcal{K}_h) \subset \mathbf{H}(\text{div}, \Omega)$ imposes the continuity of the normal trace across all internal sides $E \in \mathcal{E}_h^{int}$ which is exactly what we need for local mass conservation in (1.4) and (1.35). Recall that $\mathbf{v} \cdot \mathbf{n}_{K,E}$ is constant for all $E \in \mathcal{E}_K$ and that these *side-fluxes* denoted in the latter by $u_{K,E}$ also represent the degrees of freedom of $\mathbf{RT}_0(\mathcal{K}_h)$. By $\mathbf{n}_{K,E}$, we denote the outward unit normal to side $E \in \mathcal{E}_K$ with respect to element K .

In the following, we describe the basis functions of $\mathbf{RT}_0(\mathcal{K}_h)$ that we use on each element $K \in \mathcal{K}_h$ in \mathbb{R}^d , $d = 1, 2$. For all elements $K \in \mathcal{K}_h$, we choose the basis functions $\mathbf{w}_{K,E} \in \mathbf{RT}_0(K)$

such that

$$\mathbf{w}_{K,E} \cdot \mathbf{n}_{K,F} = \delta_{EF} \frac{1}{|E|_{d-1}}, \quad \forall E, F \in \mathcal{E}_K, \quad (4.10a)$$

$$\nabla \cdot \mathbf{w}_{K,E} = \frac{1}{|K|_d}, \quad \forall E \in \mathcal{E}_K, \quad (4.10b)$$

where d denotes the dimension of \mathbb{R}^d and δ_{EF} is the Kronecker symbol. Note that for convenience, we set $|E|_0 = 1$ for all $E \in \mathcal{E}_K$.

RT₀ Basis Functions in 1D

In \mathbb{R}^1 , all elements $K \in \mathcal{K}_h$ are segments with vertices $V_A \in \mathcal{V}_K$ and $V_B \in \mathcal{V}_K$, $V_A < V_B$, and $\mathbf{RT}_0(\mathcal{K}_h)$ coincides with the space of piecewise linear polynomials that we denote by $D_1(\mathcal{K}_h)$ (see also the definition (4.61)). Since $\mathcal{E}_K = \mathcal{V}_K$, the properties of the basis functions (4.10a) in a one-dimensional element K read as

$$\mathbf{w}_{K,V_A}(V_A) = -1, \quad \mathbf{w}_{K,V_A}(V_B) = 0, \quad (4.11a)$$

$$\mathbf{w}_{K,V_B}(V_A) = 0, \quad \mathbf{w}_{K,V_B}(V_B) = 1. \quad (4.11b)$$

Altogether, the explicit expression for the basis functions in $\mathbf{RT}_0(K)$ satisfying (4.11) is

$$\mathbf{w}_{K,V_\alpha}(x) = \frac{x - V_\alpha}{V_B - V_A} = \frac{1}{|K|_1}(x - V_\alpha), \quad (4.12)$$

for all $\alpha \in \{A, B\}$ and $x \in K = [V_A, V_B]$.

RT₀ Basis Functions in 2D

In \mathbb{R}^2 , the mesh \mathcal{K}_h consists of triangles K with vertices \mathbf{V}_A , \mathbf{V}_B , and \mathbf{V}_C from \mathcal{V}_K . For each vertex $\mathbf{V}_A \in \mathcal{V}_K$, we denote by $E_A \in \mathcal{E}_K$ the side opposite to the vertex \mathbf{V}_A , see Figure 4.1. In order to satisfy (4.10), basis vector functions are constructed as

$$\mathbf{w}_{K,E_A} = \frac{1}{2|K|_2} (\mathbf{x} - \mathbf{V}_A), \quad (4.13)$$

for all $E_A \in \mathcal{E}_K$ and $\mathbf{x} \in K$.

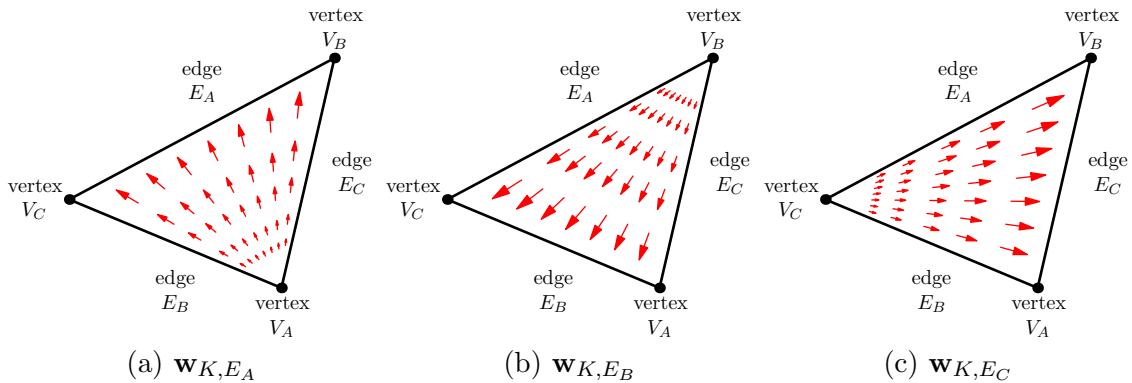


Figure 4.1.: Raviart–Thomas basis functions \mathbf{w}_{K,E_A} (a), \mathbf{w}_{K,E_B} (b), and \mathbf{w}_{K,E_C} (c) on a triangle K .

Variational Approximation of Velocity

In all dimensions, the velocity \mathbf{u}_α is approximated in the basis of $\mathbf{RT}_0(K)$, $K \in \mathcal{K}_h$, as

$$\mathbf{u}_\alpha = \sum_{E \in \mathcal{E}_K} u_{\alpha,K,E} \mathbf{w}_{K,E}, \quad \alpha \in \{a, c\}, \quad (4.14)$$

where $u_{\alpha,K,E}$ are the side–flux variables across the side $E \in \mathcal{E}_K$ in the outward direction with respect to K .

Next, we shall reveal the relationship between the potentials ψ_w and ψ_c and the side-velocities $u_{a,K,E}$ and $u_{c,K,E}$.

By inverting the permeability tensor \mathbf{K} and the total mobility λ_t in (4.3a), we obtain

$$\lambda_t^{-1} \mathbf{K}^{-1} \mathbf{u}_a = -\nabla \psi_w. \quad (4.15)$$

Recall that we assume \mathbf{K} positive definite and $\lambda_t = \lambda_t(S_w)$ strictly positive for all S_w . The variational formulation is obtained by multiplying (4.15) by the test functions from $\mathbf{H}(\text{div}, \Omega)$ that are represented on each element $K \in \mathcal{K}_h$ by the $\mathbf{RT}_0(K)$ basis functions $\mathbf{w}_{K,E}$. Then, we integrate the resulting product by parts over K and obtain

$$\int_K \lambda_t^{-1} \mathbf{w}_{K,E} \mathbf{K}^{-1} \mathbf{u}_a = - \int_K \nabla \psi_w \cdot \mathbf{w}_{K,E} \quad (4.16a)$$

$$= \int_K \psi_w \nabla \cdot \mathbf{w}_{K,E} - \int_{\partial K} \psi_w \mathbf{w}_{K,E} \cdot \mathbf{n}_{\partial K} \quad (4.16b)$$

$$= \int_K \psi_w \nabla \cdot \mathbf{w}_{K,E} - \sum_{F \in \mathcal{E}_{K,F}} \int_F \psi_w \mathbf{w}_{K,E} \cdot \mathbf{n}_{K,F} \quad (4.16c)$$

$$= \frac{1}{|K|_d} \int_K \psi_w - \frac{1}{|E|_{d-1}} \int_E \psi_w \quad (4.16d)$$

$$= \psi_{w,K} - \psi_{w,E}, \quad (4.16e)$$

where we used the properties of the Raviart–Thomas basis functions (4.10). By $\psi_{w,K}$ and $\psi_{w,E}$, we denote the average value of ψ_w over the element K and the side $E \in \mathcal{E}_K$, respectively. Since the wetting-phase potential is always continuous across the element boundary, we unified the notation $\psi_{w,E}$ for the average of the potential over the side E , where E denotes the global side $E \in \mathcal{E}_h$ independently of the parent element K .

We approximate the inversion of the total mobility term λ_t^{-1} in the left–hand–side of (4.16a) by its average value over K as

$$\int_K \lambda_t^{-1} \mathbf{w}_{K,E} \mathbf{K}^{-1} \mathbf{u}_a \approx \lambda_{t,K}^{-1} \int_K \mathbf{w}_{K,E} \mathbf{K}^{-1} \mathbf{u}_a, \quad (4.17)$$

where

$$\lambda_{t,K}^{-1} = \frac{1}{|K|_d} \int_K \lambda_t^{-1}. \quad (4.18)$$

We substitute the expression (4.14) for the velocity u_α into the integral in the right–hand–side of (4.17) and obtain

$$\int_K \mathbf{w}_{K,E} \mathbf{K}^{-1} \mathbf{u}_a = \sum_{F \in \mathcal{E}_K} u_{a,K,F} \int_K \mathbf{w}_{K,E} \mathbf{K}^{-1} \mathbf{w}_{K,F} \quad (4.19a)$$

$$= \sum_{F \in \mathcal{E}_K} u_{a,K,F} A_{K,E,F}, \quad (4.19b)$$

where the coefficients $\{A_{K,E,F}\}_{E,F \in \mathcal{E}_K}$ given by

$$A_{K,E,F} = \int_K \mathbf{w}_{K,E} \mathbf{K}^{-1} \mathbf{w}_{K,F}, \quad (4.20)$$

form a local matrix \mathbf{A}_K on K .

Putting both left and right hand side expansions (4.16) and (4.19) together, we obtain a system of $d + 1$ linear equations for $d + 1$ unknown side-fluxes $u_{a,K,E}$

$$\sum_{F \in \mathcal{E}_K} u_{a,K,F} A_{K,E,F} = \lambda_{t,K} (\psi_{w,K} - \psi_{w,E}), \quad (4.21)$$

for all $E \in \mathcal{E}_K$.

Under the assumption that \mathbf{K} is a symmetric and positive definite tensor, \mathbf{A}_K is symmetric, positive definite, and therefore invertible. By $\mathbf{a}_K = \{a_{K,E,F}\}_{E,F \in \mathcal{E}_K}$, we denote the inversion of \mathbf{A}_K , i.e., $\mathbf{a}_K = \mathbf{A}_K^{-1}$. Using this notation, we express the side fluxes $u_{a,K,E}$ in terms of the cell-average potentials $\psi_{w,K}$ and side-average potentials $\psi_{w,F}$,

$$u_{a,K,E} = \lambda_{t,K} \left(a_{K,E} \psi_{w,K} - \sum_{F \in \mathcal{E}_K} a_{K,E,F} \psi_{w,F} \right), \quad (4.22)$$

where

$$a_{K,E} = \sum_{F \in \mathcal{E}_K} a_{K,E,F}. \quad (4.23)$$

In (4.22) we assume that the side-average potentials $\psi_{w,E}$ are for all $E \in \mathcal{E}_h$ continuous across the internal sides and, therefore,

$$\psi_{w,K_1,E} = \psi_{w,K_2,E} = \psi_{w,E} \quad (4.24)$$

for all neighboring elements K_1 and K_2 of $E \in \mathcal{E}_h^{int}$. Additionally, we drop out the element index K from the side-average potential $\psi_{w,K,E} = \psi_{w,E}$ also for all external (boundary) sides $E \in \mathcal{E}_h^{ext}$.

We reproduce the steps (4.15) to (4.21) also for the expression of the capillary velocity \mathbf{u}_c in the basis of $\mathbf{RT}_0(K)$ and we obtain

$$u_{c,K,E} = \lambda_{t,K} \left(a_{K,E} \psi_{c,K} - \sum_{F \in \mathcal{E}_K} a_{K,E,F} \psi_{c,K,F} \right), \quad (4.25)$$

where $\psi_{c,K,F}$ denotes the potential ψ_c averaged over side F with respect to triangle K for all $F \in \mathcal{E}_K$.

4.1.2. System of Equations for Capillary Potentials

Internal Sides

Let us consider two neighboring elements K_1 and K_2 shown in Figure 4.2. Assuming that no mass is produced or lost on an internal side $E \in \mathcal{E}_{K_1} \cap \mathcal{E}_{K_2}$, we consider the following balance of the normal components of the phase velocities across E :

$$u_{\alpha,K_1,E} + u_{\alpha,K_2,E} = 0, \quad \alpha \in \{w, n\}. \quad (4.26)$$

It follows from the expression (4.6b) for the capillary velocity \mathbf{u}_c that a balance equation similar to (4.26) holds also for the normal components of the capillary velocity \mathbf{u}_c , [65]. Therefore, we establish the following system of equations for all $E \in \mathcal{E}_h^{int}$, $E \in \mathcal{E}_{K_1} \cap \mathcal{E}_{K_2}$:

$$u_{c,K_1,E} + u_{c,K_2,E} = 0, \quad (4.27)$$

and we use (4.25) in order to express (4.27) in terms of the side-average potentials $\psi_{c,K,E}$:

$$\begin{aligned} & \lambda_{t,K_1} a_{K_1,E} \psi_{c,K_1} - \lambda_{t,K_1} \sum_{F \in \mathcal{E}_{K_1}} a_{K_1,E,F} \psi_{c,K_1,F} + \\ & + \lambda_{t,K_2} a_{K_2,E} \psi_{c,K_2} - \lambda_{t,K_2} \sum_{F \in \mathcal{E}_{K_2}} a_{K_2,E,F} \psi_{c,K_2,F} = 0. \end{aligned} \quad (4.28)$$

When the capillary potential is continuous across side $F \in \mathcal{E}_{K_1} \cap \mathcal{E}_{K_2}$, the side-average potentials $\psi_{c,K_1,F}$ and $\psi_{c,K_2,F}$ coincide and thus we denote their common value as

$$\psi_{c,F} := \psi_{c,K_1,F} = \psi_{c,K_2,F}. \quad (4.29)$$

On the other hand in case of the barrier effect at side F , the capillary potential is discontinuous across F and by $\psi_{c,F}$, we denote the side-average capillary pressure that corresponds to the triangle with lower entry pressure. Altogether, the following side-average potentials $\psi_{c,K_1,E}$ and $\psi_{c,K_2,E}$ are used in the expression for the side-velocities in (4.28):

$$\psi_{c,K_1,E} = \begin{cases} p_{d,K_1} - (\rho_n - \rho_w) \int_E \mathbf{g} \cdot \mathbf{x} \, d\mathbf{x}, & \text{if } p_{c,K_2,E} < p_{d,K_1}, \\ \psi_{c,E}, & \text{otherwise,} \end{cases} \quad (4.30a)$$

$$\psi_{c,K_2,E} = \begin{cases} p_{d,K_2} - (\rho_n - \rho_w) \int_E \mathbf{g} \cdot \mathbf{x} \, d\mathbf{x}, & \text{if } p_{c,K_1,E} < p_{d,K_2}, \\ \psi_{c,E}, & \text{otherwise.} \end{cases} \quad (4.30b)$$

We approximate the cell-average capillary potential $\psi_{c,K}$ using its definition (1.47) as

$$\psi_{c,K} = \frac{1}{|K|_d} \int_K \psi_c \quad (4.31a)$$

$$= \frac{1}{|K|_d} \int_K [p_c - (\rho_n - \rho_w) \mathbf{g} \cdot \mathbf{x}] \quad (4.31b)$$

$$\approx p_c(S_{w,K}) - (\rho_n - \rho_w) \int_K \mathbf{g} \cdot \mathbf{x}, \quad (4.31c)$$

where $S_{w,K}$ is the cell-average of the wetting-phase saturation S_w . Therefore, the cell-average capillary potential $\psi_{c,K}$ can be directly computed for a given $S_{w,K}$ using (4.31c).

External Sides

In case of the exterior (boundary) sides $E \in \mathcal{E}_h^{ext}$, we prescribe either the Neumann boundary condition (if $E \subseteq \Gamma_{u_n} \cap \Gamma_{u_w}$) as

$$u_{c,K,E} =: u_{c,K,E}^{\mathcal{N}} = \begin{cases} 0 & \text{if } u_{w,E}^{\mathcal{N}} = u_{n,E}^{\mathcal{N}} = 0, \\ -u_{w,E}^{\mathcal{N}} & \text{if } u_{n,E}^{\mathcal{N}} = 0, \\ u_{n,E}^{\mathcal{N}} & \text{if } u_{w,E}^{\mathcal{N}} = 0, \\ f_n^{-1}(S_{w,E}^{\mathcal{D}}) u_{n,E}^{\mathcal{N}} - f_w^{-1}(S_{w,E}^{\mathcal{D}}) u_{w,E}^{\mathcal{N}} & \text{otherwise,} \end{cases} \quad (4.32)$$

or the Dirichlet boundary condition for the side-average of the capillary potential $\psi_{c,E}$ as

$$\psi_{c,E} = \psi_c(S_w^{\mathcal{D}}), \quad \text{if } E \subseteq \Gamma_{S_w} \text{ or } E \subseteq \Gamma_{S_n}. \quad (4.33)$$

In (4.33), the element index K in $\psi_{c,K,E}$ is dropped out for all $E \in \mathcal{E}_K \cap \mathcal{E}_h^{ext}$. By Γ_{ψ_c} , we shall denote segments of the domain boundary such that the boundary condition (4.33) is prescribed.

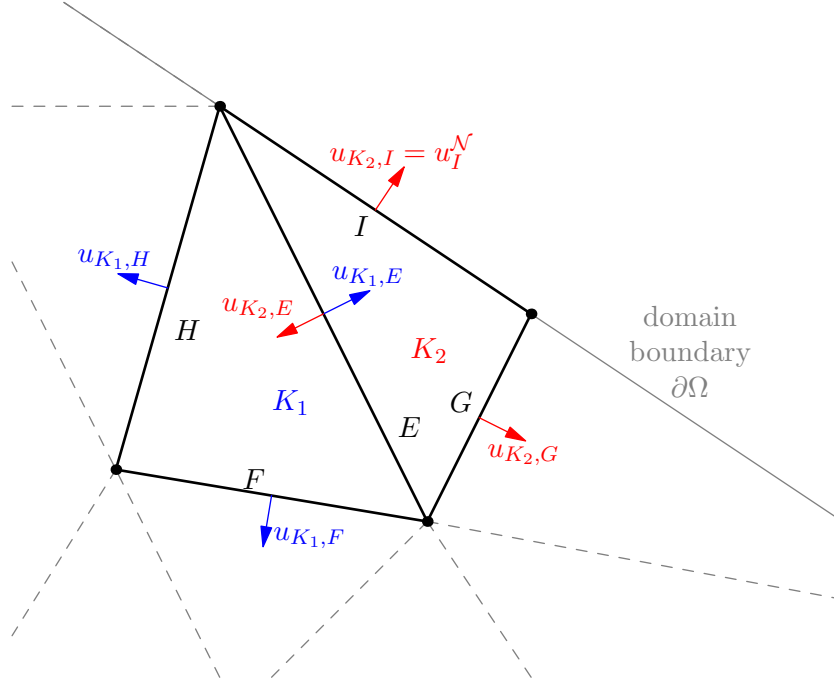


Figure 4.2.: Continuity of normal components of a velocity u expressed in $RT_0(K_1)$ and $RT_0(K_2)$ spaces, respectively, between two neighboring triangles K_1 and K_2 . Additionally, the Neumann boundary condition is illustrated at side $I \in \mathcal{E}_h^{ext} \cap \mathcal{E}_{K_2}$.

System of Linear Equations

Combining equations (4.28) and the boundary conditions (4.32) and (4.33), we obtain a sparse system of linear equations that can be written in a matrix form as

$$\mathbf{M}_c \Psi_c = \mathbf{b}_c, \quad (4.34)$$

where the square, symmetric, and positive definite matrix \mathbf{M}_c and the vectors Ψ_c and \mathbf{b}_c have dimensions $\#\mathcal{E}_h$, where $\#\mathcal{E}_h$ denotes the total number of sides in \mathcal{E}_h . The components of the vector Ψ_c are the side average potentials defined in the previous section, i.e., $[\Psi_c]_E = \psi_{c,E}$ for all $E \in \mathcal{E}_h$.

For all interior sides $E \in \mathcal{E}_h^{int} \cap \mathcal{E}_{K_1} \cap \mathcal{E}_{K_2}$, the entries of \mathbf{M}_c are given by

$$[\mathbf{M}_c]_{E,F} = \lambda_{t,K_1} a_{K_1,E,F} + \lambda_{t,K_2} a_{K_2,E,F}, \quad (4.35a)$$

if $F = E$ and the barrier effect is not simulated at side E , i.e., the capillary potential ψ_c is continuous across side E ,

$$[\mathbf{M}_c]_{E,F} = \lambda_{t,K_1} a_{K_1,E,F}, \quad (4.35b)$$

if $F \in \mathcal{E}_{K_1}$, $F \notin \mathcal{E}_{K_2}$, and $F \not\subseteq \Gamma_{\psi_c}$, or if the barrier effect is simulated at side E and $p_{c,K_1,E} < p_{d,K_2,E}$,

$$[\mathbf{M}_c]_{E,F} = \lambda_{t,K_2} a_{K_2,E,F}, \quad (4.35c)$$

if $F \in \mathcal{E}_{K_2}$, $F \notin \mathcal{E}_{K_1}$, and $F \not\subseteq \Gamma_{\psi_c}$, or if the barrier effect is simulated at side E and $p_{c,K_2,E} < p_{d,K_1,E}$. Otherwise,

$$[\mathbf{M}_c]_{E,F} = 0. \quad (4.35d)$$

For all exterior (boundary) sides $E \in \mathcal{E}_h^{ext} \cap \mathcal{E}_{K_1}$, the entries of \mathbf{M}_c are given by

$$[\mathbf{M}_c]_{E,F} = \begin{cases} \lambda_{t,K_1} a_{K_1,E,F}, & \text{if } F \in \mathcal{E}_{K_1}, F \not\subseteq \Gamma_{\psi_c}, \text{ and } E \subseteq \Gamma_{\mathbf{u}_w} \cap \Gamma_{\mathbf{u}_n}, \\ 1, & \text{if } F = E \text{ and } E \subseteq \Gamma_{\psi_c}, \\ 0, & \text{otherwise.} \end{cases} \quad (4.36)$$

To simplify the notation, we split the right–hand–side vector \mathbf{b}_c in (4.34) into three parts

$$\mathbf{b}_c = \mathbf{b}_c^\star + \mathbf{b}_c^\spadesuit + \mathbf{b}_c^\clubsuit. \quad (4.37)$$

The components of the vector \mathbf{b}_c^\star read as

$$\left[\mathbf{b}_c^\star \right]_E = \begin{cases} \lambda_{t,K_1} a_{K_1,E} + \lambda_{t,K_2} a_{K_2,E}, & \text{if } E \in \mathcal{E}_h^{int} \cap \mathcal{E}_{K_1} \cap \mathcal{E}_{K_2} \text{ and} \\ & p_{c,K_1,E}, p_{c,K_2,E} \geq \max\{p_{d,K_1,E}, p_{d,K_2,E}\}, \\ \lambda_{t,K} a_{K,E} - u_{c,K,E}^{\mathcal{N}}, & \text{if } E \in \mathcal{E}_h^{ext} \cap \mathcal{E}_K \text{ and } E \subseteq \Gamma_{\mathbf{u}_w} \cap \Gamma_{\mathbf{u}_n} \\ \psi_{c,E}^{\mathcal{D}}, & \text{if } E \in \mathcal{E}_h^{ext} \text{ and } E \subseteq \Gamma_{\psi_c}. \end{cases} \quad (4.38)$$

The vector \mathbf{b}_c^\spadesuit contains the terms with the Dirichlet boundary condition for ψ_c ,

$$\left[\mathbf{b}_c^\spadesuit \right]_E = \begin{cases} - \sum_{K=K_1, K_2} \sum_{F \in \mathcal{E}_K \cap \Gamma_{\psi_c}} \lambda_{t,K} a_{K,E,F} \psi_{c,F}^{\mathcal{D}}, & \text{if } E \in \mathcal{E}_h^{int} \cap \mathcal{E}_{K_1} \cap \mathcal{E}_{K_2} \text{ and} \\ & p_{c,K_1,E}, p_{c,K_2,E} \geq \max\{p_{d,K_1,E}, p_{d,K_2,E}\}, \\ - \sum_{F \in \mathcal{E}_K \cap \Gamma_{\psi_c}} \lambda_{t,K} a_{K,E,F} \psi_{c,F}^{\mathcal{D}}, & \text{if } E \in \mathcal{E}_h^{ext} \cap \mathcal{E}_K \text{ and } E \not\subseteq \Gamma_{\psi_c}, \\ 0, & \text{otherwise.} \end{cases} \quad (4.39)$$

The value of the vector \mathbf{b}_c^\clubsuit is zero except for the case when the expression of the continuity of $u_{c,K_1,E}$ and $u_{c,K_2,E}$ across the side E in (4.28) requires $\psi_{c,F}$ at a side $F \neq E$, where the barrier is simulated. Let K_1 and K_2 be the neighboring elements of E , i.e., $E \in \mathcal{E}_{K_1} \cap \mathcal{E}_{K_2}$. Let us assume without loss of generality that $F \in \mathcal{E}_{K_1} \cap \mathcal{E}_{K_3}$ and $F \notin \mathcal{E}_{K_2}$, where K_3 denotes the other neighboring element of F (see Figure 4.3). If K_1 contains finer material than K_3 and the barrier effect is simulated, i.e., if $p_{c,K_3} < p_{d,K_1}$, we set

$$\left[\mathbf{b}_c^\clubsuit \right]_E = -\lambda_{t,K_1} a_{K_1,E,F} \left(p_{d,K_1} - (\rho_n - \rho_w) \int_E \mathbf{g} \cdot \mathbf{x} \, dx \right). \quad (4.40)$$

Otherwise, $\left[\mathbf{b}_c^\clubsuit \right]_E = 0$.

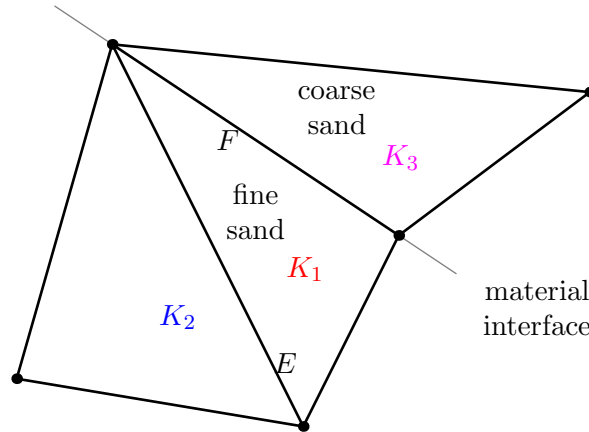


Figure 4.3.: Illustration of a situation with barrier effect at side $F \in \mathcal{E}_{K_1} \cap \mathcal{E}_{K_3}$ when treating continuity of normal fluxes across side $E \in \mathcal{E}_{K_1} \cap \mathcal{E}_{K_2}$.

4.1.3. Discretization of Volumetric Balance Equation

In order to express $u_{a,K,E}$ given by (4.22) in terms of the side–average variables $\psi_{w,E}$ and $\psi_{c,E}$, we derive an explicit formula for the cell–average of the wetting phase potential $\psi_{w,K}$. We

integrate the volumetric balance equation (4.1) for the total velocity \mathbf{u}_t over $K \in \mathcal{K}_h$,

$$\int_K \nabla \cdot (\mathbf{u}_a + f_n \mathbf{u}_c) = \int_K F_w + F_n, \quad (4.41)$$

and by using the divergence theorem, we get

$$\sum_{F \in \partial K} \int_F (\mathbf{u}_a + f_n \mathbf{u}_c) \cdot \mathbf{n}_{K,F} = F_K, \quad (4.42)$$

where F_K is the right-hand-side of (4.41). Since we approximate the fluxes \mathbf{u}_a and \mathbf{u}_c in $\mathbf{RT}_0(K)$, the properties of the basis functions (4.10) allow to rewrite (4.42) as

$$\sum_{E \in \mathcal{E}_K} u_{a,K,E} + \sum_{E \in \mathcal{E}_K} f_{n,E} u_{c,K,E} = F_K, \quad (4.43)$$

where $f_{n,E}$ is the side-average value of the non-wetting phase fractional flow function. Generally, we use either the *centered* approximation denoted by $f_{n,E}^{avg}$, or the *upwinded* approximation $f_{n,E}^{upw}$.

The centered fractional flow function $f_{n,E}^{avg}$ is always obtained by an arithmetic average as

$$f_{n,E}^{avg} = \begin{cases} \frac{1}{2} [f_n(S_{w,K_1,E}) + f_n(S_{w,K_2,E})] & \text{if } E \in \mathcal{E}_h^{int} \cap \mathcal{E}_{K_1} \cap \mathcal{E}_{K_2}, \\ f_n(S_{w,E}^D) & \text{if } E \in \mathcal{E}_h^{ext} \cap \mathcal{E}_K \text{ and } E \subseteq \Gamma_{S_w}, \\ f_n(S_{w,K,E}) & \text{if } E \in \mathcal{E}_h^{ext} \cap \mathcal{E}_K \text{ and } E \not\subseteq \Gamma_{S_w}. \end{cases} \quad (4.44)$$

The upwinded fractional flow function $f_{n,E}^{upw}$ depends on the direction of the side-flux \mathbf{u}_c across $E \in \mathcal{E}_h^{int} \cap \mathcal{E}_{K_1} \cap \mathcal{E}_{K_2}$ and is determined as follows:

$$f_{n,E}^{upw} = \begin{cases} f_n(S_{w,K_1,E}), & \text{if } u_{c,K_1,E} \geq 0, \\ f_n(S_{w,K_2,E}), & \text{otherwise.} \end{cases} \quad (4.45)$$

In case of the exterior side $E \in \mathcal{E}_h^{ext} \cap \mathcal{E}_K$, the upwinded fractional flow function is given by

$$f_{n,E}^{upw} = \begin{cases} f_n(S_{w,E}^D), & \text{if } u_{c,K,E} \leq 0 \text{ and } E \subseteq \Gamma_{S_w}, \\ f_n(S_{w,K,E}), & \text{otherwise.} \end{cases} \quad (4.46)$$

Replacing the side fluxes $u_{a,K,E}$ in (4.43) by (4.22), we obtain

$$\lambda_{t,K} a_K \psi_{w,K} - \lambda_{t,K} \sum_{E \in \mathcal{E}_K} a_{K,E} \psi_{w,E} = F_K - \sum_{E \in \mathcal{E}_K} f_{n,E} u_{c,K,E}, \quad (4.47)$$

where

$$a_K = \sum_{E \in \mathcal{E}_K} a_{K,E}. \quad (4.48)$$

Finally, we write $\psi_{w,K}$ as

$$\psi_{w,K} = \frac{F_K}{\lambda_{t,K} a_K} + \sum_{E \in \mathcal{E}_K} \frac{a_{K,E}}{a_K} \psi_{w,E} - \sum_{E \in \mathcal{E}_K} \frac{f_{n,E}}{\lambda_{t,K} a_K} u_{c,K,E}, \quad (4.49)$$

which allows to express the side fluxes $u_{a,K,E}$ given by (4.22) in terms of the unknowns $\psi_{w,E}$ only

$$u_{a,K,E} = \frac{a_{K,E}}{a_K} \left(F_K - \sum_{F \in \mathcal{E}_K} f_{n,F} u_{c,K,F} \right) + \lambda_{t,K} \sum_{F \in \mathcal{E}_K} \left(\frac{a_{K,E} a_{K,F}}{a_K} - a_{K,E,F} \right) \psi_{w,F}, \quad (4.50)$$

4.1.4. System of Equations for Wetting-Phase Potentials

Internal Sides

Similarly to the derivation presented in Section 4.1.2, we consider two neighboring elements K_1 and K_2 shown in Figure 4.2. The continuity of the normal components of the phase velocities across internal sides allows us to establish equation

$$u_{a,K_1,E} + u_{a,K_2,E} = 0, \quad (4.51)$$

for all $E \in \mathcal{E}_h^{int}$, $E \in \mathcal{E}_{K_1} \cap \mathcal{E}_{K_2}$. We use (4.50) in order to express (4.51) in terms of the side-average potentials $\psi_{w,F}$:

$$\begin{aligned} & \frac{a_{K_1,E}}{a_{K_1}} \left(F_{K_1} - \sum_{F \in \mathcal{E}_{K_1}} f_{n,F} u_{c,K_1,F} \right) + \lambda_{t,K_1} \sum_{F \in \mathcal{E}_{K_1}} \left(\frac{a_{K_1,E} a_{K_1,F}}{a_{K_1}} - a_{K_1,E,F} \right) \psi_{w,F} + \\ & + \frac{a_{K_2,E}}{a_{K_2}} \left(F_{K_2} - \sum_{F \in \mathcal{E}_{K_2}} f_{n,F} u_{c,K_2,F} \right) + \lambda_{t,K_2} \sum_{F \in \mathcal{E}_{K_2}} \left(\frac{a_{K_2,E} a_{K_2,F}}{a_{K_2}} - a_{K_2,E,F} \right) \psi_{w,F} = 0. \end{aligned} \quad (4.52)$$

In (4.52) we assume that the capillary velocities $u_{c,K,F}$ have been already computed using the procedure described in Section 4.1.2.

External Sides

In case of the exterior (boundary) sides $E \in \mathcal{E}_h^{ext}$, we prescribe either the Neumann boundary condition (if $E \subseteq \Gamma_{u_n} \cap \Gamma_{u_w}$) as

$$u_{a,K,E} =: u_{a,K,E}^N = \begin{cases} 0 & \text{if } u_{w,E}^N = 0, \\ f_w^{-1}(S_{w,E}^D) u_{w,E}^N & \text{otherwise,} \end{cases} \quad (4.53)$$

or the Dirichlet boundary condition for the side-average of the wetting-phase potential $\psi_{w,E}$ as

$$\psi_{w,E} = \psi_w^D, \quad \text{if } E \subseteq \Gamma_{\psi_w}. \quad (4.54)$$

System of Linear Equations

Combining equations (4.52) and the boundary conditions (4.53) and (4.54), we obtain a sparse system of linear equations that can be written in the matrix form as

$$\mathbf{M}_a \Psi_w = \mathbf{b}_a, \quad (4.55)$$

where the square matrix \mathbf{M}_a and the vectors Ψ_w and \mathbf{b}_a have dimensions $\#\mathcal{E}_h$. Similar to the matrix \mathbf{M}_c , the matrix \mathbf{M}_a is symmetric, positive definite, and for all interior sides $E \in \mathcal{E}_h^{int} \cap \mathcal{E}_{K_1} \cap \mathcal{E}_{K_2}$, its entries are given by

$$[\mathbf{M}_a]_{E,F} = \begin{cases} \sum_{K=K_1, K_2} \lambda_{t,K} \left(\frac{a_{K,E}^2}{a_K} - a_{K,E,E} \right), & \text{if } F = E, \\ \lambda_{t,K_1} \left(\frac{a_{K_1,E} a_{K_1,F}}{a_{K_1}} - a_{K_1,E,F} \right), & \text{if } F \in \mathcal{E}_{K_1}, F \notin \mathcal{E}_{K_2}, \text{ and } F \not\subseteq \Gamma_{\psi_w}, \\ \lambda_{t,K_2} \left(\frac{a_{K_2,E} a_{K_2,F}}{a_{K_2}} - a_{K_2,E,F} \right), & \text{if } F \in \mathcal{E}_{K_2}, F \notin \mathcal{E}_{K_1}, \text{ and } F \not\subseteq \Gamma_{\psi_w}, \\ 0, & \text{otherwise} \end{cases} \quad (4.56)$$

and for all exterior (boundary) sides $E \in \mathcal{E}_h^{ext} \cap \mathcal{E}_K$ by

$$[\mathbf{M}_a]_{E,F} = \begin{cases} \lambda_{t,K} \left(\frac{a_{K,E} a_{K,F}}{a_K} - a_{K,E,F} \right), & \text{if } F \in \mathcal{E}_{K_1} \text{ and } E \subseteq \Gamma_{\mathbf{u}_w} \cap \Gamma_{\mathbf{u}_n}, \\ 1, & \text{if } F = E \text{ and } E \subseteq \Gamma_{\psi_w}. \end{cases} \quad (4.57)$$

To simplify the notation, we split the right-hand-side vector \mathbf{b}_a in (4.55) into two parts

$$\mathbf{b}_a = \mathbf{b}_a^\star + \mathbf{b}_a^\spadesuit. \quad (4.58)$$

The components of the vector \mathbf{b}_a^\star read as

$$[\mathbf{b}_a^\star]_E = \begin{cases} - \sum_{K=K_1, K_2} \frac{a_{K,E}}{a_K} \left(F_K - \sum_{F \in \mathcal{E}_K} f_{n,F} u_{c,K,F} \right), & \text{if } E \in \mathcal{E}_h^{int} \cap \mathcal{E}_{K_1} \cap \mathcal{E}_{K_2}, \\ u_{a,K,E}^{\mathcal{N}} - \frac{a_{K,E}}{a_K} \left(F_K - \sum_{F \in \mathcal{E}_K} f_{n,F} u_{c,K,F} \right), & \text{if } E \in \mathcal{E}_h^{ext} \cap \mathcal{E}_K \text{ and } E \subseteq \Gamma_{\mathbf{u}_w} \cap \Gamma_{\mathbf{u}_n}, \\ \psi_{w,E}^{\mathcal{D}}, & \text{if } E \in \mathcal{E}_h^{ext} \text{ and } E \subseteq \Gamma_{\psi_w}. \end{cases} \quad (4.59)$$

The vector \mathbf{b}_a^\spadesuit contains the terms with the Dirichlet boundary condition for ψ_w ,

$$[\mathbf{b}_a^\spadesuit]_E = \begin{cases} - \sum_{K=K_1, K_2} \sum_{F \in \mathcal{E}_K \cap \Gamma_{\psi_w}} \lambda_{t,K} \left(\frac{a_{K,E} a_{K,F}}{a_K} - a_{K,E,F} \right) \psi_{w,F}^{\mathcal{D}}, & \text{if } E \in \mathcal{E}_h^{int} \cap \mathcal{E}_{K_1} \cap \mathcal{E}_{K_2}, \\ - \sum_{F \in \mathcal{E}_K \cap \Gamma_{\psi_w}} \lambda_{t,K} \left(\frac{a_{K,E} a_{K,F}}{a_K} - a_{K,E,F} \right) \psi_{w,F}^{\mathcal{D}}, & \text{if } E \in \mathcal{E}_h^{ext} \cap \mathcal{E}_K \text{ and } E \not\subseteq \Gamma_{\psi_w}, \\ 0, & \text{otherwise.} \end{cases} \quad (4.60)$$

4.1.5. Saturation Approximation

We discretize the saturation equation (4.7) using the discontinuous Galerkin (DG) method which is locally conservative and flexible for complex unstructured geometries. The DG method approximates the weak solution $S_w = S_w(t, \mathbf{x})$ of (4.7) by an approximation that belongs to a functional space $D_r(\mathcal{K}_h)$ of discontinuous functions containing functions that are piecewise polynomial of degree $r \geq 0$ on $K \in \mathcal{K}_h$,

$$D_r(\mathcal{K}_h) = \{p \in L^2(\Omega); p|_K \in P_r(K), \forall K \in \mathcal{K}_h\}, \quad (4.61)$$

[103], [4]. Note that there is no continuity requirements across the internal sides of \mathcal{K}_h .

We shall work with piecewise constant or piecewise linear functions per element $K \in \mathcal{K}_h$ such that the approximated weak solution is in $D_0(\mathcal{K}_h)$ or $D_1(\mathcal{K}_h)$, respectively. Recall that we assume that \mathcal{K}_h consists of segments (in 1D) or triangles (in 2D) only.

Variational Approximation of Saturation

In order to obtain the variational formulation of the continuity equation, we multiply (4.7) by a test function $\varphi \in D_r(\mathcal{K}_h)$ and integrate over Ω :

$$\int_{\Omega} \phi \frac{\partial S_w}{\partial t} \varphi + \int_{\Omega} \nabla \cdot (f_w \mathbf{u}_a) \varphi = \int_{\Omega} F_w \varphi. \quad (4.62)$$

In (4.62) we assume that the porosity Φ is constant on each $K \in \mathcal{K}_h$ and we denote its value by ϕ_K .

The approximation $S_w \in D_r(\mathcal{K}_h)$ of (4.7) satisfies (4.62) for all test functions $\varphi \in D_r(\mathcal{K}_h)$. In the following subsections, we describe basis functions of $D_0(\mathcal{K}_h)$ and $D_1(\mathcal{K}_h)$ and we express the weak solution S_w in these bases, respectively.

Piecewise Constant Approximation (FVM)

Using a piecewise constant approximation of the wetting-phase saturation $S_w \in D_0(\mathcal{K}_h)$, the discontinuous Galerkin method coincides with the cell-centered finite volume method (FVM). Thus, the basis functions φ_K of $D_0(\mathcal{K}_h)$ read as

$$\varphi_K(\mathbf{x}) = \begin{cases} 1 & \text{if } \mathbf{x} \in K, \\ 0 & \text{otherwise.} \end{cases} \quad (4.63)$$

The approximation of the wetting-phase saturation reads as

$$S_w(t, \mathbf{x}) \approx \sum_{K \in \mathcal{K}_h} S_{w,K}(t) \varphi_K(\mathbf{x}), \quad (4.64)$$

for all $\mathbf{x} \in \Omega$ and $t \in (0, T)$. In (4.64) the basis coefficients $S_{w,K}$ are time-dependent and represents the mean value of S_w over K (FVM). Using φ_K as test functions in (4.62) together with the expression of S_w in $D_0(\mathcal{K}_h)$ (4.64), we obtain

$$\phi_K \frac{dS_{w,K}}{dt} |K|_d + \int_K \nabla \cdot (f_w \mathbf{u}_a) = \int_K F_w, \quad (4.65)$$

for all elements $K \in \mathcal{K}_h$. Furthermore, we denote the average of the sink/source term as follows

$$F_{w,K} = \frac{1}{|K|_d} \int_K F_w. \quad (4.66)$$

We use the divergence theorem in (4.65) and the properties of the approximation $\mathbf{u}_a \in \mathbf{RT}_0(K)$ to obtain

$$\phi_K \frac{dS_{w,K}}{dt} = F_{w,K} - \frac{1}{|K|_d} \sum_{E \in \mathcal{E}_K} u_{a,K,E} \sum_{G \in \mathcal{E}_K} \int_G f_w \mathbf{w}_{K,E} \cdot \mathbf{n}_{K,G}, \quad (4.67a)$$

$$= F_{w,K} - \frac{1}{|K|_d} \sum_{E \in \mathcal{E}_K} u_{a,K,E} \frac{1}{|E|_{d-1}} \int_E f_w, \quad (4.67b)$$

$$= F_{w,K} - \frac{1}{|K|_d} \sum_{E \in \mathcal{E}_K} f_{w,E} u_{a,K,E}, \quad (4.67c)$$

where $f_{w,E}$ denotes the average of the fractional flow function f_w over the side E .

Piecewise Linear Approximation

By $\varphi_{K,E}$, we denote the piecewise linear basis functions of $D_1(\mathcal{K}_h)$ associated with the edges for all $K \in \mathcal{K}_h$ and $E \in \mathcal{E}_K$. In Appendix A, we describe explicit formulae for $\varphi_{K,E}$ in \mathbb{R}^1 and \mathbb{R}^2 . The approximated solution reads as

$$S_w(t, \mathbf{x}) \approx \sum_{K \in \mathcal{K}_h} \sum_{E \in \mathcal{E}_K} S_{w,K,E}(t) \varphi_{K,E}(\mathbf{x}), \quad (4.68)$$

for all $\mathbf{x} \in \Omega$ and $t \in (0, T)$, where the basis coefficients $S_{w,K,E}$ are time-dependent.

The basis functions $\varphi_{K,E} \in D_1(\mathcal{K}_h)$ fulfill

$$\text{supp } \varphi_{K,E} \subseteq K, \quad (4.69a)$$

$$\frac{1}{|F|_{d-1}} \int_F \varphi_{K,E} = \delta_{E,F}, \quad (4.69b)$$

$$\frac{1}{|K|_d} \int_K \varphi_{K,E} = \frac{1}{d+1}, \quad (4.69c)$$

for all $K \in \mathcal{K}_h$ and all $E, F \in \mathcal{E}_K$.

Using $\varphi_{K,E}$ as test functions in (4.62) together with the expression (4.68), we obtain

$$\phi_K \sum_{F \in \mathcal{E}_K} \frac{dS_{w,K,F}}{dt} \int_K \varphi_{K,E} \varphi_{K,F} + \int_K \nabla \cdot (f_w \mathbf{u}_a) \varphi_{K,E} = \int_K F_w \varphi_{K,E}, \quad (4.70)$$

for all elements $K \in \mathcal{K}_h$. In order to simplify the notation of (4.70), we introduce

$$B_{K,E,F} = \int_K \varphi_{K,E} \varphi_{K,F}, \quad (4.71a)$$

$$F_{w,K,E} = \int_K F_w \varphi_{K,E}. \quad (4.71b)$$

As a result of the properties of the basis functions $\varphi_{K,E}$ in (4.69), coefficients

$$\mathbf{B}_K = \{B_{K,E,F}\}_{E,F \in \mathcal{E}_K} \quad (4.72)$$

form a symmetric and positive definite matrix \mathbf{B}_K and by

$$\mathbf{b}_K = \{b_{K,E,F}\}_{E,F \in \mathcal{E}_K}, \quad (4.73)$$

we denote its inversion, i.e., $\mathbf{b}_K = \mathbf{B}_K^{-1}$. We apply the Green theorem to the second integral in the right-hand-side of (4.70) and obtain

$$\int_K \nabla \cdot (f_w \mathbf{u}_a) \varphi_{K,E} = \sum_{H \in \mathcal{E}_K} \int_H f_w \varphi_{K,E} \mathbf{u}_a \cdot \mathbf{n}_{K,H} - \int_K f_w \mathbf{u}_a \cdot \nabla \varphi_{K,E}. \quad (4.74)$$

In the first integral on the right-hand-side of (4.74), we approximate the fractional flow function f_w in $D_1(K)$ as

$$f_w \approx \sum_{E \in \mathcal{E}_K} f_{w,E} \varphi_{K,E}, \quad \text{in } K, \quad (4.75)$$

where $f_{w,E}$ denotes the side-average of f_w over $E \in \mathcal{E}_h$. In the other integral on the right-hand-side of (4.74), we approximate f_w by its element-average value $f_{w,K}$. Additionally, we use the expression for the velocity $\mathbf{u}_a \in \mathbf{RT}_0(K)$ in (4.74) and we get

$$\begin{aligned} \int_K \nabla \cdot (f_w \mathbf{u}_a) \varphi_{K,E} &\approx \sum_{H,G,F \in \mathcal{E}_K} u_{a,K,G} f_{w,F} \int_H \varphi_{K,F} \varphi_{K,E} \mathbf{w}_{K,G} \cdot \mathbf{n}_{K,H} - \\ &- f_{w,K} \sum_{G \in \mathcal{E}_K} u_{a,K,G} \int_K \mathbf{w}_{K,G} \cdot \nabla \varphi_{K,E}. \end{aligned} \quad (4.76)$$

Using (4.69) and the properties of the basis functions $\mathbf{w}_{K,E} \in \mathbf{RT}_0$ given by (4.10), we simplify (4.76) into

$$\begin{aligned} \int_K \nabla \cdot (f_w \mathbf{u}_a) \varphi_{K,E} &\approx \sum_{H,F \in \mathcal{E}_K} f_{w,F} u_{a,K,H} I_{K,H,E,F} - \\ &f_{w,K} \sum_{G \in \mathcal{E}_K} u_{a,K,G} \int_K \mathbf{w}_{K,G} \cdot \nabla \varphi_{K,E}, \end{aligned} \quad (4.77)$$

where

$$I_{K,H,E,F} = \frac{1}{|H|_{d-1}} \int_H \varphi_{K,F} \varphi_{K,E}. \quad (4.78)$$

We evaluate the integral on the right–hand–side of (4.77) using the Green theorem and the properties of the $\mathbf{RT}_0(K)$ and $D_1(K)$ basis functions $\mathbf{w}_{K,E}$ and $\varphi_{K,E}$, respectively:

$$\int_K \mathbf{w}_{K,G} \cdot \nabla \varphi_{K,E} = \sum_{H \in \mathcal{E}_K} \int_H \varphi_{K,E} \mathbf{w}_{K,G} \cdot \mathbf{n}_H - \int_K \varphi_{K,E} \nabla \cdot \mathbf{w}_{K,G}, \quad (4.79a)$$

$$= \frac{1}{|G|_{d-1}} \int_G \varphi_{K,E} - \frac{1}{|K|_d} \int_K \varphi_{K,E}, \quad (4.79b)$$

$$= \delta_{EG} - \frac{1}{d+1}. \quad (4.79c)$$

Altogether, the expression (4.77) reads as

$$\begin{aligned} \int_K \nabla \cdot (f_w \mathbf{u}_a) \varphi_{K,E} &\approx \sum_{H,F \in \mathcal{E}_K} f_{w,F} u_{a,K,H} I_{K,H,E,F} - \\ &- f_{w,K} \left(u_{a,K,E} - \frac{1}{d+1} \sum_{G \in \mathcal{E}_K} u_{a,K,G} \right). \end{aligned} \quad (4.80)$$

Consequently, the weak formulation of the evolution equation for the saturation S_w is approximated in the form

$$\begin{aligned} \phi_K \sum_{F \in \mathcal{E}_K} \frac{dS_{w,K,F}}{dt} B_{K,E,F} + \sum_{H,F \in \mathcal{E}_K} f_{w,F} u_{a,K,G} I_{K,H,E,F} - \\ - f_{w,K} \left(u_{a,K,E} - \frac{1}{d+1} \sum_{G \in \mathcal{E}_K} u_{a,K,G} \right) = F_{w,K,E}. \end{aligned} \quad (4.81)$$

Using the inverse matrix $\mathbf{B}_K^{-1} = \mathbf{b}_K$, the time derivatives of $S_{w,K,E}$ are explicitly given by the following system of ordinary differential equations (ODE):

$$\begin{aligned} \frac{dS_{w,K,E}}{dt} = \frac{1}{\phi_K} \sum_{H \in \mathcal{E}_K} b_{K,E,H} \left[F_{w,K,H} + \sum_{H,F \in \mathcal{E}_K} f_{w,F} u_{a,K,G} I_{K,H,E,F} - \right. \\ \left. - f_{w,K} \left(u_{a,K,E} - \frac{1}{d+1} \sum_{G \in \mathcal{E}_K} u_{a,K,G} \right) \right], \end{aligned} \quad (4.82)$$

for all $E \in \mathcal{E}_h$. Note that the matrix \mathbf{B}_K is a $(d+1) \times (d+1)$ matrix and thus the computation of its inversion is cheap.

$D_0(\Omega)$ (FV)	$[\mathbf{S}]_i = S_{w,K_i}$ $[\mathbf{F}]_i = \text{right-hand-side of (4.67c) for } K = K_i$	$i = 1, \dots, \#\mathcal{K}_h$
$D_1(\Omega)$ (DG)	$[\mathbf{S}]_{3(i-1)+j} = S_{w,K_i,E_j}$ $[\mathbf{F}]_{3(i-1)+j} = \begin{cases} \text{right-hand-side of (4.82)} \\ \text{for } K = K_i \text{ and } E = E_j \end{cases}$	$i = 1, \dots, \#\mathcal{K}_h$ $j = 1, 2, 3$

Table 4.1.: Vector representation of the unknown wetting-phase saturations and the right-hand-sides of (4.67c) and (4.82) using D_0 (FV) and D_1 (DG) approximations, respectively. The symbol $\#\mathcal{K}_h$ denotes the number of elements in \mathcal{K}_h .

Side-Average of Fractional Flow Function

In most practical cases, we use the upwind technique to determine the value of the side-average fractional flow function $f_{w,E}$ in (4.67c) and (4.82). The upwinded value, denoted by $f_{w,E}^{upw}$, depends on the direction of the side-flux \mathbf{u}_a across $E \in \mathcal{E}_h^{int} \cap \mathcal{E}_{K_1} \cap \mathcal{E}_{K_2}$ and is determined as follows:

$$f_{w,E}^{upw} = \begin{cases} f_w(S_{w,K_1,E}), & \text{if } u_{a,K_1,E} \geq 0, \\ f_w(S_{w,K_2,E}), & \text{otherwise,} \end{cases} \quad (4.83)$$

(compare to (4.45)). For the exterior sides $E \in \mathcal{E}_h^{ext} \cap \mathcal{E}_K$, the upwinded fractional flow function $f_{w,E}^{upw}$ is given by

$$f_{w,E}^{upw} = \begin{cases} f_w(S_{w,E}^D), & \text{if } u_{a,K,E} \leq 0 \text{ and } E \subseteq \Gamma_{S_w}, \\ f_w(S_{w,K,E}), & \text{otherwise.} \end{cases} \quad (4.84)$$

Another possibility is to use the centered fractional flow function $f_{w,E}^{avg}$ given by

$$f_{w,E}^{avg} = \begin{cases} \frac{1}{2} [f_w(S_{w,K_1,E}) + f_w(S_{w,K_2,E})] & \text{if } E \in \mathcal{E}_h^{int} \cap \mathcal{E}_{K_1} \cap \mathcal{E}_{K_2}, \\ f_w(S_{w,E}^D) & \text{if } E \in \mathcal{E}_h^{ext} \cap \mathcal{E}_K \text{ and } E \subseteq \Gamma_{S_w}, \\ f_w(S_{w,K,E}) & \text{if } E \in \mathcal{E}_h^{ext} \cap \mathcal{E}_K \text{ and } E \not\subseteq \Gamma_{S_w}. \end{cases} \quad (4.85)$$

It is known, however, that an explicit numerical scheme is unconditionally unstable for such a choice of $f_{w,E}$, when the flow is advection-dominated, [57], [74]. Later in Section 4.2.2, we discuss the use of $f_{w,E}^{upw}$ and $f_{w,E}^{avg}$ for a pure diffusion problem.

4.1.6. Time Discretization of Saturation Equation

As a result of the discretization techniques in the previous sections, a system of ordinary differential equations (ODEs) for the unknown saturation is derived and given by equations (4.67c) or (4.82). We use the explicit Runge–Kutta (RK) methods to solve this system of ODEs. The initial condition for the system of ODEs is given by the initial condition for the saturation (1.50). In order to describe the RK methods used in this thesis for both piecewise constant and linear discretizations, we use a general vector representation of the unknown discrete saturation. By $\mathbf{S} = \mathbf{S}(t)$ and $\mathbf{F} = \mathbf{F}(t, \mathbf{S})$, we denote a vector of unknowns and a right-hand-side of the resulting discretization of the saturation equation, respectively. In Table 4.1, we describe \mathbf{S} and $\mathbf{F}(t, \mathbf{S})$ in details for the case of piecewise constant (FV) and piecewise linear (DG) approximation of S_w in 1D and 2D, respectively.

Consequently, (4.67c) or (4.82) can be written as

$$\frac{d}{dt} \mathbf{S}(t) = \mathbf{F}(t, \mathbf{S}(t)). \quad (4.86)$$

In order to solve the system of ordinary differential equations (4.86) numerically, we discretize the time interval $[0, T]$ in the same way as in (3.2, page 37) by

$$\mathcal{T}_M = \{0 = t_0 < t_1 < \dots < t_M = T\} \quad (4.87)$$

and use an explicit Runge–Kutta method in the form

$$\mathbf{S}^{i+1} = \mathbf{F}_{RK}(t_i, \Delta t_i, \mathbf{S}^i), \quad (4.88)$$

where the function \mathbf{F}_{RK} represents different choices of the Runge–Kutta methods, [112], [113]. In this thesis, we have tested either the first order forward Euler method in (4.88), where

$$\mathbf{F}_{RK_1} = \mathbf{S}^i + \Delta t_i \mathbf{F}(t_i, \mathbf{S}^i), \quad (4.89)$$

or the fourth order method

$$\mathbf{F}_{RK_4} = \mathbf{S}^i + \Delta t_i \frac{1}{6} \left(\mathbf{C}_{RK_4}^{(1)} + 2\mathbf{C}_{RK_4}^{(2)} + 2\mathbf{C}_{RK_4}^{(3)} + \mathbf{C}_{RK_4}^{(4)} \right), \quad (4.90)$$

where the coefficients $\mathbf{C}_{RK_4}^{(j)}$ for $j = 1, 2, 3, 4$ are given by

$$\mathbf{C}_{RK_4}^{(1)} = \mathbf{F}(t_i, \mathbf{S}^i), \quad (4.91a)$$

$$\mathbf{C}_{RK_4}^{(2)} = \mathbf{F}\left(t_i + \frac{1}{2}\Delta t_i, \mathbf{S}^i + \frac{1}{2}\Delta t_i \mathbf{C}_{RK_4}^{(1)}\right), \quad (4.91b)$$

$$\mathbf{C}_{RK_4}^{(3)} = \mathbf{F}\left(t_i + \frac{1}{2}\Delta t_i, \mathbf{S}^i + \frac{1}{2}\Delta t_i \mathbf{C}_{RK_4}^{(2)}\right), \quad (4.91c)$$

$$\mathbf{C}_{RK_4}^{(4)} = \mathbf{F}\left(t_i + \Delta t_i, \mathbf{S}^i + \Delta t_i \mathbf{C}_{RK_4}^{(3)}\right). \quad (4.91d)$$

We investigated the convergence of the numerical scheme using the benchmark solutions for both first and fourth order methods (4.89) and (4.90), respectively. However, the difference in error norms between the forward Euler and the fourth–order Runge–Kutta methods was negligible. Therefore, we present results obtained by using the forward Euler method (4.89) only.

4.1.7. Slope Limiter

When using the higher–order approximation of the unknown functions in the discontinuous Galerkin method, the numerical scheme produces non-physical oscillations near shocks, [62], [65]. These spurious oscillations can be avoided by reconstructing the approximated discontinuous Galerkin solution using a *slope limiter procedure*. To stabilize the MHFE-DG numerical scheme, we use the slope limiter introduced by Chavent and Jaffré, [15], in the form described in [62].

By $\check{S}_w^{i+1} \in D_1(\Omega)$, we denote the solution of (4.88). On each element $K \in \mathcal{K}_h$, we shall work with a local slope limiting operator \mathcal{L}_K that modifies $\check{S}_w^{i+1} \in D_1(K)$ such that the approximation of S_w on a new time level t_{i+1} is given by

$$S_w^{i+1} = \mathcal{L}_K(\check{S}_w^{i+1}). \quad (4.92)$$

In order to satisfy an appropriate maximum principle, the limiting operator \mathcal{L}_K modifies the gradient of \check{S}_w^{i+1} and preserves the mass in K , i.e.,

$$\frac{1}{|K|_d} \int_K S_w^{i+1} = \frac{1}{|K|_d} \int_K \check{S}_w^{i+1}, \quad \text{for all } K \in \mathcal{K}_h. \quad (4.93)$$

Apparently, the average of \check{S}_w^{i+1} over K denoted by $\check{S}_{w,K}^{i+1}$ can be used as the reconstructed solution in (4.92) which gives the finite volume approximation of $S_{w,K,E}^{i+1} = \check{S}_{w,K}^{i+1}$ for all $E \in \mathcal{E}_K$ (MHFE-FV). However, the reconstructed solution should be modified as little as possible. Therefore, we require that the reconstructed solution S_w^{i+1} is the solution of the following least squares problem with linear constraints:

$$\|S_w^{i+1} - \check{S}_w^{i+1}\|_{L^2(K)} = \min_{W \in D_1(K)} \|W - \check{S}_w^{i+1}\|_{L^2(K)}, \quad (4.94a)$$

$$\frac{1}{|K|_d} \int_K S_w^{i+1} = \frac{1}{|K|_d} \int_K \check{S}_w^{i+1}, \quad (4.94b)$$

$$S_{w,K,E}^{\min} \leq S_{w,K,E} \leq S_{w,K,E}^{\max}, \quad \text{for all } E \in \mathcal{E}_K, \quad (4.94c)$$

where

$$S_{w,K,E}^{\min} = \min \left\{ S_{w,K}^{i+1}; K \in \mathcal{N}_{K,E} \right\}, \quad (4.95a)$$

$$S_{w,K,E}^{\max} = \max \left\{ S_{w,K}^{i+1}; K \in \mathcal{N}_{K,E} \right\}, \quad (4.95b)$$

for all $E \in \mathcal{E}_K$. The set $\mathcal{N}_{K,E}$ contains all neighboring elements of the side E (including K itself):

$$\mathcal{N}_{K,E} = \{L \in \mathcal{K}_h; L \cap K = E\}. \quad (4.96)$$

A comprehensive algorithm for the least-squares minimization of (4.94) is given in [62]. By $\mathcal{L}_K(\check{S}_w^{i+1})$, we denote the optimal solution of (4.94) and set

$$S_{w,K,E}^{i+1} = [\mathcal{L}_K(\check{S}_w^{i+1})]_E, \quad (4.97)$$

for all $E \in \mathcal{E}_K$. Although the limiting procedure is iterative, the algorithm in [62] is not expensive from a computational point of view. On each element $K \in \mathcal{K}_h$, the optimal solution is reached with at most $2(d+1)$ steps. Note, that the limiting procedure needs to be applied after each step of the Runge–Kutta methods, i.e., after (4.91a)–(4.91d) in case of the fourth-order Runge–Kutta method (4.90).

4.1.8. Computational Algorithm

We summarize the complete computational algorithm for obtaining the numerical solution of the two-phase flow system (1.49) using the MHFE-FV and MHFE-DG methods described in previous sections.

The computation proceeds in the following order:

1. For a given mesh \mathcal{K}_h , compute the mesh-dependent coefficients $a_{K,E,F}$, $a_{K,E}$, and a_K for all $K \in \mathcal{K}_h$ and $E, F \in \mathcal{E}_K$.
2. At $t = t_0$, use the initial condition (1.50) to initialize $\mathbf{S}^0 = \mathbf{S}^{ini}$.
3. Set $i = 0$, and choose an initial time step Δt_0 .
4. Repeat the following steps until the predetermined final time T of the simulation is reached.
 - a) Compute the Runge–Kutta vector function $\mathbf{F}_{RK}(t_i, \Delta t_i, \mathbf{S}^i)$ using (4.89) or (4.90). In the evaluation of \mathbf{F}_{RK} , use the following procedure of obtaining the value of the right–hand–side vector function $\mathbf{F}(t, \mathbf{S})$ of the equation (4.86).
 - i. Based on a given saturation vector \mathbf{S} , compute the cell-average capillary pressure potentials $\psi_{c,K}$ for all $K \in \mathcal{K}_h$ using (4.31c).
 - ii. Assemble matrix \mathbf{M}_c given by (4.35) and (4.36).
 - iii. Assemble right–hand–side vector \mathbf{b}_c given by (4.37).
 - iv. Solve (4.34): $\mathbf{M}_c \Psi_c = \mathbf{b}_c$.
 - v. Compute $q_{c,K,E}$ for all $K \in \mathcal{K}_h$ and $E \in \mathcal{E}_K$ using (4.25).
 - vi. Assemble matrix \mathbf{M}_a given by (4.56) and (4.57).
 - vii. Assemble right–hand–side vector \mathbf{b}_a given by (4.58).
 - viii. Solve (4.55): $\mathbf{M}_a \Psi_w = \mathbf{b}_a$.
 - ix. Compute $q_{a,K,E}$ for all $K \in \mathcal{K}_h$ and $E \in \mathcal{E}_K$ using (4.50).
 - x. Evaluate the right–hand–side vector function \mathbf{F} using (4.67c) or (4.82).
 - b) If the MHFE-DG scheme is used together with the fourth order Runge–Kutta method, apply the slope limiting procedure (4.97) after each evaluation of the Runge-Kutta coefficients in (4.91).
 - c) Set $\mathbf{S}^{i+1} = \mathbf{F}_{RK}(t_i, \Delta t_i, \mathbf{S}^i)$.
 - d) If the MHFE-DG scheme is used, apply the slope limiting procedure (4.97).
 - e) Use the following heuristic condition to determine spurious oscillations of the numerical solution \mathbf{S}^{i+1} on each $K \in \mathcal{K}_h$.
 - i. Determine the maximal and minimal cell-average values of the wetting-phase saturation on the previous time level $S_{w,K}^{i,\min}$ and $S_{w,K}^{i,\max}$ over all neighboring elements of K including the element K itself.
 - ii. Compute the cell-average value $S_{w,K}^{i+1}$ on a new time level.
 - iii. If $S_{w,K}^{i+1} < (1 - \epsilon_{tol})S_{w,K}^{i,\min}$ or $S_{w,K}^{i+1} > (1 + \epsilon_{tol})S_{w,K}^{i,\max}$, decrease the time step $\Delta t_i := \Delta t_i / \zeta_{\Delta t}$ and restart the Runge–Kutta time step (4.a). If such a condition is not satisfied, divide the time step Δt_i by the time step modification factor denoted by $\zeta_{\Delta t} > 1$ and restart the Runge-Kutta method on the current time level $t = t_i$.
 - f) Set $t_{i+1} = t_i + \Delta t_i$.
 - g) If previous ζ_{in} steps were successful, set $\Delta t_{i+1} = \zeta_{\Delta t} \Delta t_i$, otherwise set $\Delta t_{i+1} = \Delta t_i$.
 - h) Set $i := i + 1$.

In steps 4.a.iv and 4.a.viii of the computational algorithm, a direct or an iterative linear solver for sparse, symmetric, and positive definite matrices can be used. In this thesis, we use the LU factorization method (direct solver) implemented in the package UMFPACK, [24], [25], [26], [27]. By ϵ_{tol} in the step 4.e.iii of the algorithm, we denote an arbitrary given tolerance that describes the maximal admissible deviation of the cell-average $S_{w,K}^{i+1}$ from the minimal and maximal cell-average values $S_{w,K}^{i,\min}$ and $S_{w,K}^{i,\max}$ on the previous time level over all neighboring elements of K including K itself. Generally, we set $\zeta_{in} = 100$, $\zeta_{\Delta t} = 1.5$, and $\epsilon_{tol} = 10^{-3}$.

4.2. Verification of Numerical Scheme in Homogeneous Medium

The correctness and accuracy of the MHFE-DG numerical scheme will be verified by means of the same benchmark problems as in Section 3.2. Additionally, our aim is to determine pros and cons of the MHFE-DG and the fully-implicit VCFVM method used in Chapter 3. For that sake, we compare absolute values of the L_1 and L_2 error norms as a function of the number of nodes N since both methods involve resolution of several linear systems of equations with a $N \times N$ matrix. In all benchmark problems, we compare experimental orders of convergence for numerical solutions obtained using the piecewise constant (denoted as MHFE-FV) and linear (denoted as MHFE-DG) approximations, respectively.

In each benchmark problem I–III., water is displaced by air in a one-dimensional horizontally placed tube due to an imposed flux at the boundary. We assume zero gravity ($\mathbf{g} = \mathbf{0}$) and no dynamic effect in capillarity ($\tau = 0$). We select the final time T such that the front of the benchmark solution stays inside the domain $\Omega = (0, 1)$.

4.2.1. Benchmark I: Pure Advection

As in Section 3.2.1, we start with the pure advection benchmark problem (2.14) with $S_0 = 0.265$ (residual water saturation), $S_i = 1$ (maximal water saturation), and $u_T(t) = 10^{-4} \text{ m s}^{-1}$.

In the MHFE-FV and MHFE-DG numerical schemes, we set $S_w^{ini} = S_i = 1$ and at the inlet ($x = 0$), we prescribe the Neumann boundary condition as $u_n^N(t, 0) = u_T(t)$ and $\psi_w^D(t, 0) = 0 \text{ Pa}$. We choose the final time $T = 1000 \text{ s}$ so that the front of the analytical solution stays inside Ω . In Figure 4.5, we compare the numerical solutions computed on a regular mesh with mesh size $h = 1/4 \text{ cm}$ to the Buckley and Leverett analytical solution and also to the numerical solution using VCFVM for the same degrees of freedom. The saturation profile obtained using the MHFE-DG method contains substantially less numerical diffusion than the VCFVM and the MHFE-DG approximation of S_n for $h = 1/2 \text{ cm}$ (c.f. Figure 4.5a) is even more accurate than the VCFVM approximation computed on a two times refined mesh with $h = 1/8 \text{ cm}$ (c.f. Figure 4.5c).

The experimental orders of convergence (*eoC*) shown in Table 4.2 indicate that both the MHFE-FV and MHFE-DG methods converge with a slightly higher order than the VCFVM (the ratio $\Delta t/h$ is kept constant). However, the difference between the piecewise constant D_0 (MHFE-FV) and piecewise linear D_1 (MHFE-DG) approximations is negligible and absolute values of their error norms are almost identical for denser meshes (c.f. Figure 4.4). Compared to the VCFVM method in Figure 4.4, the L_1 or L_2 error norms are more than two times better using the same number of nodes.

$h_1 \rightarrow h_2$ [cm]	eoc_1			eoc_2		
	MHFE-FV	MHFE-DG	VCFVM	MHFE-FV	MHFE-DG	VCFVM
$2 \rightarrow 1$	0.93	0.91	0.62	0.52	0.48	0.38
$1 \rightarrow 1/2$	0.77	0.75	0.77	0.43	0.38	0.39
$1/2 \rightarrow 1/4$	0.92	0.91	0.75	0.52	0.50	0.36
$1/4 \rightarrow 1/8$	0.78	0.77	0.80	0.42	0.40	0.4
$1/8 \rightarrow 1/16$	0.90	0.89	0.83	0.49	0.49	0.41
$1/16 \rightarrow 1/32$	0.92	0.91	0.85	0.51	0.51	0.43

Table 4.2.: Experimental orders of convergence eoc_1 and eoc_2 computed for Benchmark Problem I in L_1 and L_2 norms, respectively. Comparison between the MHFE-FV, MHFE-DG, and VCFVM method. The ratio $\Delta t/h$ is kept constant for each case.

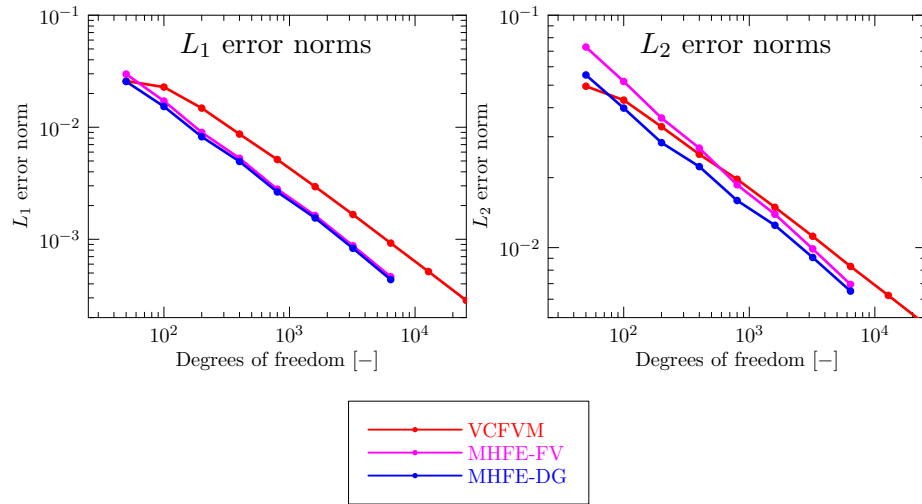


Figure 4.4.: Absolute values of the L_1 and L_2 error norms computed for Benchmark Problem I. Comparison between the MHFE-FV, MHFE-DG, and VCFVM method.

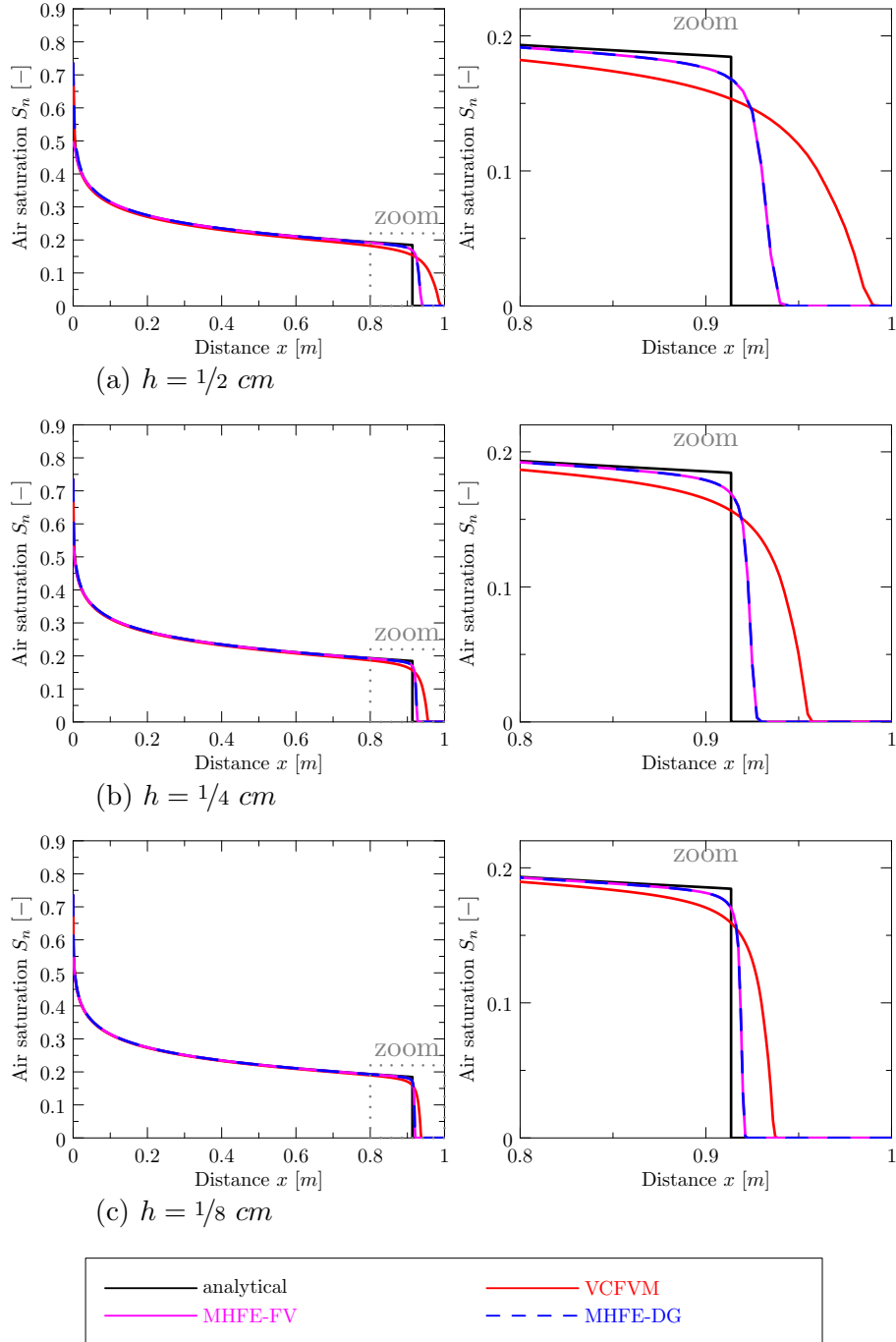


Figure 4.5.: Numerical solutions compared to the Buckley and Leverett analytical solution; $t = 1000 \text{ s}$, $h = 1/2, 1/4,$ and $1/8 \text{ cm}$, $\Delta t/h = 1/5$ is kept constant.

4.2.2. Benchmark II: Pure Capillarity in Homogeneous Medium

As a second benchmark problem, we use the pure diffusion problem formulation (2.32) with $R = 0$, $S_0 = 0.5$, and $S_i = 1$, i.e., we simulate a one-dimensional counter-current flow.

In the MHFE-FV and MHFE-DG numerical schemes, we set $S_w^{ini} = S_i = 1$ and prescribe the following boundary conditions. At the inlet ($x = 0$), we set the Dirichlet boundary condition for $S_w^D(t, 0) = S_0 = 0.5$ and $\psi_w^D(t, 0) = 0$ Pa and at $x = 1$ m, we impose zero Neumann boundary velocities $u_n^N(t, 1) = u_w^N(t, 1) = 0$ m s⁻¹. By choosing the final time of the simulation as $T = 15000$ s, we assure that the air-front stays inside Ω during the simulation. We compute numerical solutions on a series of regular meshes with decreasing mesh sizes h and compare them to the McWhorter and Sunada semi-analytical solution and also to the VCFVM method in Figure 4.6. The ratio $\Delta t/h^2$ is kept constant.

Once the flow is driven by capillarity only, we can use both upwinding ((4.45) and (4.83)) or central averaging ((4.44) and (4.85)) technique to approximate fractional flow f_n and f_w on a side $E \in \mathcal{E}_h$, respectively. In Table 4.3, we present the experimental orders of convergence *eoc* computed for the MHFE-FV and MHFE-DG numerical scheme. In the piecewise linear case (MHFE-DG), we use either upwinding or central averaging techniques. As follows from the comparison in Table 4.3 of the experimental order of convergence of the MHFE-DG method and the VCFVM discussed in Section 3.2.2, the upwinding technique leads to a first order numerical scheme. The central averaging technique exhibits higher order of convergence for coarse meshes, however, *eoc* collapses substantially as we increase the number of nodes. This is caused by the slope-limiting technique used to stabilize the numerical scheme (see Section 4.1.7). The slope limiter is mainly applied to the front of the numerical solution which, in the present case, is placed in the second half of the domain Ω , i.e., in $[0.5, 1]$, see Figure 4.6. In order to determine the experimental order of convergence without being affected by the limiting procedure, we measure the error norms of the numerical solutions in the first half of Ω , i.e., in $[0, 0.5]$, only. The resulting experimental orders of convergence in Table 4.4 show that the MHFE-DG method with central averaging technique converges with the order of convergence 2, whereas the rest of the numerical methods that are using the upwinding technique converges with the order of convergence 1. Despite the distortion of the *eoc* by the limiting procedure, the absolute error norms measured in the whole domain Ω are substantially better when using the central averaging technique, cf. the black line in Figure 4.7.

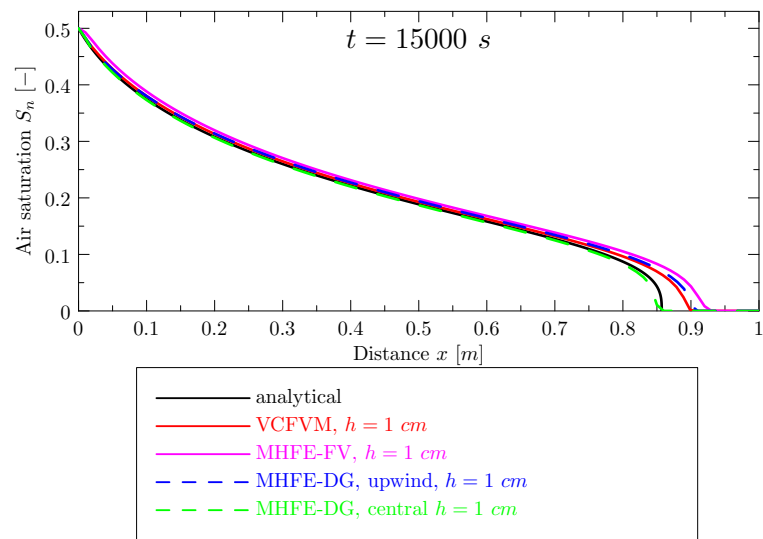


Figure 4.6.: Numerical solution of the pure diffusion McWhorter and Sunada problem in a homogeneous porous medium; $t = 15000$ s, $h = 1$ cm, and $\Delta t = 0.1$ s.

$h_1 \rightarrow h_2$ [cm]	eoc_1				eoc_2			
	MHFE-FV	MHFE-DG (upwind)	MHFE-DG (central)	VCFVM	MHFE-VFM	MHFE-DG (upwind)	MHFE-DG (central)	VCFVM
$2 \rightarrow 1$	0.84	0.36	1.93	0.93	0.73	0.59	1.83	0.74
$1 \rightarrow 1/2$	0.89	0.70	1.70	0.93	0.74	0.68	1.59	0.76
$1/2 \rightarrow 1/4$	0.92	0.82	1.35	0.89	0.76	0.70	1.21	0.66
$1/4 \rightarrow 1/8$	0.92	0.86	0.85	0.88	0.73	0.70	0.78	0.75
$1/8 \rightarrow 1/16$	0.92	0.85	0.34	0.80	0.77	0.74	0.15	0.74

Table 4.3.: Experimental orders of convergence eoc_1 and eoc_2 computed for Benchmark Problem II in L_1 and L_2 norms, respectively. Comparison between the MHFE-FV, MHFE-DG, and VCFVM.

$h_1 \rightarrow h_2$ [cm]	eoc_1				eoc_2			
	MHFE-FV	MHFE-DG (upwind)	MHFE-DG (central)	VCFVM	MHFE-FV	MHFE-DG (upwind)	MHFE-DG (central)	VCFVM
$2 \rightarrow 1$	0.88	0.18	2.02	0.90	0.88	0.19	2.01	0.91
$1 \rightarrow 1/2$	0.93	0.65	1.95	0.94	0.93	0.66	1.95	0.95
$1/2 \rightarrow 1/4$	0.96	0.82	1.94	0.97	0.96	0.83	1.93	0.97
$1/4 \rightarrow 1/8$	0.97	0.91	1.94	0.98	0.97	0.91	1.94	0.98
$1/8 \rightarrow 1/16$	0.98	0.95	1.94	0.98	0.98	0.95	1.94	0.99

Table 4.4.: Experimental orders of convergence eoc_1 and eoc_2 computed in L_1 and L_2 norms, respectively, for Benchmark Problem II using only first half of the domain Ω , i.e., $[0, 0.5]$. Comparison between the MHFE-FV, MHFE-DG, and VCFVM.

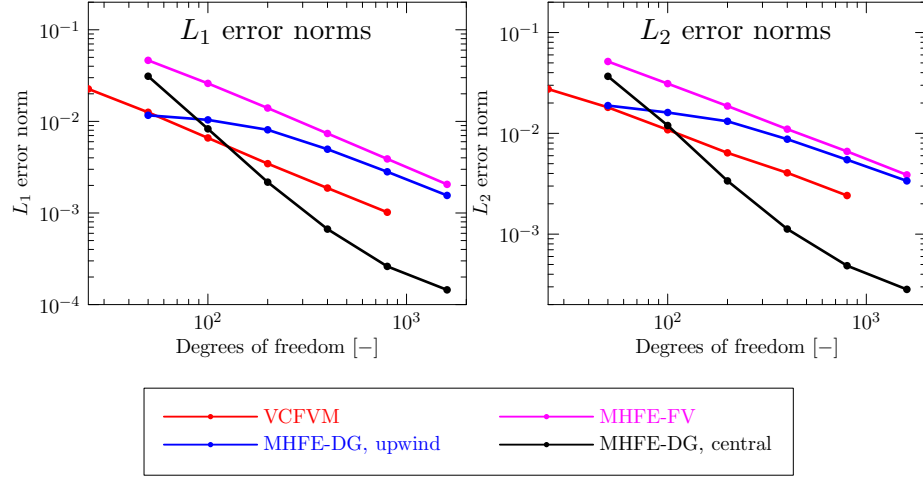


Figure 4.7.: Absolute values of the L_1 and L_2 error norms computed for Benchmark Problem II. Comparison between the MHFE-FV, MHFE-DG, and VCFVM.

$h_1 \rightarrow h_2$ [cm]	eoc_1			eoc_2		
	MHFE-FV	MHFE-DG	VCFVM	MHFE-FV	MHFE-DG	VCFVM
2 \rightarrow 1	0.87	0.78	0.68	0.52	0.48	0.34
1 \rightarrow 1/2	0.98	0.91	0.74	0.71	0.75	0.47
1/2 \rightarrow 1/4	0.99	0.92	0.76	0.77	0.89	0.55
1/4 \rightarrow 1/8	0.99	0.83	0.85	0.83	1.04	0.61
1/8 \rightarrow 1/16	0.91	0.53	0.87	1.12	1.32	0.7

Table 4.5.: Experimental orders of convergence eoc_1 and eoc_2 computed for Benchmark Problem III in L_1 and L_2 norms, respectively. Comparison between the MHFE-FV, MHFE-DG, and VCFVM.

4.2.3. Benchmark III: Advection and Diffusion in Homogeneous Medium

Third, we test both advection and diffusion by means of the McWhorter and Sunada problem formulation (2.32) with $R = 0.92$, $S_0 = 0.5$ and $S_i = 1$. We use (2.48) to compute the McWhorter and Sunada input flux rate parameter A . For the selected parameters S_0 and R , $A = 1.53 \cdot 10^{-3} \text{ ms}^{-\frac{1}{2}}$.

In the MHFE-FV and MHFE-DG numerical schemes, we set $S_w^{ini} = S_i = 1$. At the inlet ($x = 0$), we prescribe the air and water Neumann boundary velocities to $u_n^N(t, 0) = At^{-\frac{1}{2}}$ and $u_w^N(t, 0) = (R - 1)At^{-\frac{1}{2}}$, respectively. At the outlet ($x = 1 \text{ m}$), we set $u_w^N(t, 1) = RAt^{-\frac{1}{2}} \text{ ms}^{-1}$ and $S_w^D(t, 1) = S_i = 1$. We choose the final time $T = 1000 \text{ s}$ so that the air-front stays inside Ω . We compute the numerical solutions on a series of regular meshes with decreasing mesh sizes and compare them to the semi-analytical solution in Figure 4.8. The ratio $\Delta t/h^2$ is kept constant.

Similar to the previous cases, we compare the numerical solutions obtained on a series of regular meshes with the McWhorter and Sunada semi-analytical solution. We present the eoc in Table 4.5 and plot the absolute values of the error norms in Figure 4.9. In case of the advection and diffusion driven flow, the MHFE-FV and MHFE-DG method converges with a slightly higher order than the VCFVM, especially for the L_2 -norm.

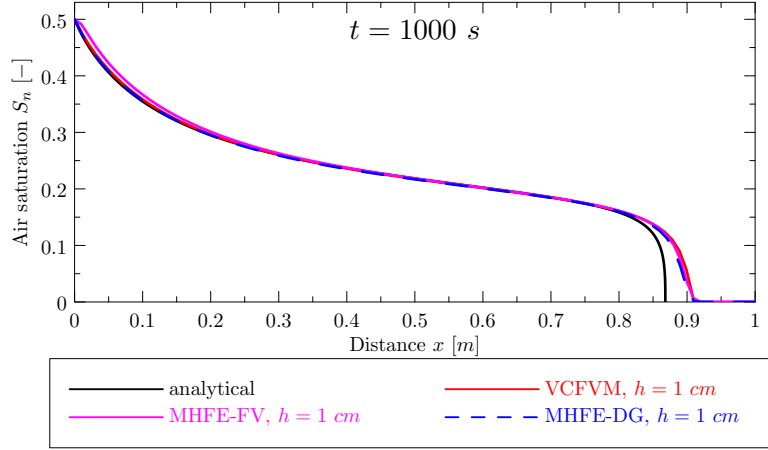


Figure 4.8.: Numerical solution of the advection–diffusion McWhorter and Sunada problem in a homogeneous porous medium; $t = 1000$ s, $h = 1$ cm, and $\Delta t = 0.1$ s.

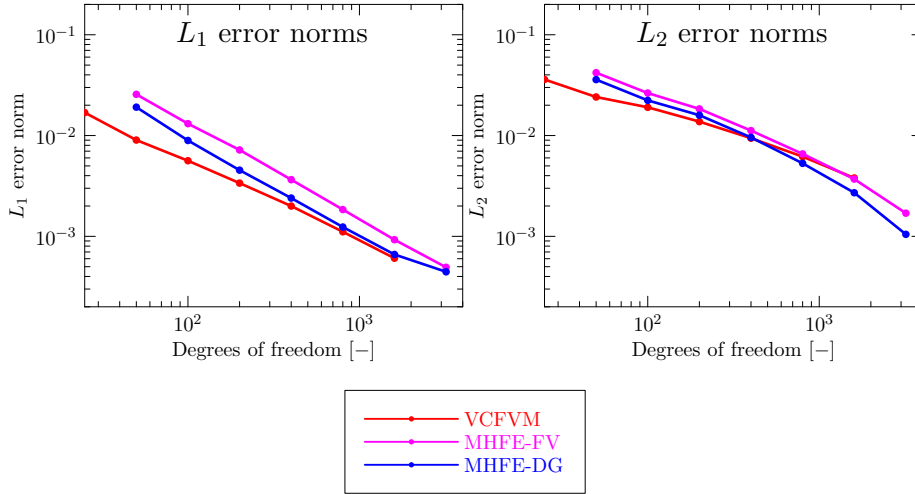


Figure 4.9.: Absolute values of the L_1 and L_2 error norms computed for Benchmark Problem III. Comparison between the MHFE-FV, MHFE-DG, and VCFVM.

4.3. Simulation of Flow in Layered Media

In this thesis, one of our primary goals is to determine the correct treatment of the conditions at material interfaces within the MHFE-DG numerical scheme which was not properly discussed in the original paper [65]. First, we use Benchmark Problems IV and V to demonstrate convergence of the numerical scheme in a one-dimensional layered medium in cases without the barrier effect. Then, we discuss the simulation of the barrier effect using the test problem introduced in Section 3.2.7 (Benchmark Problem VI) in both 1D and 2D.

4.3.1. Benchmark IV: Pure Diffusion in Layered Medium

Similar to Section 3.2.4, we consider the pure diffusion benchmark problem with a single material discontinuity (2.56) with $R = 0$, $S_i^I = 0.3$, and $S_i^{II} = 1$. The problem setup is sketched in Figure 2.2b, page 23. We assume that $\Omega = (0, 1)$ is composed of two homogeneous subdomains filled with sands A and B in $\Omega^I = (0, 1/2)$ and $\Omega^{II} = (1/2, 1)$, respectively, where sand B is finer than sand A. The sand properties are shown in Tables B.2 and B.3 in Appendix B.

We set the following initial and boundary conditions. Initially, $S_w(0, x) = 0.3$ in Ω^I and

$h_1 \rightarrow h_2$ [cm]	eoc_1			eoc_2		
	(D_0)	(D_1)		(D_0)	(D_1)	
	MHFE-DG	MHFE-DG	VCFVM	MHFE-DG	MHFE-DG	VCFVM
2 \rightarrow 1	1.07	1.07	0.82	0.97	0.97	0.48
1 \rightarrow 1/2	0.85	0.85	0.89	0.67	0.67	0.55
1/2 \rightarrow 1/4	0.87	0.87	0.91	0.67	0.67	0.55
1/4 \rightarrow 1/8	0.92	0.92	0.91	0.75	0.75	0.56
1/8 \rightarrow 1/16	0.57	0.57	0.92	0.52	0.53	0.55
1/16 \rightarrow 1/32	0.97	0.97	0.96	0.52	0.52	0.55

Table 4.6.: Experimental orders of convergence eoc_1 and eoc_2 computed for Benchmark Problem IV in L_1 and L_2 norms, respectively. Comparison between the MHFE-DG and the fully-implicit VCFVM method.

$S_w(0, x) = 1$ in Ω^{II} . At $x = 0$, we prescribe $S_w^D(t, 0) = 0.3$ and a constant water pressure $\psi_w^D(t, 0) = 0$ Pa, while on the other boundary at $x = 1$, we set $u_n^N(t, 1) = u_w^N(t, 1) = 0$ ms $^{-1}$. We compute the numerical solutions on a series of meshes and compare them to the van Duijn and de Neef semi-analytical solution and the VCFVM method, see Figure 4.11. The ratio $\Delta t/h^2$ is kept constant.

The experimental orders of convergence eoc shown in Table 4.6 indicate that both the MHFE-DG and the VCFVM methods converge with the order of convergence 1 in L_1 and $1/2$ in L_2 . No difference between the absolute error norms of the piecewise constant (MHFE-FV) and piecewise linear (MHFE-DG) approximation is observed in Figure 4.10 which indicates that the MHFE-DG (D_1) solution is strongly influenced by the limiting procedure.

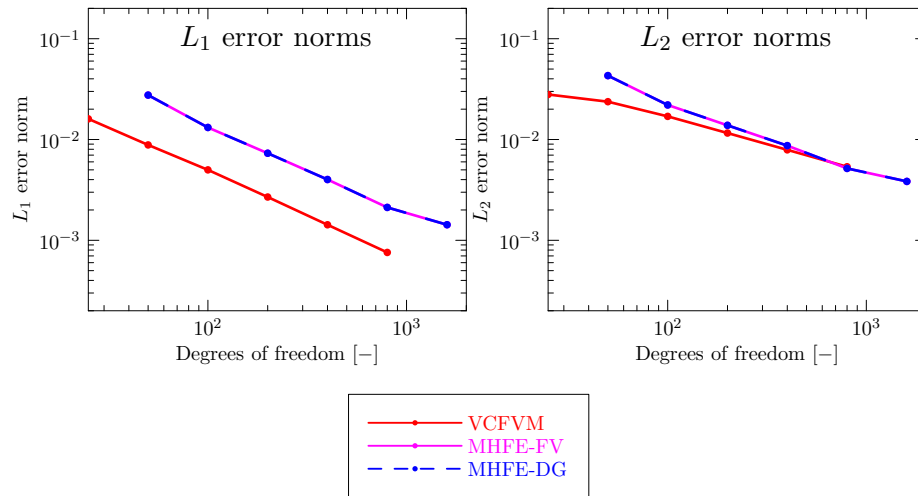


Figure 4.10.: Absolute values of the L_1 and L_2 error norms computed for Benchmark Problem IV. Comparison between the MHFE-DG and the fully-implicit VCFVM method.

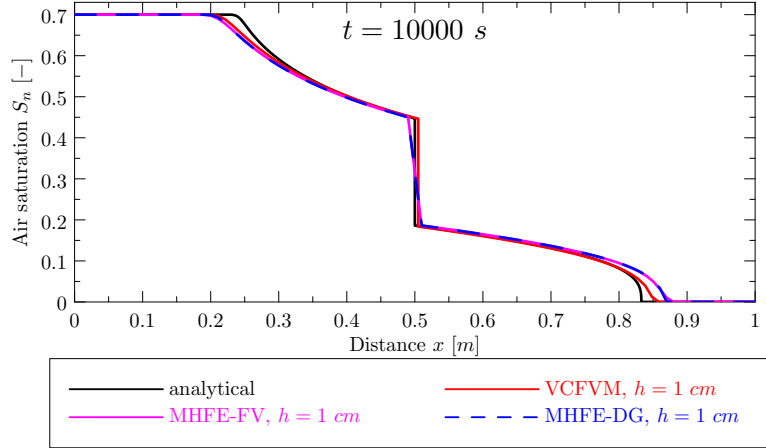


Figure 4.11.: Numerical solution of the pure diffusion problem in a layered porous medium; $t = 10000$ s, $h = 1$ cm and $\Delta t = 1$ s. Problem IV.

$h_1 \rightarrow h_2$ [cm]	eoc_1			eoc_2		
	MHFE-DG (D_0)	MHFE-DG (D_1)	VCFVM	MHFE-DG (D_0)	MHFE-DG (D_1)	VCFVM
2 \rightarrow 1	0.81	0.81	0.47	0.55	0.55	0.29
1 \rightarrow 1/2	0.87	0.87	0.99	0.62	0.62	0.58
1/2 \rightarrow 1/4	0.93	0.93	1.12	0.72	0.72	0.67
1/4 \rightarrow 1/8	0.91	0.91	1.12	0.63	0.63	0.73
1/8 \rightarrow 1/16	0.92	0.92	1.04	0.63	0.63	0.65
1/16 \rightarrow 1/32	0.91	0.91	1.01	0.60	0.60	0.64

Table 4.7.: Experimental orders of convergence eoc_1 and eoc_2 computed for Benchmark Problem V in L_1 and L_2 norms, respectively. Comparison between the MHFE-FV, MHFE-DG, and VCFVM.

4.3.2. Benchmark V : Advection and Diffusion in Layered Medium

We consider the semi-analytical solution for the diffusion and advection driven flow in a porous medium with a single material discontinuity (2.56) with $R = 0.9$, $S_i^I = 0.3$, and $S_i^{II} = 1$.

In the numerical model, we consider the following initial and boundary conditions. Initially, $S_w(0, x) = 0.3$ in Ω^I and $S_w(0, x) = 1$ in Ω^{II} . At $x = 0$, we set $S_w^D(t, 0) = 0.3$ and $\psi^D(t, 0) = 0$ Pa. The boundary conditions at $x = 1$ read as $u_n^N(t, 1) = 0$ ms^{-1} and $u_w^N(t, 1) = RA t^{-\frac{1}{2}}$, where $A = 5.61 \cdot 10^{-4}$ $ms^{-\frac{1}{2}}$. The numerical solutions compared to the semi-analytical solution and the VCFVM method are shown in Figure 4.13. Again, the experimental orders of convergence eoc in Table 4.7 and the absolute error norms in Figure 4.12 show that the MHFE-DG method converges similarly as the VCFVM method and that the difference between the piecewise constant and linear approximations is negligible.

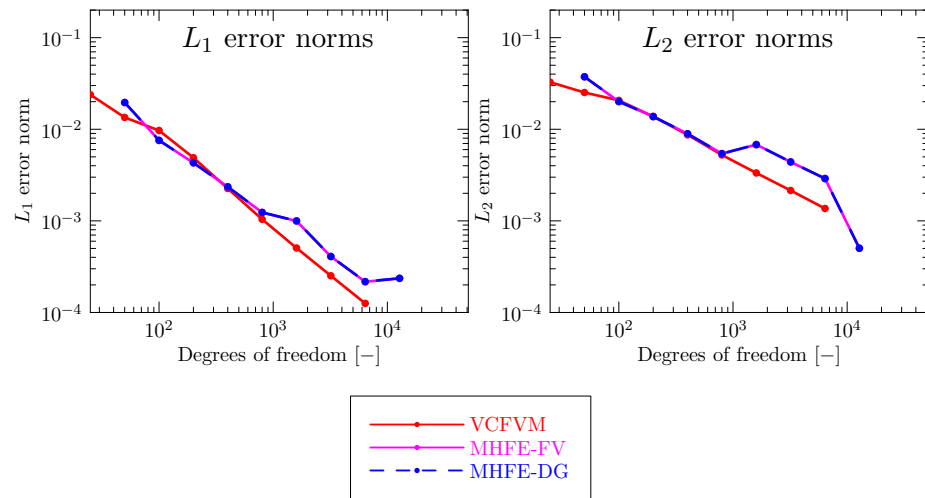


Figure 4.12.: Absolute values of the L_1 and L_2 error norms computed for Benchmark Problem V. Comparison between the MHFE-FV, MHFE-DG, and VCFVM.

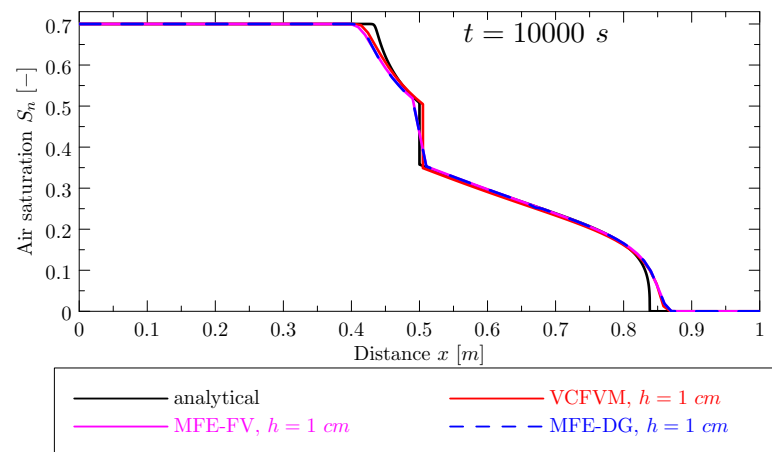


Figure 4.13.: Numerical solution of the advection–diffusion problem in a layered porous medium; $t = 1000$ s, $h = 1$ cm, and $\Delta t = 1$ s. Problem V.

4.3.3. Barrier Effect Test Problem in Layered Porous Medium

In this section, we simulate the layered medium Benchmark Problem VI introduced in Section 3.2.7 to show that the barrier effect is simulated correctly by the MHFE-DG numerical scheme. We consider a vertical column that consists of three sand layers combined of two different sands denoted as Sand D and E (their properties are given in Tables B.5, respectively). Sharp material interfaces are placed at $x = 0.145 \text{ m}$ and $x = 0.345 \text{ m}$. We compute the numerical solutions for both one- and two-dimensional cases.

The problem setup in 1D is sketched in Figure 3.7, page 47. At the inlet ($x = 0$), a DNAPL denoted as NAPL A (c.f. Table B.1) flows into the domain with a constant rate $u_n(t, 0) = 3.57 \cdot 10^{-5} \text{ ms}^{-1}$ whereas the water velocity is zero. At the bottom of the column, the maximal wetting-phase saturation $S_w = 1$ is prescribed and the water pressure is kept constant at $2 \cdot 10^5 \text{ Pa}$. The final time of the simulation is $T = 1650 \text{ s}$. In Figure 4.15, we plot the numerical solutions and compare them to the numerical solution obtained using the VCFVM method on a very fine mesh with mesh size $h = 5/1280$. Additionally, we plot the VCFVM solution on the same mesh (the dotted line in Figure 4.15) to show that the MHFE-DG method contains less numerical diffusion and that the fronts are sharper. The numerical results show a very good agreement with the results published in [57, page 275].

The two-dimensional setup of the same problem is shown in Figure 4.14a, where a rectangular domain Ω of dimensions $0.5\text{m} \times 0.5\text{m}$ is sketched. We use the following boundary conditions:

$$\mathbf{u}_n \cdot \mathbf{n} = -3.57 \cdot 10^{-5} \text{ ms}^{-1} \quad \text{and} \quad \mathbf{u}_w \cdot \mathbf{n} = 0 \quad \text{on } \Gamma_1, \quad (4.98a)$$

$$S_w = 1 \quad \text{and} \quad \psi_w = 2 \cdot 10^5 + 4905 \text{ Pa} \quad \text{on } \Gamma_3, \quad (4.98b)$$

$$\mathbf{u}_n \cdot \mathbf{n} = 0 \quad \text{and} \quad \mathbf{u}_w \cdot \mathbf{n} = 0 \quad \text{on } \Gamma_2 \cup \Gamma_4, \quad (4.98c)$$

where \mathbf{n} is the outer normal to the domain boundary. Initially, the column is fully water saturated, i.e., $S_w = 1$ in Ω . The initial mesh is shown in Figure 4.14b. In order to show convergence of the numerical simulations, the initial mesh is refined uniformly. In Figures 4.16 and 4.17, we plot the numerical solution using the MHFE-FV and the MHFE-DG method, respectively. For each mesh refinement, we compare the numerical solution on a slice $x = 0.25$ with the numerical solution obtained using the VCFVM on a very fine mesh. In both situations, the numerical solutions converge to the VCFVM solution whereas the piecewise linear approximation (MHFE-DG) gives substantially better approximation of the solution. In case of coarse meshes (cf. Figures 4.16a and 4.17a), the near-boundary irregularities of the front of the numerical solutions are caused by the non-uniform triangulation of the domain. These effects vanish when finer meshes are used (cf. Figures 4.16c and 4.17c).

Altogether, the MHFE-DG numerical solutions converge towards the VCFVM solution obtained on a very fine mesh and the barrier effect is captured correctly in both 1D and 2D cases.

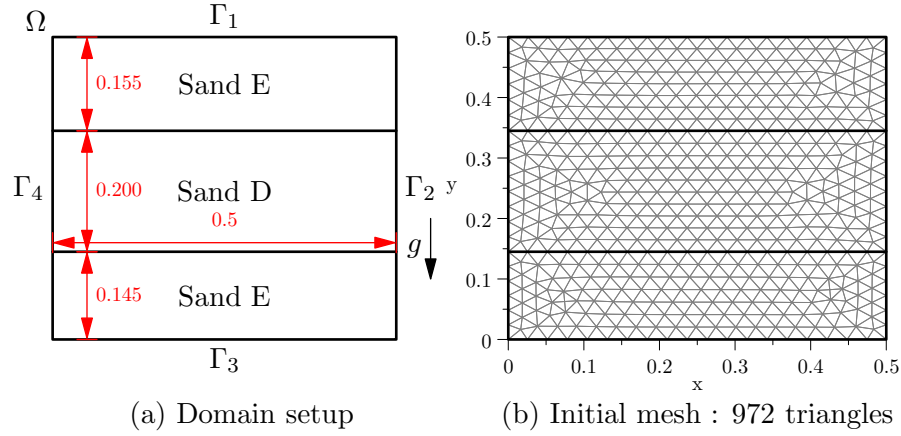


Figure 4.14.: Setup and the initial mesh for the Benchmark Problem VI in a two-dimensional space. Properties of the Sands E and D are given in Table B.5.

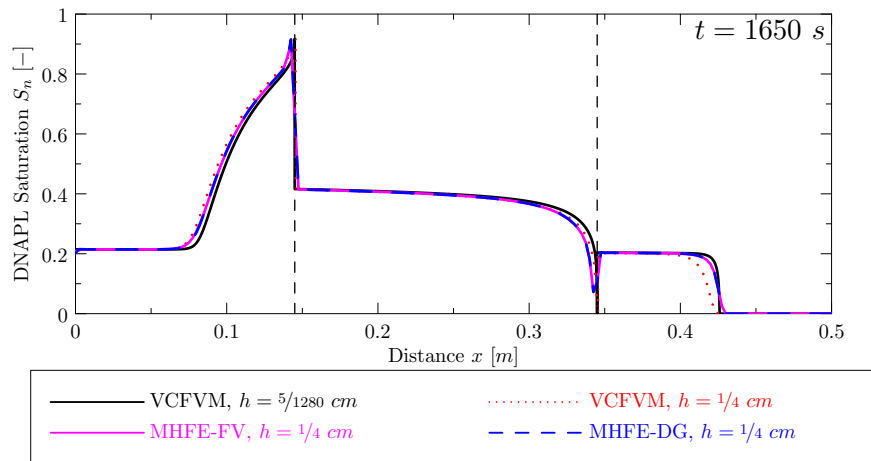


Figure 4.15.: Comparison of the MHFE-FV and MHFE-DG method and the numerical solution obtained using the VCFVM on a very fine mesh for the Benchmark Problem VI. The time step Δt is chosen adaptively.

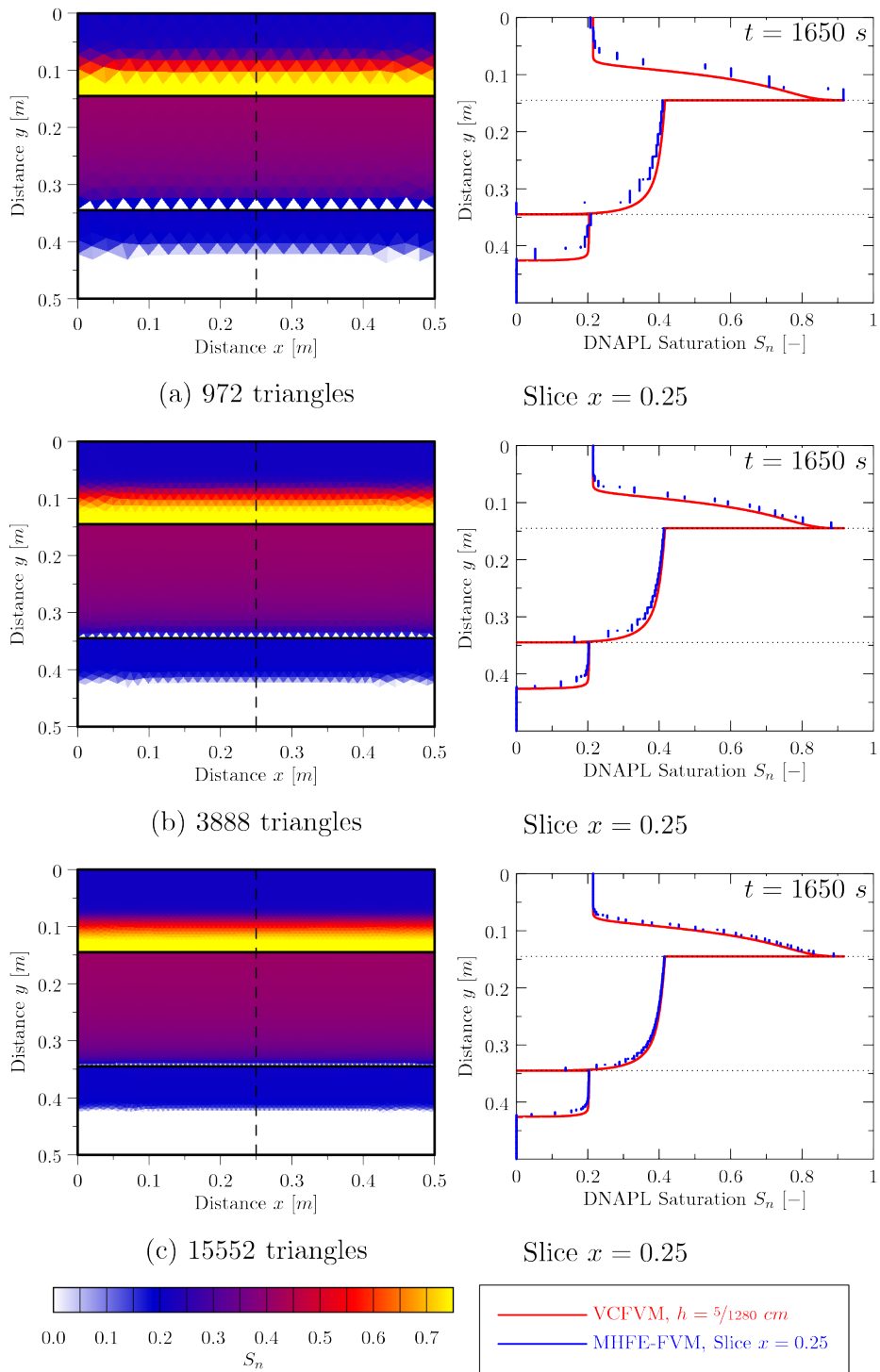


Figure 4.16.: Numerical solutions of the Benchmark Problem VI using the MHFE-FV method in 2D. Slices of the numerical solution at $x = 0.25$ are compared to the numerical solution obtained using the VCFVM in 1D on a very fine mesh. The time step Δt is chosen adaptively.

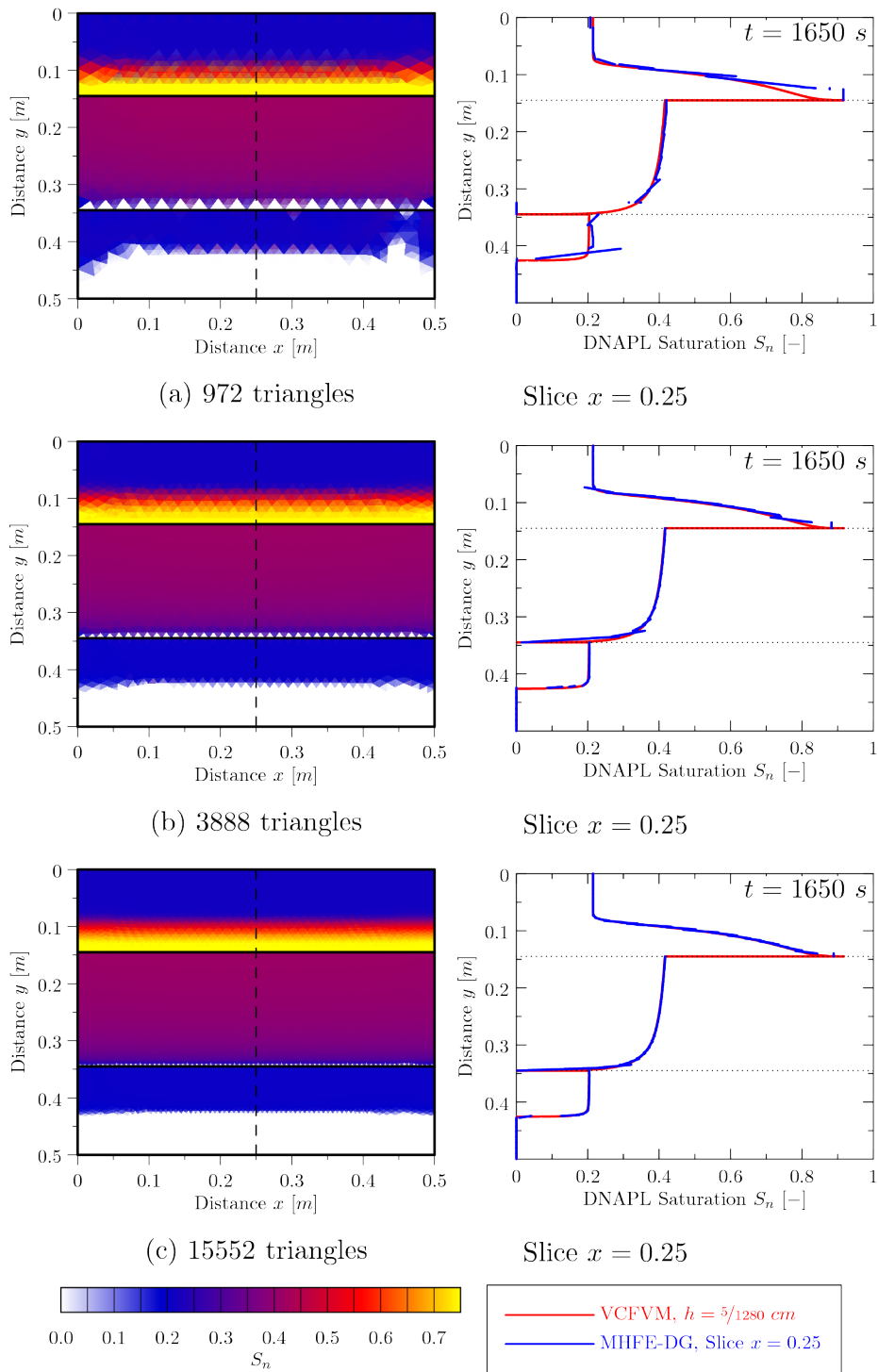


Figure 4.17.: Numerical solutions of the Benchmark Problem VI using the MHFE-DG method in 2D. Slices of the numerical solution at $x = 0.25$ are compared to the numerical solution obtained using the VCFVM in 1D on a very fine mesh. The time step Δt is chosen adaptively.

4.4. Application of MHFE-DG Method in 2D Heterogeneous Problems

In the final section of this chapter, we use the MHFE-FV and MHFE-DG methods to simulate two-dimensional problems in heterogeneous porous media. We use two textbook problems published in [57] to demonstrate reliability and accuracy of the MHFE-FV and MHFE-DG methods in Subsections 4.4.1 and 4.4.2. In the last Subsection 4.4.3, we simulate a laboratory experiment involving a light NAPL in a layered porous medium with an inclined material interface and compare the results of the numerical solutions to the experimental data.

4.4.1. Low Permeable Lens in a Sandbox

A typical test problem in a two-dimensional layered medium is the DNAPL contamination problem of a vertically-placed sandbox illustrated in Figure 4.18a. The domain Ω is composed of a box with a rectangular lens. The lens is filled with sand G which is finer than the sand F in the rest of the box. In the lens, we shall consider sand G_1 or G_2 with different values of the entry pressure (see Table B.6, page 125) in order to simulate cases, where the non-wetting phase can or cannot enter the lens, respectively.

Initially, the domain is fully water saturated and at $t = 0$, the DNAPL trichloroethylene (TCE, see Table B.1) starts to flow with a constant flow rate through Γ_1 . Boundaries Γ_2 , Γ_4 , and Γ_6 are considered impermeable and a hydrostatic water pressure (therefore constant ψ_w) is prescribed on Γ_3 and Γ_5 , i.e.,

$$\mathbf{u}_n \cdot \mathbf{n} = -5.13 \cdot 10^{-5} \text{ m s}^{-1} \quad \text{and} \quad \mathbf{u}_w \cdot \mathbf{n} = 0 \quad \text{on } \Gamma_1, \quad (4.99a)$$

$$S_w = 1 \quad \text{and} \quad \psi_w = 10^5 \text{ Pa} \quad \text{on } \Gamma_3 \cup \Gamma_5, \quad (4.99b)$$

$$\mathbf{u}_n \cdot \mathbf{n} = 0 \quad \text{and} \quad \mathbf{u}_w \cdot \mathbf{n} = 0 \quad \text{on } \Gamma_2 \cup \Gamma_4 \cup \Gamma_6, \quad (4.99c)$$

where \mathbf{n} denotes the outer normal to the domain boundary. We compute the numerical solutions on a series of six meshes with an increasing number of triangles. The coarsest mesh shown in Figure 4.18b contains 1225 triangles and the finest mesh consists of 42112 triangles. To illustrate the difference between the piecewise constant (MHFE-FV) and piecewise linear (MHFE-DG) approximations of S_w , we plot a one-dimensional slice $x = 0.45$ for each of the numerical solutions.

First, we simulate the case with a lower permeable lens filled with sand G_1 . In Figures 4.19 and 4.20, we plot numerical results obtained using the MHFE-FV and the MHFE-DG method, respectively. In both cases, the sharp front of the final solution at $t = 4500 \text{ s}$ is captured correctly even on the coarse mesh (case (a)). Comparing the one-dimensional slices $x = 0.45$ in cases (a), (b), and (c), we observe the convergence of the numerical solutions and also a good agreement with the results published in [58] and [57].

In the second case, we simulate a situation, where the DNAPL pools on top of the lower permeable lens filled with sand G_2 . The sand G_2 has a higher entry pressure than G_1 . During the simulation, the capillary pressure of the DNAPL pooled at the material interface does not attain the required entry pressure p_d of the sand G_2 . Therefore, it does not penetrate the low-permeable lens as shown in Figure 4.21 and 4.22 for the MHFE-FV and the MHFE-DG methods, respectively. Again, the distributions of S_w at $t = 4500 \text{ s}$ exhibit a good agreement with the results published in [58] and [57].

The comparison between the MHFE-FV and the MHFE-DG methods is shown in Figures 4.23 and 4.24 using contours of the numerical solutions given in Figures 4.19–4.22. All contour lines corresponding to the MHFE-DG method are slightly more closely spaced at the front of the solution than in the case of the MHFE-FV method but the difference is small. This indicates that the MHFE-DG numerical solution is slightly less influenced by the numerical diffusion

than in the finite volume method. Unlike in pure advection problems (cf. the Buckley and Leverett problem in Section 4.2.1), the difference between the MHFE-FV and MHFE-DG is almost negligible in capillarity-dominant problems.

Computational times on a Dual-Core AMD Opteron™ Processor 2216 with 8 GB RAM are given in Tables 4.8 and 4.9.

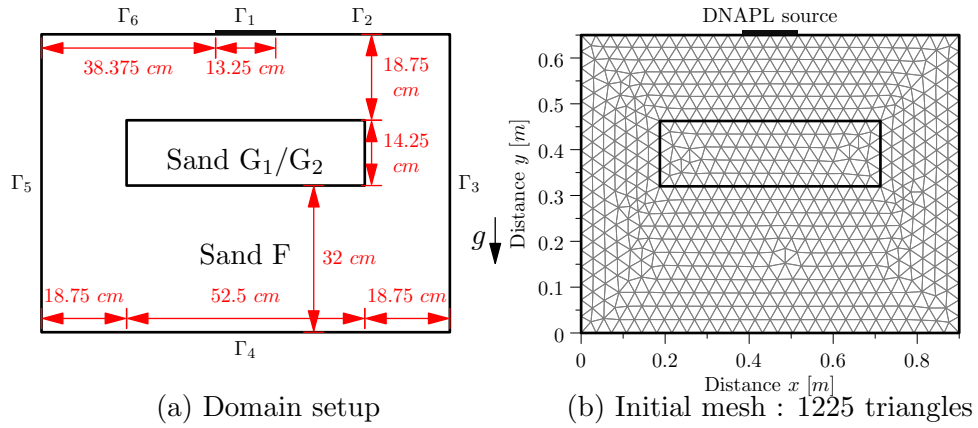


Figure 4.18.: Setup and the coarsest mesh (1225 triangles) for the porous medium with a heterogeneity in a two-dimensional space. Properties of the Sands F, G₁, and G₂ are given in Table B.6.

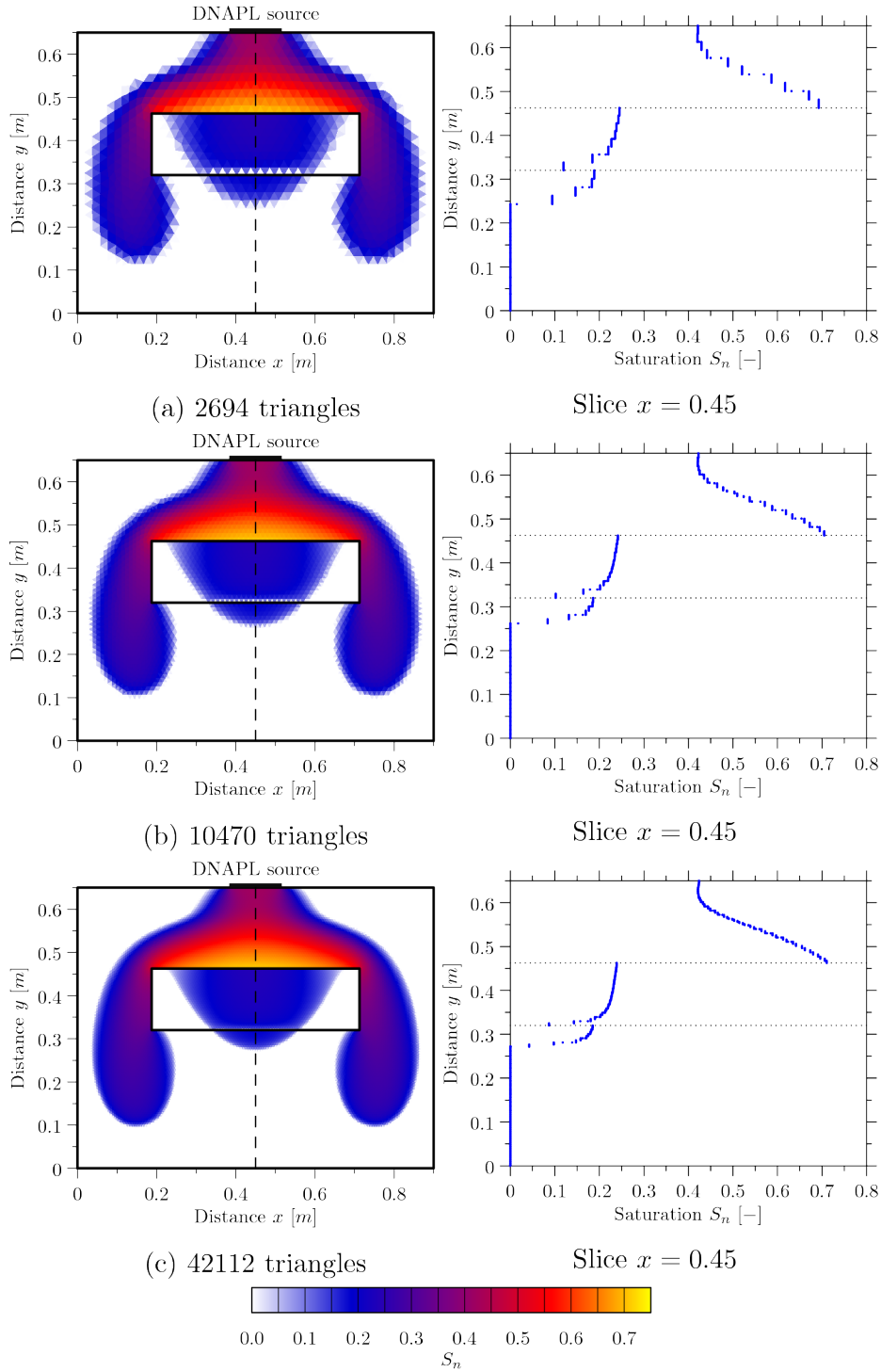


Figure 4.19.: DNAPL saturation distribution of the contamination problem of a heterogeneous sandbox with low permeable lens filled with Sand G_1 . Results obtained using piecewise constant (MHFE-FV) approximation of S_w . Time step Δt is chosen adaptively.

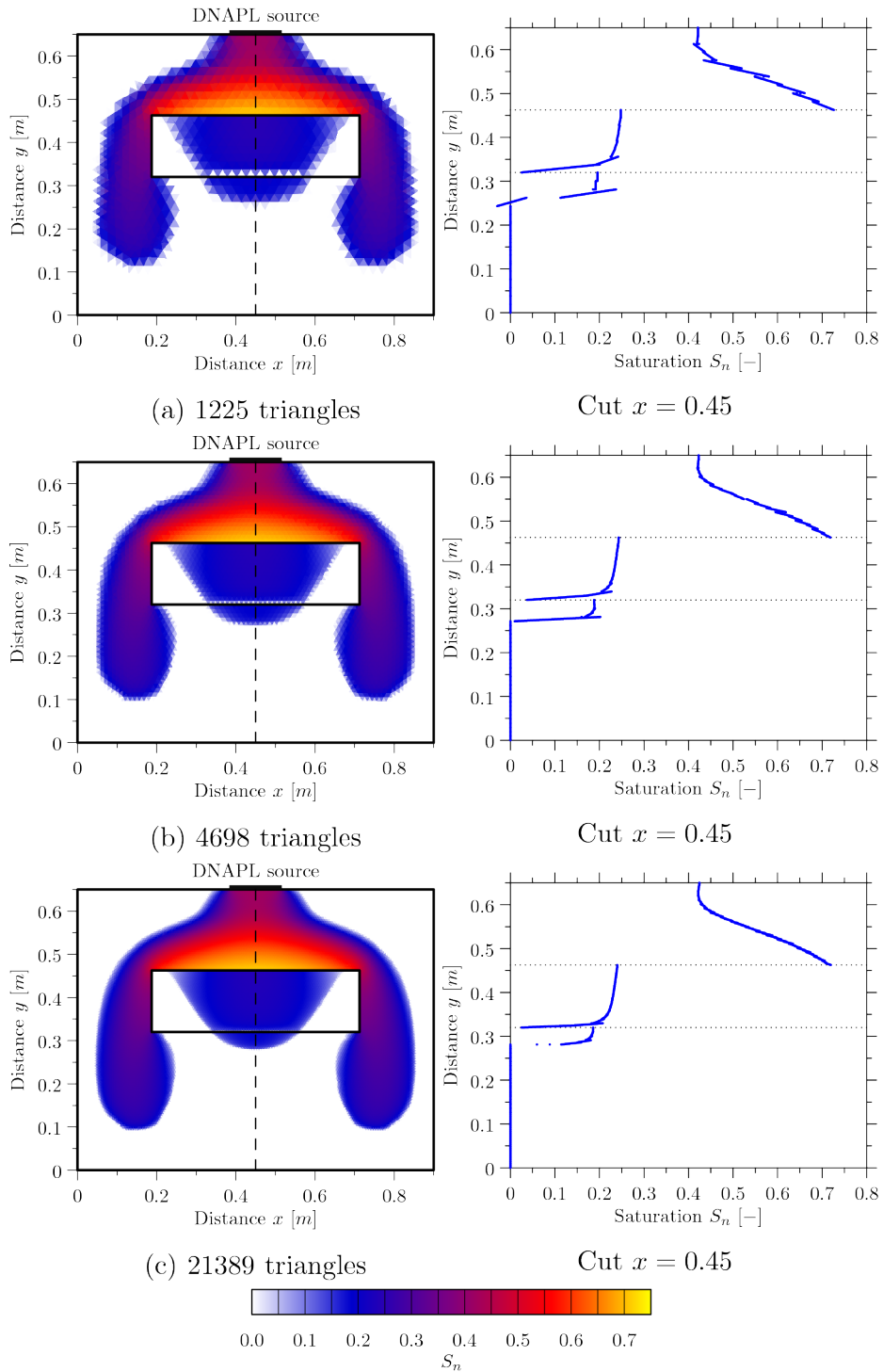


Figure 4.20.: DNAPL saturation distribution of the contamination problem of a heterogeneous sandbox with low permeable lens filled with Sand G_1 . Results obtained using piecewise linear (MHFE-DG) approximation of S_w . Time step Δt is chosen adaptively.

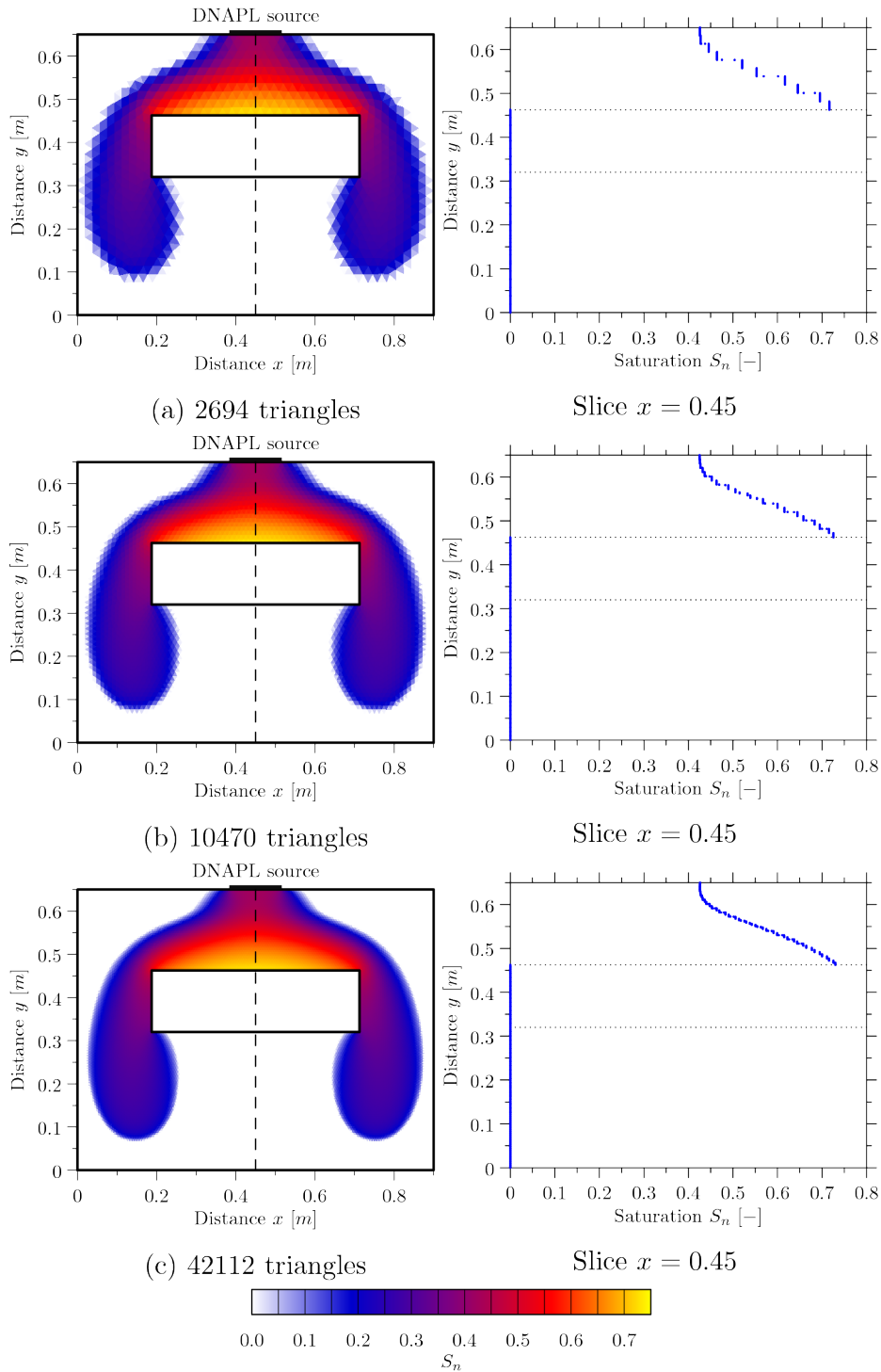


Figure 4.21.: DNAPL saturation distribution of the contamination problem of a heterogeneous sandbox with low permeable lens filled with Sand G_2 . Results obtained using piecewise constant (MHFE-FV) approximation of S_w . Time step Δt is chosen adaptively.

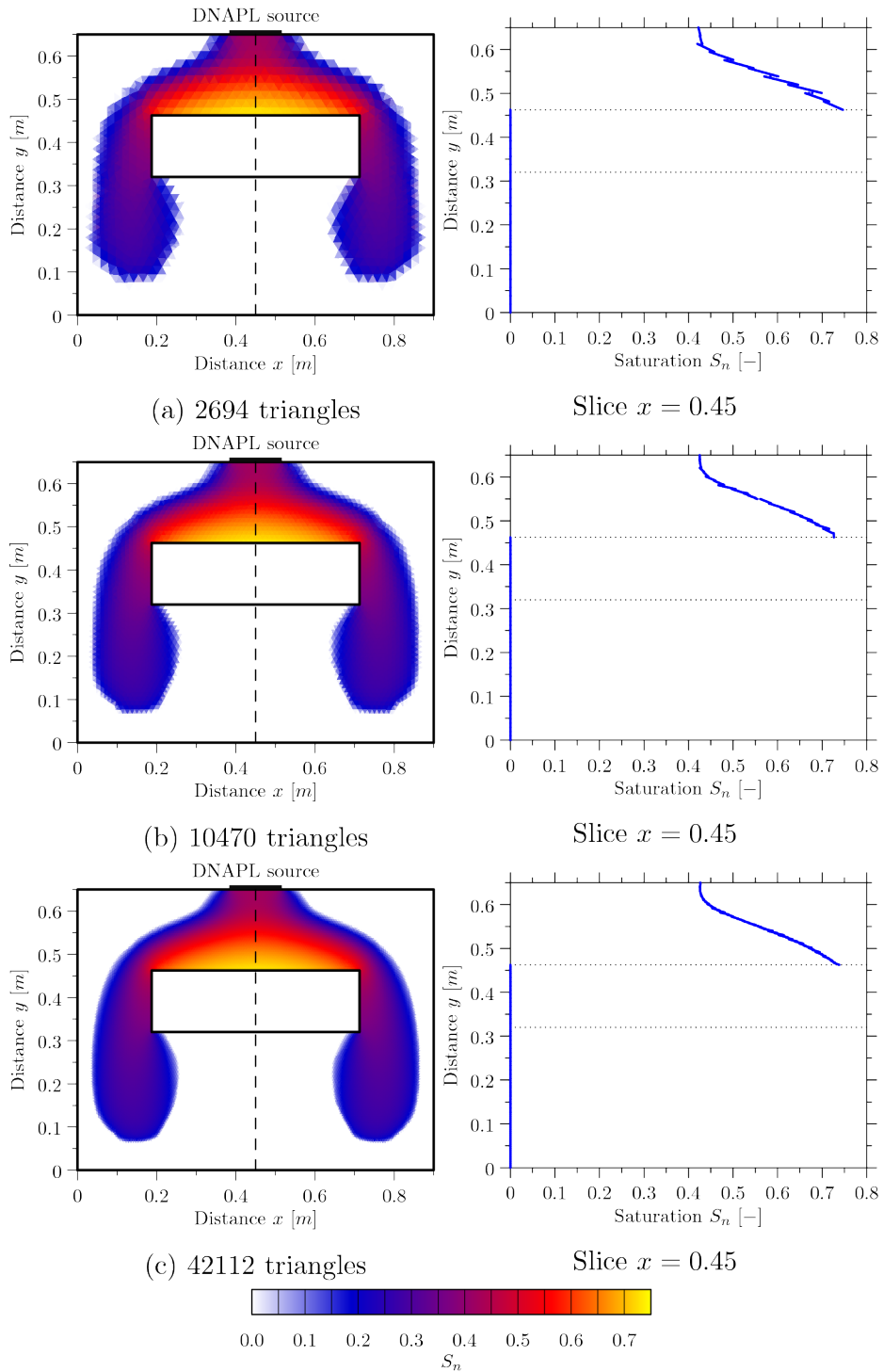


Figure 4.22.: DNAPL saturation distribution of the contamination problem of a heterogeneous sandbox with low permeable lens filled with Sand G_2 . Results obtained using piecewise linear (MHFE-DG) approximation of S_w . Time step Δt is chosen adaptively.

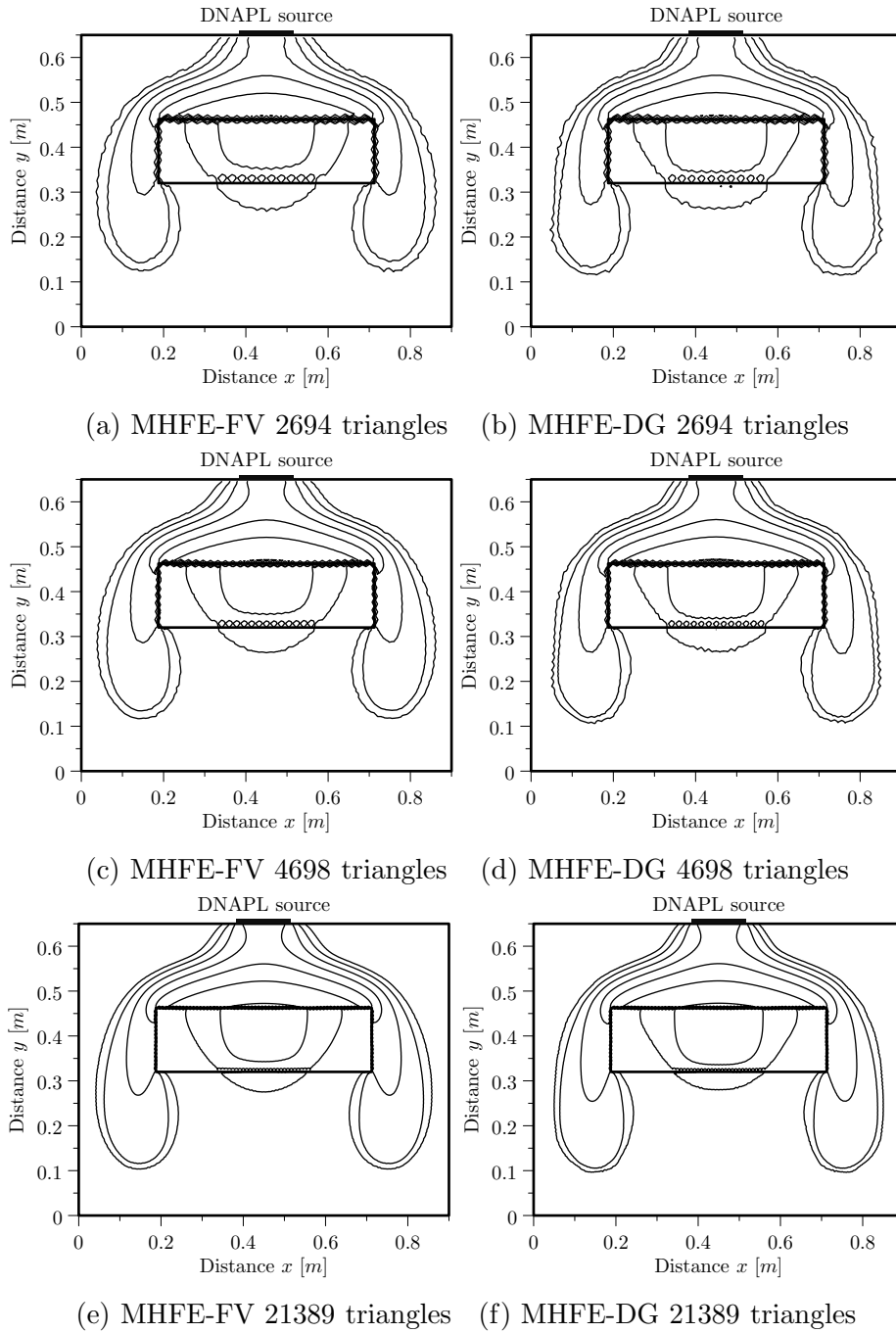


Figure 4.23.: Contours of the DNAPL saturation S_n of the contamination problem of a heterogeneous sandbox with low permeable lens filled with Sand G_1 . Comparison between the MHFE-FV (left figures) and the MHFE-DG (right figures) approach. The contour lines spacing is 0.1 starting from $S_n = 0.1$ (the outer-most one).

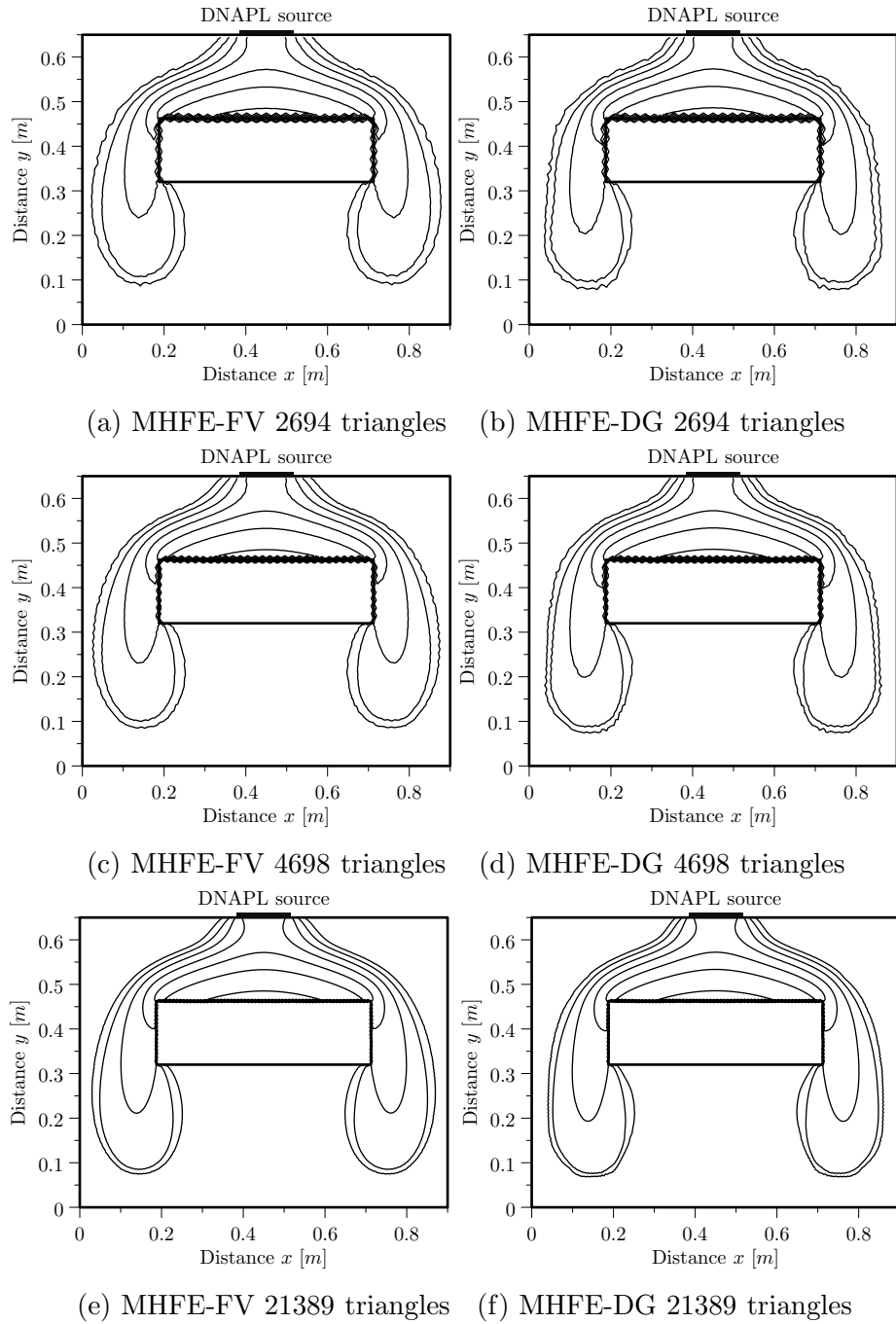


Figure 4.24.: Contours of the DNAPL saturation S_n of the contamination problem of a heterogeneous sandbox with low permeable lens filled with Sand G₂. Comparison between the MHFE-FV (left figures) and the MHFE-DG (right figures) approach. The contour lines spacing is 0.1 starting from $S_n = 0.1$ (the outer-most one).

Triangles	MHFE-FV		MHFE-DG	
1225	3 min 56 s	(236 s)	4 min 24 s	(264 s)
2694	16 min 32 s	(992 s)	18 min 9 s	(1089 s)
4698	43 min 27 s	(2607 s)	47 min 30 s	(2910 s)
10470	3 h 26 min 45 s	(13946 s)	3 h 52 min 26 s	(13946 s)
21389	16 h 42 min 31 s	(60151 s)	18 h 53 min 53 s	(68033 s)
42112	2 d 17 h 19 min 38 s	(235178 s)	3 d 1 h 14 min 54 s	(263694 s)

Table 4.8.: Computational times on a Dual-Core AMD Opteron™ Processor 2216 with 8 GB RAM: Low permeable lens filled with Sand G₁ in a sandbox (Figures 4.19 and 4.20).

Triangles	MHFE-FV		MHFE-DG	
1225	3 min 14 s	(194 s)	3 min 54 s	(234 s)
2694	14 min 39 s	(879 s)	17 min 26 s	(1046 s)
4698	51 min 21 s	(3081 s)	54 min 53 s	(3293 s)
10470	4 h 18 min 0 s	(15480 s)	4 h 53 min 27 s	(17607 s)
21389	20 h 27 min 8 s	(73628 s)	22 h 41 min 25 s	(81685 s)
42112	3 d 7 h 41 min 34 s	(286894 s)	3 d 16 h 21 min 53 s	(318113 s)

Table 4.9.: Computational times on a Dual-Core AMD Opteron™ Processor 2216 with 8 GB RAM: Low permeable lens filled with Sand G₂ in a sandbox (Figure 4.21 and 4.22).

4.4.2. Highly Heterogeneous Medium

As another example problem, we simulate a laboratory experiment described in [69], [70], [71], and [57, page 307]. In this experiment, tetrachloroethylene (PCE, see Table B.1) contaminates a vertically-placed acrylic glass flume which is initially fully water-saturated. The flume is packed with four different sands (denoted by H, I, J, and K), see Figure 4.25a. The sand properties are given in Table B.7. On Γ_1 , a constant DNAPL saturation is prescribed as $S_n = 0.6$. Boundaries Γ_2 , Γ_4 , and Γ_6 are considered impermeable. The hydrostatic water pressure is prescribed on Γ_3 , and Γ_5 . Altogether, the boundary conditions are given as follows

$$S_w = 0.4 \quad \text{and} \quad \psi_w = 10^5 \text{ Pa} \quad \text{on } \Gamma_1, \quad (4.100a)$$

$$S_w = 1 \quad \text{and} \quad \psi_w = 10^5 \text{ Pa} \quad \text{on } \Gamma_3 \cup \Gamma_5, \quad (4.100b)$$

$$\mathbf{u}_n \cdot \mathbf{n} = 0 \quad \text{and} \quad \mathbf{u}_w \cdot \mathbf{n} = 0 \quad \text{on } \Gamma_2 \cup \Gamma_4 \cup \Gamma_6, \quad (4.100c)$$

where \mathbf{n} denotes the outer normal to the domain boundary.

In [70] the experimental results are shown after 34, 126, 184, 220, 245, and 313 seconds. By using the MHFE-FV and MHFE-DG numerical schemes, our goal is to obtain patterns that resemble the experimental results at these times. As in the previous sections, we compare the piecewise constant (D_0) and linear (D_1) approach and plot the results computed on a series of four meshes with an increasing number of triangles. The coarsest mesh is shown in Figure 4.25b.

Numerical results in Figure 4.26 (at $t = 34$ s), 4.27 (at $t = 126$ s), 4.28 (at $t = 184$ s), 4.29 (at $t = 220$ s), 4.30 (at $t = 244$ s), and 4.31 (at $t = 313$ s) show a very good agreement with the experimentally measured saturation distributions in [70] and also the numerical convergence is apparent when the left-hand-side and right-hand-side subfigures (a,c,e) and (b,d,f), respectively, are compared to each other for all Figures 4.26–4.31.

Triangles	MHFE-FV	MHFE-DG
978	5 min 26 s (326 s)	6 min 44 s (404 s)
1968	14 min 43 s (883 s)	18 min 20 s (1100 s)
4506	45 min 44 s (2744 s)	57 min 23 s (3443 s)
9064	2 h 15 min 34 s (8134 s)	2 h 50 min 8 s (10208 s)

Table 4.10.: Computational times on a Dual-Core AMD Opteron™ Processor 2216 with 8 GB RAM: Highly heterogeneous medium (at $t = 313$ s, Figure 4.31).

Computational times on a Dual-Core AMD Opteron™ Processor 2216 with 8 GB RAM are given in Table 4.10.

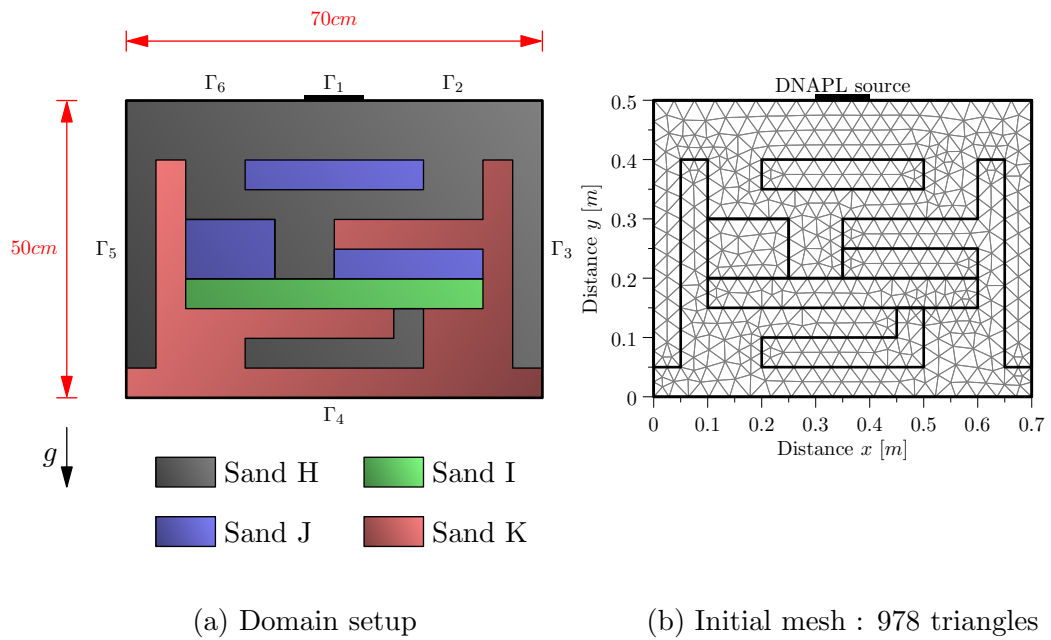


Figure 4.25.: Setup and an initial mesh for a highly heterogeneous porous medium in 2D. Properties of the Sands H, I, J, and K are given in Table B.7.

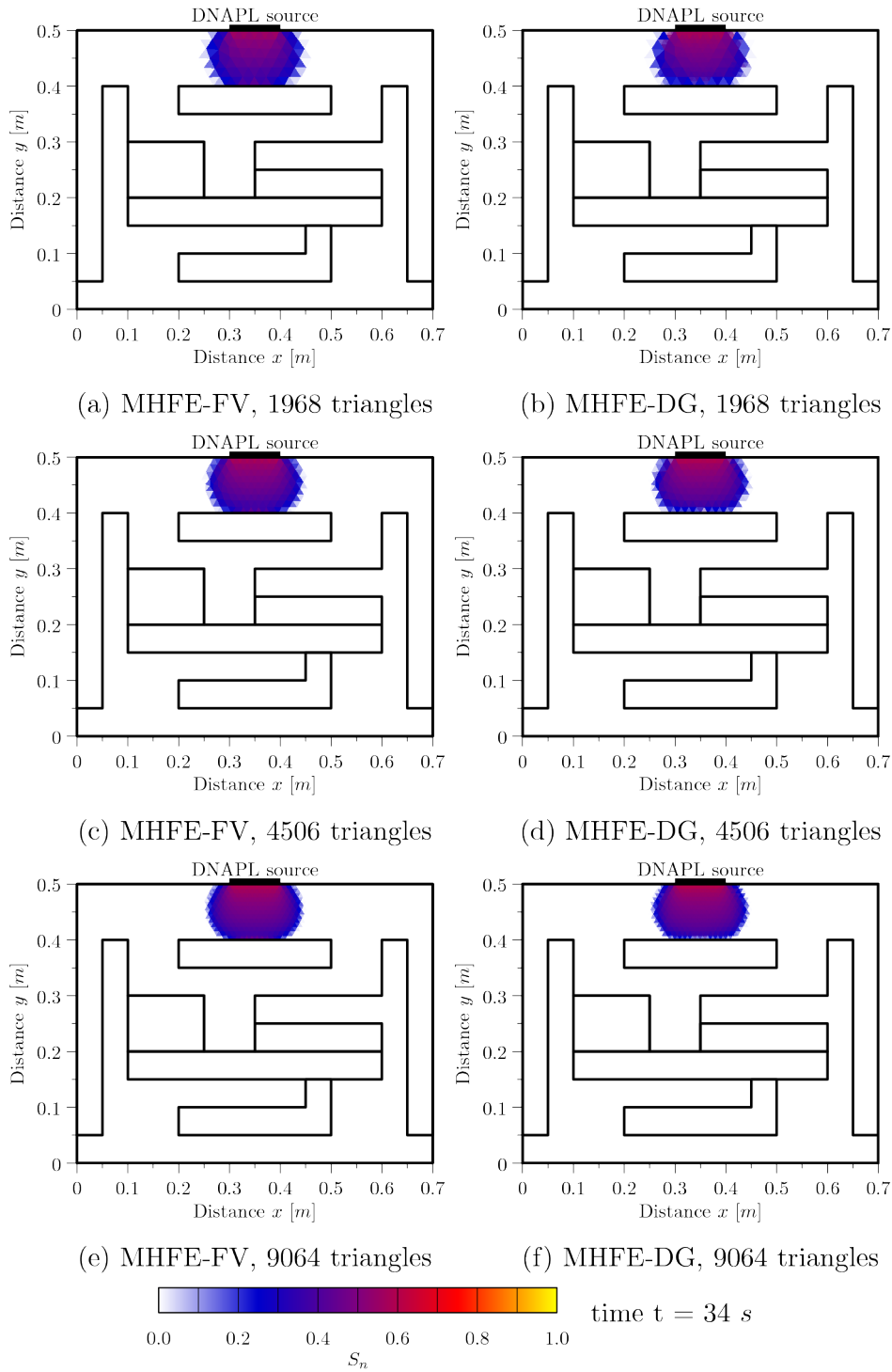


Figure 4.26.: MHFE-FV (left) and MHFE-DG (right) DNAPL saturation at $t = 34$ s for the highly heterogeneous problem on three structured meshes with 1968 triangles (a,b), 4506 triangles (c,d), and 9064 triangles (e,f).

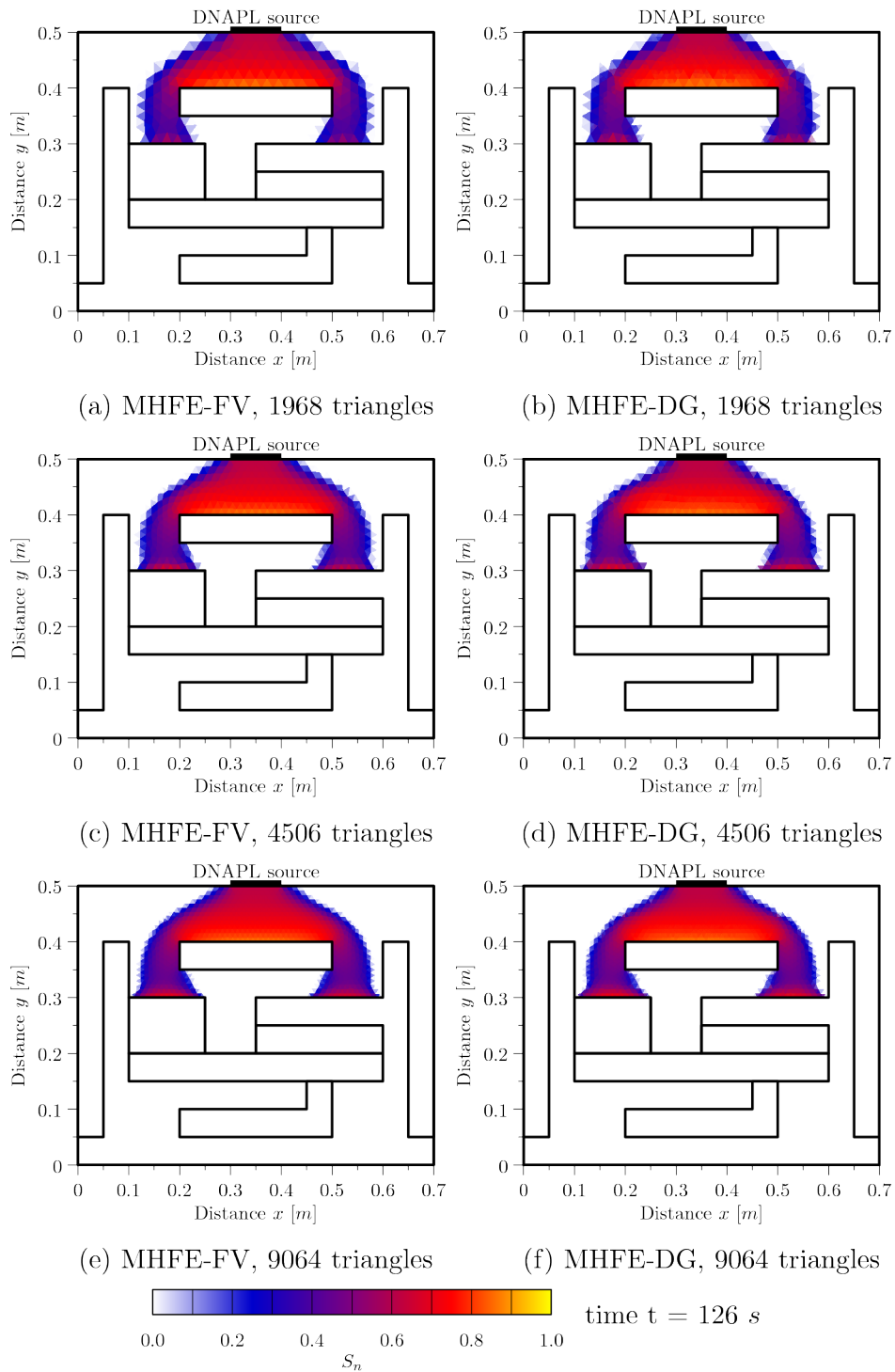


Figure 4.27.: MHFE-FV (left) and MHFE-DG (right) DNAPL saturation at $t = 126$ s for the highly heterogeneous problem on three structured meshes with 1968 triangles (a,b), 4506 triangles (c,d), and 9064 triangles (e,f).

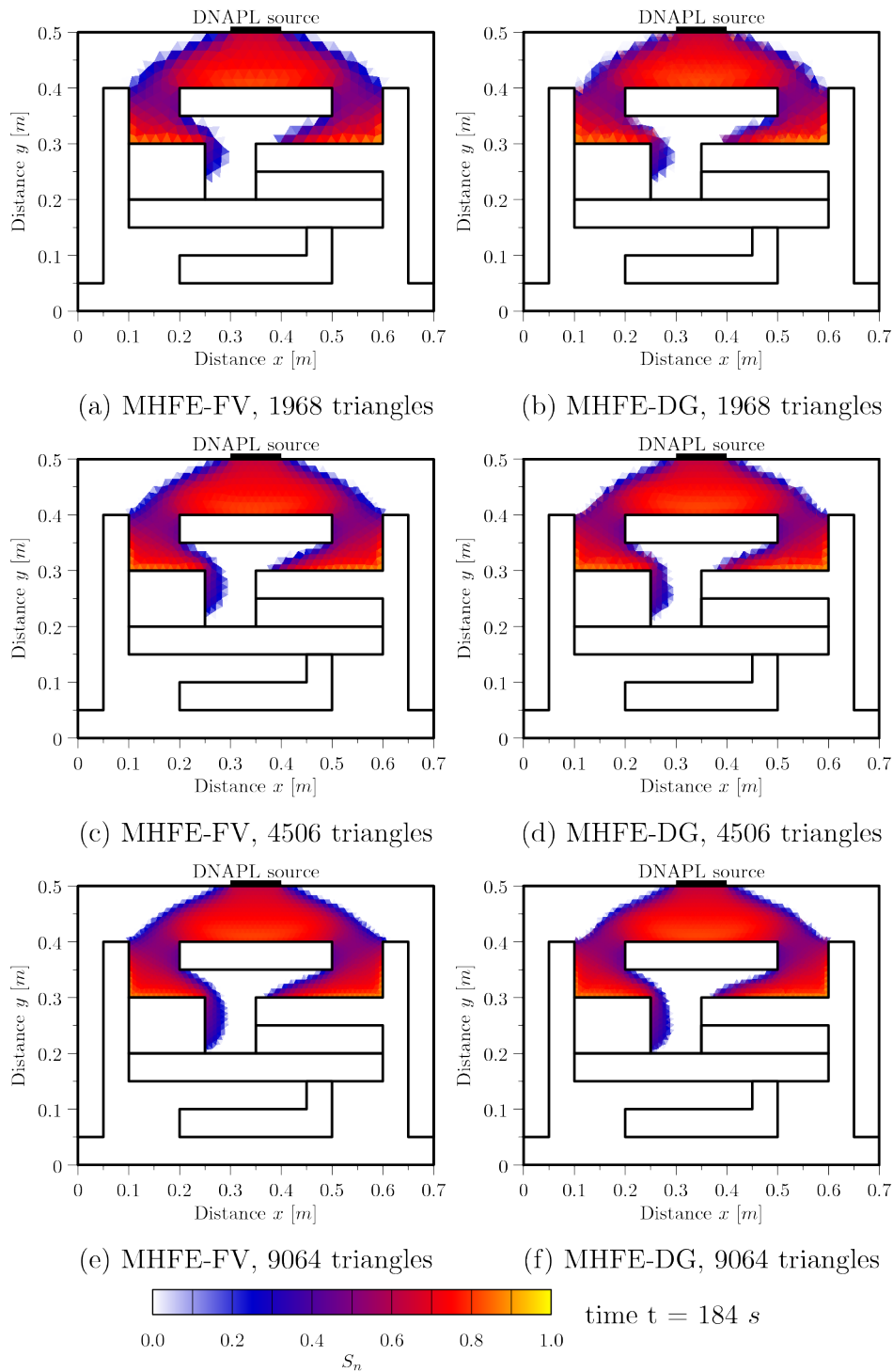


Figure 4.28.: MHFE-FV (left) and MHFE-DG (right) DNAPL saturation at $t = 184$ s for the highly heterogeneous problem on three structured meshes with 1968 triangles (a,b), 4506 triangles (c,d), and 9064 triangles (e,f).

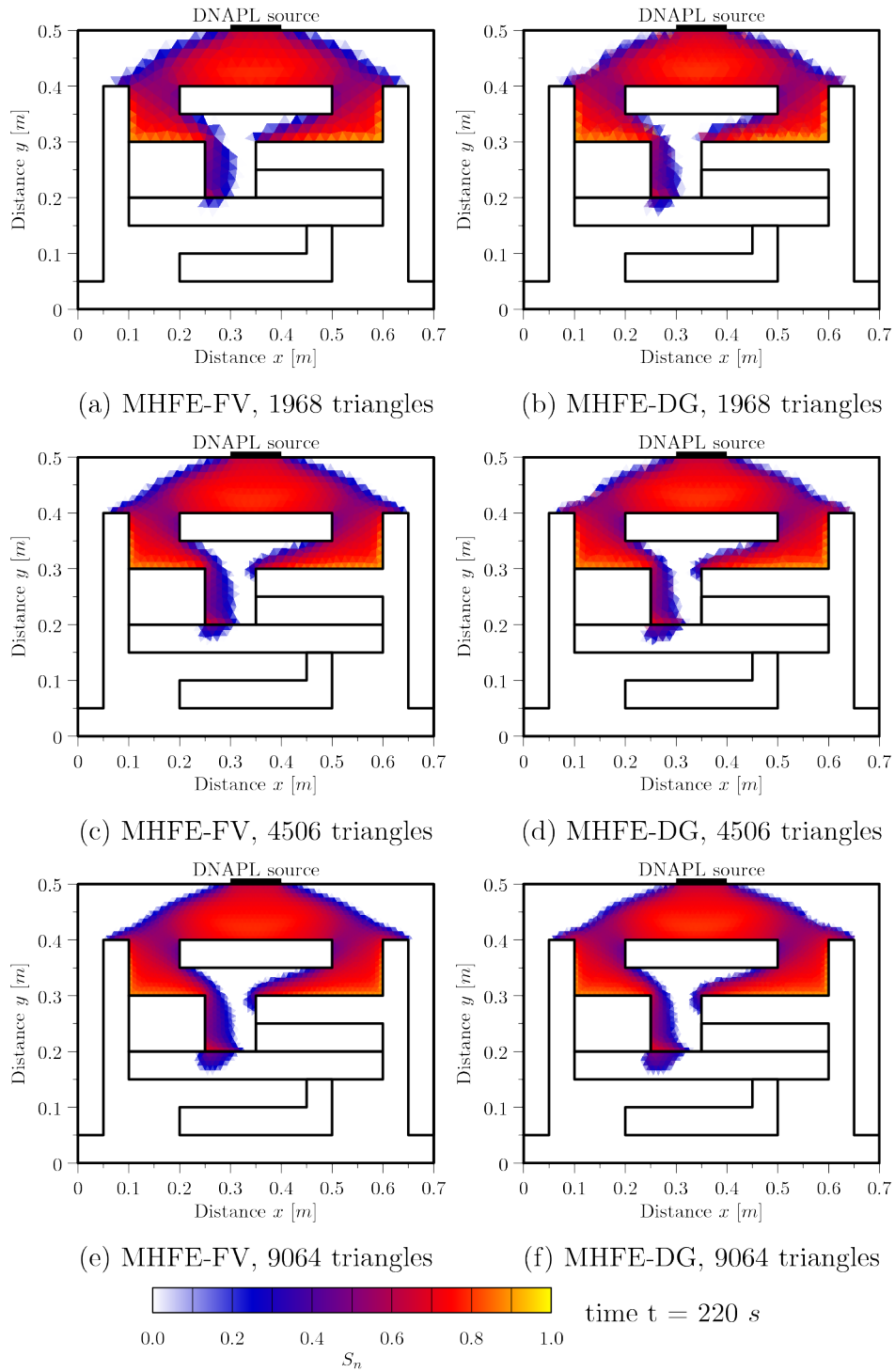


Figure 4.29.: MHFE-FV (left) and MHFE-DG (right) DNAPL saturation at $t = 220$ s for the highly heterogeneous problem on three structured meshes with 1968 triangles (a,b), 4506 triangles (c,d), and 9064 triangles (e,f).

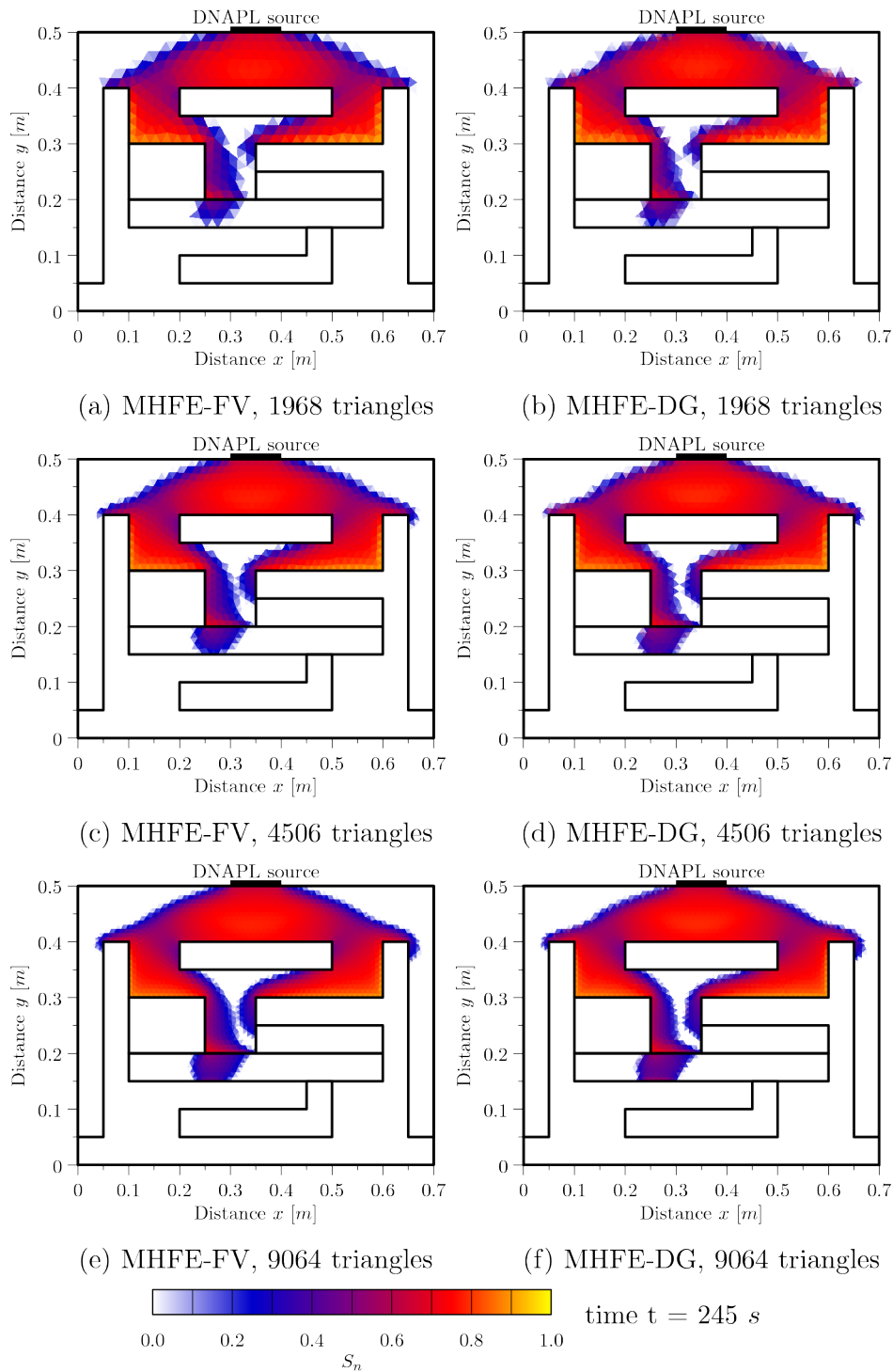


Figure 4.30.: MHFE-FV (left) and MHFE-DG (right) DNAPL saturation at $t = 245$ s for the highly heterogeneous problem on three structured meshes with 1968 triangles (a,b), 4506 triangles (c,d), and 9064 triangles (e,f).

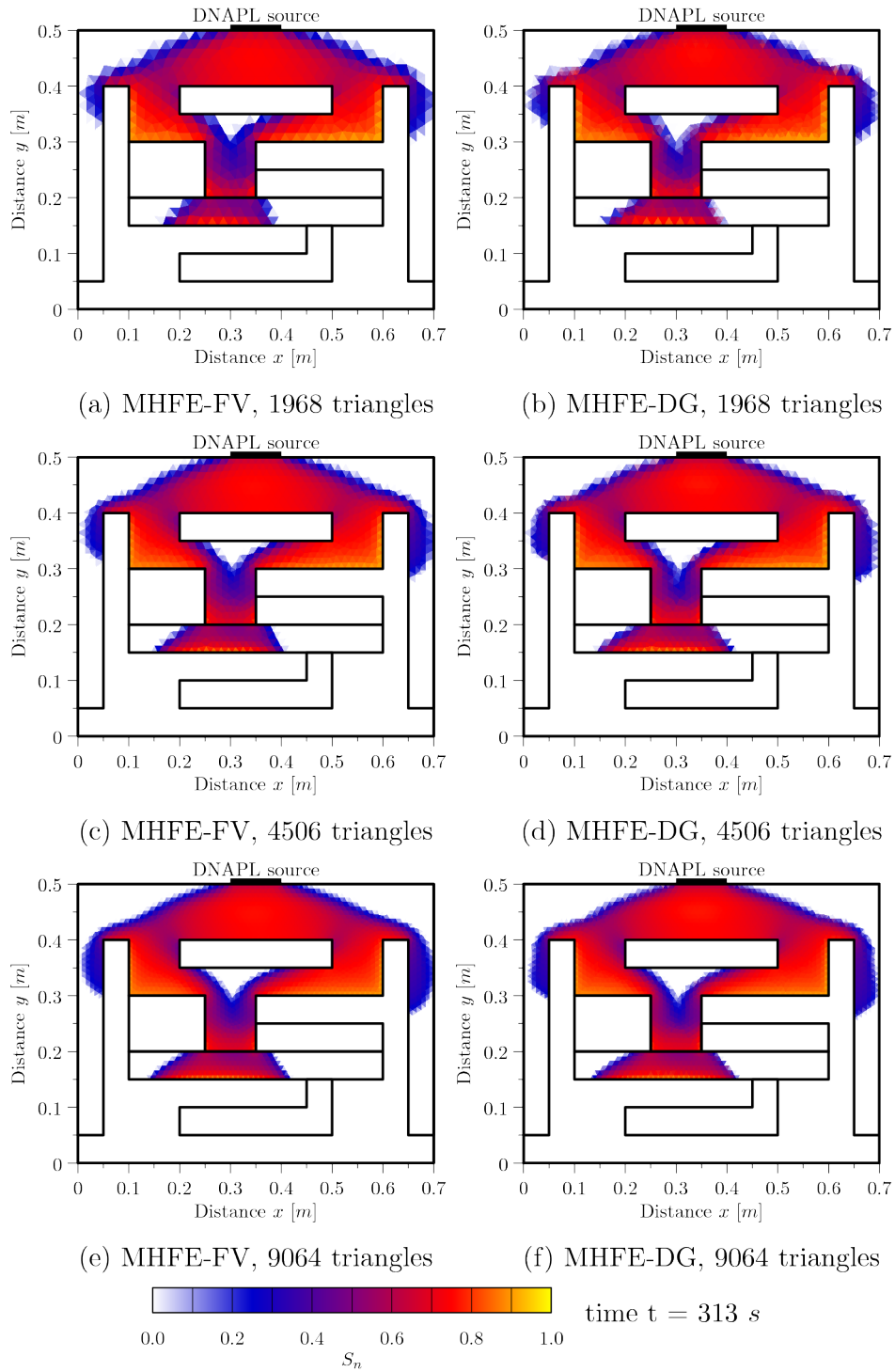


Figure 4.31.: MHFE-FV (left) and MHFE-DG (right) DNAPL saturation at $t = 313$ s for the highly heterogeneous problem on three structured meshes with 1968 triangles (a,b), 4506 triangles (c,d), and 9064 triangles (e,f).

4.4.3. Inclined Interface

In the last problem, we investigate behavior of a light non-aqueous phase liquid (LNAPL) at an inclined material interface using laboratory determined data provided by CESEP, Colorado School of Mines, Golden, Colorado, [35], [36], [37]. The experimental setup consists of a tank filled with two different sands L and M whose properties are given in Table B.8 and which is assumed as two-dimensional in this work. The geometry of a considered domain is shown in Figure 4.32a, where the LNAPL source of dimensions $1\text{ cm} \times 1\text{ cm}$ is placed in the lower part. We use a series of three meshes with an increasing number of triangles (844, 5013, and 10791) which are locally refined around the injection zone (see the coarsest mesh in Figure 4.32b). Initially, the domain was fully water-saturated and during the whole experiment, a pressure gradient between the boundaries Γ_2 and Γ_4 was maintained such that a slow flow of water persisted in the domain from the right to the left hand side of Figure 4.32). At $t = 0\text{ s}$, the LNAPL (Sudan IV dyed Soltrol 220, see Table B.1) starts to flow through the source zone with velocity $2.17 \cdot 10^{-5}\text{ m s}^{-1}$ and the injection lasts for 3.61 hours. After 3.61 hours, the injection is stopped. The boundary conditions for the MHFE-DG formulation are given as

$$S_w = 1 \quad \text{and} \quad \psi_w = 10^5 + 0.015\rho_w g \text{ Pa} \quad \text{on } \Gamma_2, \quad (4.101a)$$

$$S_w = 1 \quad \text{and} \quad \psi_w = 10^5 \text{ Pa} \quad \text{on } \Gamma_4, \quad (4.101b)$$

$$\mathbf{u}_n \cdot \mathbf{n} = 0 \quad \text{and} \quad \mathbf{u}_w \cdot \mathbf{n} = 0 \quad \text{on } \Gamma_1 \cup \Gamma_3, \quad (4.101c)$$

where \mathbf{n} denotes the outer normal to the domain boundary.

We compare the numerical results with the laboratory determined LNAPL distribution in the porous medium in Figure 4.33 at time $t = 3.5\text{ h}$. Here, the LNAPL still flows into the domain and starts to accumulate at the inclined interface of the lower permeable sand L. At $t = 24\text{ h}$ in Figure 4.34, the most of the injected LNAPL is trapped at the inclined interface and the simulated pattern resembles the experimentally determined LNAPL distribution in [37], [83].

The comparison between the MHFE-FV and the MHFE-DG method is shown in Figures 4.35 and 4.36 using contours of the numerical solutions S_n given in Figures 4.33 and 4.34, respectively. The MHFE-DG numerical solution is slightly less influenced by the numerical diffusion than the MHFE-FV solution, however, the difference is negligible. The distribution of the LNAPL saturation agrees to the results computed using the VODA numerical code in [82].

Computational times on a Dual-Core AMD Opteron™ Processor 2216 with 8 GB RAM are given in Table 4.11.

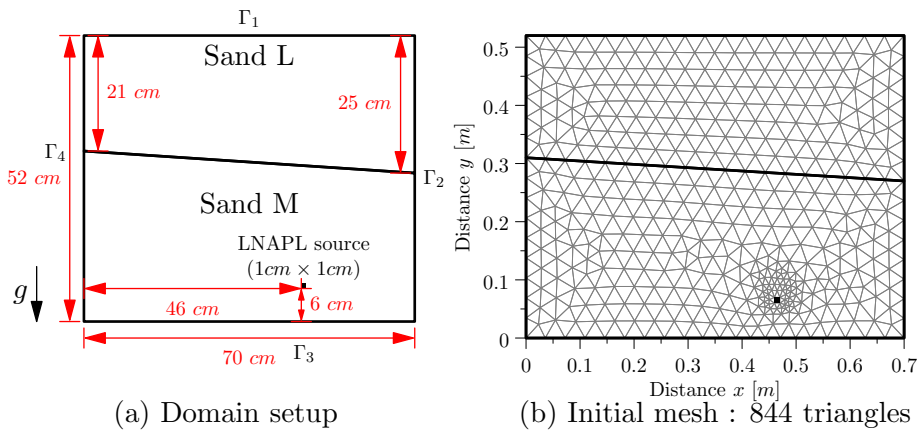


Figure 4.32.: Setup and an initial mesh for the inclined interface problem. Properties of the Sands L and M are given in Table B.8, page 127.

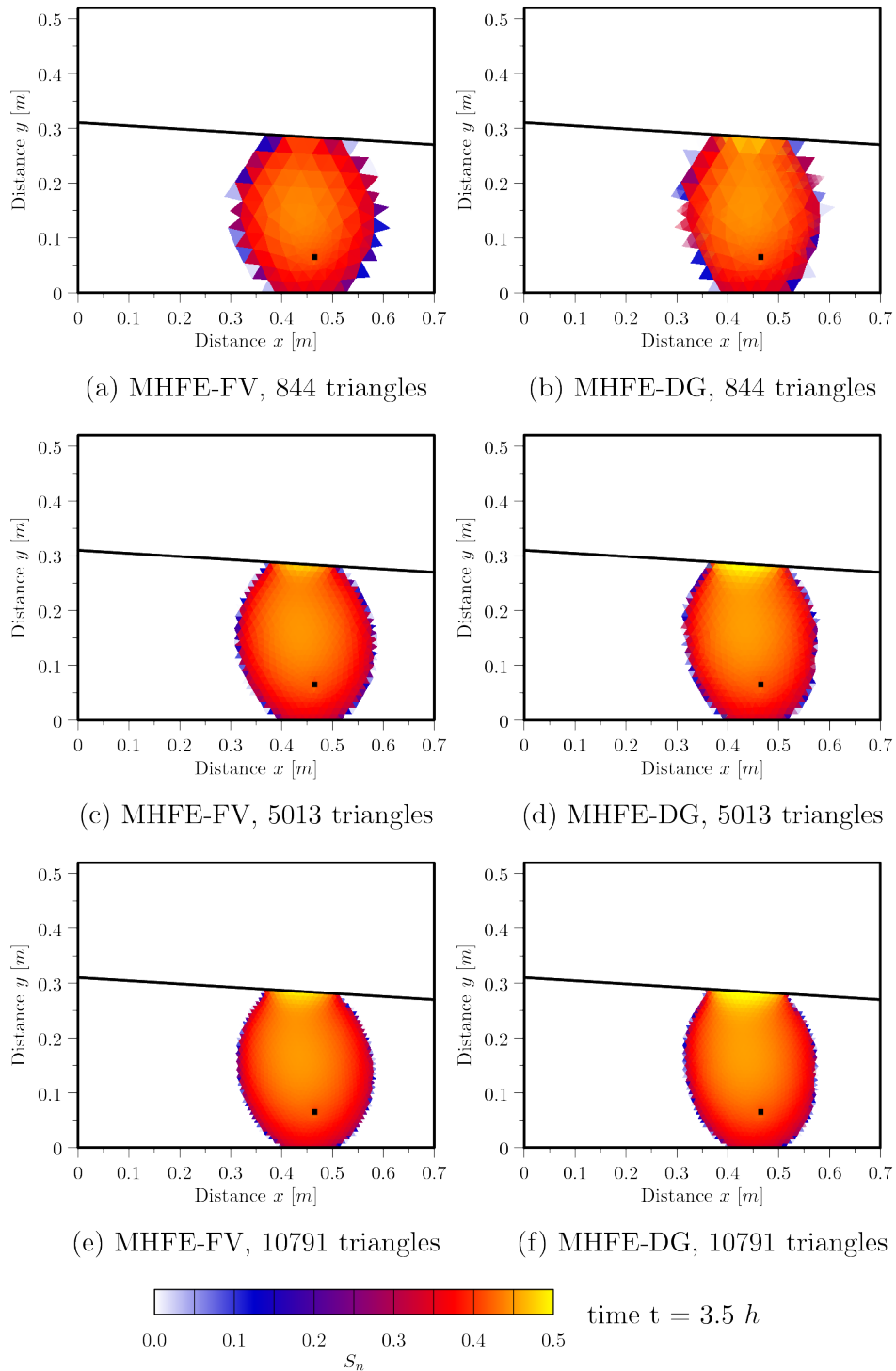


Figure 4.33.: MHFE-FV (left) and MHFE-DG (right) LNAPL saturation at $t = 3.5 h$ for the inclined interface problem.

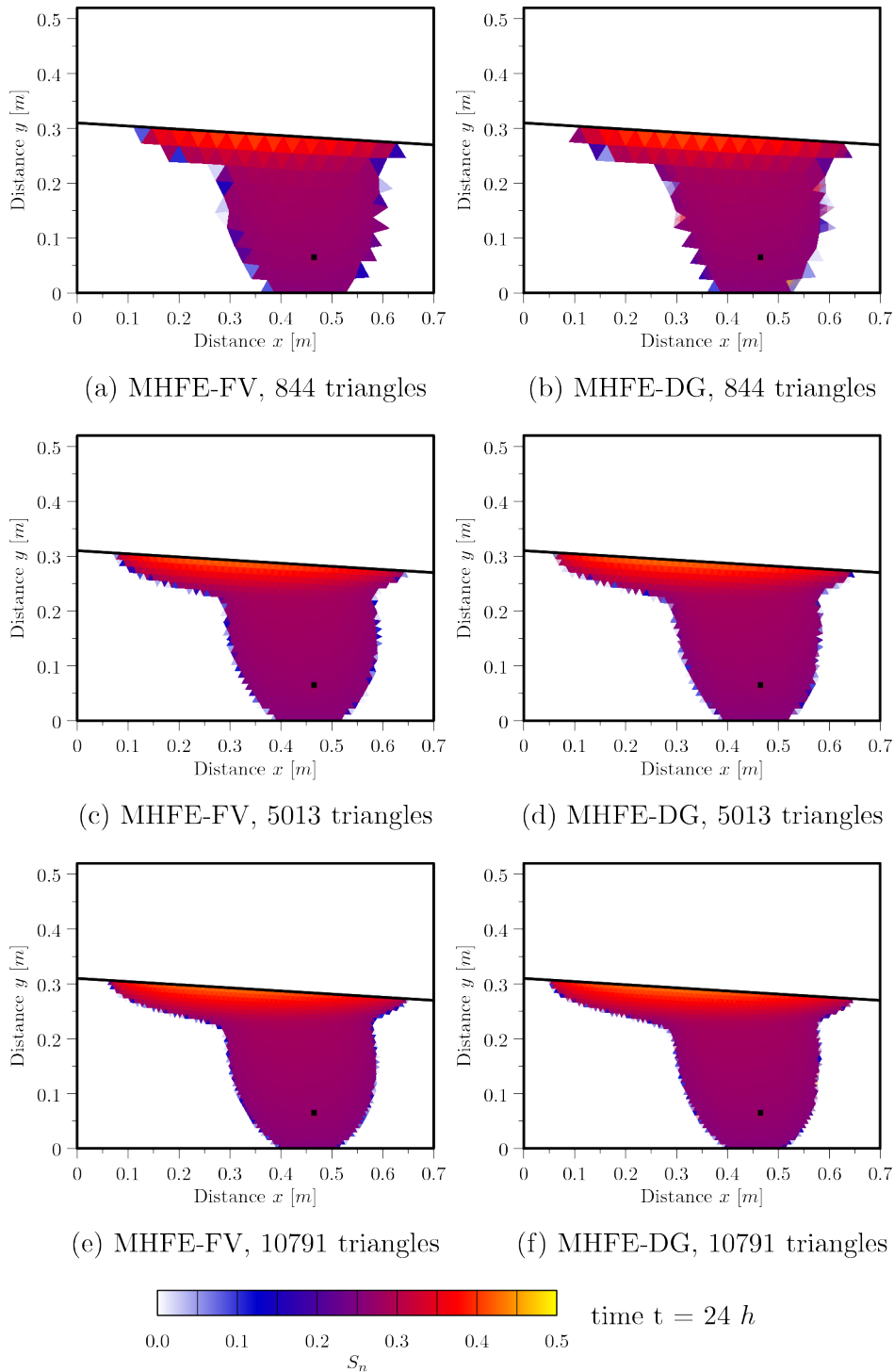


Figure 4.34.: MHFE-FV (left) and MHFE-DG (right) LNAPL saturation at $t = 24 h$ for the inclined interface problem.

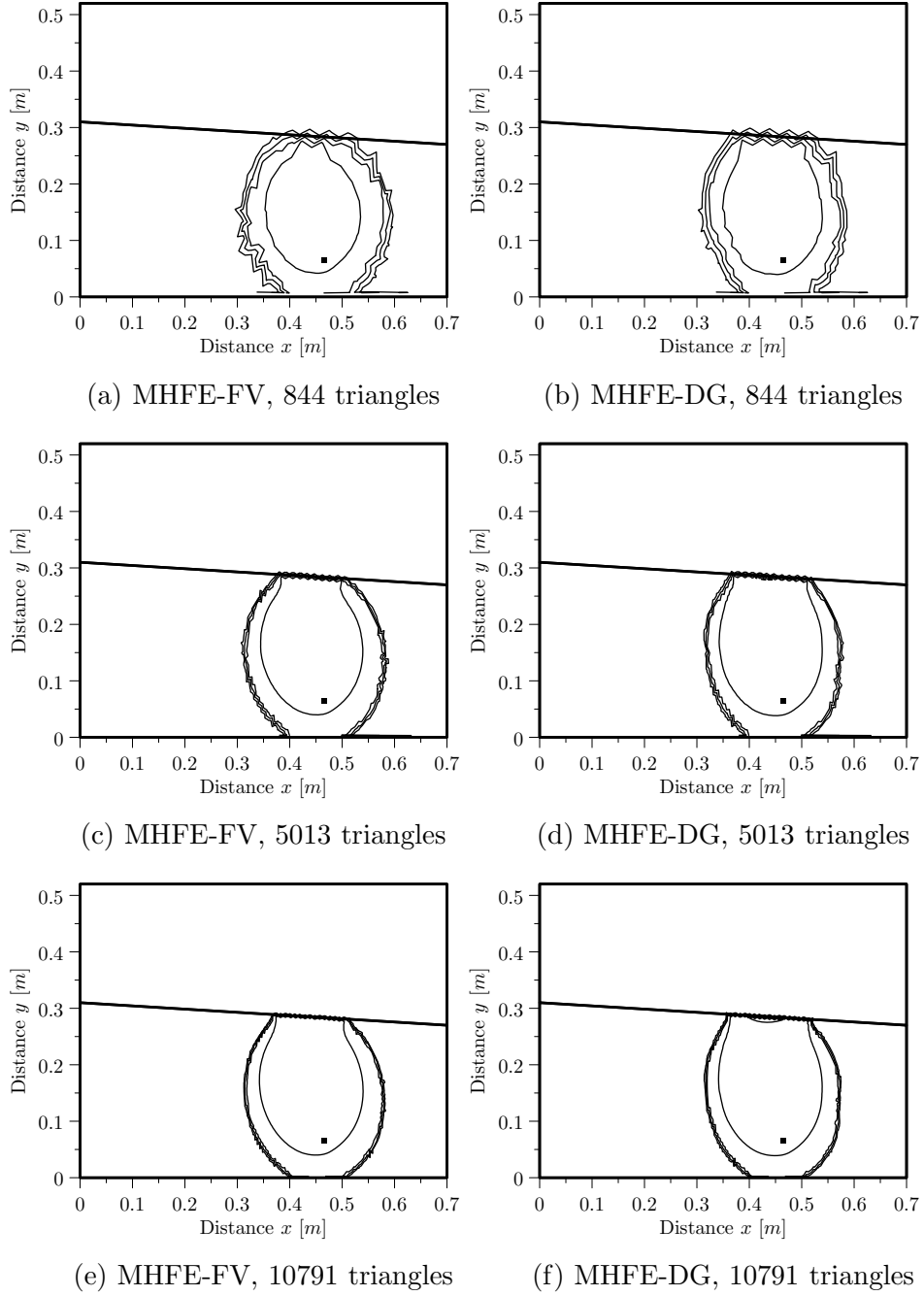


Figure 4.35.: Contours of LNAPL saturation S_n at $t = 3.5 h$ of the LNAPL contamination problem with inclined interface. Comparison between the MHFE-FV (left figures) and the MHFE-DG (right figures) approach. The contour lines spacing is 0.1 starting from $S_n = 0.1$ (the outer-most one).

Triangles	MHFE-FV	MHFE-DG
844	9 min 27 s (567 s)	9 min 35 s (575 s)
5013	2 h 4 min 0 s (7440 s)	2 h 3 min 23 s (7403 s)
10791	17 h 4 min 36 s (61476 s)	17 h 34 min 31 s (63271 s)

Table 4.11.: Computational times on a Dual-Core AMD Opteron™ Processor 2216 with 8 GB RAM: Highly heterogeneous medium (at $t = 24 h$, Figure 4.34).

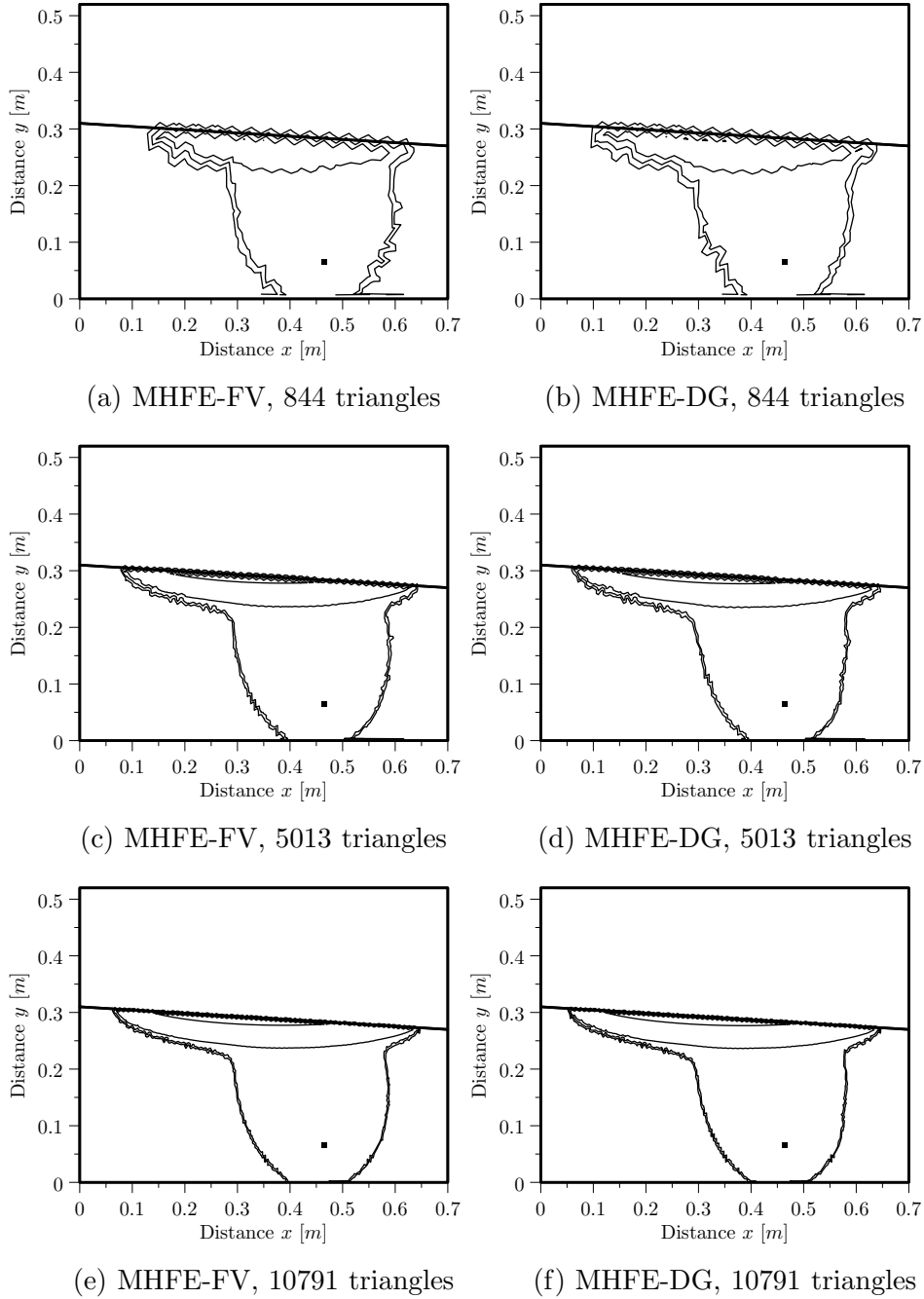


Figure 4.36.: Contours of LNAPL saturation S_n at $t = 24 h$ of the LNAPL contamination problem with inclined interface. Comparison between the MHFE-FV (left figures) and the MHFE-DG (right figures) approach. The contour lines spacing is 0.1 starting from $S_n = 0.1$ (the outer-most one).

4.5. Concluding Remarks

In this section, we summarize the key results of the MHFE-DG approach presented in this chapter. In contrast with [65], the MHFE-DG approach presented here uses a more mathematically suitable splitting of the total velocity \mathbf{u}_t described in Section 4.1 which does not produce unbounded capillary potential gradients when the medium is fully water saturated (cf. the definitions (4.3b) and (4.4) in the equation (4.15)).

Moreover, we improved the MHFE-DG approach presented in [65] when treating material discontinuities. In [65] the authors claim that no additional conditions are required at material interfaces in order to simulate barrier (NAPL pooling) effects. In order to support their statement, they used the van Duijn and de Neef semi-analytical solutions (see Section 2.4, page 30). However, this semi-analytical solution requires nonzero flux of the non-wetting phase across the material interface and, therefore, it cannot simulate the barrier effects. We succeeded to include the extended capillary pressure condition (1.37, page 17) into the formulation of the MHFE-DG method (and MHFE-FV) which allows for simulating the barrier effect observed in laboratory experiments. We presented four two-dimensional problems in heterogeneous porous materials that simulate laboratory experiments described in literature. In these simulations, we show that the barrier effect is simulated correctly and that the MHFE-DG approach gives more accurate solution than the MHFE-FV method. The difference between these approaches, in particular, can be determined on coarse meshes. The MHFE-DG method gives a slightly sharper front of the NAPL distribution when simulating the NAPL pooling at the inclined interface in the problem discussed in Section (4.4.3) whilst the amount of work required to compute the MHFE-DG solution is nearly the same as in the MHFE-FV method, cf. Table 4.11. Unlike in pure advection problems such as the Buckley and Leverett problem in Section 4.2.1, the difference between the MHFE-FV and the MHFE-DG is almost negligible when the flow is mainly driven by the capillarity.

In this thesis, we dealt with several problems related to mathematical modelling of flow of two incompressible and immiscible phases in porous media. A topic that appears recurrently in many parts is the behavior of a non-wetting phase at sharp material discontinuities. We reviewed the available theory of multiphase flow in the porous media including approaches to model capillarity on the pore-scale and macro-scale levels, respectively. We presented analytical and semi-analytical solutions that can be obtained under special conditions for both homogeneous and heterogeneous porous medium. Among these solutions, we developed the semi-analytical solution for a porous medium with a single discontinuity. Furthermore, we investigated significance of the dynamic effect in the capillary pressure-saturation relationship in the two-phase flow in layered porous materials, especially its influence on the capillary barrier effect phenomenon. Finally, we derived a higher-order numerical method for simulating two-phase flow through homogeneous and heterogeneous porous media that is capable of simulating NAPL pooling at material interfaces (the barrier effect) in one and two dimensional domains.

In Chapter 2, we summarized available closed-form solutions, where we revealed a new possibility of obtaining semi-analytical solutions for a porous medium consisting of two soils separated by a sharp interface. This result is based on the approach presented in [45], [46], and [98] that dealt with the advection-diffusion problem in a homogeneous medium. Treatment of interfaces in a heterogeneous medium follows the formulation in [28], [98] and [99] was limited to the diffusion case only. Our approach allows consideration of diffusion together with advection. There are many situations in two-phase flow where both advection and diffusion terms have to be considered. The solution is obtained by an iterative procedure adjusting the flows in both homogeneous subdomains to reach the required condition at the interface. This solution serves as a benchmark solution to verify convergence of numerical schemes.

In Chapter 3, we investigate implications of the dynamic effect in the capillary pressure-saturation relationship on flow in heterogeneous porous medium. Dynamic effects have been observed in laboratory experiments in homogeneous porous material held in CESEP, Colorado School of Mines, and in other laboratories as well, however, none of these experiments involved discontinuities in the porous materials. Therefore, we have developed a numerical model based on the vertex-centered finite volume method (VCFVM) capable of simulating flow of two immiscible and incompressible phases in heterogeneous porous materials under dynamic conditions. The numerical scheme is verified and its order of convergence is estimated using the semi-analytical solutions for homogeneous and heterogeneous porous medium, respectively. The results show that the use of various functional models (e.g., constant, linear, or exponential) of the dynamic effect coefficient $\tau = \tau(S_w)$ may substantially influence the propagation speed of the front as well as the accumulation time of the non-wetting phase at material interfaces. Laboratory measured parameters were used in the numerical simulation to show that the dynamic effect

has a significant impact on the magnitude of the capillary pressure while the change in the saturation profiles may be considered negligible in some cases. The constant model of τ showed rather unrealistic profile of the numerical approximation of the capillary pressure when compared to the laboratory measured data. Results of the simulation indicate that the dynamic effect may not be so important in drainage problems in a homogeneous porous medium, but, it may be important in heterogeneous media where the capillarity governs flow across material interfaces. The linear model of τ accelerates flow of air across the interface for both configurations of the coarse and fine porous media, when the ratio between entry pressures of the media is close to 1. In all other cases, the use of the dynamic effect seems to increase the time needed for the non-wetting fluid to accumulate at a finer sand interface (delay due to barrier effect). This suggests that without dynamic effects, the travel time of the non-wetting phase can be possibly estimated to be smaller or larger than the actual time. The conclusion can be settled by laboratory experiment only.

In the final part of the dissertation thesis, we used the mixed-hybrid finite element (MHFE) method together with the discontinuous Galerkin (DG) approach to develop a higher-order numerical scheme capable of simulating flow of two immiscible and incompressible fluids in heterogeneous porous materials in one- and two-dimensional domains. As in the case of VCFVM, we used the benchmark solutions to investigate its convergence towards the exact solution. In case of the pure hyperbolic benchmark problem in 1D, we show that the MHFE-FV and MHFE-DG approach involves substantially less numerical diffusion than the VCFVM. In case of heterogeneous porous materials, we used example problems from literature to show that the behavior of the non-wetting phase at material discontinuities is treated correctly and that the numerical scheme is capable of simulating the barrier effect. Therefore, we extended the approach described in [65] so that the barrier effect can be simulated. In two dimensions, we used the MHFE-DG method to simulate two benchmark problems described in literature and showed a good agreement with the published numerical and experimental results. Finally, we simulated a laboratory experiment involving light non-aqueous phase liquid (LNAPL) in a layered porous medium with an inclined material interface. A good match between the numerical and laboratory determined results was observed. Altogether, we showed that the MHFE-DG method gives more accurate results than the MHFE-FV method in case of advection-dominated flow. However, both MHFE-FV and MHFE-DG methods give similar results in all capillarity-driven problems that were considered in this thesis. This indicates that the use of the considered higher-order discontinuous Galerkin approach together with the mixed-hybrid finite element (MHFE-DG) method instead of the finite volume method (MHFE-FV) does not improve significantly the accuracy of the numerical approximation when the capillarity dominates.

APPENDIX A

PIECEWISE LINEAR BASIS FUNCTIONS

In this section we describe the piecewise linear basis functions of $D_1(\mathcal{K}_h)$ used in Chapter 4.

A.1. Piecewise Linear Basis Functions in 1D

In \mathbb{R}^1 , the explicit formulae for the basis functions $\varphi_{K,E}$ for all $x \in K = [V_A, V_B]$ are given as

$$\varphi_{K,V_A} = \frac{V_B - x}{V_B - V_A}, \quad (\text{A.1a})$$

$$\varphi_{K,V_B} = \frac{x - V_A}{V_B - V_A}, \quad (\text{A.1b})$$

where $V_A, V_B \in \mathcal{E}_K = \mathcal{V}_K$, $V_A < V_B$. Therefore, the coefficient $S_{w,K,E}$ in (4.68) represents the value of the wetting phase saturation at $V_E \in \mathcal{E}_K = \mathcal{V}_K$ with respect to K . Together with the explicit formulae (4.11) for the basis functions of $\mathbf{RT}_0(K)$, the coefficients (4.71a) are given for all $E, F \in \{A, B\}$ as

$$B_{K,V_E,V_F} = \frac{1}{6}(1 + \delta_{EF})(V_B - V_A) \quad (\text{A.2})$$

and the inverse matrix $\mathbf{b}_K = \mathbf{B}_K^{-1}$ can be easily expressed as

$$b_{K,V_E,V_F} = \frac{2}{V_B - V_A}(3\delta_{EF} - 1). \quad (\text{A.3})$$

Finally, the coefficient $I_{K,H,E,F}$ defined by (4.78) yields

$$I_{K,H,E,F} = \delta_{EH}\delta_{FH}. \quad (\text{A.4})$$

A.2. Piecewise Linear Basis Functions in 2D

In \mathbb{R}^2 , we use the same notation as in (4.13), i.e., $\mathbf{V}_E \in \mathcal{V}_K$ always denotes the opposite vertex to side $E \in \mathcal{E}_K$. The basis functions $\varphi_{K,E}$ read as

$$\varphi_{K,E} = C_{E,0} + C_{E,1} [\mathbf{x}]_1 + C_{E,2} [\mathbf{x}]_2, \quad (\text{A.5})$$

where the coefficients $\{C_{E,k}\}_{k=0,1,2}$, are for all $E \in \mathcal{E}_K$ given by the following system of linear equations to satisfy (4.69):

$$\varphi_{K,E}(\mathbf{V}_E) = C_{E,0} + C_{E,1} [\mathbf{V}_E]_1 + C_{E,2} [\mathbf{V}_E]_2 = -1, \quad (\text{A.6a})$$

$$\varphi_{K,E}(\mathbf{V}_F) = C_{E,0} + C_{E,1} [\mathbf{V}_F]_1 + C_{E,2} [\mathbf{V}_F]_2 = 1, \quad (\text{A.6b})$$

$$\varphi_{K,E}(\mathbf{V}_G) = C_{E,0} + C_{E,1} [\mathbf{V}_G]_1 + C_{E,2} [\mathbf{V}_G]_2 = 1, \quad (\text{A.6c})$$

where $\mathcal{V}_K = \{\mathbf{V}_E, \mathbf{V}_F, \mathbf{V}_G\}$ and $\mathcal{E}_K = \{E, F, G\}$. The coefficient $S_{w,K,E}$ in (4.68) represents the average value of the wetting phase saturation over $E \in \mathcal{E}_K$ with respect to K and it can be also interpreted as the value of S_w in the midpoint of E .

Combining (A.5) and the explicit formulae (4.13) for the basis functions of $\mathbf{RT}_0(K)$, we obtain the coefficients (4.71a) for all $E, F, G \in \mathcal{E}_K$ in the form

$$B_{K,E,F} = \frac{1}{3} \delta_{EF} |K|_2 \quad (\text{A.7})$$

and the inverse matrix $\mathbf{b}_K = \mathbf{B}_K^{-1}$ reads as

$$b_{K,E,F} = \frac{3}{|K|_2} \delta_{EF}. \quad (\text{A.8})$$

Finally, the integration of the coefficient $I_{K,H,E,F}$ defined by (4.78) reveals that

$$I_{K,H,E,F} = \delta_{EH} \delta_{FH} + \frac{1}{3} (1 - \delta_{EH})(1 - \delta_{FH})(2\delta_{EF} - 1). \quad (\text{A.9})$$

APPENDIX B

FLUID AND MATERIAL PROPERTIES

B.1. Fluids

Property	Density (at 20°C) ρ [kg m ⁻³]	Dynamic viscosity μ [kg m ⁻¹ s ⁻¹]
Water ¹	997.78	$9.772 \cdot 10^{-4}$
Air ¹	1.20470	$1.8205 \cdot 10^{-5}$
NAPL A ²	1400	$1 \cdot 10^{-3}$
Sudan IV dyed Soltrol 220 ¹	836	$3.6 \cdot 10^{-3}$
Tetrachlorethylene PCE ¹	1623	$8.9 \cdot 10^{-4}$
Trichlorethylene TCE ¹	1460	$9 \cdot 10^{-4}$

¹ Provided by CESEP, Colorado School of Mines, Colorado.

² Taken over from [57].

Table B.1.: Fluid properties used in this thesis.

B.2. Sand A

Property			Sand A
CESEP label			Ohji sand (field sand)
Cycle			drainage
Porosity	Φ	[-]	0.448
Intrinsic permeability	K	$[m^2]$	$1.631 \cdot 10^{-11}$
Residual saturation	S_{wr}	[-]	0.265
Brooks and Corey param.	λ	[-]	4.660
Brooks and Corey param.	p_d	$[Pa]$	3450.18
van Genuchten parameter	n	[-]	n/a
van Genuchten parameter	α	$[Pa^{-1}]$	n/a
Stauffer model τ	τ_S	$[kg\ m^{-1}\ s^{-1}]$	$\tau_{S,A} = 3.3 \cdot 10^5$
Constant model τ	τ_{const}	$[kg\ m^{-1}\ s^{-1}]$	$\tau_{const,A}(S_w) = 1.1 \cdot 10^6$
Linear model τ	τ_{lin}	$[kg\ m^{-1}\ s^{-1}]$	$\tau_{lin,A}(S_w) = 2 \cdot 10^6(1 - S_w)$
Exponential model τ	τ_{exp}	$[kg\ m^{-1}\ s^{-1}]$	$\tau_{exp,A}(S_w) = 10^8 \exp(-7.7S_w)$
			

Table B.2.: Properties of a field sand from Ohji site, Tokyo, denoted as Sand A. Samples provided by CESEP, Colorado School of Mines, Colorado.

B.3. Sand B

Property			Sand B	
CESEP label			Sand #70 (silica sand)	
Cycle			drainage	wetting
Porosity	Φ	[-]	0.418	
Intrinsic permeability	K	$[m^2]$	$1.437 \cdot 10^{-11}$	
Residual saturation	S_{wr}	[-]	0.037	
Brooks and Corey param.	λ	[-]	5.323	2.793
Brooks and Corey param.	p_d	$[Pa]$	4041.72	2501.55
van Genuchten parameter	n	[-]	11.53	5.28
van Genuchten parameter	α	$[Pa^{-1}]$	$2.14 \cdot 10^{-4}$	$3.24 \cdot 10^{-4}$
Stauffer model τ	τ_S	$[kg\ m^{-1}\ s^{-1}]$	$\tau_{S,B} = 4.85 \cdot 10^5$	
Constant model τ	τ_{const}	$[kg\ m^{-1}\ s^{-1}]$	$\tau_{const,B} = \frac{\tau_{S,B}}{\tau_{S,A}} \tau_{const,A}$	
Linear model τ	τ_{lin}	$[kg\ m^{-1}\ s^{-1}]$	$\tau_{lin,B} = \frac{\tau_{S,B}}{\tau_{S,A}} \tau_{lin,A}$	
Exponential model τ	τ_{exp}	$[kg\ m^{-1}\ s^{-1}]$	$\tau_{exp,B} = \frac{\tau_{S,B}}{\tau_{S,A}} \tau_{exp,A}$	
				

Table B.3.: Properties of a silica sand #70 denoted as Sand B. Samples provided by CESEP, Colorado School of Mines, Colorado.

B.4. Sand C

Property			Sand C	
CESEP label			Sand #110 (silica sand)	
Cycle			drainage	wetting
Porosity	Φ	[-]	0.343	
Intrinsic permeability	K	$[m^2]$	$5.168 \cdot 10^{-12}$	
Residual saturation	S_{wr}	[-]	0.040	
Brooks and Corey param.	λ	[-]	5.408	2.857
Brooks and Corey param.	p_d	$[Pa]$	8027.52	4605.80
van Genuchten parameter	n	[-]	12.49	6.64
van Genuchten parameter	α	$[Pa^{-1}]$	$1.08 \cdot 10^{-4}$	$1.71 \cdot 10^{-4}$
Stauffer model τ	τ_S	$[kg\ m^{-1}\ s^{-1}]$	$\tau_{S,C} = 4.25 \cdot 10^6$	
Constant model τ	τ_{const}	$[kg\ m^{-1}\ s^{-1}]$	$\tau_{const,C} = \frac{\tau_{S,C}}{\tau_{S,A}} \tau_{const,A}$	
Linear model τ	τ_{lin}	$[kg\ m^{-1}\ s^{-1}]$	$\tau_{lin,C} = \frac{\tau_{S,C}}{\tau_{S,A}} \tau_{lin,A}$	
Exponential model τ	τ_{exp}	$[kg\ m^{-1}\ s^{-1}]$	$\tau_{exp,C} = \frac{\tau_{S,C}}{\tau_{S,A}} \tau_{exp,A}$	
				

Table B.4.: Properties of a silica sand #110 denoted as Sand C. Samples provided by CESEP, Colorado School of Mines, Colorado.

B.5. Sands D and E

Property			Sand D	Sand E
Original label in [57, page 277]			Sand I	Sand II
Porosity	Φ	[-]	0.40	0.39
Intrinsic permeability	K	[m^2]	$5.04 \cdot 10^{-10}$	$5.26 \cdot 10^{-11}$
Residual saturation	S_{wr}	[-]	0.08	0.10
Pore size distribution index	λ	[-]	3.86	2.49
Entry pressure	p_d	[Pa]	370	1324

Table B.5.: Properties of the sands used in Benchmark Problem VI taken over from [57, page 277].

B.6. Sands F and G

Property			Sand F	Sand G ₁	Sand G ₂
Original label in [57] ([3])			Sand 1 (matrix)	Sand 2 (lens)	
Porosity	Φ	[-]	0.40	0.39	
Intrinsic permeability	K	[m^2]	$6.64 \cdot 10^{-11}$	$3.32 \cdot 10^{-12}$	
Residual saturation	S_{wr}	[-]	0.10	0.12	
Pore size distribution index	λ	[-]	2.7	2.0	
Entry pressure	p_d	[Pa]	755	1163.5	1466.1

Table B.6.: Properties of the sands used in numerical simulations in Section 4.4.1, taken over from [57, page 300] and [3, page 26].

B.7. Sands H, I, J, and K

Property			Sand H	Sand I
Original label in [57]			Sand 1	Sand 2
Porosity	Φ	[-]	0.40	0.39
Intrinsic permeability	K	[m^2]	$5.041 \cdot 10^{-10}$	$2.051 \cdot 10^{-10}$
Residual saturation	S_{wr}	[-]	0.078	0.069
Pore size distribution index	λ	[-]	3.86	3.51
Entry pressure	p_d	[Pa]	369.73	434.45
Property			Sand J	Sand K
Original label in [57]			Sand 3	Sand 4
Porosity	Φ	[-]	0.39	0.41
Intrinsic permeability	K	[m^2]	$5.621 \cdot 10^{-11}$	$8.191 \cdot 10^{-12}$
Residual saturation	S_{wr}	[-]	0.098	0.189
Pore size distribution index	λ	[-]	2.49	3.30
Entry pressure	p_d	[Pa]	1323.95	3246.15

Table B.7.: Properties of the sands used in numerical simulations in Section 4.4.2, taken over from [57, page 308].

B.8. Sand L and M

Property			Sand L	Sand M
CESEP label			Sand #70 (silica sand)	Sand #30 (silica sand)
Cycle			drainage	drainage
Porosity	Φ	[-]	0.444	0.443
Intrinsic permeability	K	$[m^2]$	$2.18 \cdot 10^{-11}$	$1.75 \cdot 10^{-10}$
Residual saturation	S_{wr}	[-]	0.088	0.073
Residual saturation	S_{nr}	[-]	0.117	0.17
Brooks and Corey param.	λ	[-]	5.32	3.78
Brooks and Corey param.	p_d	$[Pa]$	4042	1633
				

Table B.8.: Properties of the silica sands #30 and #70 denoted as Sand L and Sand M, respectively, and used in numerical simulations in Section 4.4.3. Samples provided by CESEP, Colorado School of Mines, Colorado.

A

- [1] D. N. ARNOLD AND J. DOUGLAS JR, *Superconvergence of a Finite Element Approximation to the Solution of a Sobolev Equation in a Single Space Variable*, Mathematics of Computation, 36 (1981), pp. 53–63.

B

- [2] P. BASTIAN, *Numerical Computation of Multiphase Flows in Porous Media*, Habilitation Thesis, Kiel university, (1999).
- [3] P. BASTIAN AND R. HELMIG, *Efficient Fully-Coupled Solution Techniques for Two-Phase Flow in Porous Media*, Advances in Water Resources, 23 (1999), pp. 199–216.
- [4] P. BASTIAN AND B. RIVIÈRE, *Discontinuous Galerkin Methods for Two-Phase Flow in Porous Media*, Tech. Rep. 2004-28, University of Heidelberg, 2004.
- [5] J. BEAR AND A. VERRUIJT, *Modeling Groundwater Flow and Pollution*, D. Reidel, Holland, Dordrecht, 1990.
- [6] A. Y. BELIAEV AND S. M. HASSANIZADEH, *A Theoretical Model of Hysteresis and Dynamic Effects in the Capillary Relation for Two-phase Flow in Porous Media*, Transport in Porous Media, 43 (2001), pp. 487–510.
- [7] A. Y. BELIAEV AND R. J. SCHOTTING, *Analysis of a New Model for Unsaturated Flow in Porous Media Including Hysteresis and Dynamic Effects*, Computational Geosciences, 5 (2002), pp. 345–368.
- [8] M. BENEŠ, FUČÍK, J. MIKYŠKA, AND T. H. ILLANGASEKARE, *Analytical and Numerical Solution for One-Dimensional Two-Phase Flow in Homogeneous Porous Medium*, in Proceedings of the 2nd International Conference on Porous Media and its Applications in Science and Engineering ICPM2, K. Vafai, ed., Engineering Conferences International, 2007, pp. CD-ROM.
- [9] M. BENEŠ, R. FUČÍK, J. MIKYŠKA, AND T. H. ILLANGASEKARE, *Analytical and Numerical Solution for One-Dimensional Two-Phase Flow in Homogeneous Porous Medium*, Journal of Porous Media, 12 (2009), pp. 1139–1152.

- [10] R. H. BROOKS AND A. T. COREY, *Hydraulic Properties of Porous Media*, Hydrology Paper 3, 27 (1964).
- [11] S. E. BUCKLEY AND M. C. LEVERETT, *Mechanism of Fluid Displacement in Sands*, Trans. AIME, 146 (1942), pp. 107–116.
- [12] N. T. BURDINE, *Relative Permeability Calculations from Pore-Size Distribution Data*, Trans. AIME, 198 (1953), pp. 71–78.
- [13] N. T. BURDINE, L. S. GOURNAY, AND P. P. REICHERTZ, *Pore Size Distribution Of Petroleum Reservoir Rocks*, Transactions of the American Institute of Mining, Metallurgical and Petroleum Engineers, (1950), p. 195.

C

- [14] D. M. O'CARROLL, T. J. PHELAN, AND L. M. ABRIOLA, *Exploring Dynamic Effects in Capillary Pressure in Multistep Outflow Experiments*, Water Resources Research, 41 (2005).
- [15] G. CHAVENT AND J. JAFFRÉ, *Mathematical Models and Finite Elements for Reservoir Simulation.*, North-Holland: Amsterdam, 1986.
- [16] I. CHEDDADI, R. FUČÍK, M. PRIETO, AND M. VOHRALÍK, *Guaranteed and Robust A Posteriori Error Estimates For Singularly Perturbed Reaction–Diffusion Problems*, ESAIM: Mathematical Modelling and Numerical Analysis, 43 (2009), pp. 867–888.
- [17] I. CHEDDADI, R. FUČÍK, M. I. PRIETO, AND M. VOHRALÍK, *Computable a Posteriori Error Estimates in the Finite Element Method Based on its Local Conservativity: Improvements Using Local Minimization*, in ESAIM: Proc, vol. 24, 2008, pp. 77–96.
- [18] Z.-X. CHEN, G. S. BODVARSSON, AND P. A. WITHERSPOON, *Comment on 'exact integral solutions for two-phase flow'*, Water Resources Research, 28 (1992), pp. 1477–1478.
- [19] R. E. COLLINS, *Flow of Fluids through Porous Materials*, The Petroleum Publishing Company, Tulsa, 1976.
- [20] A. T. COREY, *Mechanics of Immiscible Fluids in Porous Media*, Water Resources Publication, 1994.
- [21] C. CUESTA, C. J. VAN DUIJN, AND J. HULSHOF, *Infiltration in Porous Media with Dynamic Capillary Pressure: Travelling Waves*, European Journal of Applied Mathematics, 11 (2000), pp. 381–397.

D

- [22] H. K. DAHLE, M. A. CELIA, AND M. S. HASSANIZADEH, *Bundle-of-Tubes Model for Calculating Dynamic Effects in the Capillary-Pressure-Saturation Relationship*, Transport in Porous Media, 58 (2005), pp. 5–22.
- [23] H. DARCY, *Les fontaines publiques de la ville de Dijon*, Victor Dalmont, 1856.
- [24] T. A. DAVIS, *A Column Pre-Ordering Strategy for the Unsymmetric-Pattern Multifrontal Method*, ACM Transactions on Mathematical Software, 30 (2004), pp. 165–195.

-
- [25] ———, *Algorithm 832: UMFPACK, An Unsymmetric-Pattern Multifrontal Method*, ACM Transactions on Mathematical Software, 30 (2004), pp. 196–199.
- [26] T. A. DAVIS AND I. S. DUFF, *An Unsymmetric-Pattern Multifrontal Method for Sparse LU Factorization*, SIAM Journal on Matrix Analysis and Applications, 18 (1997), pp. 140–158.
- [27] ———, *A Combined Unifrontal/Multifrontal Method for Unsymmetric Sparse Matrices*, ACM Transactions on Mathematical Software, 25 (1999), pp. 1–19.
- [28] C. J. VAN DUIJN AND M. J. DE NEEF, *Self-Similar Profiles for Capillary Diffusion Driven Flow in Heterogeneous Porous Media*, Centrum voor Wiskunde en Informatica, 1996.
- [29] ———, *Similarity Solution for Capillary Redistribution of Two Phases in a Porous Medium with a Single Discontinuity*, Advances in Water Resources, 21 (1998), pp. 451–461.
- [30] C. J. VAN DUIJN, J. MOLENAAR, AND M. J. DE NEEF, *The Effect of Capillary Forces on Immiscible Two-Phase Flow in Heterogeneous Porous Media*, Transport in Porous Media, 21 (1995), pp. 71–93.
- [31] C. J. VAN DUIJN, L. A. PELETIER, AND I. S. POP, *A New Class of Entropy Solutions of the Buckley-Leverett Equation*, Journal on Mathematical Analysis, 39 (2007), p. 507.
- [32] L. J. DURLOFSKY, *A Triangle Based Mixed Finite Element–Finite Volume Technique for Modeling Two Phase Flow through Porous Media*, Journal of Computational Physics, 105 (1993), pp. 252–266.

E

- [33] Y. EPSHTEYN AND B. RIVIÈRE, *Fully Implicit Discontinuous Finite Element Methods for Two-Phase Flow*, Applied Numerical Mathematics, 57 (2007), pp. 383–401.
- [34] R. EWING, *The Approximation of Certain Parabolic Equations Backward in Time by Sobolev Equations*, SIAM Journal on Mathematical Analysis, 6 (1975), p. 283.

F

- [35] F. FAGERLUND, T. H. ILLANGASEKARE, AND A. NIEMI, *Nonaqueous-Phase Liquid Infiltration and Immobilization in Heterogeneous Media: 1. Experimental Methods and Two-Layered Reference Case*, Vadose Zone Journal, 6 (2007), p. 471.
- [36] ———, *Nonaqueous-Phase Liquid Infiltration and Immobilization in Heterogeneous Media: 2. Application to Stochastically Heterogeneous Formations*, Vadose Zone Journal, 6 (2007), p. 483.
- [37] F. FAGERLUND, A. NIEMI, AND T. H. ILLANGASEKARE, *Modeling of Nonaqueous Phase Liquid (NAPL) Migration in Heterogeneous Saturated Media: Effects of Hysteresis and Fluid Immobility in Constitutive Relations (DOI 10.1029/2007WR005974)*, Water Resources Research, 44 (2008), p. 3409.
- [38] R. FUČÍK, *Online Implementation of the Fučík Semi-Analytical Solution in Porous Medium with a Single Discontinuity*. <http://mmg.fjfi.cvut.cz/~fucik/hetero>.

- [39] —, *Online Implementation of the McWhorter and Sunada Semi-Analytical Solution*. <http://mmg.fjfi.cvut.cz/~fucik/mcwhorter>.
- [40] —, *Numerical Solution of Multiphase Porous Media Flow, Research Work*, FNSPE of Czech Technical University in Prague, Prague, 2004.
- [41] —, *Numerical Analysis of Multiphase Porous Media Flow, Research Project*, FNSPE of Czech Technical University Prague, Prague, 2005.
- [42] —, *Numerical Analysis of Multiphase Porous Media Flow in Groundwater Contamination Problems, Graduate Thesis*, FNSPE of Czech Technical University Prague, Prague, 2006.
- [43] R. FUČÍK, M. BENEŠ, J. MIKYŠKA, AND T. H. ILLANGASEKARE, *Generalization of the benchmark solution for the two-phase porous-media flow*, in *Finite Elements Models, MODFLOW, and More : Solving Groundwater problems*, 2004, pp. 181–184.
- [44] R. FUČÍK, J. MIKYŠKA, M. BENEŠ, AND T. H. ILLANGASEKARE, *Semi-Analytical Solution of Two-Phase Flow in Porous Media with a Discontinuity*, *Proceedings on the Czech Japanese Seminar in Applied Mathematics*, (2006), pp. 1–8.
- [45] R. FUČÍK, J. MIKYŠKA, M. BENEŠ, AND T. H. ILLANGASEKARE, *An Improved Semi-Analytical Solution for Verification of Numerical Models of Two-Phase Flow in Porous Media*, *Vadose Zone Journal*, 6 (2007), pp. 93–104.
- [46] —, *Semianalytical Solution for Two-Phase Flow in Porous Media with a Discontinuity*, *Vadose Zone Journal*, 7 (2008), pp. 1001–1007.
- [47] R. FUČÍK, J. MIKYŠKA, AND T. H. ILLANGASEKARE, *Evaluation of Saturation-Dependent Flux on Two-Phase Flow Using Generalized Semi-Analytic Solution.*, in *Proceedings of the Czech Japanese Seminar in Applied Mathematics, Faculty of Nuclear Sciences and Physical Engineering, Czech Technical University in Prague*, 2005, pp. 23–35.

G

- [48] M. T. VAN GENUCHTEN, *A Closed-Form Equation for Predicting the Hydraulic Conductivity of Unsaturated Soils.*, *Soil Science Society of America Journal*, 44 (1980), pp. 892–898.
- [49] W. G. GRAY AND S. M. HASSANIZADEH, *Paradoxes and Realities in Unsaturated Flow Theory*, *Water Resources Research*, 27 (1991), pp. 1847–1854.
- [50] —, *Unsaturated Flow Theory Including Interfacial Phenomena*, *Water Resources Research*, 27 (1991), pp. 1855–1863.
- [51] W. G. GRAY AND C. T. MILLER, *Consistent Thermodynamic Formulations for Multiscale Hydrologic Systems: Fluid Pressures*, *Water Resources Research*, 43 (2007).

H

- [52] A. HANYGA AND M. SEREDYŃSKA, *A Dynamic Model of Capillary Hysteresis in Immiscible Fluid Displacement*, *Transport in Porous Media*, 59 (2005), pp. 249–265.

-
- [53] S. HASSANIZADEH, O. OUNG, AND S. MANTHEY, *Laboratory Experiments and Simulations on the Significance of Non-Equilibrium Effect in Capillary Pressure-Saturation Relationship*, Springer Proceedings in Physics, 93 (2004), pp. 3–14.
- [54] S. M. HASSANIZADEH, M. A. CELIA, AND H. K. DAHLE, *Dynamic Effect in the Capillary Pressure-Saturation Relationship and its Impacts on Unsaturated Flow*, Vadose Zone Journal, 1 (2002), pp. 38–57.
- [55] S. M. HASSANIZADEH AND W. G. GRAY, *Mechanics and Thermodynamics of Multiphase Flow in Porous Media Including Interphase Boundaries*, Adv. Water Resour, 13 (1990), pp. 169–186.
- [56] ———, *Thermodynamic Basis of Capillary Pressure in Porous Media*, Water Resources Research, 29 (1993), pp. 3389–3406.
- [57] R. HELMIG, *Multiphase Flow and Transport Processes in the Subsurface : A Contribution to the Modeling of Hydrosystems*, Springer Verlag, Berlin, 1997.
- [58] R. HELMIG AND R. HUBER, *Comparison of Galerkin-type Discretization Techniques for Two-Phase Flow in Heterogeneous Porous Media*, Advances in Water Resources, 21 (1998), pp. 697–711.
- [59] R. HELMIG, A. WEISS, AND B. I. WOHLMUTH, *Dynamic Capillary Effects in Heterogeneous Porous Media*, Computational Geosciences, 11 (2007), pp. 261–274.
- [60] ———, *Variational Inequalities for Modeling Flow in Heterogeneous Porous Media with Entry Pressure*, Computational Geosciences, (2009), pp. 1–17.
- [61] U. HORNUNG, *Homogenization and Porous Media*, Springer, New York, 1997.
- [62] H. HOTEIT, P. ACKERER, R. MOSÉ, J. ERHEL, AND B. PHILIPPE, *New Two-Dimensional Slope Limiters for Discontinuous Galerkin Methods on Arbitrary Meshes*, Int. J. Numer. Meth. Engng., (2004), pp. 2566–2593.
- [63] H. HOTEIT AND A. FIROOZABADI, *Multicomponent Fluid Flow by Discontinuous Galerkin and Mixed Methods in Unfractured and Fractured Media*, Water Resources Research, 41 (2005).
- [64] ———, *An Efficient Numerical Model for Incompressible Two-Phase Flow in Fractured Media*, Advances in Water Resources, 31 (2008), pp. 891–905.
- [65] ———, *Numerical Modeling of Two-Phase Flow in Heterogeneous Permeable Media with Different Capillarity Pressures*, Advances in Water Resources, 31 (2008), pp. 56–73.
- [66] P. S. HUYAKORN AND G. F. PINDER, *Computational Methods in Subsurface Flow*, Academic Press, A Subsidiary of Harcourt Brace Jovanovich, Publishers, New York, London, Paris, San Diego, San Francisco, São Paulo, Sydney, Tokyo, Toronto, 1983.

I

-
- [67] O. IPPISCH, H. VOGEL, AND P. BASTIAN, *Validity Limits for the van Genuchten-Mualem Model and Implications for Parameter Estimation and Numerical Simulation*, Advances in Water Resources, 29 (2006), pp. 1780–1789.

J

- [68] V. JOEKAR-NIASAR, S. M. HASSANIZADEH, AND A. LEIJNSE, *Insights into the Relationships among Capillary Pressure, Saturation, Interfacial Area and Relative Permeability Using Pore-Network Modeling*, *Transport in Porous Media*, 74 (2008), pp. 201–219.

K

- [69] B. H. KUEPER AND E. O. FRIND, *Overview of Immiscible Fingering in Porous Media*, *Journal of Contaminant Hydrology* Vol. 2, (1988), pp. 95–110.
- [70] ———, *Two-Phase Flow in Heterogeneous Porous Media 1. Model Development*, *Water Resources Research*, 27 (1991), pp. 1049–1057.
- [71] ———, *Two-Phase Flow in Heterogeneous Porous Media 2. Model Application*, *Water Resources Research*, 27 (1991).

L

- [72] R. J. LENHARD AND J. C. PARKER, *A Model for Hysteretic Constitutive Relations Governing Multiphase Flow 2. Permeability–Saturation Relations*, *Water Resources Research*, 23 (1987).
- [73] R. J. LENHARD, J. C. PARKER, AND J. J. KALUARACHCHI, *Comparing Simulated and Experimented Hysteretic Two-Phase Transient Fluid Flow Phenomena*, *Water Resources Research*, 27 (1991).
- [74] R. LEVEQUE, *Finite Volume Methods for Hyperbolic Problems*, Cambridge University Press, 2002.
- [75] M. C. LEVERETT, *Capillary Behavior in Porous Solids*, *Trans. AIME*, 142 (1941), pp. 152–169.
- [76] A. LIMSUWAT, T. SAKAKI, AND T. H. ILLANGASEKARE, *Experimental Quantification of Bulk Sampling Volume of ECH₂O Soil Moisture Sensors*, in *29th Annual American Geophysical Union Hydrology Days*, J. A. Ramirez, ed., Colorado State University, Fort Collins, CO, 2009, pp. 39–45.

M

- [77] S. MANTHEY, *Two-Phase Flow Processes with Dynamic Effects in Porous Media - Parameter Estimation and Simulation*, Institut für Wasserbau der Universität Stuttgart, Stuttgart, 2006.
- [78] S. MANTHEY, M. S. HASSANIZADEH, AND R. HELMIG, *Macro-Scale Dynamic Effects in Homogeneous and Heterogeneous Porous Media*, *Transport in Porous Media*, 58 (2005), pp. 121–145.
- [79] F. MARŠÍK, *Continuum Thermodynamics (in Czech)*, Academia, Praha, (1999).
- [80] D. B. MCWHORTER AND D. K. SUNADA, *Exact Integral Solutions for Two-Phase Flow*, *Water Resources Research*, 26 (1990), pp. 399–413.

- [81] ———, *Reply to "Comment on 'Exact integral solutions for two-phase flow'" by Z.-X. Chen, G. S. Bodvarsson, and P. A. Witherspoon*, *Water Resources Research*, 28 (1992), pp. 1479–1479.
- [82] J. MIKYŠKA, *Numerical Model for Simulation of Behaviour of Non-Aqueous Phase Liquids in Heterogeneous Porous Media Containing Sharp Texture Transitions*, *Ph.D. Thesis*, FNSPE of Czech Technical University, Prague, 2005.
- [83] J. MIKYŠKA, M. BENEŠ, AND T. H. ILLANGASEKARE, *Numerical Investigation of Non-Aqueous Phase Liquid Behavior at Heterogeneous Sand Layers Using VODA Multiphase Flow Code*, *Journal of Porous Media*, 12 (2009), pp. 685–694.
- [84] J. MIKYŠKA AND A. FIROOZABADI, *Implementation of Higher-Order Methods for Robust and Efficient Compositional Simulation*, *Journal of Computational Physics*, (2010), pp. 2898–2913.
- [85] Y. MUALEM, *Modified Approach to Capillary Hysteresis Based on a Similarity Hypothesis*, *Water Resources Research*, 9 (1973), pp. 1324–1331.
- [86] ———, *A Conceptual Model of Hysteresis*, *Water Resources Research*, 10 (1974), pp. 514–520.
- [87] ———, *A New Model for Predicting the Hydraulic Conductivity of Unsaturated Porous Media*, *Water Resources Research*, 12 (1975).

N

- [88] M. T. NAKAO, *Error Estimates of a Galerkin Method for Some Nonlinear Sobolev Equations in One Space Dimension*, *Numerische Mathematik*, 47 (1985), pp. 139–157.
- [89] D. NAYAGUM, G. SCHÄFER, AND R. MOSÉ, *Modelling Two-Phase Incompressible Flow in Porous Media Using Mixed Hybrid and Discontinuous Finite Elements*, *Computational Geosciences*, 8 (2004), pp. 49–73.
- [90] M. I. DE NEEF AND J. MOLENAAR, *Analysis of DNAPL Infiltration in a Medium with a Low-Permeable Lens*, *Computational Geosciences*, 1 (1997), pp. 191–214.
- [91] J. L. NIEBER, R. Z. DAUTOV, A. G. EGOROV, AND A. Y. SHESHUKOV, *Dynamic Capillary Pressure Mechanism for Instability in Gravity-Driven Flows; Review and Extension to Very Dry Conditions*, *Transport in Porous Media*, 58 (2005), pp. 147–172.
- [92] J. NIESSNER AND S. M. HASSANIZADEH, *A Model for Two-Phase Flow in Porous Media Including Fluid–Fluid Interfacial Area*, *Water Resour. Res.*, 44 (2008).
- [93] J. NORDBOTTEN AND G. EIGESTAD, *Discretization on Quadrilateral Grids with Improved Monotonicity Properties*, *Journal of Computational Physics*, 203 (2005), pp. 744–760.
- [94] J. M. NORDBOTTEN, M. A. CELIA, H. K. DAHLE, AND S. M. HASSANIZADEH, *Interpretation of Macroscale Variables in Darcy's Law*, *Water Resources Research*, 43 (2007).
- [95] ———, *On the Definition of Macroscale Pressure for Multiphase Flow in Porous Media*, *Water Resources Research*, 44 (2008), p. W06S02.

P

- [96] J. C. PARKER AND R. J. LENHARD, *A Model for Hysteretic Constitutive Relations Governing Multiphase Flow 1. Saturation–Pressure Relations*, Water Resources Research, 23 (1987).
- [97] M. PESZYŃSKA AND S. Y. YI, *Numerical Methods for Unsaturated Flow with Dynamic Capillary Pressure in Heterogeneous Porous Media*, International Journal of Numerical Analysis and Modeling, 5 (2008), pp. 126–149.
- [98] J. PHILIP AND C. VAN DUJIN, *Redistribution with Air Diffusion*, Water Resources Research, 35 (1999), pp. 2295–2300.
- [99] J. R. PHILIP, *Horizontal Redistribution with Capillary Hysteresis*, Water Resources Research, 27 (1991).
- [100] I. S. POP, C. J. VAN DUJIN, J. NIESSNER, AND S. M. HASSANIZADEH, *Horizontal Redistribution of Fluids in a Porous Medium: The Role of Interfacial Area in Modeling Hysteresis*, Advances in Water Resources, 32 (2009), pp. 383–390.
- [101] K. PRUESS, *Grid Orientation and Capillary Pressure Effects in the Simulation of Water Injection into Depleted Vapor Zones*, Geothermics, 20 (1991), pp. 257–277.

R

- [102] L. A. RICHARDS, *Capillary Conduction of Liquids through Porous Mediums*, Physics, 1 (1931), pp. 318–333.
- [103] B. RIVIÈRE, *Discontinuous Galerkin Methods for Solving the Miscible Displacement Problem in Porous Media*, Ph. D. Thesis, The University of Texas at Austin, (2000).

S

- [104] T. SAKAKI AND T. H. ILLANGASEKARE, *Comparison of Height-Averaged and Point-Measured Capillary Pressure–Saturation Relations for Sands Using a Modified Tempe Cell*, Water Resources Research, 43 (2007).
- [105] T. SAKAKI, D. M. O’CARROLL, AND T. H. ILLANGASEKARE, *Direct Laboratory Quantification of Dynamic Coefficient of a Field Soil for Drainage and Wetting Cycles*, American Geophysical Union, Fall Meeting 2007, abstract# H53F-1486, (2007).
- [106] ———, *Direct Quantification of Dynamic Effects in Capillary Pressure for Drainage and Wetting Cycles*, Vadose Zone Journal, 1 (2010), pp. 1–14, DOI: 10.2136/vzj2009.0105.
- [107] M. SARWARUDDIN, A. SKAUGE, AND O. TORSÆTER, *Modelling of Capillary Pressure for Heterogeneous Reservoirs by a Method J -Function*, SCA paper, 35 (2001), pp. 16–19.
- [108] M. H. SCHROTH, S. J. AHEARN, J. S. SELKER, AND J. D. ISTOK, *Characterization of Miller-Similar Silica Sands for Laboratory Hydrologic Studies*, Soil Science Society of America Journal, 60 (1996), pp. 1331–1339.
- [109] R. E. SHOWALTER, *Existence and Representation Theorems for a Semilinear Sobolev Equation in Banach Space*, SIAM Journal on Mathematical Analysis, 3 (1972), p. 527.

- [110] F. STAUFFER, *Time Dependence of the Relations Between Capillary Pressure, Water Content and Conductivity During Drainage of Porous Media*, in *On Scale Effects in Porous Media*, IAHR, Thessaloniki, Greece, 1978.
- [111] S. P. SUTERA AND R. SKALAK, *The History of Poiseuille's Law*, *Annual Review of Fluid Mechanics*, 25 (1993), pp. 1–20.

V

- [112] E. VITÁSEK, *Numerical Methods (in Czech)*, SNTL, Praha, 1987.
- [113] —, *Basics of Numerical Methods for Solving Differential Equations (in Czech)*, Academia, Praha, 1994.

W

- [114] S. WHITAKER, *Flow in Porous Media I: A Theoretical Derivation of Darcy's Law*, *Transport in Porous Media*, 1 (1986), pp. 3–25.